Two-dimensional magnetisation problems in electrical steels

by

Stanislaw Zurek

A thesis submitted to the Cardiff University
in candidature for the degree of Doctor of Philosophy

Wolfson Centre for Magnetics Technology
Cardiff School of Engineering
Cardiff University
Wales, United Kingdom

March 2005

ProQuest LLC
789 East Eisenhower Parkway
P.O. Box 1346
Ann Arbor, MI 48106-1346

To my beloved Wife Anetka

Acknowledgements

The work has been carried out at the Wolfson Centre for Magnetics Technology, Cardiff School of Engineering, Cardiff University, to which I am grateful for providing me the resources needed to complete this project.

I would like to express my gratitude to Dr T. Meydan who supervised this project and also for the guidance and valuable discussion during the investigation.

I would like to thank ORB Electrical Steels Ltd., Newport, United Kingdom for the providing and preparation of most of the specimens used in this investigation.

I am grateful to all the staff and students at the Wolfson Centre for their help, discussions and friendly atmosphere throughout my studies.

Special thanks to Dr R. Rygal and Prof. M. Soinski from Technical University of Czestochowa, Poland, for their incessant encouragement and also for valuable discussion.

Finally, I would like to appreciate the inestimable support, patience and encouragement, which I received from my beloved Wife and Family.

Summary

The power losses occurring under two-dimensional magnetising conditions have received a great deal of attention in recent years. They are very important in the three-phase electrical machines, and have been investigated for a long time in order to understand the physical processes and the mechanism of such losses. However, the accuracy of the measurements of rotational power loss is proved to be not sufficient and the differences between clockwise and anticlockwise power losses have been unexplained for many years.

A computerised two-dimensional single sheet tester for the measurements of power losses in electrical sheet steel have been developed. A unique adaptive iterative digital feedback algorithm has been developed; it allows magnetisation under controlled flux density and magnetic field patterns in wide range of frequency from 1 Hz to 1000 Hz and in various magnetising yokes.

A new type of flux density sensor has been proposed and discussed. The experimentation did not confirm theoretical predictions. Further work needs to be carried out on this subject.

It was found that the power losses measured in clockwise and anticlockwise direction of rotation differ significantly and that this difference is caused mainly by the angular displacement of the flux density and magnetic field sensors. The error of averaging from clockwise and anticlockwise losses has been estimated and the technique for minimising the difference has been mathematically proposed and implemented for the first time. Also, several factors contributing to the clockwise-anticlockwise loss difference have been discussed and their influence assessed.

It has been found that the peak value of power losses measured under controlled flux density or controlled magnetic field patterns differ, and that this difference depends on the anisotropy of the sample. It has been proved that the peak losses for controlled magnetic field might be as much as six times of the losses measured under standardised alternating magnetisation.

The quasi-static hysteresis component of power loss has been investigated for a non-oriented electrical sheet steel. Despite very high flux density of 2.0 T the static loss does not drop to zero. At higher frequencies the eddy current component of the total power loss takes over and causes the peak of the power loss characteristic to vanish. The effect is more visible for thick laminations, as expected.

List of contents

Appendices

Chapter One
Introduction

The losses in soft magnetic materials, especially in electrical sheet steels, are of great economical importance in almost all energy converting electrical machines.

The magnetic cores of three-phase transformers work mostly under pure alternating magnetisation. However, different type of magnetisation is produced in the T-joints of three-limb three-phase transformers. It has been widely reported that in these regions the magnetic material is subjected to rotational magnetisation, which could be of elliptical, circular or lozenge shape [*1.1-1.3*]. In any of these types of magnetisation the power losses are reported to be much higher than under standardised alternating excitation [*1.4-1.11*]. Magnetic excitation, which produces elliptical, circular and also alternating magnetisation at arbitrary direction within the plane of the lamination is termed as "two-dimensional magnetisation". If the excitation causes the rotation of flux density vector, then such magnetisation is also referred to as "rotational magnetisation" or "circular" for the cases where the loci resemble the shape of a circle.

Also in three-phase rotating machines, there are regions where the magnetic material (non-oriented or grain-oriented electrical steel) is magnetised under rotational magnetisation of various shapes. Again, the reported power losses significantly exceed those measured under alternating conditions for given material under test. It is estimated, that the rotational power losses in rotating machines could be responsible for as much as 50% of the total core loss [*1.12*].

Core losses in laminated cores are estimated to dissipate over 3% of all generated electricity [*1.12*]. Therefore, the manufacturers of electrical steel and electrical machines are continuously attempting to lower the intrinsic losses by developing new types of magnetic materials and by using them more effectively through better designs.

The measurement of power losses under alternating magnetisation conditions are precisely defined by the international standards [*1.13*]. However, the power losses generated under non-alternating excitation are not standardised, and an international agreement is still to be proposed. Moreover, similar measurement techniques yield large scattering of measured results, and the power losses measured in clockwise and anticlockwise direction of rotation differ to an unreasonable extent – in some cases reaching even non-physical negative values [*1.14*]. This phenomenon has not been explained so far, in spite of extensive study on the power losses under rotational and two-dimensional magnetising conditions. This investigation provides a thorough analysis of the clockwise-anticlockwise differences. Detailed explanation of the cause of such differences is given together with theoretical calculations and experimental results confirming the findings.

Generally, it is attempted to measure magnetic properties of magnetic materials under circular flux density or magnetic field. The former type is much more frequently used, partially because the power loss measurements under alternating magnetisation are standardised only for controlled flux density conditions, but partially because the controlled magnetic field conditions are more difficult to achieve.

For that reason, there is a lack of comparisons between the power losses measured under circular flux density and circular magnetic field. However, the research indicates that the magnetisation occurring in some parts of magnetic cores of real electrical machines is more synonymous with the controlled magnetic field conditions [*1.15*], rather than with controlled flux density. Part of this project will closely focus on such comparison and will clearly indicate the difference between the losses measured under controlled rotational magnetic field and controlled alternating magnetisation, which is widely used in the characterisation of the soft magnetic materials.

The controlled magnetisation has been always challenging to the researchers. Before the age of computers, the electronic analogue feedback could not provide sufficient control under circular magnetisation – the highest practically obtainable controlled rotational magnetisation was at the level of 1.2 T for grain-oriented electrical steel [*1.14*]. Today, when the processing power of fast computers can be utilised the controlled conditions up to 2.0 T are achievable not only for circular, but also for arbitrary type of magnetisation [*1.16*]. This will be shown in the following chapters.

The aim of this investigation is to understand the influence of various factors on the value of total power loss measured under controlled rotational flux density or controlled rotational magnetic field. In summary, the main objectives of this work are as follows:

1. To design, develop and construct a computerised two-dimensional magnetising and measuring system, capable of characterising electrical sheet steels under two-dimensional and rotational clockwise and anticlockwise magnetisation.

2. To develop a digital adaptive iterative feedback algorithm capable of controlling the arbitrary shape of flux density and magnetic field waveforms/patterns in a frequency range from 1 Hz to 1000 Hz in clockwise and anticlockwise direction of rotation.

3. To carry out the measurements under frequency range from 10 Hz to 250 Hz and under controlled rotational flux density and controlled rotational magnetic field conditions for electrical sheet steels.

4. To study the influence of various theoretical and physical factors affecting the accuracy of power losses measured under rotational magnetising conditions.

5. To analyse the measured results and to interpret them in order to deliver explanation of the phenomena causing the difference in rotational power losses measured in the clockwise and anticlockwise direction of rotation.

6. To compare the total power losses measured under controlled rotational flux density and controlled rotational magnetic field conditions.

1.1. References to Chapter 1

[*1.1*] Radley B., Moses A.J., Apparatus for experimental simulation of magnetic flux and power loss distribution in a turbogenerator stator core, IEEE Transactions on Magnetics, Vol. Mag-17, No 3, 1981, pp. 1311-1316

[*1.2*] Anuszczyk J., Analiza rozkladu indukcji i strat mocy przy przemagnesowaniu obrotowym w obwodach magnetycznych maszyn elektrycznych (*Analysis of localisation of flux density and power loss in rotational magnetisation in magnetic circuits of electric machines*, in Polish), Zeszyty Naukowe Politechniki Lodzkiej, Nr 629, Rozprawy Naukowe z. 158, Lodz, 1991

[*1.3*] Kanada T., Enokizono M., Kawamura K., Sievert J.D., Distributions on localised iron loss of three-phase amorphous transformer model core by using two-dimensional magnetic sensor, IEEE Transactions on Magnetics, Vol. 32, No 5, 1996, pp. 4797-4799

[*1.4*] Proceedings of 1st international workshop on magnetic properties of electrical sheet steel under two-dimensional excitation, Braunschweig, Germany, September 1991

[*1.5*] Proceedings of 2nd international workshop on two-dimensional magnetic measurement and its properties, Oita, Japan, January-February 1992

[*1.6*] Proceedings of 3rd international workshop on magnetic properties of electrical steel sheets under two-dimensional excitation, Torino, Italy, October 1993

[*1.7*] Proceedings of 4th international workshop on 2-dimensional magnetization problems, Cardiff, United Kingdom, September 1995

[*1.8*] Proceedings of 5th international workshop on two-dimensional magnetization problems, Grenoble, France, September 1997

[*1.9*] Proceedings of 6th international workshop on 1&2-dimensional magnetic measurement and testing, Bad Gastein, Austria, September 2000

[*1.10*] Proceedings of 7th international workshop on 1&2 dimensional magnetic measurement and testing, Ludenscheid, Germany, September 2002

[*1.11*] Proceedings of 8th international workshop on 1&2-dimensional magnetic measurement and testing, Ghent, Belgium, September 2004

[*1.12*] Moses A.J., Importance of rotational losses in rotating machines and transformers, Journal of Materials Engineering and Performance, Vol. 1(2), 1992, pp. 235-244

[*1.13*] International Electrotechnical Commission IEC 60404-2 (1996-03), Magnetic materials - Part 2: Methods of measurement of the magnetic properties of electrical steel sheet and strip by means of an Epstein frame

[*1.14*] Sievert J., Ahlers H., Birkfeld M., Conrnut B., Fiorillo F., Hempel K.A., Kochmann T., Lebouc A., Meydan T., Moses A.J., Rietto A.M., Intercomparison of measurements of magnetic losses in electrical sheet steel under rotation flux conditions, Commission of the European Communities, Report EUR 16255 EN, EC Brussels, Luxembourg, 1995

[*1.15*] Hasenzagl A., Pfutzner H., A 3-phase excited test system for simultaneous studies of field vectors, losses, magnetostriction and domains for multi-directional magnetisation, Proceedings of 4th international workshop on 2-dimensional magnetization problems, Cardiff, United Kingdom, September 1995

[*1.16*] **Zurek S.**, Marketos P., Meydan T., Moses A. J., Use of novel adaptive digital feedback for magnetic measurements under controlled magnetizing conditions, IEEE Transactions on Magnetics, (in press, accepted for publication in September 2004)

Chapter Two

Magnetism and rotational magnetisation

2.1. Basic terms

The magnetic field is produced whenever there is an electrical charge in motion. The strength of the magnetic field, *H*, is measured in amperes per metre, [A/m]. The response of a medium to a magnetic field is called flux density, or magnetic induction, *B*, which is measured in teslas, [T]. In the case of free space the relationship between *B* and *H* is linear and can be calculated as

$$B = \mu_0 \cdot H \qquad [\mathrm{T}] \qquad (2.1)$$

where: H is the strength of magnetic field, [A/m]; $\mu_0 = 4 \cdot \pi \cdot 10^{-7}$ is the permeability of free space, [H/m].

For any other non-hysteretic medium the correlation between *B* and *H* should be written as

$$B = \mu_r \cdot \mu_0 \cdot H \qquad [\mathrm{T}] \qquad (2.2)$$

where: μ_r is the relative permeability of the material (dimensionless).

The materials can be classified by the value of their relative permeability: the μ_r is slightly greater than unity for paramagnets and slightly smaller than unity for diamagnets; for ferromagnets[1] μ_r is a function of many factors and its maximum value is much greater than one. Table 2.1 presents μ_r for some paramagnetic, diamagnetic and ferromagnetic materials. (There are also other types of magnetic materials, like ferrimagnetic and anti-ferromagnetic, but since they are of minor importance to this investigation they will not be discussed here.)

Some of the non-ferromagnetic materials are essential in engineering applications. For example, the diamagnetic copper is one of the most common and vital conductors used in most electrical devices, and many of these devices or

---

[1] The terms: para-, dia- and ferromagnets are commonly used instead of para-, dia- and ferromagnetic materials, respectively.

their parts are immersed in the paramagnetic air. The importance of these materials will be further discussed with the description of the *H*-coil (in section 4.1.3).

Table 2.1. The maximum values of relative permeability μ_r for some paramagnets, diamagnets and ferromagnets (after [*2.1*] and [*2.2*])

Material	μ_r	B_{sat}
Free space	1.000 000 00	-
Air	1.000 000 37	-
Al	1.000 02	-
Cu	0.999 99	-
96% Fe, 4% Si (non-oriented)	7 000*	1.97
97% Fe, 3% Si (grain-oriented)[2]	100 000*	2.00
50% Co, 50% Fe (Permendur)	5 000*	2.45
79% Ni, 16% Fe, 5% Mo (Supermalloy)	1 000 000*	0.79
97% Fe, 3% Si (monocrystal)	3 800 000*	2.14

* for ferromagnets only the maximum value of permeability is given - see description in the text below

The value of μ_r can be also treated as a measure of the capability of a material to concentrate the magnetic field. As can be seen from Table 2.1, the ferromagnets are the best "concentrators". However, for these materials, under alternating magnetisation, μ_r is not longer a constant - it is a non-linear function of many parameters (magnetic field, temperature, frequency, mechanical stress etc.), which themselves may vary during the magnetisation process.

For paramagnets and diamagnets the relationship between B and H is linear. The magnetisation curves (or rather lines) can be presented as in Fig. 2.1. For these types of materials relatively low flux density (≈ 0.1T) is produced by very high magnetic field ($\approx 10^5$ A/m). In the case of ferromagnets flux density higher by one order of magnitude can be achieved by magnetic field lower by 3-4 orders [*2.2*].

Ferromagnets respond very well especially to low magnetic field strength (as compared to para- and diamagnets), which in consequence leads to non-linear magnetising characteristics (see Fig. 2.2a).

---

[2] The types of soft magnetic materials are described in section 2.6.

The magnetic cores of electrical machines are designed taking into account the magnetisation curve for specific ferromagnetic material and magnetising conditions, for example in order to make use of the highest obtainable μ_r (see Fig. 2.2b).

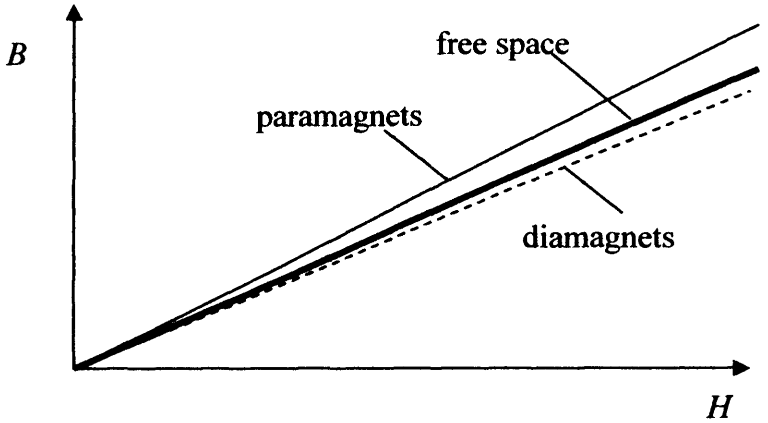

Fig. 2.1. Typical magnetisation curves for para- and diamagnets, [*2.2*]

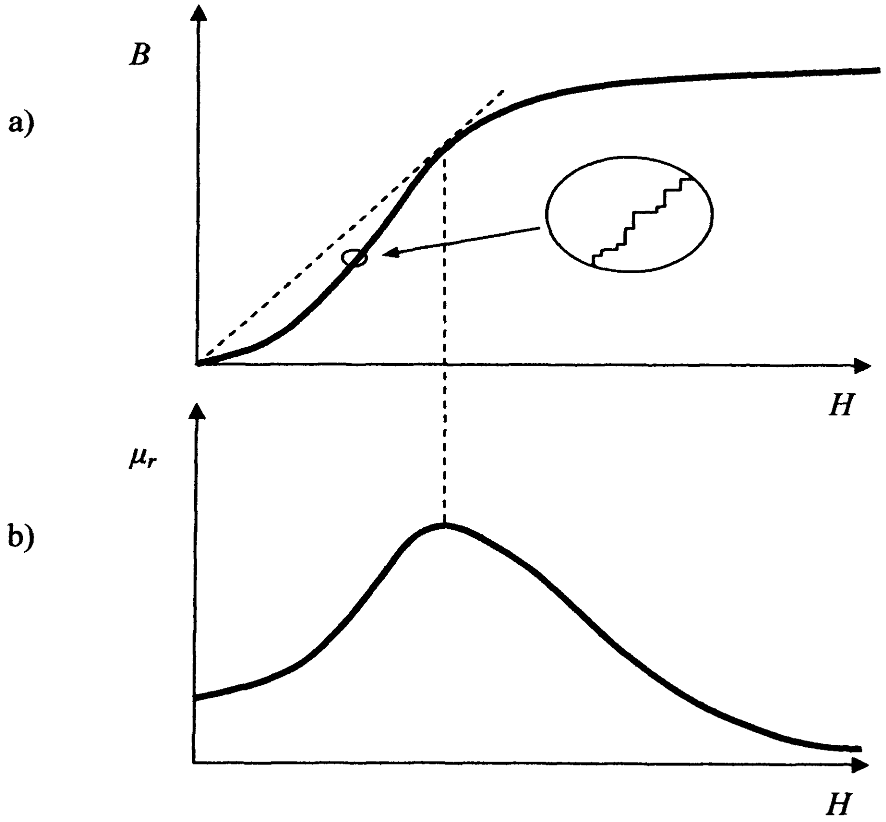

Fig. 2.2. Typical characteristics of ferromagnets: a) *B*-*H* curve (the inset shows the Barkhausen noise explained later in the text), b) corresponding curve of relative permeability μ_r; [*2.2*]

The non-linearity of magnetic properties of ferromagnets is a well known difficulty in designing magnetic circuits. Commonly, the magnetisation curve below the knee is approximated with a straight line. However, this approach is often not sufficient and it is very important to measure, investigate and model phenomena occurring in magnetic materials.

2.2. Alternating magnetisation

As can be seen from the magnification in Fig. 2.2a, the magnetisation curve is not smooth - it consists of many tiny steps. This phenomenon is termed Barkhausen noise and it is caused by the internal magnetic structure of the ferromagnets. Even without an external magnetic field the body of a ferromagnet is divided into many small regions called magnetic domains, which are spontaneously magnetised up to the saturation.

The domains tend to distribute themselves in order to minimise the energy so that the material does not produce any external field (Fig. 2.3). The domains are separated by domain walls, which are positioned in local energy minima caused by: local impurities, crystal dislocations, surface defects, etc. [*2.3*]. Therefore, in practice, the domain structure is usually much more complex than that shown in Fig. 2.3c.

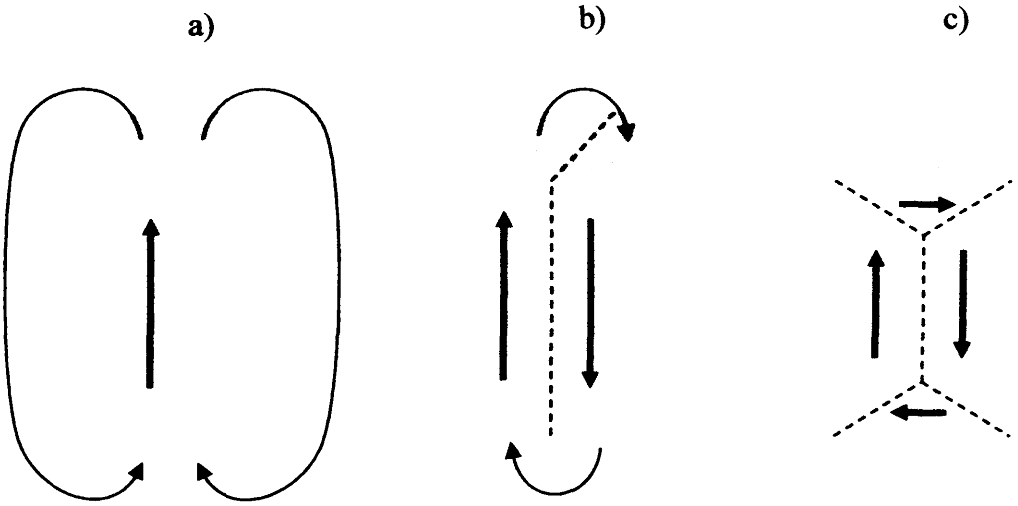

Fig. 2.3. The explanation of energy minimisation in ferromagnets: a) single-domain state producing large external magnetic field, b) two-domain state with much lower external field, c) four-domain state with closure domains and zero external field; (after [*2.4*])

When the ferromagnetic material is subjected to an external magnetic field then the conditions for local energy minima are altered; the domain walls move and therefore the domains size change. The higher the external field is, the bigger are the domains whose spontaneous magnetisation directions are close to the direction of the external field (see Fig. 2.4). Further increase of the external field causes the domains with favoured direction to occupy the whole volume of the magnetised material (point *4* in Fig. 2.4). If the external field is even greater, the vectors of magnetisation in each domain rotate and become closer and closer to the direction of the external field. For very high fields the whole body of a ferromagnet is a single domain (point *6* in Fig. 2.4), with the magnetisation direction parallel to the direction of external field. This state is called saturation - further increase in external field does not cause any increase of polarisation, J.

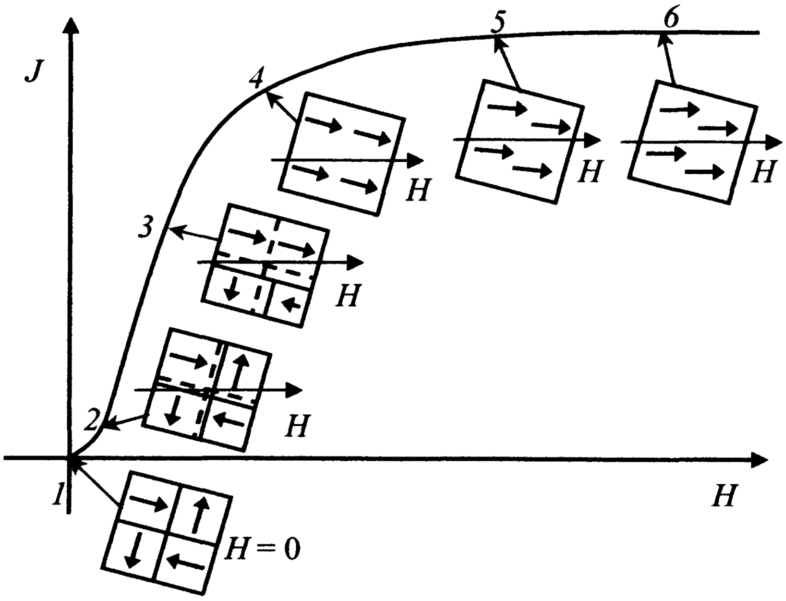

Fig. 2.4. Changes in domain structure as the material is magnetised up to saturation: *1* - demagnetised state with no external field, *2* - domain wall movement, *3* - rapid change of domain direction, *4* - single domain state, *5* - rotation of the domain, *6* - saturation; *J* - polarisation (see equation 2.4); (after [*2.5*])

Nonetheless, the flux density in the ferromagnet will increase with the increase of the external field due to the contribution of the "$\mu_0 \cdot H$" in equation (2.1). Therefore, for the ferromagnets, the equation (2.2) can be written as

$$B = \mu_0 \cdot (H + M) \qquad [\mathrm{T}] \qquad (2.3)$$

where M is the magnetisation of the material, [A/m].

Equation (2.3) is equivalent to

$$B = \mu_0 \cdot H + J \qquad [\mathrm{T}] \qquad (2.4)$$

where J is the polarisation of the material, [T].

(For lower fields $B \cong J$ and often the "$\mu_0 \cdot H$" part is neglected in the measurements. However, standardised methods of measuring of magnetic properties require that only J should be measured. This can be achieved by compensation of the free space contribution, as recommended in [*2.6*].)

The subsequent stages in Fig. 2.4 can be matched with appropriate points on the magnetisation curve (compare Fig. 2.4 and Fig. 2.5). However, if the magnetising field is decreased from the saturation (point *6* in Fig. 2.4 and Fig. 2.5) to zero, then the polarisation will follow a different path than in the initial process, that is from point *6* to *7*, rather than to point *1*. This is because some of the processes during the magnetisation are irreversible. The energy used in these processes is partially dissipated and partially stored in the ferromagnet in the form of residual polarisation, J_R. Hence, there will be also a residual flux density, which is also called remanence, B_R,

The magnetic field needed to bring the residual flux density to zero is called coercive force, H_C, and it is shown in Fig. 2.5 as the point *8*. Further increase of the magnetic field in the opposite direction will again saturate the ferromagnet (point *6'*). If the process is repeated once again in the initial direction, then the magnetisation will be moved back to the point *6*.

It can be seen from Fig. 2.5 than one complete cycle of magnetisation produces a *B-H* loop (also referred as a hysteresis loop). The area enclosed by the *B-H* loop is proportional to the total power loss dissipated in the ferromagnet during one cycle of magnetisation.

The properties of the *B-H* loop are used to characterise ferromagnets. If the loop is narrow (low power losses and low magnetic energy storing) then such ferromagnets are called "soft magnetic materials"; if the loop is wide (high power losses, but also high magnetic energy storage) then such ferromagnets are named as "hard magnetic materials". Obviously, the ideal soft magnetic material would have anhysteretic *B-H* characteristic, hence no losses.

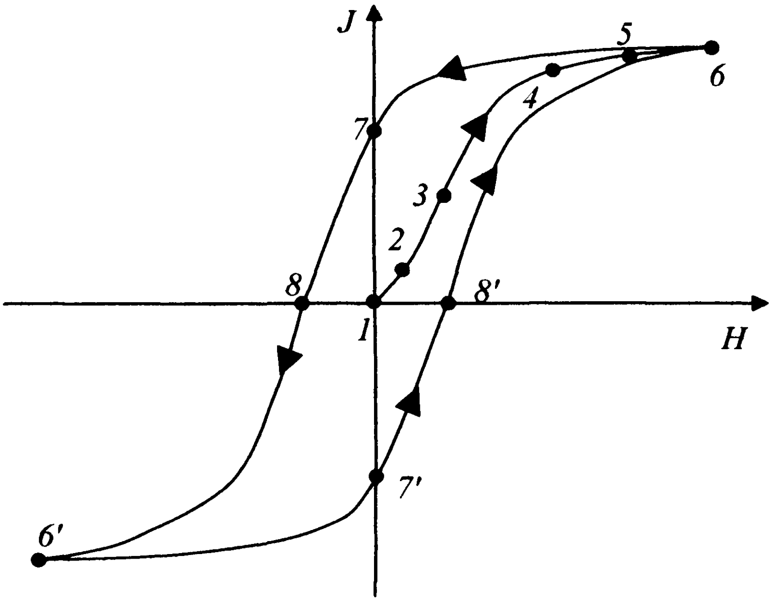

Fig. 2.5. *B-H* loop (hysteresis loop) of ferromagnets: points *1* to *6* are equivalent to those from Fig. 2.4; *7* - state after removing the magnetic field (B_R); *8* - negative magnetic field applied in order to bring the flux density to zero (H_C); *6'*, *7'* and *8'* - points equivalent to 6, 7 and 8, respectively

2.3. Power losses under alternating magnetisation

The shapes of *B-H* loops vary for different magnetic materials and magnetising conditions. For example, the influence of eddy currents causes higher energy loss at higher frequencies of magnetisation (due to the Joule heat effect), which is visible in the increased width of the *B-H* loop. Under certain assumptions (thin lamination, uniform flux density in the lamination) the eddy current contribution to the power loss can be calculated providing that the physical properties of the magnetic material and its dimensions are known:

$$P_e = \frac{\pi^2 \cdot d^2 \cdot B_{peak}{}^2 \cdot f^2}{6 \cdot \rho \cdot D} \qquad [\mathrm{W/kg}] \qquad (2.5)$$

where: d - thickness, [m]; B_{peak} - peak flux density, [T]; f - frequency, [Hz]; ρ - resistivity, [Ω·m]; D - density, [kg/m^3]; (after [*2.4*]).

As it can be seen from equation (2.5) the eddy current component of power loss is proportional to the square of thickness of ferromagnetic material under magnetisation. Therefore, the magnetic cores of electrical machines are made from thin laminations in order to minimise the thickness, and thus the power loss, which otherwise could reach very high values, especially at higher frequencies.

Hysteresis loss cannot be as easily estimated as the eddy current loss, but at very low magnetising frequency (below 1 Hz) the eddy currents become negligible and only the hysteresis component is assumed to be present [*2.7, 2.8*]. This allows using a very simplistic method (thus inaccurate) of separating the power loss into eddy current and hysteresis component, which is thought to be linearly dependent on frequency (Fig. 2.6).

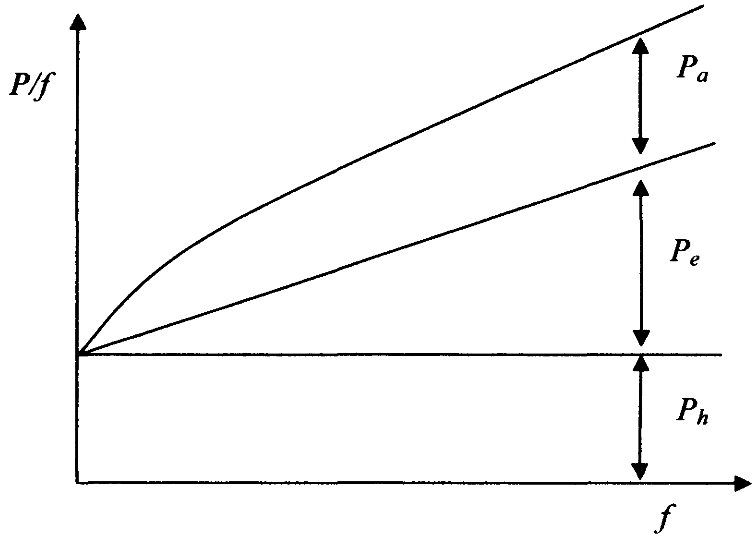

Fig. 2.6. The simplistic concept of separating the power loss into hysteresis and eddy currents components, P_h - hysteresis loss, P_e - eddy current loss, P_a - anomalous loss (excess loss), [*2.9*]

However, as it is shown in Fig. 2.6, the estimated eddy current loss added to the estimated hysteresis loss obtained by low-frequency measurements does not result in the total measured power loss. The difference has been named as anomalous loss or excess loss. Therefore, the equation for total power loss (in the simplistic method showed above) can be written as:

$$P_{tot} = P_h + P_e + P_a \qquad \text{[W/kg]} \qquad (2.6)$$

where: P_{tot} - total power loss, P_h - hysteresis loss, P_e - eddy current loss, P_a - anomalous loss.

Some empirical equations were proposed, which relate the hysteresis, eddy currents and anomalous losses [*2.7*], but so far a full explanation of anomalous loss is still to be achieved.

The total power loss in a ferromagnetic material subjected to an alternating magnetic field is directly proportional to the area of the hysteresis loop and can be calculated by means of fieldmetric method from the following equation:

$$P_t = \frac{f}{D} \cdot \int_0^T \left(H \cdot \frac{\mathrm{d}B}{\mathrm{d}t} \right) \mathrm{d}t \qquad [\mathrm{W/kg}] \qquad (2.7)$$

where: P_t – total power loss, [W/kg]; f – frequency of magnetisation, [Hz]; D – specific density of magnetised material, [kg/m^3]; T - cycle of magnetisation, [s]; H – magnetising field, [A/m]; B – flux density, [T]; t – time, [s]

2.4. Rotational magnetisation

Independent from the alternating magnetisation there is also rotational magnetisation condition, in which the vector of flux density (or magnetic field) changes not only the magnitude as in alternating conditions, but also its direction. The rotational magnetisation occurs commonly in the cores of three-phase transformers and rotating machines as depicted in Fig. 2.7. The phenomenon is known for many years and widely reported [*2.10-2.15*]. In rotating machines, the rotational magnetisation occurs behind the teeth and might be responsible for as much as 50% of total core loss [*2.16*]. In the three-phase three-limb transformers the rotational magnetisation appears mainly in the T-joints; the contribution to total power loss is rather small, but it may cause local overheating of the magnetic material, which could lead even to destruction of such transformer.

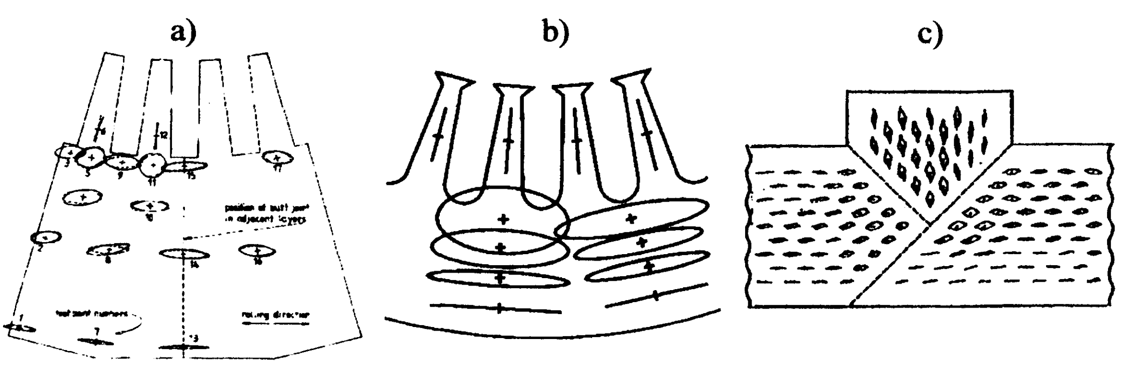

Fig. 2.7. Rotational magnetisation in three-phase machines: a) in turbogenerator stator core [*2.11*], b) in electric motor core [*2.14*], c) at the T-join of three-limb power transformer [*2.15*]

2.5. Power losses under rotational magnetisation

The rotational magnetisation can be analysed as a superposition of alternating and circular processes, as presented in Fig. 2.8. The alternating magnetisation is quite well understood and described, therefore most of the investigation of rotational magnetisation is focused only on the pure circular component, which is much more difficult to study and explain than the alternating one.

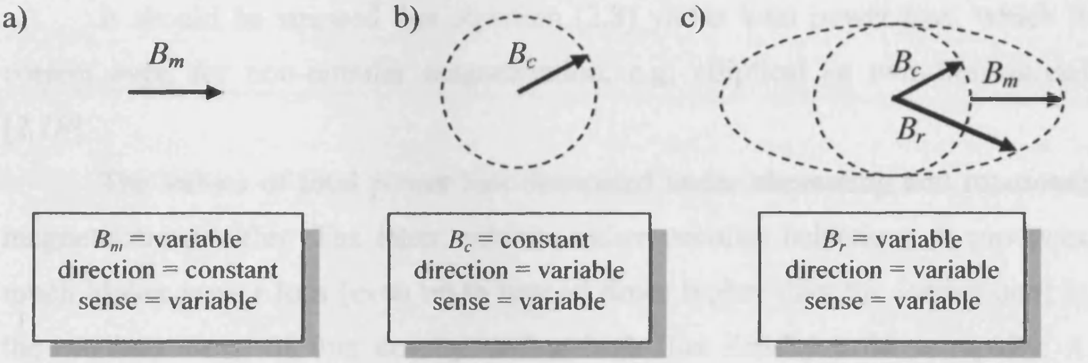

Fig. 2.8. Three types of magnetisation: a) alternating (the magnitude B_m changes, while the direction is constant), b) circular (only direction changes, the magnitude B_c of circular flux density is constant), c) rotational (the magnitude and direction of rotational flux density vector, B_r, changes); (after [*2.17*])

If the rotational magnetic field is applied to a specimen of isotropic ferromagnetic material, then the vector of flux density rotates at the same angular frequency and velocity, but it lags the magnetic field by some angle, ϕ. This can be schematically presented as in Fig. 2.9.

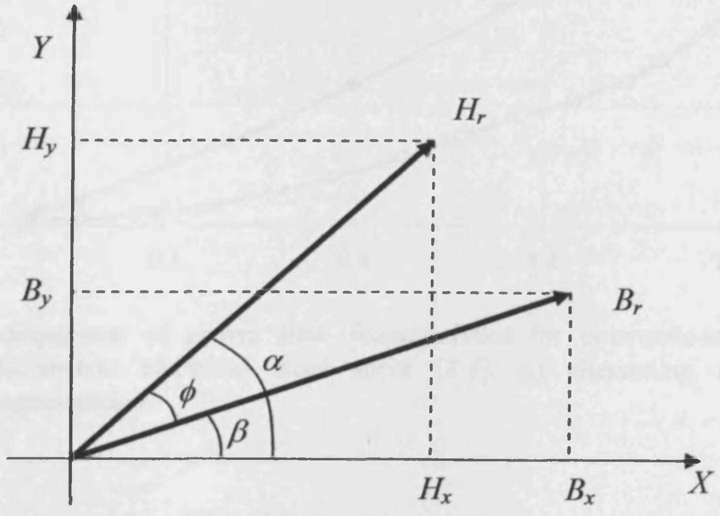

Fig. 2.9. Representation of rotational magnetisation and orthogonal components of magnetic field and flux density.

For rotational or two-dimensional magnetisation (i.e. different from alternating) the H and B vectors can be decomposed into two components - for X and Y directions. Therefore the equation (2.7) becomes equivalent to:

$$P = \frac{f}{D} \cdot \int_0^T \left(H_X \cdot \frac{\mathrm{d}B_X}{\mathrm{d}t} + H_Y \cdot \frac{\mathrm{d}B_Y}{\mathrm{d}t} \right) \mathrm{d}t \qquad [\mathrm{W/kg}] \qquad (2.8)$$

where: X, Y – denote components of the vectors in directions X and Y, respectively.

It should be stressed that equation (2.8) yields total power loss, which is correct even for non-circular magnetisation, e.g. elliptical or two-dimensional [*2.18*].

The values of total power loss dissipated under alternating and rotational magnetisations differ. The latter exhibits rather peculiar behaviour. It produces much higher power loss (even up to several times higher than the former one) in the medium range of flux density, and at high flux density it drops rapidly. A comparison of typical power loss characteristics under alternating and rotational magnetisation is presented in Fig. 2.10.

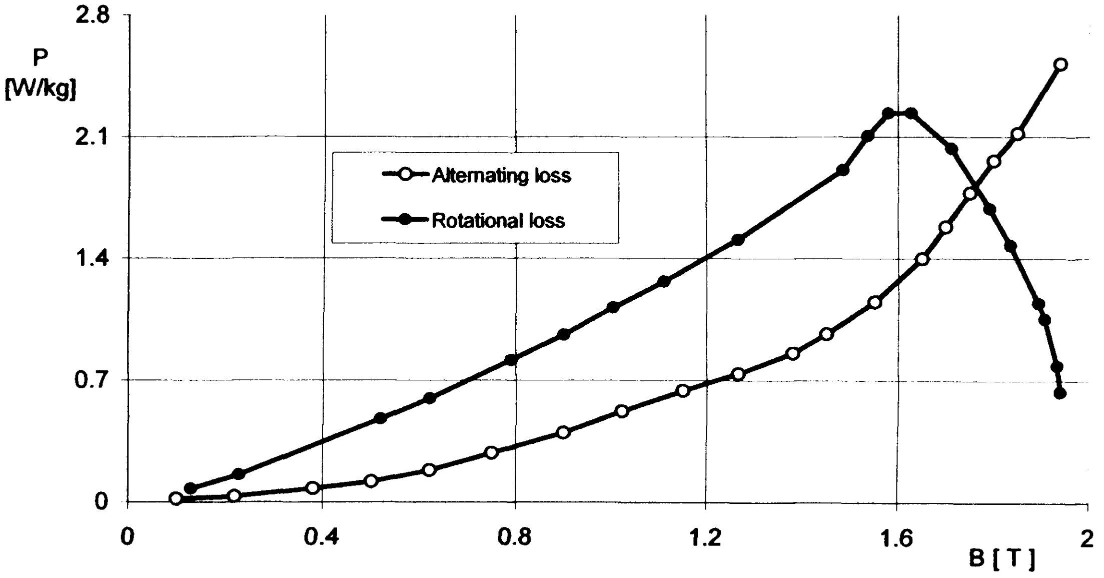

Fig. 2.10. Comparison of power loss characteristics for conventional grain-oriented silicon-iron electrical steel sheet [*2.4*]: a) alternating and b) circular magnetisation

The magnetic cores of three-phase electrical machines made out of conventional electrical steels are designed to work at sinusoidal (alternating) flux density with the peak value B_m between 1.3 T and 1.7 T. As can be seen from Fig. 2.10, this is the range where the rotational power loss achieves its peak. The rotational power loss in rotating machines may be responsible even up to 50% of total loss in the core (see Fig. 2.7a and 2.7b) [*2.16*]. There are two distinct disadvantages: first - because the rotational magnetisation is not taken directly into account in the design process, which causes poorer performance of the magnetic core in the regions subjected to the rotational magnetisation; and second - because dissipation of much higher power loss may cause local overheating of the core, which may in turn cause degradation of the magnetic properties or in extreme case even destruction of the electrical machine.

The change of the monotonicity of the characteristic in Fig. 2.10 is caused by a hysteresis component of the power loss. The higher the flux density the more the magnetic material is saturated. In effect, there is less domain walls, whose movement, creation and annihilation cause hysteresis loss. At very high flux density the material is almost saturated, hence only one domain exist. In the absence of domain walls the hysteresis component of power loss drops rapidly.

The decrease of power loss near to saturation of magnetisation is more pronounced for circular magnetisation than for elliptical. This is because the elliptical one contains an alternating component (see Fig. 2.8), in which the power loss increases with the flux density (see also Fig. 2.10).

As for alternating magnetisation, under very low magnetising frequency the influence of eddy currents in the total power loss can be neglected for circular magnetisation (see Fig. 2.6). Typical characteristics $P/f = \mathrm{f}\ (f)$ for circular magnetisation have similar shapes as those presented in Fig. 2.6 for alternating conditions. However, at higher frequencies the eddy current component of power loss becomes much higher than the hysteresis one, thus the drop in the power loss becomes less and less visible. For thick laminations, e.g. non-oriented electrical steel, magnetised at higher frequencies (above 250 Hz) there is no drop in the characteristics of total power loss. This will be discussed in **Chapter 5**.

2.6. Soft magnetic materials subjected to rotational magnetisation

There are three most important metals, which exhibit ferromagnetic properties: iron (Fe), cobalt (Co) and nickel (Ni). These metals and their alloys are commonly used for magnetic cores of electrical machines.

The rotational magnetisation occurs in magnetic cores of three-phase machines, which are usually designed for medium and high power applications. Such machines are commonly of large size, because the power capacity of a device is proportional to the cross-section area of the magnetic core used. Therefore, the designer of an electrical machine is forced to compromise the magnetic properties of given material as well as its commercial and practical use.

In three-phase rotating machines the core is magnetised in various directions: along the teeth of the stator, and perpendicularly at the back of the core (see Fig. 2.7a and 2.7b). The manufacturing regime requires that the laminations must be cut from a single piece of electrical steel sheet. Therefore, it is obvious that the material used must have good magnetic properties at any direction, which means that ideally it should be as isotropic as possible. The cheapest available ferromagnetic material, which fulfils this condition is so-called non-oriented electrical steel sheet. Although this material is meant to be "cheap", its manufacturing is quite a complex process and will not be described here. However, rolling of the material increases its price, therefore the thinner the lamination, the more expensive is to manufacture it (thin lamination is more efficient, but also more expensive). As a result, cheap low-efficient three-phase motors are made of thick laminations (0.5 mm and thicker). Highly efficient and therefore expensive machines are made from thin sheets (e.g. 0.35 mm).

Due to the relatively high thickness of these type of materials the eddy current loss is larger than in other types of electrical steels. Also, small grains increase the hysteresis power loss. Therefore the total power loss is relatively high at alternating as well as at rotational magnetising conditions.

There are many grades of non-oriented steel. The classification is based on many factors, like for example: thickness, specific power loss, content of silicon, type of used insulation, thermal processing, etc. Nonetheless, all these grades have quite high isotropy and rather easily allow producing rotational (circular) magnetisation in experimental conditions.

In three-phase transformers, the vast volume of a magnetic core is magnetised in an alternating manner, thus the requirements of good magnetic properties regard only the direction at which the material is magnetised (see Fig. 2.7c). Thus, the electrical steel used for transformers is manufactured in a way, so as to induce optimal magnetic properties in the direction concerned, which is often synonymous with the rolling direction. In such materials, termed grain-oriented electrical steel, many techniques are used in order to reduce the power loss and increase the permeability. The grain-oriented steel has usually high silicon content and low thickness, which reduces the power loss. Also optimal grain size and methods of refining the domain structure allow achieving very high permeability and further lowering of the power loss. However, all of these processes are focused only on improving of the properties in the privileged direction; at the expense of the properties in the other directions.

Thus, if grain-oriented steel is magnetised at some angle to the rolling direction much higher losses occur. If such material is exposed to rotational field the losses will be even higher (see Fig. 2.10).

The measurements of power loss under rotational magnetisation is not an easy task, and tends to be more difficult for higher grades of grain-oriented electrical steels. This is due to very high anisotropy of such materials. With the aid of special magnetising systems the measurements of rotational power loss in grain-oriented laminations is possible in laboratory conditions, but the accuracy is still being questioned [*2.19*].

2.7. References to Chapter 2

[*2.1*] Jiles D., Introduction to magnetism and magnetic materials, Chapman & Hall, London, UK, 1991

[*2.2*] Soinski M,. Materialy magnetyczne w technice (*Magnetic materials in engineering*, in Polish), Biblioteka COSiW SEP, Warsaw, Poland, 2001

[*2.3*] Aharoni A., Introduction to the theory of ferromagnetism, Oxford Science Publications, Clarendon Press, Oxford, UK, 1996

[*2.4*] Bozorth R.M., Ferromagnetism, D. Van Nostrand Company, Inc., Princeton, New Jersey, USA, 1951

[*2.5*] Braisford F., Magnetic materials, Methuen & Co. Ltd., London, UK, 1954

[*2.6*] International Electrotechnical Commission IEC 60404-2 (1996-03), Magnetic materials - Part 2: Methods of measurement of the magnetic properties of electrical steel sheet and strip by means of an Epstein frame

[*2.7*] Bertotti G., General properties of power losses in soft ferromagnetic materials, IEEE Transactions on Magnetics, Vol. 24, No 1, 1998, pp. 621-630

[*2.8*] Gozdur R., Wyznaczanie quasi-statycznej petli histerezy blach elektrotechnicznych, (*Determination of quasi-static hysteresis loop of electrical steel,* in Polish), Przeglad Elektrotechniczny, Nr 80, 2-2004, pp.147-149

[*2.9*] Beckley P., Electrical Steels, European Electrical Steels, Newport, South Wales, UK, 2000

[*2.10*] Moses A.J., Thomas B., Problems in the design of power transformers, IEEE Transactions on Magnetics, Vol. Mag-10, No 2, 1974, pp. 148-150

[*2.11*] Radley B., Moses A.J., Apparatus for experimental simulation of magnetic flux and power loss distribution in a turbogenerator stator core, IEEE Transactions on Magnetics, Vol. Mag-17, No 3, 1981, pp. 1311-1316

[*2.12*] Moghadam A.T., Moses A.J., Comparison of flux distribution in three-phase transformer cores assembled from amorphous material and grain oriented silicon iron, IEEE Transactions on Magnetics, Vol. 25, No 5, 1989, pp. 3964-3966

[*2.13*] Moses A.J., Comparison of transformer loss prediction from computed and measured flux density distribution, IEEE Transactions on Magnetics, Vol. 34, No. 4, 1998, pp. 1186-1188

[*2.14*] Anuszczyk J., Analiza rozkladu indukcji i strat mocy przy przemagnesowaniu obrotowym w obwodach magnetycznych maszyn elektrycznych (*Analysis of localisation of flux density and power loss in rotational magnetisation in magnetic circuits of electric machines*, in Polish), Zeszyty Naukowe Politechniki Lodzkiej, Nr 629, Rozprawy Naukowe z. 158, Lodz, 1991

[*2.15*] Kanada T., Enokizono M., Kawamura K., Sievert J.D., Distributions on localised iron loss of three-phase amorphous transformer model core by using two-dimensional magnetic sensor, IEEE Transactions on Magnetics, Vol. 32, No 5, 1996, pp. 4797-4799

[*2.16*] Moses A.J., Importance of rotational losses in rotating machines and transformers, Journal of Materials Engineering and Performance, Vol. 1(2), 1992, pp. 235-244

[*2.17*] Pluta W., Wplyw anizotropii magnetycznej blach elektrotechnicznych na straty mocy przy przemagnesowaniu obrotowym, (*The influence of magnetic anisotropy of electrical steel sheets on the power loss under rotational magnetisation*, in Polish), PhD thesis, Technical University of Lodz, Poland, 2001

[*2.18*] Alinejad-Beromi Y., Moses A.J., Meydan T., New aspects of rotational field and flux measurement in electrical steel, Journal of Magnetism and Magnetic Materials, Vol. 112, 1992, pp. 135-138

[*2.19*] Sievert J., Ahlers H., Birkfeld M., Conrnut B., Fiorillo F., Hempel K.A., Kochmann T., Lebouc A., Meydan T., Moses A.J., Rietto A.M., Intercomparison of measurements of magnetic losses in electrical sheet steel under rotation flux conditions, Commission of the European Communities, Report EUR 16255 EN, EC Brussels, Luxembourg, 1995

Chapter Three

Previous research in rotational magnetisation

The general shape of rotational hysteresis loss characteristic was for the first time published by Baily in 1896, after it was predicted as a consequence of the Ewing theory [*3.1*]. Initially, the researchers used the magnetometer method, where the round sample under test was slowly rotated in the applied magnetic field. This approach was used in 1938 by Brailsford [*3.2*]; the apparatus is shown in Fig. 3.1.

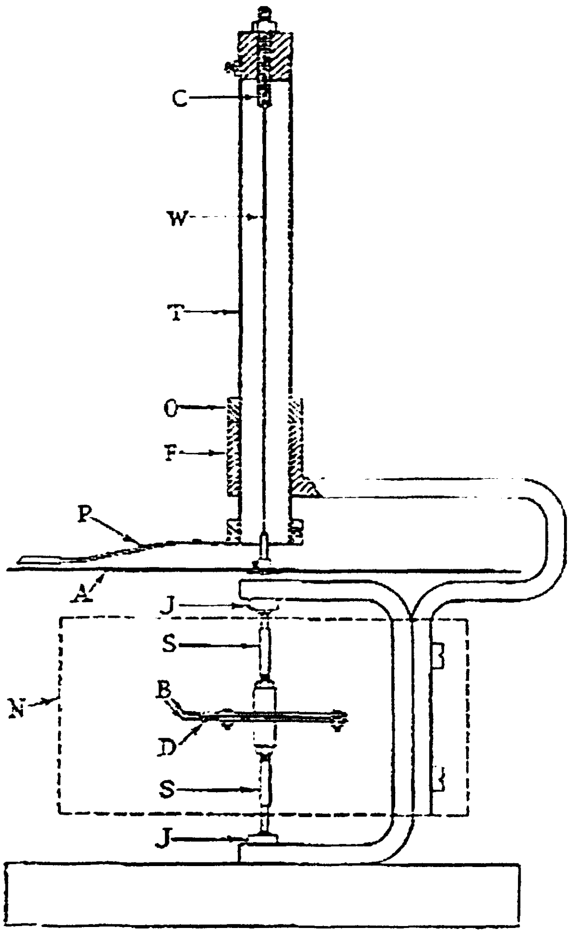

Fig. 3.1. Magnetometer used by Brailsford for measuring the rotational loss [*3.2*]: C – adjusting screw, W – phosphor-bronze wire, T – brass tube, O – collar, F – supporting frame, P – pointer, A – aluminium disk, J – jewel bearings, S – spindles, N – electromagnet, B – brass discs

The magnetometer allowed measuring the rotational power loss up to high flux density; hence, the drop in total power loss near the saturation of the sample has been observed. The measurements were taken at very low speed of rotation to avoid the influence of eddy currents. Therefore, other approaches had to been taken in order to measure the losses at higher frequencies of magnetising field.

In 1947 Brailsford [*3.3*] developed a rotational field apparatus and measured eddy current loss in a disc sample. The rotating field in the specimen was produced by means of three pairs of Helmholtz coils. The coils had different diameters as to enable to position them at 0, 120 and 240 degrees respectively (Fig. 3.2).

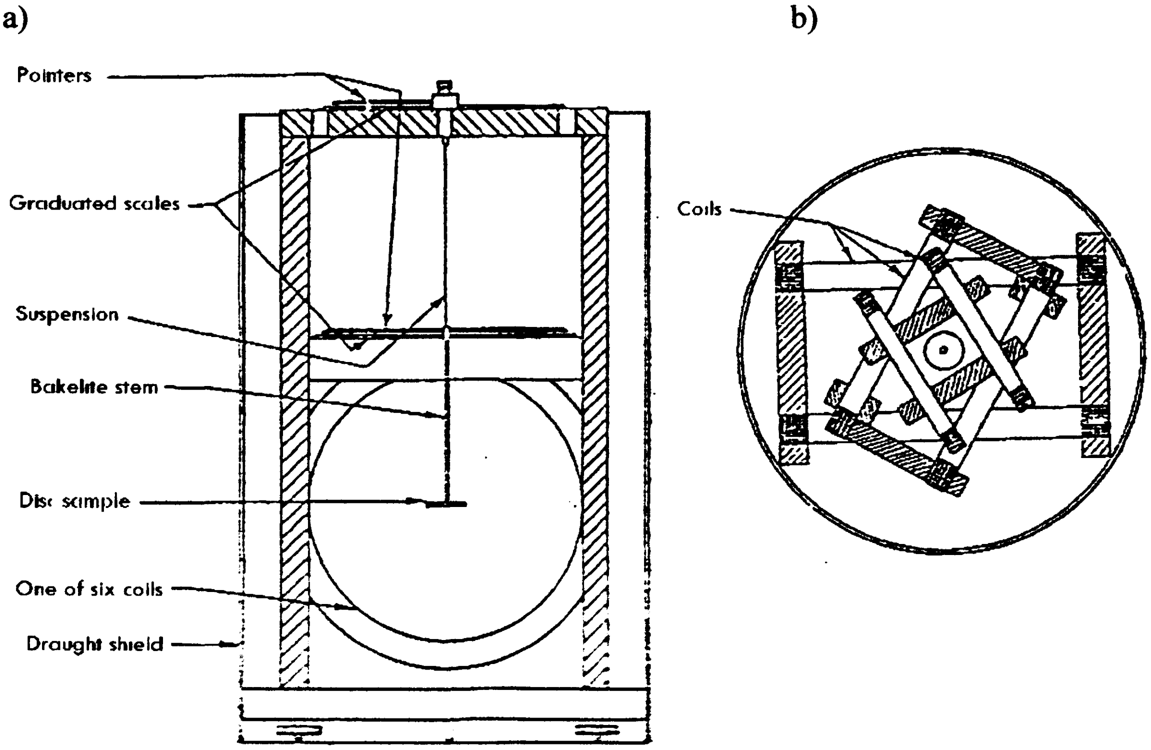

Fig. 3.2. A three-phase magnetising setup utilising three pairs of Helmholtz coils used by Braislford [*3.3*]: a) side view, b) top view

In 1955, Kornetzki and Lucas introduced a theory of hysteresis loss based on simple domain structure [*3.4*], as shown in Fig. 3.3. They postulated that under alternating magnetic field only 180° domains are affected, thus producing power loss. However, under rotational magnetisation all the domains (i.e. 180° and also 90°) would expand or contract. Therefore the ratio 2:1 of the power loss under rotating and alternating conditions was predicted for most of the magnetisation range. However, due to additional Barkhausen jumps during the rotation, this simple interpretation was not expected to be exact.

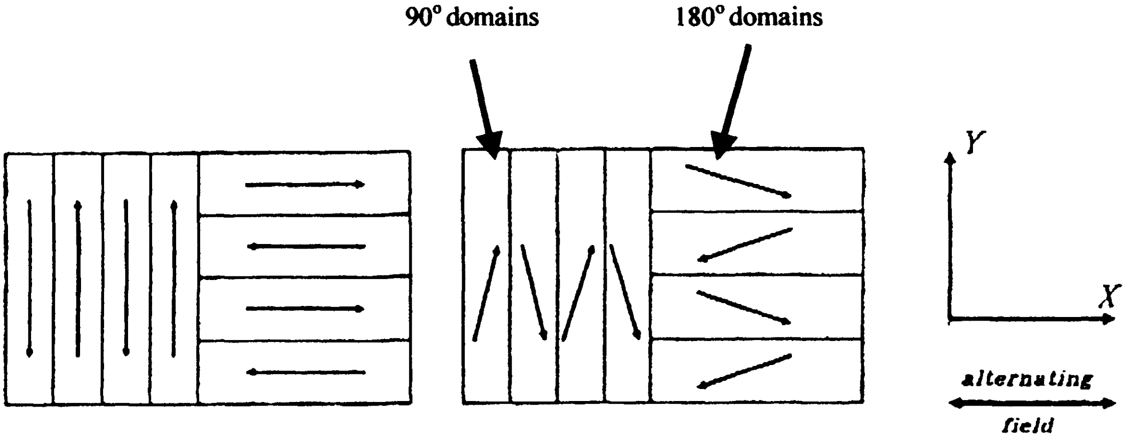

Fig. 3.3. Simple configuration showing 90^0 and 180^0 domains used by Kornetzki and Lucas [*3.4*]

In 1964, Boon and Thompson [*3.5*] using the magnetometer technique studied the rotational hysteresis in single crystals of silicon-iron. They investigated the static domain structures at different angles of magnetisation, and showed that the rotational hysteresis loss could be as high as eight times the alternating one for some cases of rotational magnetisation.

In 1965 Boon and Thompson [*3.6*] developed an apparatus for the measurement of alternating and rotational power loss at 50 Hz in 3% Si-Fe samples. The basic features of the apparatus are shown in Fig. 3.4. The power loss was measured by means of thermocouples, which were attached to a specimen (1 inch square), located at the centre of a stack of similar pieces of Si-Fe. Alternating and rotational flux was obtained from two pairs of C-cores mounted perpendicular to each other.

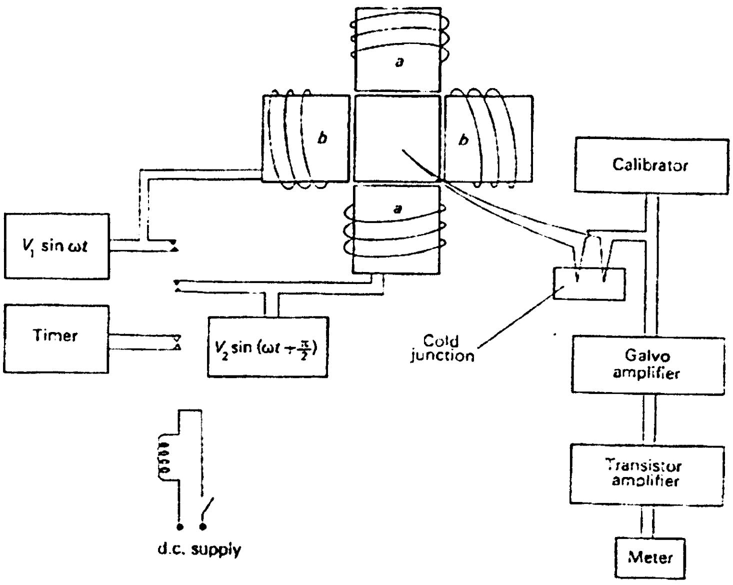

Fig. 3.4. A two-phase magnetising system with the thermometric method of power loss measurement used by Boon and Thompson [*3.6*]

In 1972 Moses, Thomas and Thompson studied the distribution of the power loss in the T-joint of a three-phase transformer core [*3.7*]. The experiments was carried out by means of a great number of small search coils placed in the T-joint of the transformer, as shown in Fig. 3.5a.

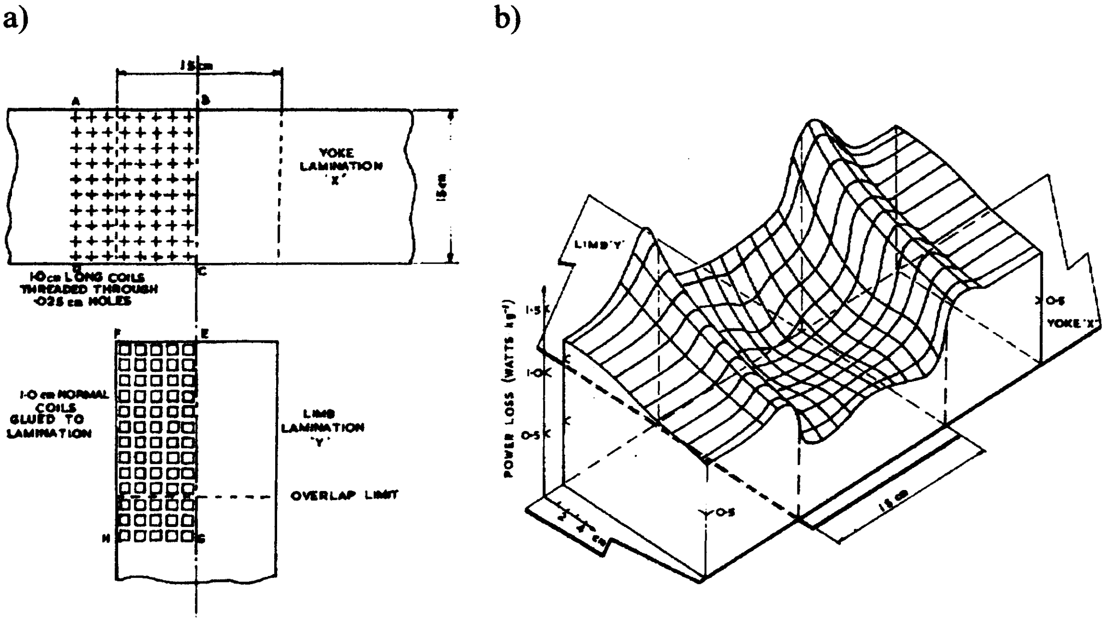

Fig. 3.5. The investigation of T-joint of transformer: a) positioning of the sensors, b) power loss pattern [*3.7*]

The results revealed that the power loss dissipated in the T-joint of a three-phase transformer is significantly higher than in the limbs (Fig. 3.5b). Later work confirmed the findings with similar results [*3.8*, *3.9*], see Fig. 3.6.

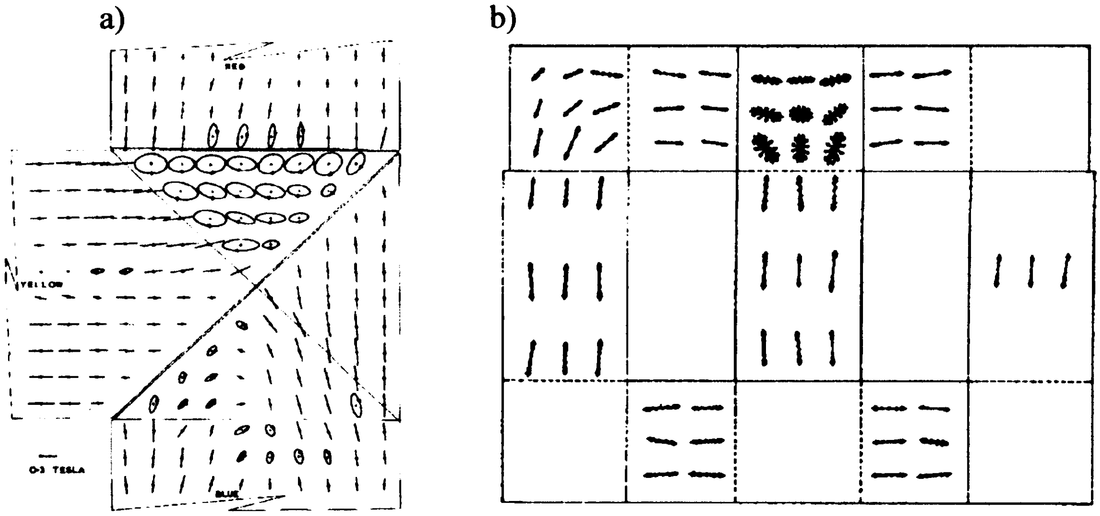

Fig. 3.6. Examples of rotational flux in the T-joint of three-phase transformer made of: a) grain-oriented electrical steel sheet [*3.8*], b) amorphous ribbon [*3.9*]

In 1973 Moses and Thomas described a method for calculating the magnitude and direction of the instantaneous flux density in the thin lamination of magnetic material [*3.10*]. The schematic diagram of the apparatus used for measuring the alternating and rotating flux in a cross shaped sample is shown in Fig. 3.7. The magnetising coils were energised from 50 Hz sinusoidal voltage source 90 degrees out of phase, whose relative magnitudes could be arbitrarily varied.

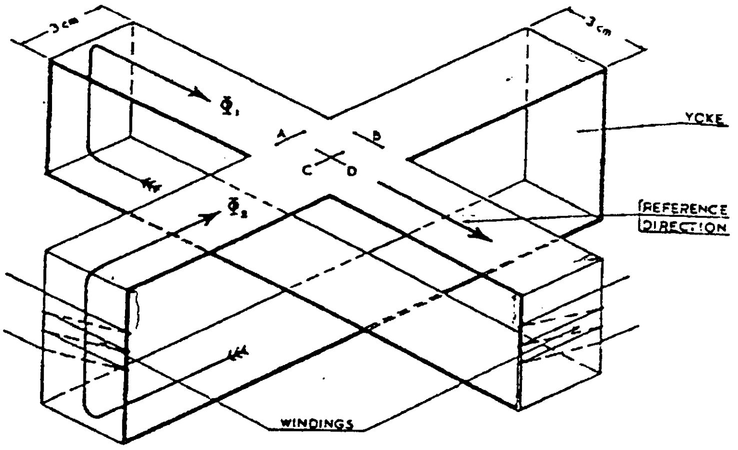

Fig. 3.7. A cross-shaped sample used by Moses and Thomas [*3.10*]

In 1981 Radley and Moses simulated the magnetisation of turbogenerator stator core [*3.11*]. The experimental setup and an example of measured results are presented in Fig. 3.8.

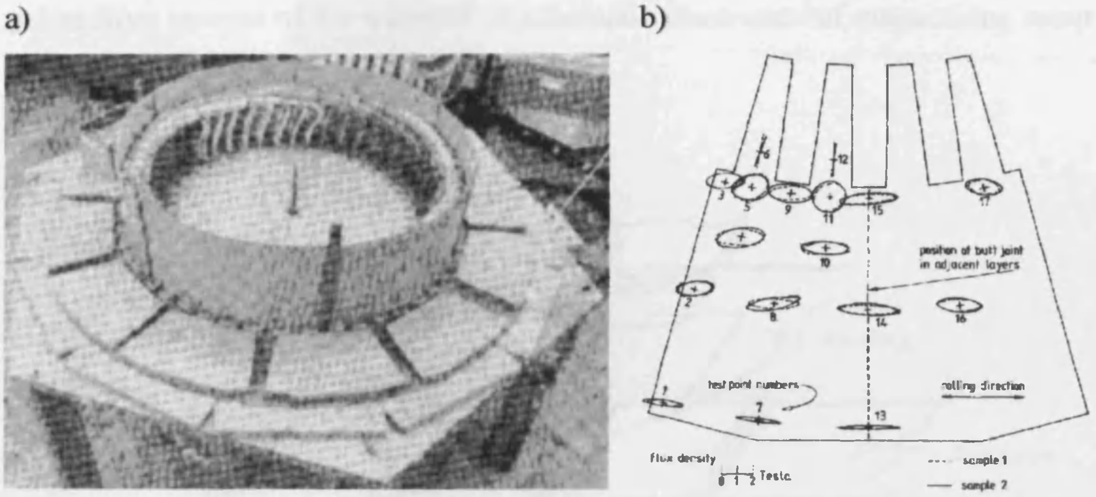

Fig. 3.8. The simulation of turbogenerator stator core: a) the view of the setup, b) the loci of rotational flux density [*3.11*]

In 1982 Brix used an experimental apparatus, illustrated in Fig. 3.9, for the measurement of rotational power loss in 3% Si-Fe sample at various magnetising frequencies [*3.12*]. This device utilised a torque magnetometer method. The external field applied to the disc sample was produced from two pairs of Helmholtz coils, whose axes were perpendicular to each other.

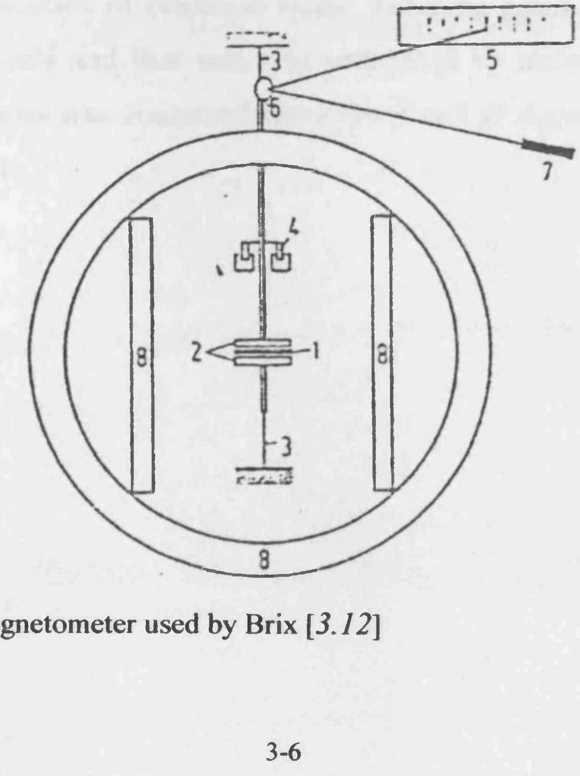

Fig. 3.9. Torque magnetometer used by Brix [*3.12*]

In 1985 Sasaki et al. [*3.13*] developed a rotational power loss measuring system based on the fieldmetric method for a single Epstein strip. Magnetisation along the longitude direction of the specimen was achieved with a solenoid, into which the pick-up coils were fixed. The transverse direction is magnetised with yokes from outside of the solenoid. A schematic illustration of magnetising setup is shown in Fig. 3.10.

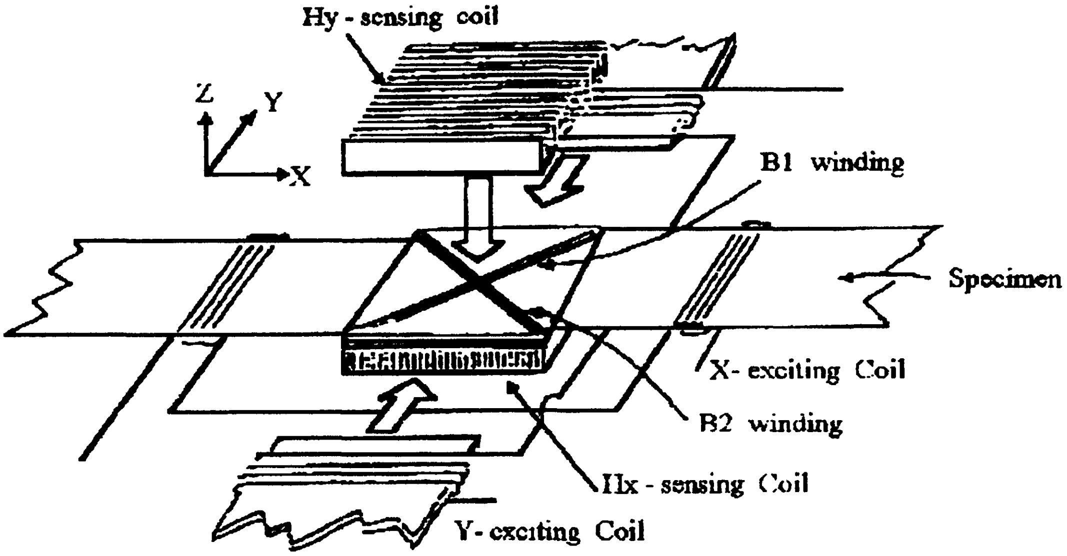

Fig. 3.10. Magnetising setup used by Sasaki et al. [*3.13*]

In 1990 Enokizono et al. developed another system for two-dimensional measurements [*3.14*]. Again this system was designed to evaluate the rotational magnetic characteristics of electrical steels including grain oriented steels. The measurement of field and flux was also performed by means of *B* and *H*-coils. The total power loss was computed from the *B* and *H* signals. The apparatus is shown in Fig. 3.11.

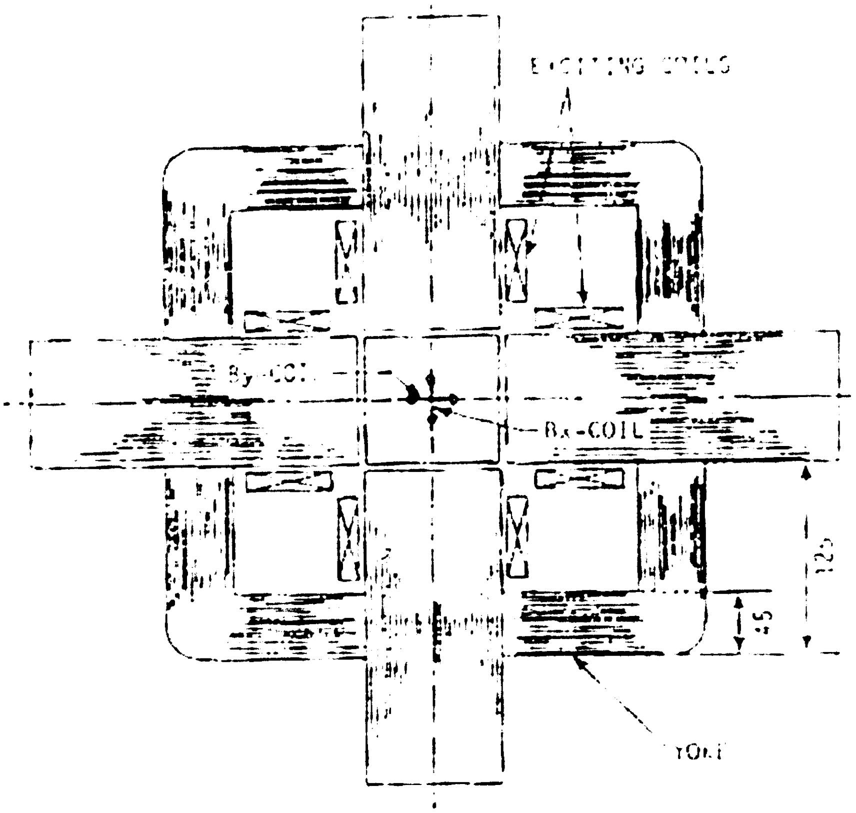

Fig. 3.11. An apparatus for two-dimensional measurements used by Enokizono [*3.14*]

In 1990 Sievert summarised the research carried out on rotational magnetisation – he referred to 55 publications in [*3.15*]. He highlighted the importance of the influence of sensor misalignment on the differences in measurement of power losses in clockwise and anticlockwise direction of rotation.

It has been well known from previous investigations that the power losses measured in clockwise and anticlockwise rotation differ. The origin of this difference was not known, but it was suggested that in order to find the "true" value the power losses needed to be averaged from clockwise and anticlockwise direction of rotation. Investigating the positioning of the *H* sensors Sievert confirmed that the assumption was correct and that the averaging method yields correct value [*3.15*], as presented in Fig. 3.12.

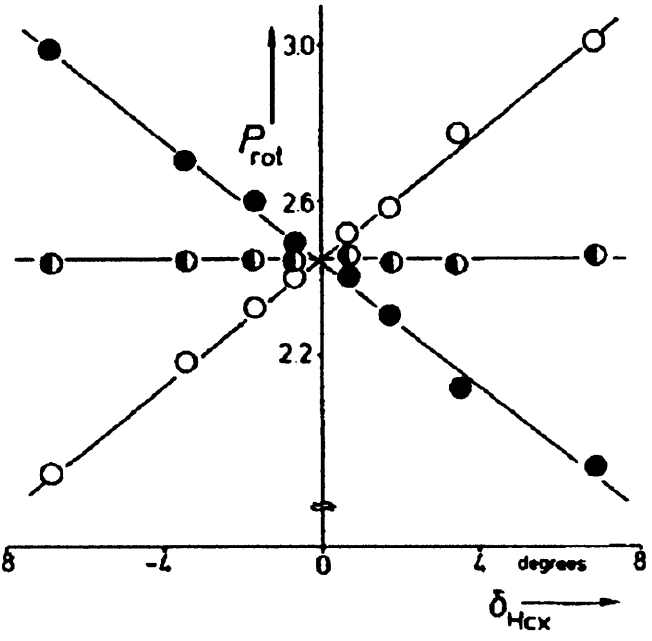

Fig. 3.12. Minimisation of the influence of sensor misalignment by means of averaging from clockwise and anticlockwise measurements [*3.15*]

In 1992 Sievert extended the studies on the orthogonality of the *H*-coils [*3.16*]. He examined the *H*-coils in a long solenoid with sophisticated method using laser beam (see Fig. 3.13), and found the orthogonality to be deviated from 90 degrees by more than 1 degree in some cases. Again, the averaging method has been proposed as a solution to the problem. Basing on the obtained results, Sievert postulated that the position of the sensors is not of prime importance – just the orthogonality is crucial to the power loss measurements [*3.16*].

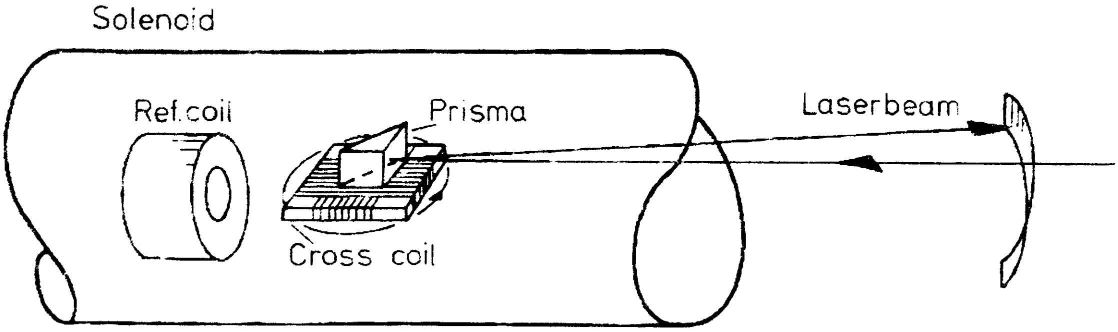

Fig. 3.13. The arrangement used for determination of the angle between the *H*-coils presented in [*3.16*].

Fiorillo and Rietto in 1992 presented a three-phase magnetising system [*3.17*] utilising a round sample. Active feedback circuit was not used, but the results show that achievable rotational flux density was at the level of 1.8 T for non-oriented electrical steel. The authors suggested, that the power loss measurements by means of fieldmetric method are sensitive to the phase shifts between the *B* and *H* signals down to as small values as 0.5 degree.

The power loss was measured by means of thermometric method under low air pressure (to emulate the adiabatic thermal conditions). The arrangement of the specimen disks with the thermocouples is shown in Fig. 3.14.

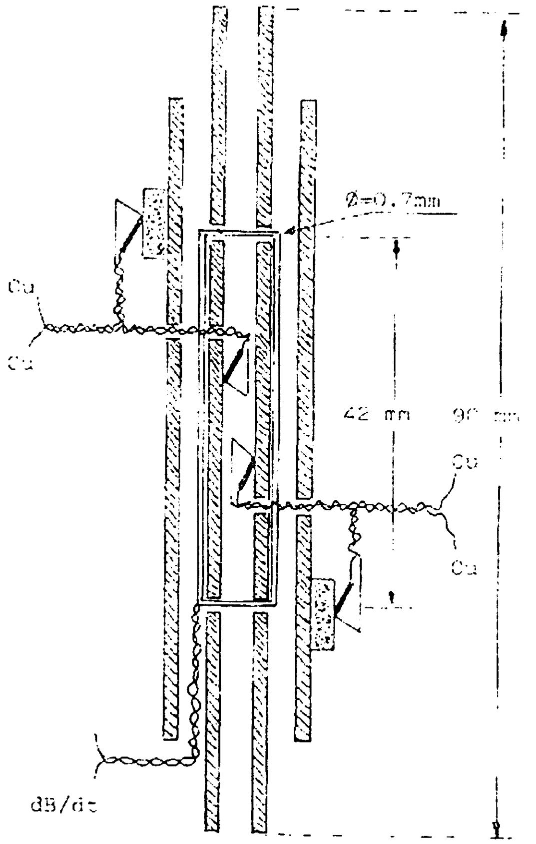

Fig. 3.14. The cross-sectional view of the sample arrangement used in [*3.17*]

In 1992 Alinejad-Beromi [*3.18*] used a magnetising apparatus, which consisted of magnetising winding wound around four magnetising coil formers, with two yokes used to close the magnetic paths in the *X* and *Y* directions. The apparatus is shown in Fig. 3.15 and it utilises the fieldmetric method.

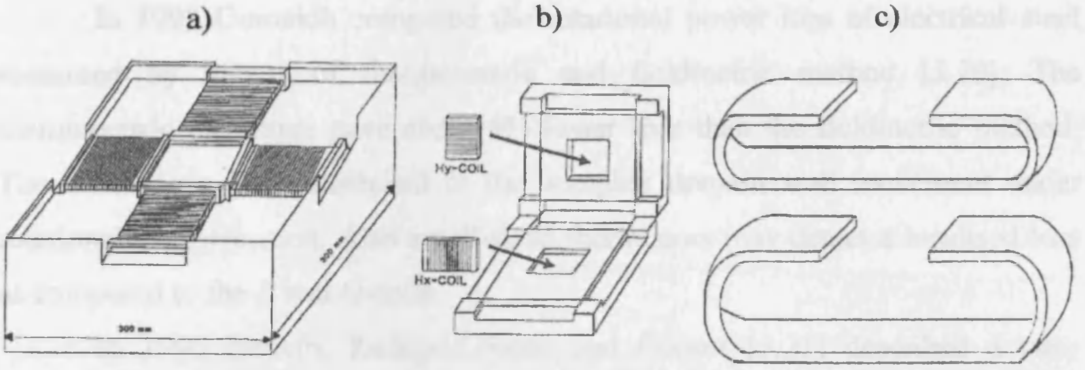

Fig. 3.15. The magnetising system used by Alinejad-Beromi: a) general view, b) sample and sensors holder, c) C-shaped yokes [*3.18*]

Also in 1992, Kedous-Lebouc, Zouzou and Brissonneau [*3.19*] studied the magnetic losses of electrical steel using a system made of two double perpendicular yokes and used search coils for the measurement of the flux density and magnetic field (Fig. 3.16). A square sample 80 x 80 mm is set in the central part of two double yokes. A rotational flux is produced in the sample by two primary coils wound on the *X* and *Y* arms, which correspond to the rolling and transverse directions of the sample, respectively.

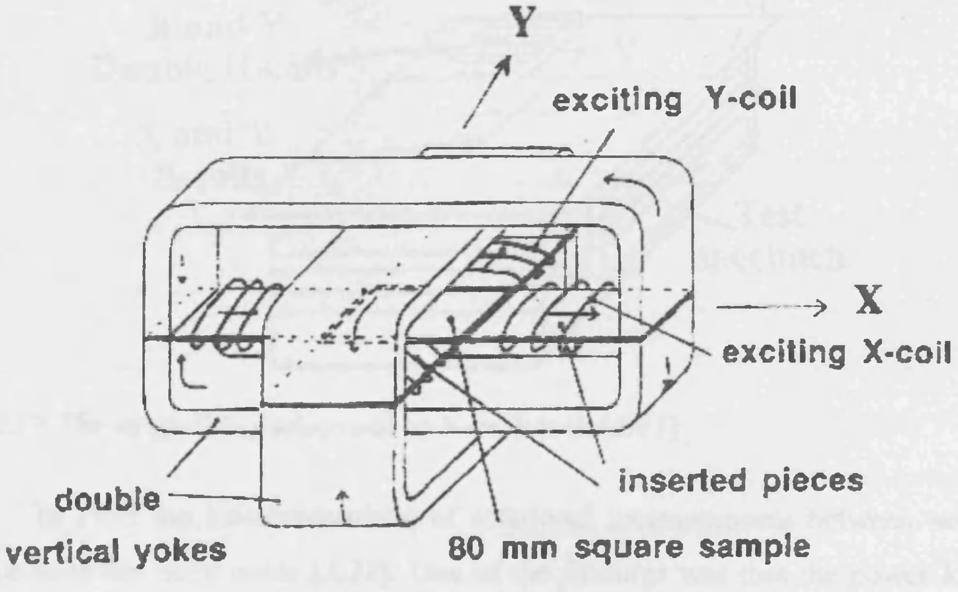

Fig. 3.16. The magnetising setup used by Kedous-Lebouc et al. [*3.19*]

In 1993 Gumaidh compared the rotational power loss of electrical steel measured by means of thermometric and fieldmetric method [*3.20*]. The thermometric technique gave about 4% lower loss than the fieldmetric method. The differences were attributed to the complex domain wall movement under rotational magnetisation. Also small-sized thermistors may detect a localised loss as compared to the *B* and *H*-coils.

In 1996 Nencib, Kedous-Lebouc and Cornut [*3.21*] described a two-dimensional system designed for testing samples of larger sample size and to investigate the magnetising field homogeneity (Fig. 3.17).

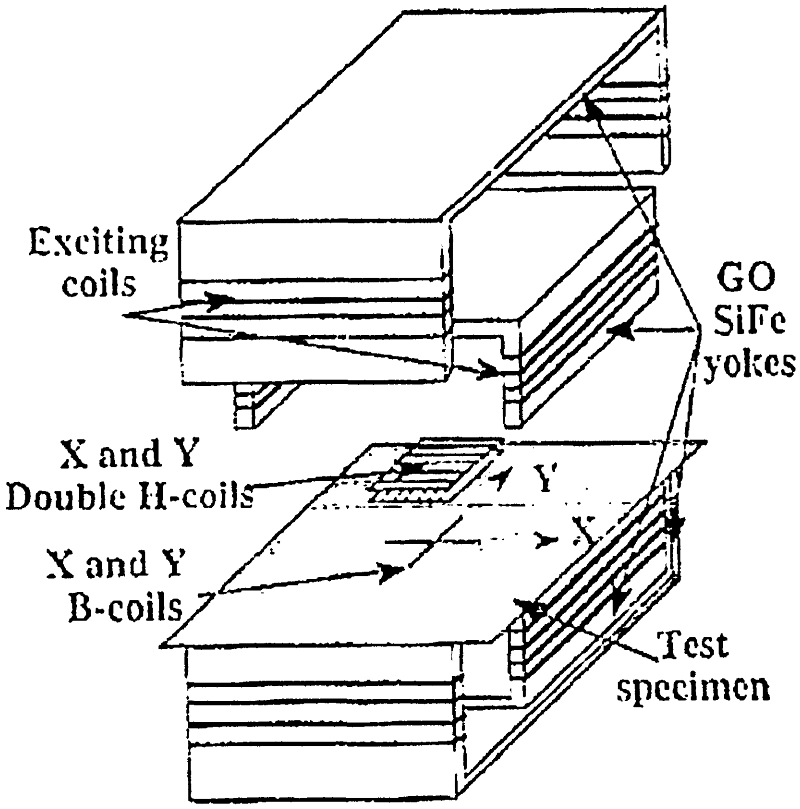

Fig. 3.17. The magnetising setup used by Nencib et al. [*3.21*]

In 1995 the intercomparison of rotational measurements between several laboratories has been made [*3.22*]. One of the findings was that the power losses measured by various systems varied significantly, even up to several tens of percent. The maximum rotational flux density was 1.5 T for non-oriented and 1.2 T for grain-oriented electrical steel sheet. Only the power loss averaged from clockwise and anticlockwise direction of rotation has been reported, so there was no information on the divergence between clockwise and anticlockwise measurements. However, it was revealed elsewhere that for the controllable range of flux density such divergence reached in some cases several hundred percent. There were also measurements, where the anticlockwise power loss was reported negative [*3.23*].

In 1995, Nencib, Kedous-Lebouc and Cornut [*3.24*] performed a two-dimensional FEM simulation of the influence of the shape of sample on the magnetic field homogeneity. It has been shown that the square-shaped samples are superior to round ones as far as the homogeneity of the field in the centre of the sample is concerned (Fig. 3.18).

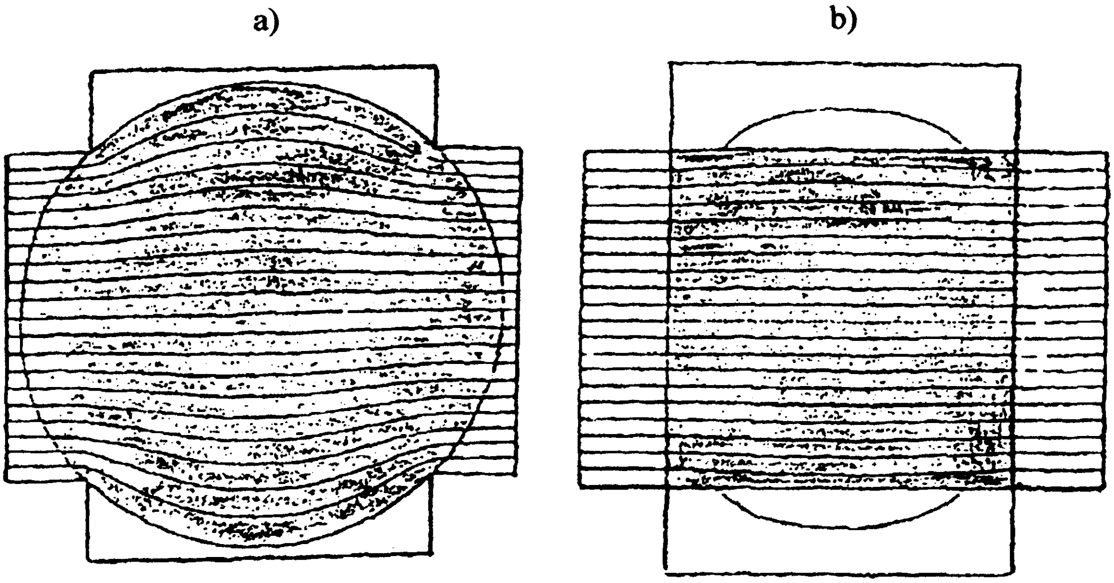

Fig. 3.18. The influence of the shape of the sample on the magnetic field homogeneity [*3.24*]: a) round sample, b) square sample

In 1996 Hasenzagl, Weiser and Pfutzner introduced a three-phase excited single sheet tester for rotational magnetisation [*3.25*]. The design of the apparatus requires a hexagonally shaped sample (Fig. 3.19). The authors suggested that by using a three-phase power source the most important rotational magnetisation patterns could be produced even without an active feedback circuit.

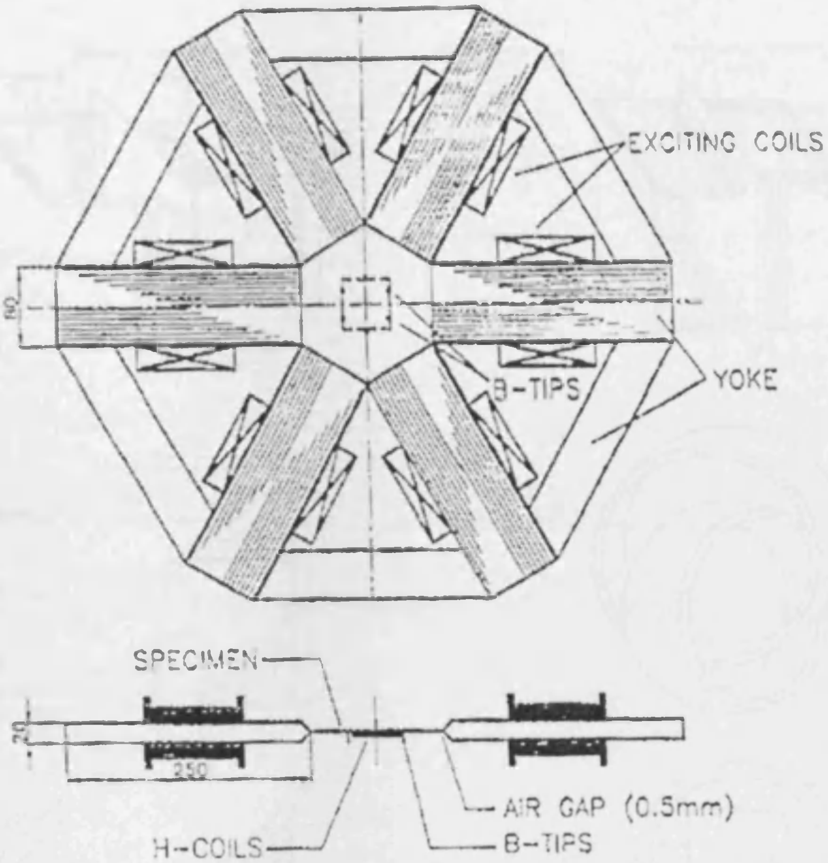

Fig. 3.19. Three-phase magnetising system used by Hasenzagl et al. [*3.25*]

Also in 1996, Wan Mahadi [*3.26*] investigated and compared the performance of several magnetising yokes (Fig. 3.20). The design and shape of the yokes have been studied so as to correlate it with the homogeneity of the magnetic field in the sample. Also the influence of the grain structure on the localised power loss has been investigated. The author suggested that there is correlation between the anisotropy of the material and the difference in power loss measured in clockwise and anticlockwise direction.

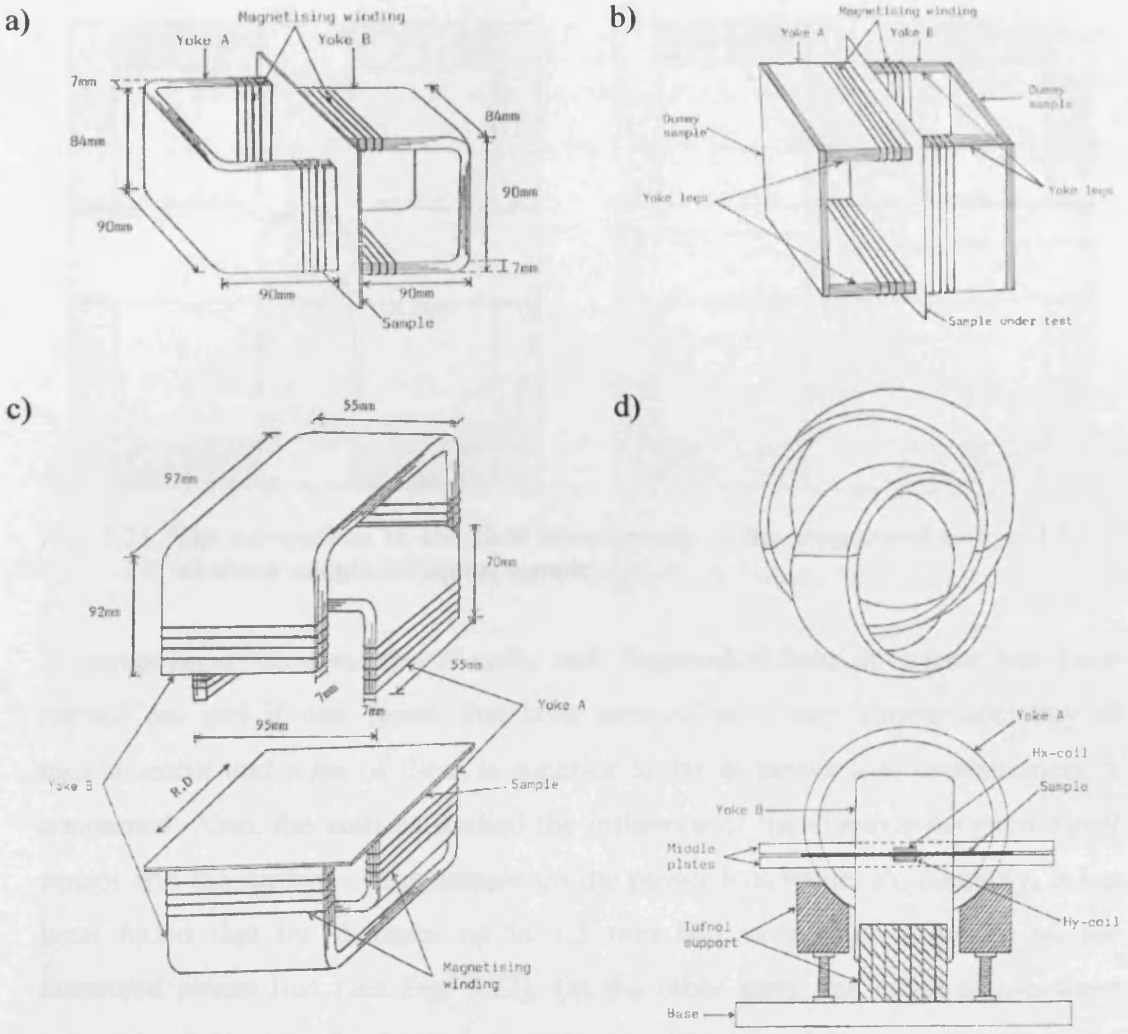

Fig. 3.20. Different types of magnetising yokes used by Wan Mahadi [*3.26*]

In 1997, Xu and Sievert studied different factors influencing the accuracy of power loss measurement under two-dimensional excitation [*3.27*]. The authors performed two-dimensional FEM calculations to study the influence of the shape of the sample on the homogeneity of the magnetic field. Similarly to [*3.24*] it has been found that the square shape provides better magnetic field homogeneity (Fig. 3.21).

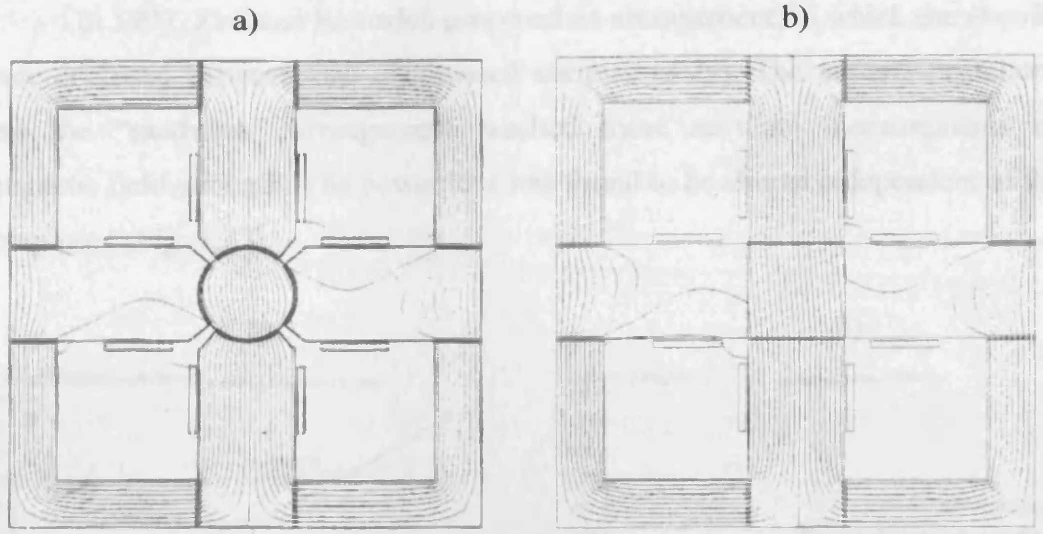

Fig. 3.21. The comparison of the field homogeneity in the magnetised sample [*3.27*]: a) round sample, b) square sample

A comparison between the *H*-coils and Rogowski-Chattock sensor has been carried out and it was found that both sensors have very similar accuracy of measurement and none of them is superior as far as power loss measurement is concerned. Also, the authors studied the influence of the distance between the *H* sensor and the surface of the sample on the power loss value. Remarkably, it has been found that the distance up to 1.5 mm had very little influence on the measured power loss (see Fig. 3.22). On the other hand, the value of measured magnetic field strongly depended on the positioning of the sensor above the sample, which was in agreement with other research [*3.28*].

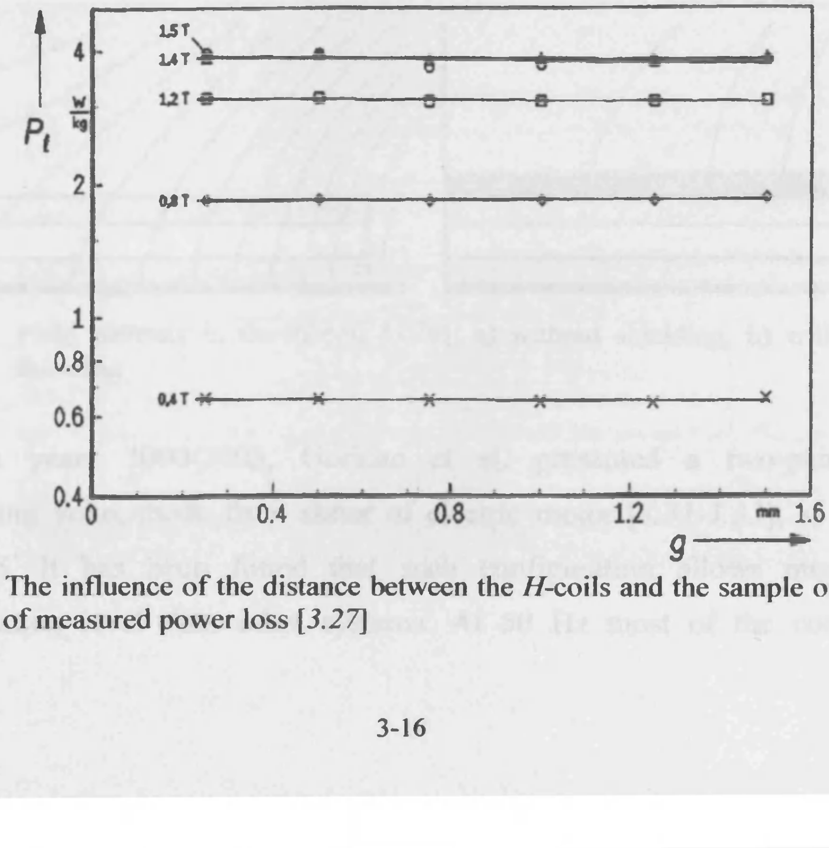

Fig. 3.22. The influence of the distance between the *H*-coils and the sample on the value of measured power loss [*3.27*]

In 1997, Zhu and Ramsden proposed an arrangement, in which the *H*-coils were enclosed between two magnetised samples [*3.29*]. The authors postulated that the "sandwich" arrangement resulted more accurate measurements of magnetic field strength. The power loss was found to be almost independent of the setup used (Fig. 3.23).

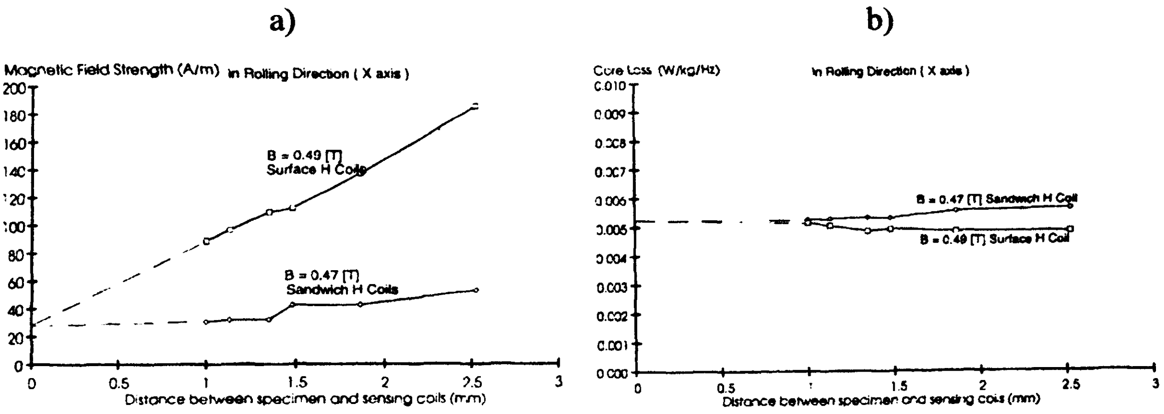

Fig. 3.23. The results presented in [*3.29*]: a) improvement of measurements of magnetic field strength, b) influence of the arrangement on the power loss value

In 2000, Makaveev et al. [*3.30*] made FEM calculations, in which they obtained results similar to those by Zhu and Ramsden in [*3.29*]. It has been found that using magnetic shielding above the *H*-coils decreases the normal gradient of the magnetic field penetrating the *H*-sensor. The cases described in [*3.29*] and [*3.30*] concerned only square samples.

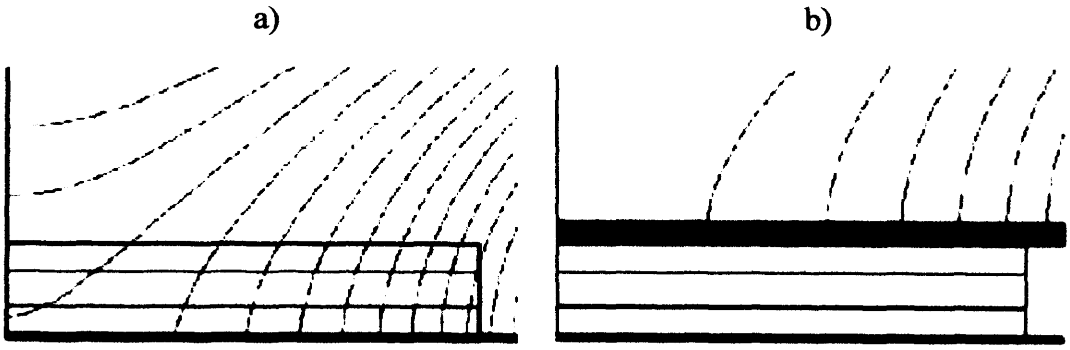

Fig. 3.24. Field patterns in the *H*-coil [*3.30*]: a) without shielding, b) with magnetic shielding

In years 2000-2003, Gorican et al. presented a two-phase round magnetising yoke, made from stator of electric motor [*3.31-3.33*], as shown in Fig. 3.25. It has been found that such configuration allows much higher magnetisation level than other systems. At 50 Hz most of the conventional materials (e.g. non-oriented and grain-oriented electrical steel sheet) can be magnetised up to 2.0 T under rotational magnetisation, which was not possible with other two-phase excitation systems. Previously, the effect of decreasing of the total power loss could be observed only in the magnetometer-type, but the round single sheet testers also allowed to clearly see such effect as well.

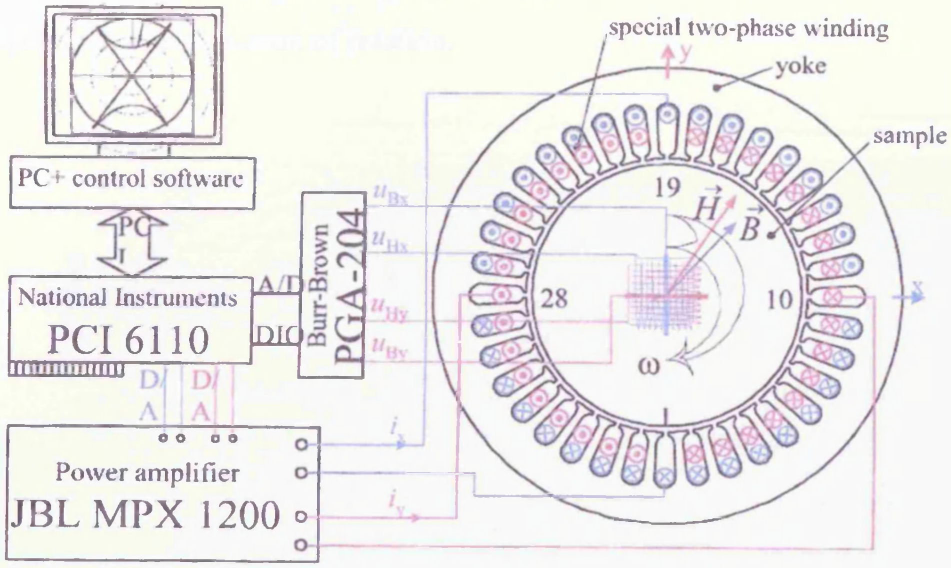

Fig. 3.25. Round rotational single sheet tester used by Gorican et al. in [*3.31*]

The data published by Gorican et al. (see Fig. 3.26) showed that at high flux density the difference between clockwise and anticlockwise power loss can differ much more than the 70% documented in [*3.23*].

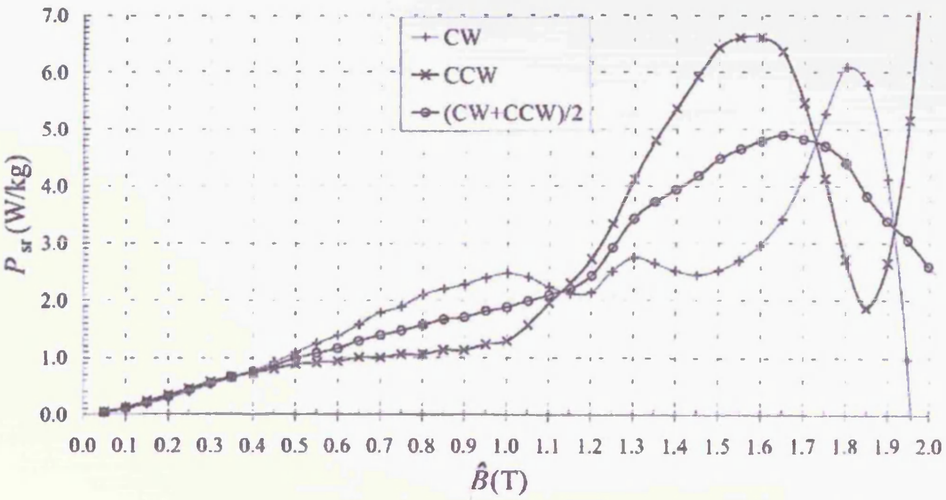

Fig. 3.26. Clockwise and anticlockwise power losses [*3.32*]

It was suggested that genuine magnetic properties of the material under test may be a cause for such divergence – the claims were based on directional properties presented in [*3.32*], as shown in Fig. 3.27. The difference between clockwise and anticlockwise power losses will be thoroughly analysed in **Chapter 5**. It will also be shown that the genuine magnetic properties cannot be responsible for such a high divergence in the power losses measured in clockwise and anticlockwise direction of rotation.

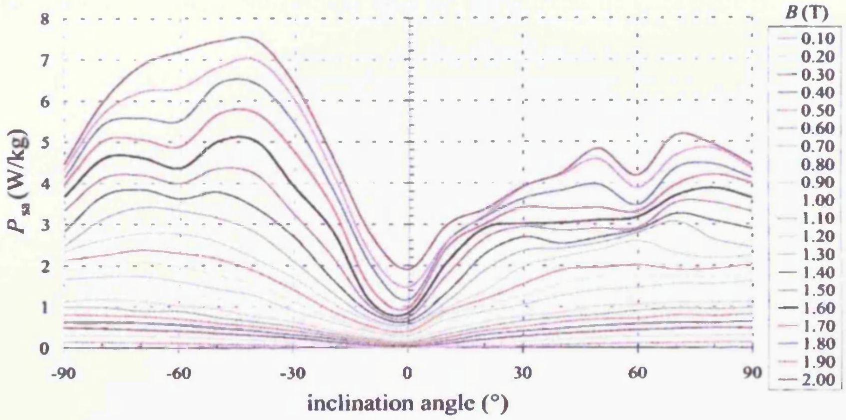

Fig. 3.27. Alternating power loss versus inclination angle [*3.32*]

In 2004, Sugimoto et al. presented a new type of magnetising yoke, which somewhat resembles the stator core of motor [*3.34*], but the apparatus is designed to accommodate square-shape samples, as shown in Fig. 3.28.

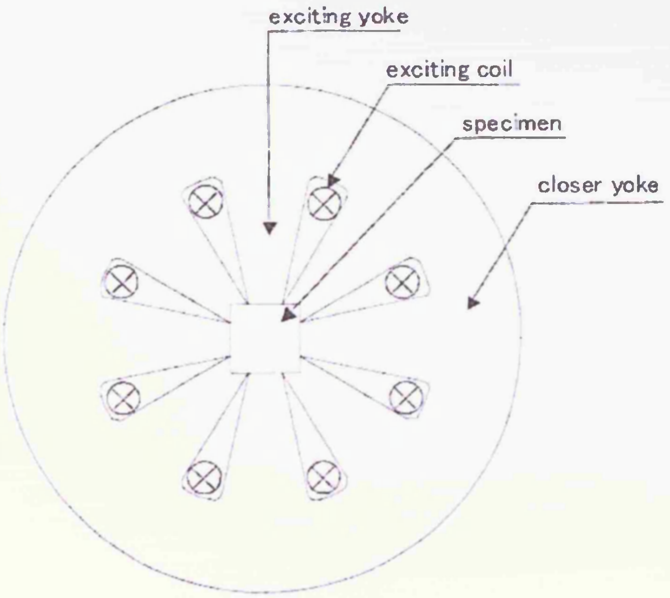

Fig. 3.28. Magnetising yoke presented in [*3.34*]

It has been suggested previously in various publications that the *H*-controlled magnetising conditions are more relevant to the real process taking place in three-phase machines than the *B*-controlled magnetisation [*3.20*, *3.25*, *3.35*]. However, the latter has been widely used, mostly because researchers followed the requirements for alternating power loss measurements, which are standardised only for sinusoidal (controlled) shape of *B*. It has been suggested again in 2004 by Moses [*3.36*] that the *H*-controlled measurements should be of importance as well. This postulation will be supported in **Chapter 5**.

3.1. References to Chapter 3

[*3.1*] Bozorth R.M., Ferromagnetism, D. Van Nostrand Company Inc., London, United Kingdom, 1951

[*3.2*] Brailsford F., Rotational hysteresis loss in electrical sheet steels, Journal of the Institution of Electrical Engineers, Vol. 83, 1938, pp. 566-575

[*3.3*] Brailsford F., Investigation of the eddy-current anomaly in electrical sheet steels, Journal of Institution of Electrical Engineers, Vol. 95, Part II, 1948, pp. 38-48

[*3.4*] Kornetzki M., Lucas I., Zur Theorie der Hystereseverluste im magnetischen Drehfeld (*On the theory of hysteresis loss in rotating magnetic field*, in German), Zeitschrift fur Physik, Bd. 142, 1955, pp. 70-82

[*3.5*] Boon C.R., Thompson J.E., Rotational hysteresis loss in single crystal silicon iron, Proceedings of the Institution of Electrical Engineers, Vol. 111, No 3, 1964, pp. 605-609

[*3.6*] Boon C.R., Thompson J.E., Alternating and rotational power loss at 50 c/s in 3% silicon-iron sheets, Proceedings of the Institution of Electrical Engineers, Vol. 112, No. 11, 1965, pp. 2147-2151

[*3.7*] Moses A.J., Thomas B., Thompson J.E., Power loss and flux density distributions in the T-joint of a three phase transformer core, IEEE Transactions on Magnetics, Vol. Mag-8, No. 4, 1972, pp. 785-790

[*3.8*] Moses A.J., Thomas B., Problems in design of power transformers, IEEE Transactions on Magnetics, Vol. Mag-10, No. 2, 1974, pp. 148-150

[*3.9*] Moghadam A.T, Moses A.J., Comparison of flux distribution in three-phase transformer core assembled from amorphous material and grain-oriented silicon iron, IEEE Transactions on Magnetics, Vol. 25, No. 5, 1989, pp. 3964-3966

[*3.10*] Moses A.J., Thomas B., Measurement of rotating flux in silicon iron laminations, IEEE Transactions on Magnetics, Vol. Mag-9, No. 4, 1973, pp. 651-654

[*3.11*] Radley G.S., Moses A.J, Apparatus for experimental simulation of magnetic flux and power loss distribution in a turbogenerator stator core, IEEE Transactions on Magnetics, Vol. Mag-17, No. 3, 1981, pp. 1311-1316

[*3.12*] Brix W., Measurements of the rotational power loss in 3% silicon-iron at barious frequencies using a torque magnetometer, Journal of Magnetism and Magnetic Materials, Vol. 26, 1982, pp. 193-195

[*3.13*] Sasaki T., Imamura M., Takada S., Suzuki Y., IEEE Transactions on Magnetics, Vol. Mag-21, No. 5, 1985, pp. 1918-1920

[*3.14*] Enokizono M., Suzuki T., Sievert J., Xu J,. Rotational power loss of silicon steel sheet, IEEE Transactions on Magnetics, Vol. 26, No. 5, 1990, pp. 2562-2564

[*3.15*] Sievert J., Recent advances in the one- and two-dimensional magnetic measurement technique for electrical sheet steel, IEEE Transactions on Magnetics, Vol. 26, No. 5, 1990, pp. 2553-2558

[*3.16*] Sievert J., Studies on the measurement of two-dimensional magnetic phenomena in electrical sheet steel at PTB, Proceedings of 1st international workshop on magnetic properties of electrical sheet steel under two-dimensional excitation, Braunschweig, Germany, April 1992

[*3.17*] Fiorillo F., Rietto A.M., The measurement of rotational losses at I.E.N.: Use of the thermometric method, Proceedings of 1st international workshop on magnetic properties of electrical sheet steel under two-dimensional excitation, Braunschweig, Germany, April 1992

[*3.18*] Alinejad-Beromi Y., Rotational power loss measurement system under controlled magnetisation, PhD thesis, University of Wales College of Cardiff, United Kingdom, 1992

[*3.19*] Kedous-Lebouc A., Zouzou S., Brissonneau P., On the magnetization processes in electrical steel in unidirectional and rotational field, Proceedings of 1st international workshop on magnetic properties of electrical sheet steel under two-dimensional excitation, Braunschweig, Germany, April 1992

[*3.20*] Gumaidh A.M., Meydan T., Moses A.J., Characterisation of magnetic materials under two-dimensional excitation, Proceedings of IEEE, Intermag Conference, Stockholm, 1993

[*3.21*] Nencib N., Kedous-Lebouc A., Cornut B., Performance evaluation of a large rotational single sheet tester, Journal of Magnetism and Magnetic Materials, 160 (1996), pp. 174-176

[*3.22*] Sievert J., Ahlers H., Birkfeld M., Cornut B., Fiorillo F., Hempel K.A., Kochmann T., Kedous-Lebouc A., Meydan T., Moses A.J., Rietto A.M., European intercomparison of measurements of rotational power loss in electrical sheet steel, Journal of Magnetism and Magnetic Materials, 160, 1996, pp. 115-118

[*3.23*] Sievert J., Ahlers H., Birkfeld M., Cornut B., Fiorillo F., Hempel K.A., Kochmann T., Kedous-Lebouc A., Meydan T., Moses A.J., Rietto A.M., Intercomparison of measurements of magnetic losses in electrical sheet steel under rotating flux conditions, Report EUR 16225 EN, Commission of the European Communities, Brussels, Luxembourg, 1995

[*3.24*] Nencib N., Kedous-Lebouc A., Cornut B., 2D analysis of rotational loss tester, IEEE Transactions on Magnetics, Vol. 31, No 6, 1995, pp. 3388-3390

[*3.25*] Hasenzagl A., Weiser B., Pfützner H., Novel 3-phase excited single sheet tester for rotational magnetization, Journal of Magnetism and Magnetic Materials, 160, 1996, pp. 180-182

[*3.26*] Wan Mahadi W.N.L., Design and development of a novel two-dimensional magnetic measurement system for electrical steels, PhD thesis, University of Wales College of Cardiff, United Kingdom, 1996

[*3.27*] Xu J., Sievert J., On the reproducibility, standardization aspects and error sources of the fieldmetric method for the determination of 2D magnetic properties of electrical sheet steel, Proceedings of 5th international workshop on two-dimensional magnetization problems, Grenoble, France, September 1997

[*3.28*] Nakata T., Kawase Y., Nakano M., Improvement of measuring accuracy of magnetic field strength in single sheet testers by using two H coils, IEEE Transactions on Magnetics, Vol. Mag-23, No 5, 1987, pp. 2596-2598

[*3.29*] Zhu G., Ramsden V.S., Measurement and modelling of losses under two dimensional excitation in rotating electrical machines, Proceedings of 5th international workshop on two-dimensional magnetization problems, Grenoble, France, September 1997

[*3.30*] Makaveev D., von Rauch M., De Wulf M., Melkebeek J., Accurate field strength measurement in rotational single sheet testers, Journal of Magnetism and Magnetic Materials, Vol. 215-216, 2000, pp. 673-676

[*3.31*] Gorican V., Hamler A,. Kribernik B., Jesenik M., Trlep M., 2-D measurements of magnetic properties using a round RSST, Proceedings of 6th international workshop on 1&2-dimensional magnetic measurement and testing, Bad Gastein, Austria, September 2000

[*3.32*] Gorican V., Jesenik M., Hamler A,. Stumberger B., Trlep M., Performance of round rotational single sheet tester (RRSST) at higher flux densities in the case of GO materials, Proceedings of 7th international workshop on 1&2 dimensional magnetic measurement and testing, Ludenscheid, Germany, September 2002

[*3.33*] Gorican V., Hamler A,. Jesenik M., Stumberger B., Trlep M., Unreliable determination of vector *B* in 2-D SST, Journal of Magnetism and Magnetic Materials, 254-255, 2003, pp. 130-132

[*3.34*] Sugimoto S., Urata S., Ikariga A., Shimoji H., Todaka T., Enokizono M., A new measurement device for two-dimensional vector-magnetic-property in high magnetic flux density range, Proceedings of 8th international workshop on 1&2-dimensional magnetic measurement and testing, Ghent, Belgium, September 2004

[*3.35*] Moses A.J., Meydan T., **Zurek S.**, Potential problems in interpretation of angular variation of B and *H* in electrical steel under rotational magnetisation conditions, Proceedings of 11th International Symposium on Applied Electromagnetics & Mechanics (ISEM), Versailles, France, May 2003

[*3.36*] Moses A.J., The case for characterisation of rotational losses under pure rotational field conditions, Proceedings of 8th international workshop on 1&2-dimensional magnetic measurement and testing, Ghent, Belgium, September 2004

Chapter Four

Design and development of two-dimensional magnetising and measuring system

4.1. Sensors

4.1.1. Flux density sensors

The localised flux density measurements are usually measured by means of two techniques: so-called *B*-coil and needle probes technique. The former one is very reliable and hence is most frequently used. However, a theoretical approach to another type of sensor designed and developed in the course of this investigation, which is a capacitive modification of the needle probes, will also be presented.

The average flux density in any material can be detected by means of a *B*-coil (named also as "search coil" or "pick-up coil"). The operation of such a sensor is based on a principle that changing flux density induces voltage in a surrounding coil. The voltage is proportional to the rate of change of flux density, the number of turns of the coil, and the area enclosed (see Fig. 4.1):

$$V = -N \cdot A \cdot \frac{\mathrm{d}B}{\mathrm{d}t} \qquad [\mathrm{V}] \qquad (4.1)$$

where: N - number of turns of the coil, (dimensionless); A - cross-section area of the coil, [m^2]; $\mathrm{d}B/\mathrm{d}t$ - rate of change of flux density with respect to time, [T/s].

Therefore the flux density waveform can be calculated by integrating the voltage induced in the coil:

$$B = -\frac{1}{N \cdot A} \cdot \int V \,\mathrm{d}t \qquad [\mathrm{T}] \qquad (4.2)$$

The *B*-coil, schematically presented in Fig. 4.1, detects flux density averaged over the area A.

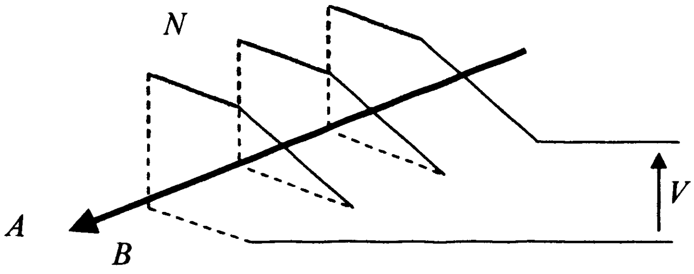

Fig. 4.1. The concept of the search coil technique: V - voltage induced in the coil, N - number of turns in the coil, A - area enclosed by the coil, B - flux density

If the flux density is to be measured in a localised area then there is a need for two holes to be drilled in the sample under test; through these holes the winding is positioned over the area of interest (see Fig. 4.2). The twisting of the wires helps minimising the influence of the stray flux.

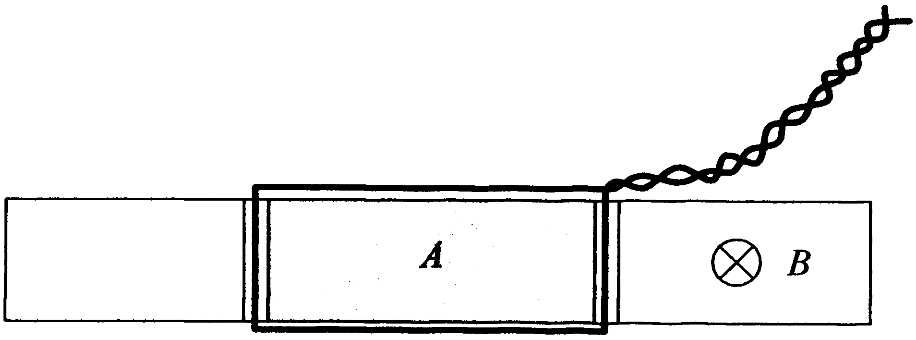

Fig. 4.2. The concept of a B-coil measuring localised flux density. The coil is threaded through the holes drilled in the sample under test. The connecting wires are twisted in order to minimise picking up the stray flux. A - measured area, over which the flux density is averaged, B - direction of flux density

Therefore, all the tested samples were drilled in order to thread two perpendicular B-coils through the specimens, see Fig. 4.3. The drilling process deteriorates the magnetic properties of the material to some degree [*4.1*, *4.2*]. Therefore, the diameter of the holes should be as small as possible – 0.3 mm was selected as a compromise between the dimension of the holes and the diameter of copper wire 0.1 mm threaded through the holes.

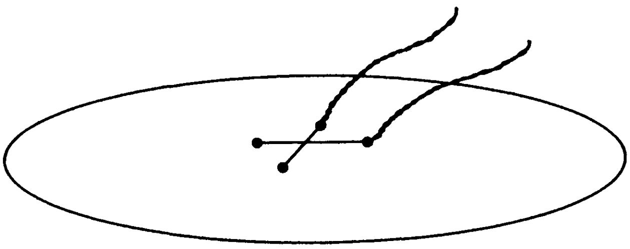

Fig. 4.3. A specimen with a pair of perpendicular *B*-coils

The samples were drilled with an aid of a drilling machine equipped with a precise positioning table. The holes are positioned with accuracy better than 0.1 mm. The distance between the centres of the holes is 20.00 mm; hence the length of active magnetic material under test is 19.70 mm, as shown in Fig. 4.4.

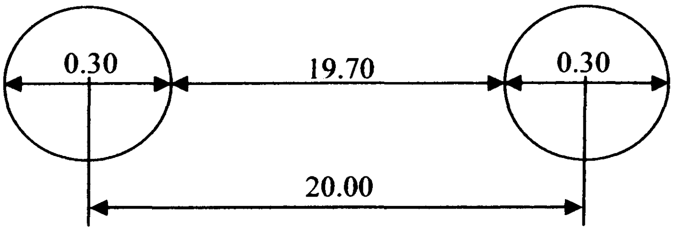

Fig. 4.4. Dimensions of the holes drilled in the specimen (not in scale)

4.1.2. Novel capacitive sensor

Ordinarily, only two techniques have been used for detecting localised flux density: the *B*-coil described above and the needle probes technique (NPT). However, recently another novel method has been suggested in [*4.3*].

The NPT was described for the first time in [*4.4*]. The potential difference between two points at the surface of a magnetised piece of lamination is proportional to the voltage induced in the coil wrapped around proportional cross-section area of the lamination (see Fig. 4.5). Variable flux density induces eddy currents, which cause a potential gradient at the conductive (and resistive) surface of the sample.

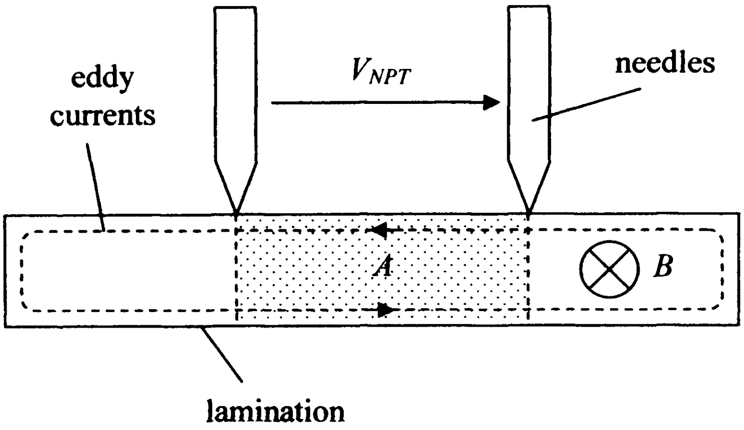

Fig. 4.5. The concept of the needle probes technique: A - active area of the sensor, B - flux density, V_{NPT} - potential difference (voltage) between the needles

However, the relationship is not strict and depends on the thickness of the lamination, but for thin materials (i.e. when thickness of the lamination is much smaller than the distance between the needles) and uniform magnetisation it can be assumed that:

$$V_{NPT} \approx -\frac{1}{2} \cdot A \cdot \frac{\mathrm{d}B}{\mathrm{d}t} \qquad \text{[V]} \qquad (4.3)$$

The NPT is quite popular in localised flux density measurements, because the only alternative is a B-coil method, which requires that holes must be drilled in the sample. Therefore the NPT allows measuring the flux density in far less destructive way than the B-coil method.

On the other hand, the method is less accurate than the B-coil method. Part of the problem is that the equation (4.3) is not strict, but there are more factors affecting the accuracy: non-homogeneity of the flux distribution in the thickness of the lamination, positioning of the needles is usually prone to small displacements, some force must be applied to the needles in order to ensure electrical contact with the body of the lamination, wiring must be made very carefully to avoid picking up the stray flux, etc. Some refinements have been suggested in [*4.1*], but they are not practically applicable for the rotational measurements.

By definition, the NPT works only for variable flux density. Therefore, the voltage between the two needles in Fig. 4.5 is also variable.

Capacitors are used in electronics for passing the processed signal from one part of the circuit to another. If the reactance of the capacitor is low enough it can be neglected [*4.5*]. Thus, for certain conditions, the electrical contacts between the needles and the lamination could be replaced by capacitors. The schematic drawing of the needles replaced by the capacitors is presented in Fig. 4.6 (compare with Fig. 4.5).

The transition from electrical contacts to capacitive coupling does not change the expected input signal (that is the voltage V_{NPT}), which is to be detected by the sensor. The voltage induced between the pads in Fig. 4.6 obeys equation (4.3), since the potential is averaged over the area of the pads. However, the properties of the sensor are modified drastically. Since there is no need for electrical contact between the measuring device (e.g. voltmeter) and the body of the sample, there is also no need for removing the sample coating or for applying any force to the surface of the specimen. This feature cancels two major problems of the NPT: firstly – it does not affect the magnetic properties of the sample under test, and secondly – it does not introduce any micro-damages to the surface of the specimen under test.

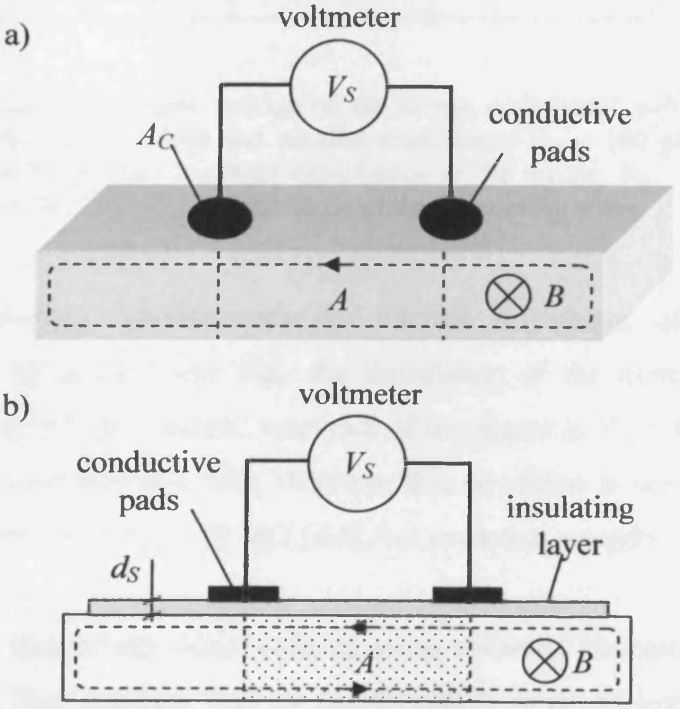

Fig. 4.6. The concept of the capacitive sensor. Two conductive pads are placed on the top of the lamination. The capacitors are created by the conductive pads, an insulating coating of the lamination and the lamination itself: a) general view, b) cross-section view; A_C - area of a pad, d_S - thickness of insulating layer, V_S - voltage measured between pads

Unfortunately, the capacitors also influence the conditions of the voltage measurement. The resistance of the specimen is usually low (below 1 Ω) for conventional electrical steel sheet, depending on the resistivity and the dimensions of the sample under test. The impedance of the connecting wires also affects the properties of such a sensor.

The behaviour of the capacitive sensor can be simulated as in Fig. 4.7, taking into account a negligible resistance of the sample, serial connection of the coupling capacitors, capacitance and resistance of the wires, and the impedance of the measuring device, e.g. voltmeter. The calculations were carried out with the values measured or calculated for a typical sensor.

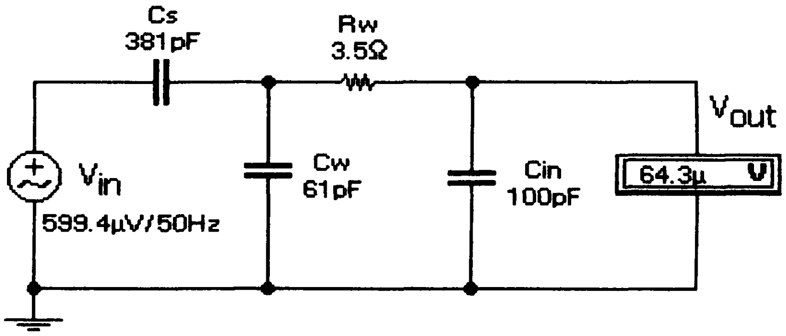

Fig. 4.7. Simulation the output voltage of the sensor with "real" voltmeter with serial resistance R_{in} = 1 MΩ and parallel capacitance C_{in} = 100 pF; V_{in} – expected input voltage, C_S – resultant capacitance of the sensor, R_W – resistance of the connecting wires, C_W – capacitance of the connecting wires

For accurate measurements the internal impedance of the measured element must be much lower than the impedance of the meter. For the case presented in Fig. 4.7 the resultant reactance of the sensor is X_{Cs} = 8.35 MΩ, whilst the R_{in} of the voltmeter is 1 MΩ, therefore this condition is not satisfied. Some digital voltmeters have R_{in} = 10 MΩ [*4.6*], but even that would not be sufficiently high.

All the simulations were made by using software Electronics Workbench (version 5.1). This package has an option called *Bode plotter*, which allows visualising of the properties of the circuit automatically for a range of frequencies. A typical response is presented in Fig. 4.8. It can be seen that the error of measured peak value is less than 1% for frequencies above 400 Hz. (Obviously for different capacitances or different voltmeter, i.e. different R_{in} and C_{in}, the characteristic will have different shape.)

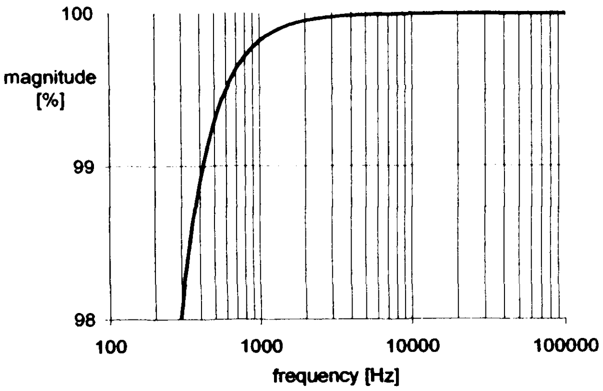

Fig. 4.8. The magnitude of the voltage simulated in the circuit from Fig. 4.7 with the "voltmeter" with R_{in} = 10 MΩ.

The calculations presented above are made for the ideal case, where the signals are not affected by noise or interference. In reality, there are very low voltages (order of 10^{-3} V) and very high impedances (order of 10^{6} Ω), hence the currents are extremely low (order of 10^{-9} A); therefore, the sensor is very vulnerable to interference. Additionally, there are parasite capacitances between the sample, the magnetising yoke, the exciting coils, etc. These, in conjunction with much higher currents and voltages present in magnetising setup, introduce severe disturbances and common mode interference to the measured voltage.

For the case from Fig. 4.7 preliminary tests on a real circuit revealed that the voltmeter [*4.6-4.8*] detected voltage much greater than the calculated (expected) potential difference between the coupling capacitors, that is conductive pads. When the body of the magnetising yoke and the sample were earthed this voltage decreased, but it was still greater than the expected value.

Increased frequency of magnetisation of the sample would produce higher potential difference between the pads and would decrease the impedance of the sensor. However, the internal reactance of the voltmeter and the parasite reactance of magnetising setup would also drop. Furthermore, the higher the magnetising frequency, the more pronounced is the skin effect. As in the NPT, the capacitive sensor would detect only the flux density on the surface of the specimen under test. Therefore, despite that graph in Fig. 4.8 is extended up to 100 kHz, flux density at such frequencies would not probably be detected properly by commonly available voltmeters and data acquisition cards. Instead, specially designed voltmeters with very high internal impedance should be used.

4.1.3. Magnetic field sensors

Most of the techniques for the rotational magnetic field strength measurements utilise a theoretical prediction that the tangential component of magnetic field remains the same at the transition from one medium to another [*4.9*], as presented in Fig. 4.9. It is also possible to calculate the magnetic field strength from the magnetising current. Nevertheless, this method was not used in investigations of rotational magnetisation; therefore it will not be described here.

If a medium with permeability μ_1 represents the air and another medium with permeability μ_2 is the magnetic material, then measuring tangential component of the magnetic field strength in the air just at the surface of the material will result with measuring of the tangential component of the magnetic field strength just inside of the magnetic material.

Obviously, the major problem is to place the sensor as close as possible to the surface of the sample under test. Not all sensors are small enough to be positioned in such manner; only the most commonly used sensors of magnetic field strength will be presented here.

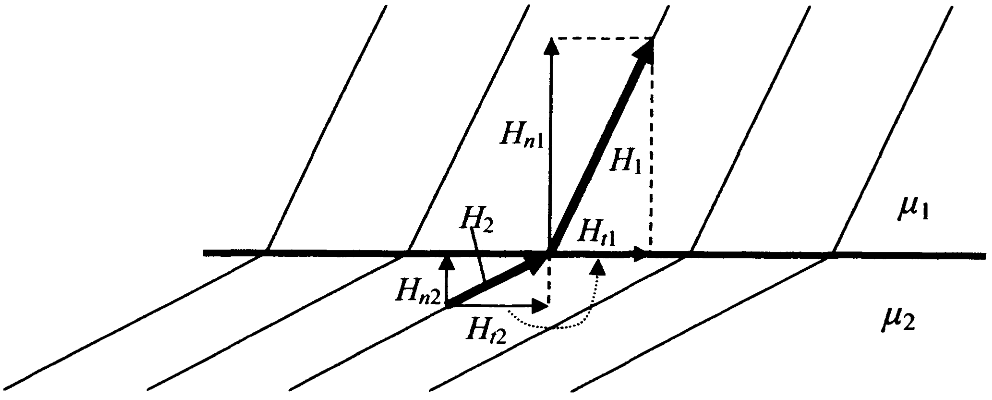

Fig. 4.9. The component of magnetic field at the boundary between two media with different permeability: H_1 - vector of magnetic field in medium with permeability μ_1; H_2 - vector of magnetic field in medium with permeability μ_2; H_{n1} and H_{n2} - normal components of vector H_1 and H_2, respectively; H_{t1} and H_{t2} - tangential components of vector H_1 and H_2, respectively. The tangential components of magnetic field are equal at the boundary: $H_{t1} = H_{t2}$; (after [*4.9*])

The *H*-coil method combines properties of a *B*-coil with the linearity of *B*-*H* characteristic of paramagnetic materials. If the equation (2.1) is substituted into (4.2) then:

$$\mu_0 \cdot H = -\frac{1}{N \cdot A} \cdot \int V \, \mathrm{d}t \qquad [\mathrm{T}] \qquad (4.4)$$

therefore

$$H = -\frac{1}{\mu_0 \cdot N \cdot A} \cdot \int V \, \mathrm{d}t \qquad [\mathrm{A/m}] \qquad (4.5)$$

where: μ_0 - permeability of free space, [H/m]; N - number of turns of the *H*-coil, (dimensionless); A - cross-section area of the *H*-coil, [m^2]; V - voltage induced in the *H*-coil, [V]

Thus, the strength of magnetic field can be derived from the voltage induced in the coil uniformly wound around a paramagnetic core. The core should be very thin in order to position the sensor as close as possible to the surface of the sample under test. Figure 4.10 depicts a typical *H*-coil.

It can be seen from Table 2.1 that the relative permeability of paramagnetic materials it very close to unity and in *H*-coil this difference is neglected. The error of such assumption does not exceed 0.002% and is negligibly small comparing to other errors contributing to the accuracy of the sensor.

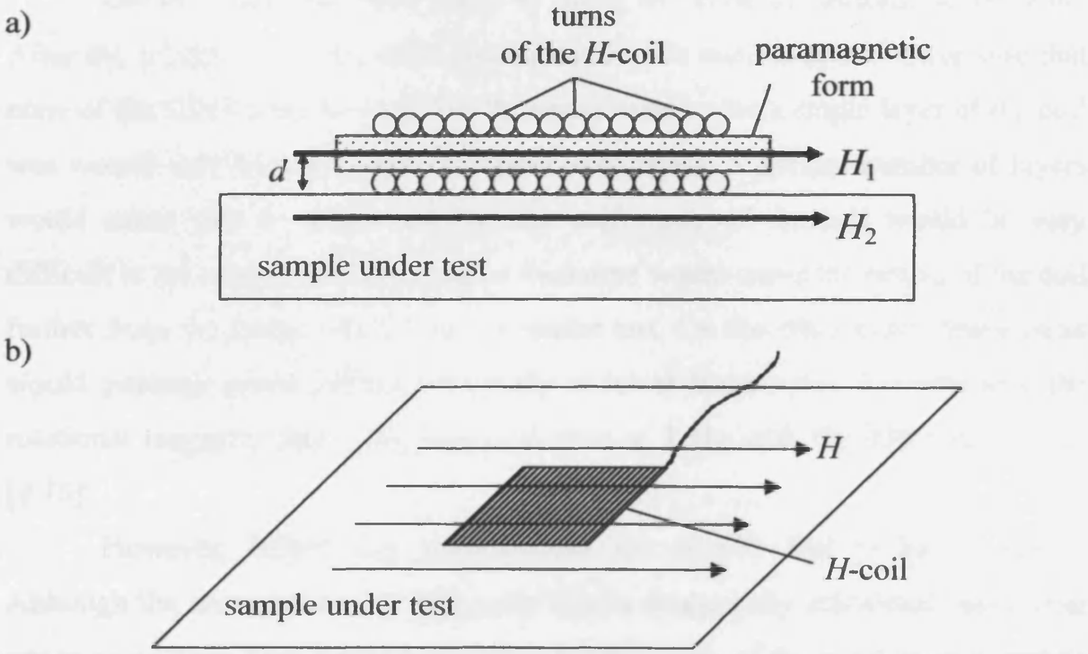

Fig. 4.10. The *H*-coil: a) cross-section, $H_1 \approx H_2$ (compare with Fig. 4.9); d - the distance between the surface of the sample and the centre of the *H*-coil; b) top view

The *H*-coils used in this project were made as a pair of perpendicular coils wound on one flat paramagnetic former, as depicted in Fig. 4.11.

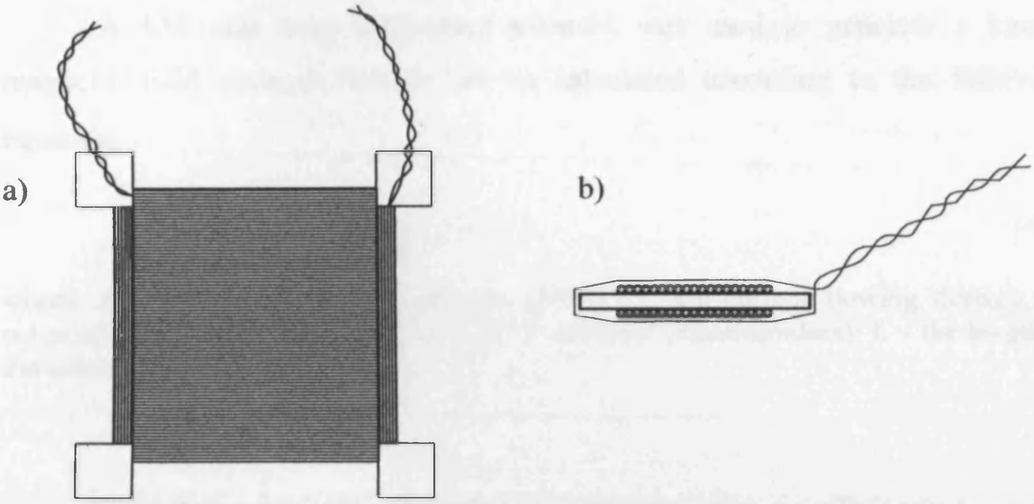

Fig. 4.11. Two orthogonal *H*-coils wound on one former: a) top view, b) cross section

The former was made of 0.25 mm thick plastic sheet and was cut by precise machining with accuracy ±0.01 mm. The width of the former for each coil was 20.00 mm. Each coil had 230 turns and has been wound with 0.05 mm enamelled copper wire.

Greatest care has been taken to make the coils as uniform as possible. After the winding the coils were checked under the microscope to make sure that none of the wires were crossed. For the same reason only a single layer of the coil was wound and therefore only 230 turns were made. A greater number of layers would cause two problems. Firstly, the uniformity of the coil would be very difficult to maintain. Secondly, higher thickness would move the centre of the coil further from the surface of the sample under test. On the other hand, fewer turns would generate lower voltage, especially at lower frequencies. Nevertheless, the rotational magnetic field was measured even at 1 Hz with the 230-turn *H*-coils [*4.10*].

However, before any measurement the *H*-coils had to be calibrated. Although the cross-section of such coils can be analytically calculated, additional errors could have been introduced due to the thickness of the winding wire and its insulation, the non-rectangular windings (see Fig. 4.11b) and other factors, which affect the cross-section in a generally unknown manner. If the *H*-coil is exposed to a known magnetic field strength it is possible to calculate the calibration factor, by which the integrated coil voltage has be multiplied in order to obtain the applied magnetic field strength.

A 538 mm long calibrating solenoid was used to generate a known magnetic field strength, which can be calculated according to the following equation:

$$H = (I \cdot N) / L \tag{4.6}$$

where: H – the magnetic field strength [A/m]; I – the current flowing through the solenoid [A]; N – the number of turns of the solenoid (dimensionless); L – the length of the solenoid [m].

Therefore, a known alternating current applied to a sufficiently long coil with a known number of turns and known length, so as to produce a uniform magnetic field at the centre of such solenoid, can be used for calibration purposes. A schematic drawing of such coil is presented in Fig. 4.12.

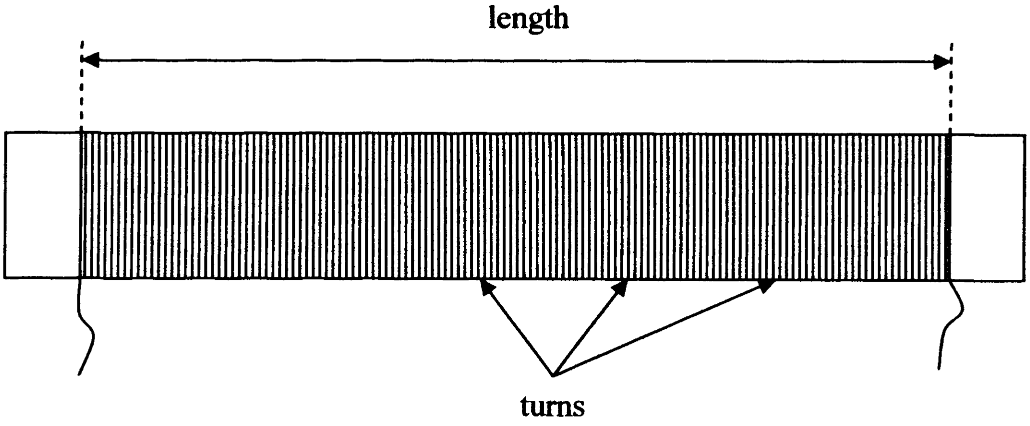

Fig. 4.12. Calibrating solenoid with known number of turns and known length

The H-coils were calibrated within a frequency range from 5 to 500 Hz and within a magnetic field range of 5 to 10000 A/m. The voltages measured from the sensors have been integrated, so the values given in the program have been directly proportional to the magnetic field strength applied.

The calibrating constants for the H-coils were found to be for X and Y coils $N_X \cdot A_X = 0.003319387\ \text{m}^2$ and $N_Y \cdot A_Y = 0.00236372\ \text{m}^2$, respectively. These values were substituted into equation (4.5) and used to calculate the magnetic field strength for all the experiments in this investigation.

As will be discussed in **Chapter 5**, the orthogonality of *H*-coils is of great importance. The paramagnetic former was cut with the aid of precise machining, so the sides of the former were as orthogonal as was practically possible. The winding machine has been carefully levelled and the wire direction was set with a small weight hung on the end of it, which allowed a good right angle to be achieved between the wire and the former.

The "mechanical" direction (that is the direction parallel to the sides of the former) does not necessarily align with the sensing direction of an *H*-coil – sophisticated method using laser beam was used by some scientists to measure those misalignments [*4.11*].

A special high-ratio gearbox has been made in order to allow precise rotation of the *H*-coils, and to investigate the angle between them (Fig. 4.13).

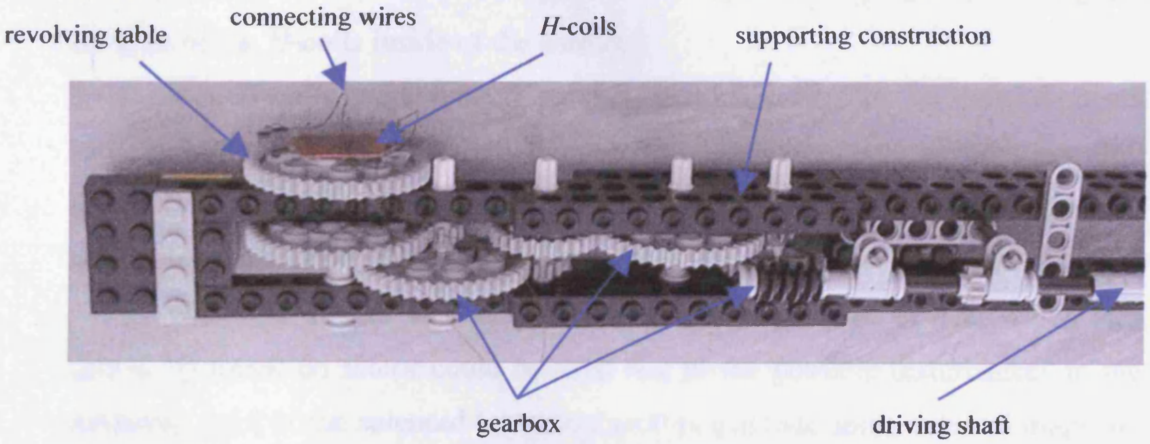

Fig. 4.13. The photo of high-ratio gearbox (1800:1) used to measure the angle between the *H*-coils

The whole setup (i.e. the gearbox with the *H*-coils) was placed in a long calibrating solenoid (see Fig. 4.14). The *H*-coils were placed in such way that the axis of one of the *H*-coils was parallel to the magnetic field direction; therefore it was picking up maximum voltage. The other *H*-coil was obviously aligned perpendicularly to the magnetic field, so there was no voltage induced (a similar approach has also been taken in [*4.11*]). Rotating the coils by 90 degrees would invert the situation: the first *H*-coil would detect zero voltage, and the latter one – the maximum. If the angle between the *H*-coils was different from 90 degrees then rotation by 90 degrees would mean that one of the coils would still detect some voltage instead of zero.

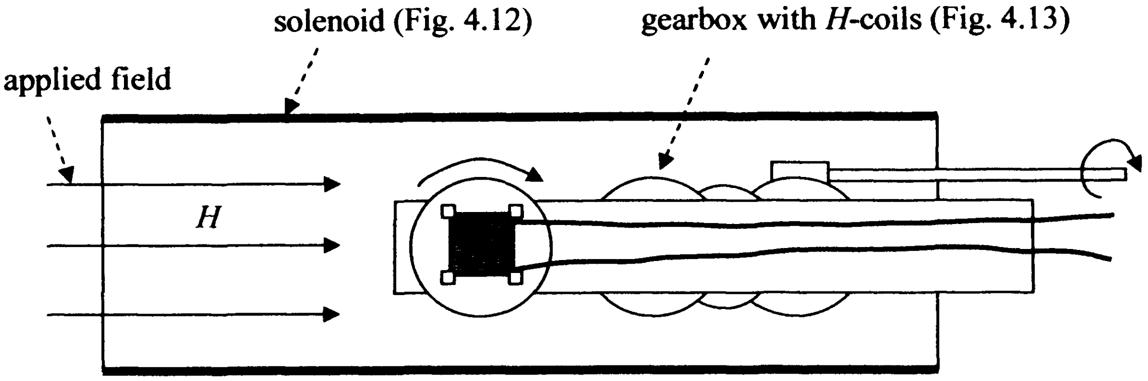

Fig. 4.14. Calibrating solenoid with the revolving table and *H*-coils inside

The ratio of the gear was 1800:1, which means than one turn of the driving shaft corresponded to rotation of 0.2 degree of the revolving table, hence the attached *H*-coils. Therefore 450 turns of the shaft corresponds to 90 degrees rotation of the *H*-coils inside of the solenoid.

The *H*-coils were rotated several times and always the measurements indicated that they were angularly displaced by 90 degrees (450 revolutions · 360 degrees / ratio 1800 = 90 degrees). The accuracy of the gear was not better than 0.2 degree since only whole revolutions of the driving shaft were counted.

The ratio 1800:1 was dictated by the usability of the device, which was driven by hand; no motor could be used due to the possible disturbances in the magnetic field of the solenoid (electrical motors generate some external magnetic field and contain ferromagnetic materials – both these factors have some influence on the strength and direction of the magnetic field).

With the existing setup the measurements could be taken only if the revolutions were made in one direction during one measurement. Reversing the revolutions was introducing some mechanical hysteresis. Therefore great care has been taken in order to rotate the driving shaft without reversing.

The procedure was repeated in both directions of rotation: clockwise and anticlockwise. In both cases the relative angle between the *H*-coils was found to be 90 ±0.2 degrees that is exactly after each 450 revolutions of the driving shaft the voltage from one of the *H*-coils was crossing zero as expected. Possibly, the coils were positioned better than ±0.2 degree, but this was beyond the resolution of the existing setup.

4.1.4. Magnetising current sensors

The digital feedback algorithm requires information about not only the shape of flux density and magnetic field, but also the magnetising currents waveforms. This will be described in detail in section 4.4.2.1. The designed system measures power loss, which is calculated from the values of flux density and magnetic field. The magnetising currents are not needed in the loss calculations – they are measured solely for the purpose of the digital feedback algorithm. Therefore, the accuracy of the measurement of the currents has no specific influence on the total accuracy of the measurement system.

To detect the currents 0.1 Ω shunt resistors were inserted between the isolating transformers and magnetising yoke. (The block diagram of the system will be presented later in section 4.4.2.1; also see Fig. 4.16).

The magnetising currents can reach up to 20 A at high flux density – that would produce a voltage drop of 2 V across the shunt resistor, whilst the voltage from the sensors (*B*-coils and *H*-coils) could be around a few mV, that is lower by three orders of magnitude (-60 dB). The data acquisition card [*4.12*] used in the measuring system has an interchannel cross-talk of -80 dB. However, it has been experimentally confirmed that the lower voltage had been significantly affected by the cross-talk between the channels. To minimise this effect, the actual voltage drop across the shunt resistor was measured through a voltage divider with the ratio 1:101, as shown in Fig. 4.15. In such case the crosstalk was brought down to an undetectable level.

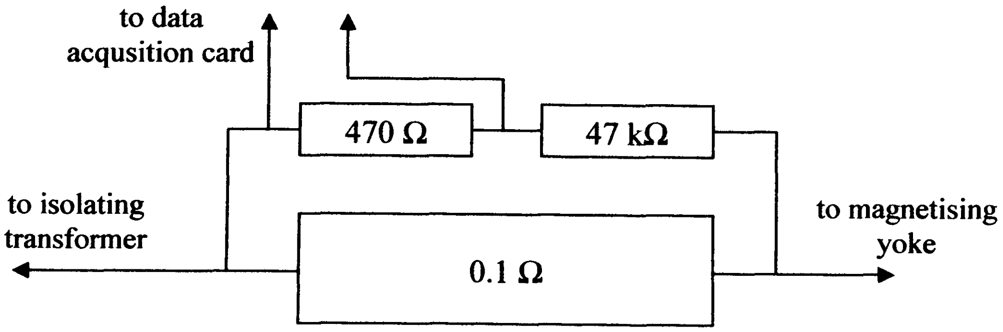

Fig. 4.15. The connection diagram for shunt resistor with voltage divider

4.1.5. Temperature sensor

The temperature in the laboratory has been measured with a stand alone digital thermometer. All the measurements were made in a range of temperatures between 20 and 25 Centigrade. No attempt was made to normalise the measured results through the variations of temperature.

Cooling was implemented in a form of a fan driven by a brushless dc motor to ensure that the sample under test remained within a temperature range between 20 and 25 Centigrade. If necessary the cooling system was working during measurements to keep the temperature down – especially at higher frequencies, where the eddy currents were causing extensive losses (hence heating) not only in the specimen under test, but also in the magnetising yoke.

4.2. Signal conditioning

One of the most important factors in the signal conditioning in any magnetic measurements is twisting of the connecting wires. There are very few publications concerning this problem, although this method is commonly used by all researchers in the area of magnetism.

To ensure minimisation of the influence of any stray flux all the wires were twisted with the aid of a small electrical motor, which allowed achieving high degree of density and uniformity of twisting. It is important to mention that such good twisting is extremely difficult to make by hand. It will be shown in **Chapter 5** that even the best twisting is not able to completely cancel the influence of the stray flux, which interferes with the useful measured signals.

Also, all other wires carrying any signals or currents (even wires supplying the dc fan) were carefully twisted to reduce any stray magnetic field.

Often, precise and low-noise signal amplifiers are used in order to amplify the sensor voltages to improve the signal-to-noise ratio. That was particularly important if 12-bit data acquisition card were used as the low voltages disallowed using full resolution of the card or other measuring equipment [*4.13*, *4.14*]. However, even with a 16-bit card this technique is still used [*4.15*, *4.16*]

Initially, techniques employed in previous studies [*4.14*, *4.15*] were implemented. Each voltage measured by the data acquisition card was initially amplified by precise low-noise instrumentation amplifiers (PGA204A) with selectable gain of 1, 10, 100 and 1000 [*4.17*]. In order to increase the stability of the pre-amplifiers they were supplied from a battery, rather than from a stabilised power supply. However, the dynamic and phase characteristics for each gain are different and using several amplifiers with different gains would create more problems than advantages. Thus, if the preamplifiers are used they all have to be set to have the same gain [*4.18*]. Large gain introduces larger phase delays between the input and the output of the amplifiers. Furthermore, in the case of greater gains the higher harmonics would be attenuated [*4.17*], which is not acceptable if distorted waveforms are to be measured.

For that reason it has been decided not to use any pre-amplifiers at all. The resolution of the used data acquisition card is in order of 1.5 μV [*4.12*], but it can be significantly improved by using dithering and averaging techniques – see description and explanation in section 4.4.3.

Avoiding preamplifiers allowed the electrical connections to be simplified in the system and also to minimise most of variable and unknown phase shifts and non-linearity in the measured signals.

The influence of the phase shift between acquired signals on the measured power loss is a known problem and therefore researchers always try to minimise it [*4.13*, *4.18*]. However, it seems that the influence is even greater than initially thought. Thus the use of preamplifiers was given up to avoid any phase shifts as much as possible. Obviously the data acquisition card [*4.12*] has internal built-in preamplifiers to enable using different measurement limits for various voltages. However, the manufacturer uses a specially designed and patented technique, in which the phase lag of the instrumentation amplifiers does not depend on their gain [*4.19*].

In essence, the phase shift between the acquired signals is similar in nature to the misalignment of the sensors. This will be shown in analysis in **Chapter 5**.

The importance of settling time and its influence on the accuracy of voltage measurements was highlighted in [*4.19*]. The settling time is defined there as: ***the amount of time required for a signal that is being amplified to reach a certain accuracy and stay within the specified range of accuracy***. The settling time depends not only on the internal characteristics of the data acquisition card, but also on the properties of the measured voltage. Especially, the magnitude of two voltages being measured one after the other plays a major role.

The order of connections of the sensors to the card was: B_X, B_Y, H_X, H_Y, I_X and I_Y. The B and H signals were all of similar magnitude, thus they did not influenced the settling time significantly. However, the voltages measured across the shunt resistors described above were usually much higher than the other signals, and the impedance of the voltage source was also higher than for the other signals (around 470 Ω). Thus, switching from the last signal (I_Y) to the first one (B_X) could cause disturbances in the settling time and inaccuracy in the voltage measurement. (Because the currents signals were measured after the B and H waveforms then the accuracy was not of prime importance, since the current waveforms were used only for the digital feedback algorithm and not for the power loss measurement.) To avoid such influence, the B_X signal was measured twice: firstly as a dummy voltage to give time for settling of the instruments, and secondly for the proper voltage measurement.

There was no clear indication that this affected anyhow the final accuracy of the power loss measurement, but this approach was used for all the measurements.

4.3. Power amplifiers and isolating transformers

The power amplifiers are very important components of any magnetising system, since their role is to supply the magnetising currents, without which the magnetisation could not be made in the first place.

It is well known that although the power amplifiers are capable of supplying very high currents, they are also quite vulnerable to unexpected working conditions. For that reason, the selection of the power amplifiers was partially based on the available output power, but also on the reliability. Thus, current mode amplifiers were chosen – model MT2400 [*4.20*]. The MT2400 can operate at any frequency between dc and 20 kHz. The amplifier is equipped with a thermal protection, which will shut down the device if it overheats. Its maximum output voltage is 55 V, and there is another electronic circuit protecting the amplifier from over voltage at the output. These two protections (thermal and voltage) make the MT2400 very useful in research, since they save the amplifier from damage in a very efficient way. During the whole period of this project none of three MT2400 amplifiers was damaged, although they were overheated and overloaded several times.

The dc coupling of the output of the amplifiers introduces a dc offset in the magnetising current. This offset can be minimised by internal potentiometers [*4.20*], but it cannot be eliminated, because its level floats for different ambient temperature. Therefore, it would be extremely difficult to keep it down just by settings of the potentiometer. Thus, all the measurements were carried out with the magnetising yoke connected to the amplifiers through isolating transformers, which do not transfer any dc component in the current to the load.

The magnetising current can be increased by forcing output currents from two power amplifiers into one magnetising coil of the yoke. This increases the available magnetising field and allows achieving higher magnetisation levels. In such configuration two power amplifiers work in parallel, amplifying the same voltage signal. The output currents from the amplifier are "bridged" together through the isolating transformer, as it is shown in Fig. 4.16.

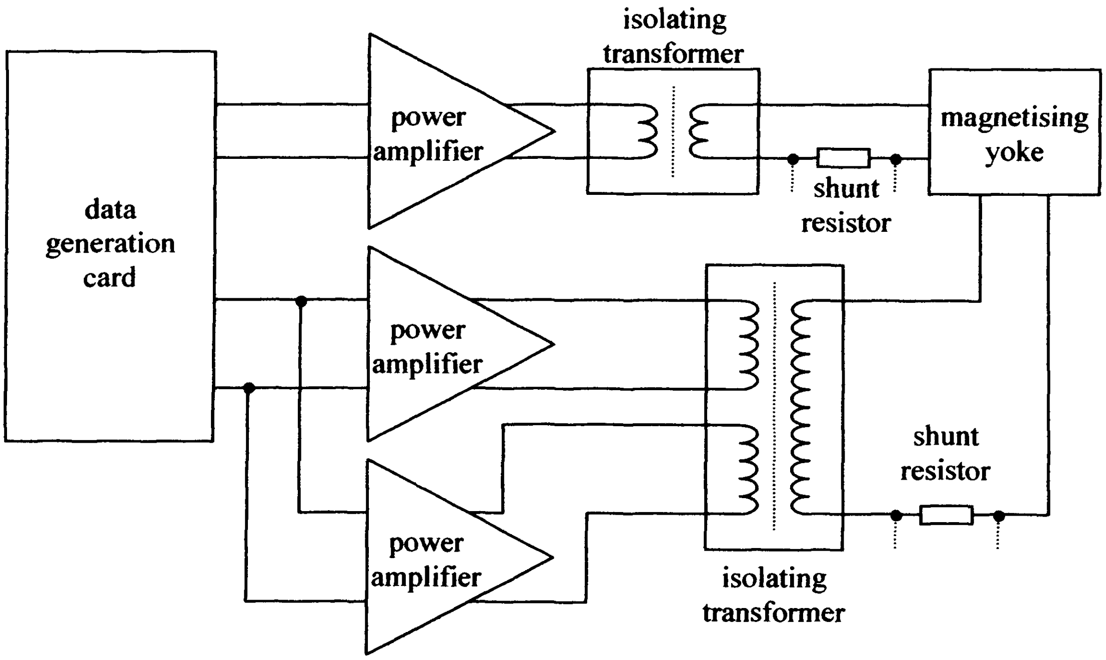

Fig. 4.16. The diagram of electrical connections in the magnetising circuit [*4.21*]

Despite two amplifiers working together there is only one magnetising current. Thus only this current is sensed through a shunt resistor. The voltage across this resistor is fed to the card and is used in the feedback algorithm, which does not "know" that there are two amplifiers. This method is possible only for power amplifiers with identical or very similar characteristics and also under condition that both primary windings in the isolating transformers are identical.

The dc coupling of the output of MT2400 posed another problem – the interference in the output current. In voltage mode amplifiers such noise is much less noticeable due to better attenuation; however, in current mode amplifiers it is more difficult to suppress it. The initial measurements with the MT2400 showed that in the output current there is 50 Hz hum, which in some cases, e.g. when low magnetising currents are used, is unacceptable for precise measurements.

All MT2400 were returned to the manufacturer for modification of the electronic circuit in order to minimise this interference. The results of the modification of the amplifiers are shown in Fig. 4.17.

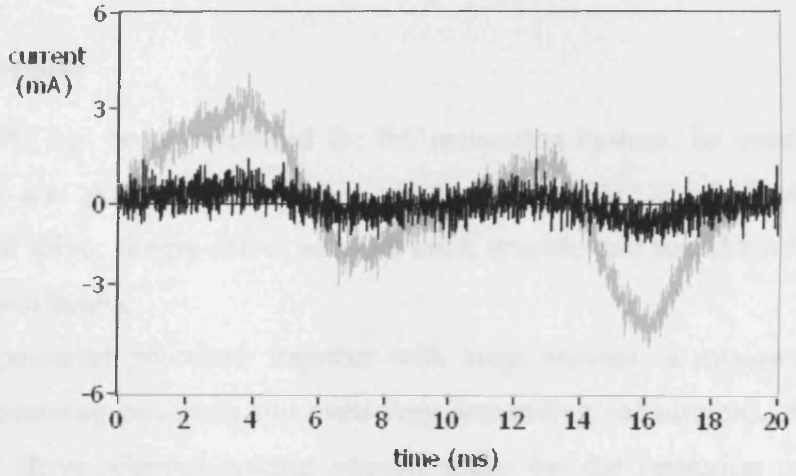

Fig. 4.17. The output current of the MT2400 power amplifier with zero input signal; grey waveform – before modification, black waveform – after modification

The magnitude of the interference in the output current was suppressed to a large degree, that is, better than 15 dB. The 50 Hz noise was not eliminated completely, but since the peak was at the level of 500-800 μA the influence dropped below detectable level in the measured results.

The MT2400 has a load-dependant characteristic, which means that every single power amplifier should be "tuned" to a specific load. If the amplifier is not tuned it will still work, but its characteristic will be far from linear, thus will worsen the working conditions for the feedback algorithm. Therefore, all the amplifiers were carefully tuned according to the procedure given by manufacturer [*4.20*]. However, for practical reasons, the amplifiers could not be tuned for every single load (i.e. every specimen), thus the tuning was set for one sample and kept the same for all experiments since the properties of the magnetising yoke were far more influential than the properties of each specimen.

4.4. Development of the computerised system and software

A very important part of any measuring setup is the interface, through which the user can interact with the system and understand the measured results. In the case of the rotational system concerned, the role is even wider – the software is responsible not only for interaction with the user, but also for the digital feedback algorithm, without which repeatable rotational measurements would not be possible.

4.4.1. Computer

A PC has been purchased for the measuring system. Its most important parameters are: processor Pentium 4 clocked at 1 GHz, 256 MB of memory, 30 GB hard drive, floppy drive, network card, graphic and sound card integrated with the main board.

A powerful processor together with large amount of memory provided enough processing power to run even very demanding calculations. A medium-sized hard drive allowed having enough space for the operating system, the software (see also section 4.4.2) and the acquired data. The floppy drive was very useful for transporting the measured results to another computer for analysis – similarly the network adapter made possible to easy transfer the data to any computer in the local network, as well as downloading any required drivers through the internet. Since the visualisation of the measured results was not very demanding the graphic card did not have to be powerful and fast. A sound card was useful to produce warning and informing sounds for the user.

4.4.2. Software

The computer was equipped with operating system Windows NT 4.0™ and the programming package LabVIEW 5.1™. Windows NT 4.0 proved to be very stable operating system under very demanding calculations and time consuming calculations and analysis. The LabVIEW package is a graphic programming language. The programmer operates only with libraries, so-called "wires" and icons, which are connected together on the computer screen in order to create a working algorithm [*4.22*].

The solutions used in LabVIEW package are very user-friendly and allow creating and altering written programs virtually within minutes, since no compilation is required. Visual representation of the data flow in the program diagram makes the program understandable to any user, even who knows only the basics of LabVIEW programming. LabVIEW allows creating extremely complex applications, which would very difficult to write with any other programming environment.

Any LabVIEW program consists of two parts: the block diagram, where all the functions, libraries, calculations and data flow are programmed, and the front panel, which is used for the communication with the user (see Fig. 4.18).

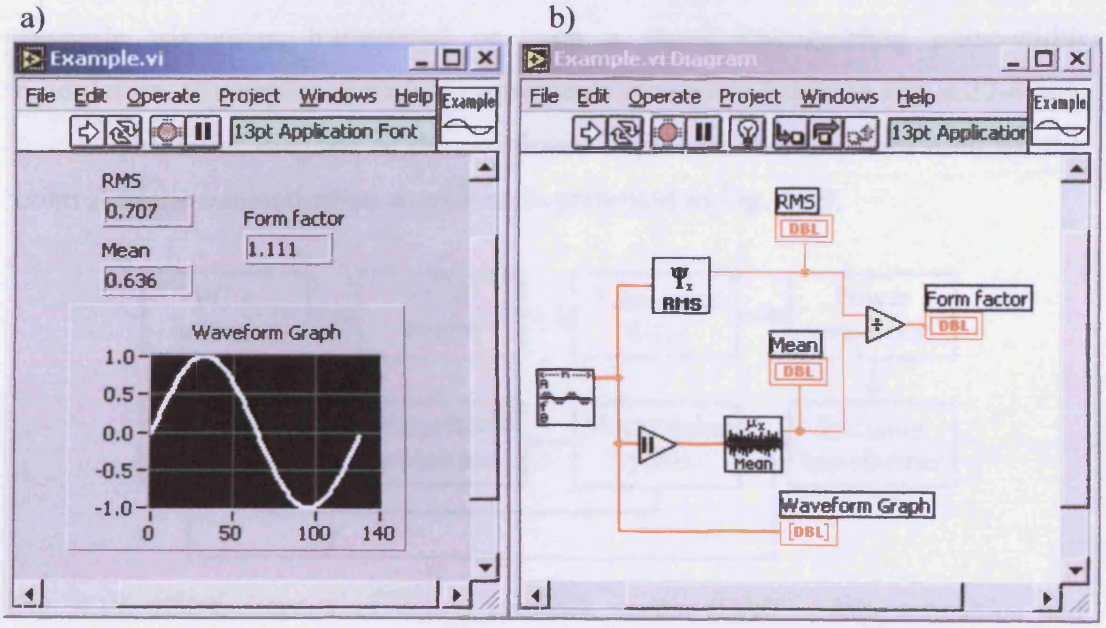

RMS 0.707
Mean 0.636
Form factor 1.111

Fig. 4.18. An example of LabVIEW program: a) front panel, b) block diagram

4.4.2.1. Adaptive iterative digital feedback algorithm

In order to make any repeatable and comparable measurements under rotational magnetisation it is required that the shape of the flux density or magnetic field is controlled. Previous research showed that analogue electronic feedback was not versatile enough to ensure required control or stability, especially for high flux density measurements [*4.23*].

As soon as the computer technology became widely available, people started implementing computerised system, since they were exhibiting better stability and were promising to achieve greater control over the magnetising process. Software-based feedback algorithms proved to be capable of controlling the flux density also in rotational measurements [*4.10*, *4.15*].

Once the digital feedback algorithm has been developed for elliptical and circular magnetisation, it was developed further in order to make it possible to carry out the measurements under arbitrary shape of flux density or magnetic field. The digital feedback algorithm described below is the "brain" of the whole measuring system. The amount of calculations carried out in every single iteration of the program is tremendous, but in return it allows achieving magnetising conditions, which were not used in research before anywhere in the world. Not only the frequency range is very wide (from 1 Hz to 1 kHz [*4.10*]), but also the flux density and the magnetic field can be controlled to any arbitrary shape, for example triangular, trapezoidal or even a shape reassembling pulse-width modulation. (Examples of such measurements are shown below in Fig. 4.27-4.30).

The block diagram of the developed digital feedback system used for the control of the magnetisation waveform is presented in Fig. 4.19.

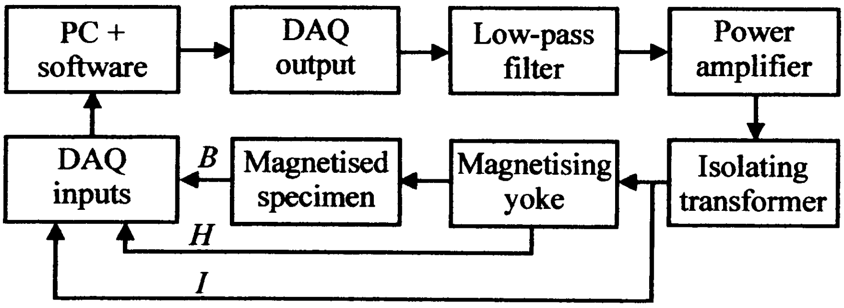

Fig. 4.19. Block diagram of digital feedback system (DAQ – data acquisition and generation card)

In summary: a computer, with LabVIEW and a data acquisition and generation card generates a voltage waveform. This voltage is fed through a low-pass filter to a power amplifier. An isolating transformer removes any dc component in the magnetising current. The magnetising current is fed to a magnetising yoke through a shunt resistor, which allows current measurement. All measured signals are connected to the inputs of the data acquisition card, from where they are acquired by the software.

The feedback algorithm presented here is called "digital" because all the operations like: low-pass filtering of the input signals, integration, differentiation, Fourier transform, proportional controller, etc., are completely realised in the software. No external signal conditioning or analogue signal processing is used, which in conjunction with arbitrary waveform control makes the presented adaptive digital feedback algorithm superior to the analogue systems.

The digital feedback algorithm consists of four main parts (Fig. 4.20). The first is the measuring thread (**A** in Fig. 4.20), in which acquired signals are used to calculate the flux density, ***B*** [T], magnetic field strength, ***H*** [A/m], power loss per unit mass P [W/kg], etc. (The bold italic symbols: ***B***, ***H***, ***I***, etc. denote one-dimensional arrays of data, which represent the corresponding waveforms.)

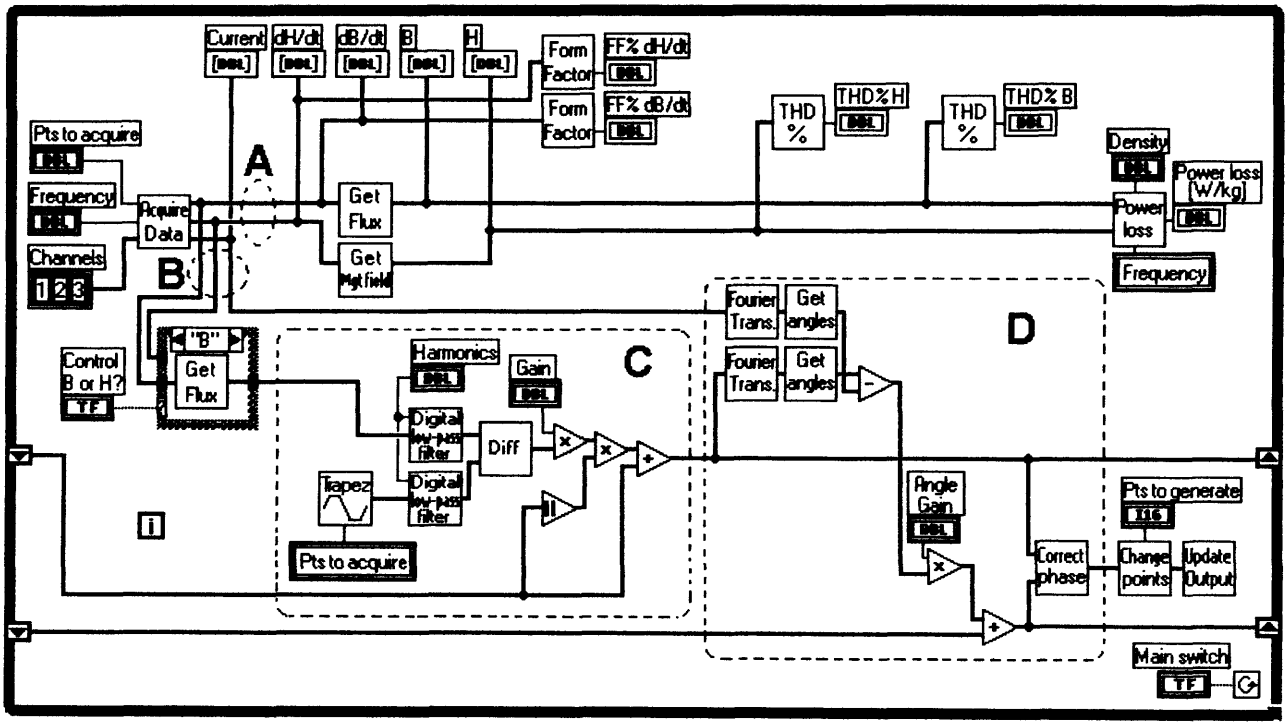

Fig. 4.20. Simplified adaptive digital feedback algorithm written in LabVIEW (not all modules are shown for clarity): **A** – measurement thread, **B** – control thread, **C** – proportional controller, **D** – adaptation module (see description in text); dH/dt – voltage from *H*-coils, dB/dt – voltage from *B*-coils, THD – total harmonic distortion

The second thread (**B** in Fig. 4.20) feeds the acquired waveforms to the digital feedback modules. The same input data are used as for the measuring thread. However, additional calculations are implemented, such as digital filtering and computation of the relative difference between reference waveform and real ***B***

$$Diff_{(i)} = (B_{ref} - B_{real\,(i)}) \;/\; \hat{B}_{ref} \qquad (4.7)$$

where: **Diff** - waveform of relative difference between reference and real waveforms, B_{ref} - reference (ideal) flux density waveform, B_{real} - real (measured) flux density waveform, $\hat{B}_{ref}$ - peak value of reference flux density waveform, i - current iteration.

In each iteration, the waveform **Diff** is used to modify the generated output voltage waveform accordingly (**C** in Fig. 4.20), until the difference between the expected and real waveform is equal or less than the user defined value.

The algorithm initially assumes that **B** depends linearly on the magnetising current **I**. The non-linearity between measured **B** and applied **H** or magnetising current **I** is very complicated and strongly dependent on the shape and magnetic properties of the yoke and the specimen. The passive low-pass filter and power amplifier introduce a phase lag up to several tens of degrees for different harmonics. The phase lead/lag functions of the low-pass filter and the power amplifier can be found relatively easily (as depicted in Fig. 4.21), but the magnetising yoke, the various air-gaps as well as the *B-H* characteristics of the specimen cause the transfer function of the whole system to continually change. In order to compensate for this, a module that calculates the phase lead/lag between the output voltage generated by the data acquisition card and actual magnetising current for each harmonic is implemented (**D** in Fig. 4.20).

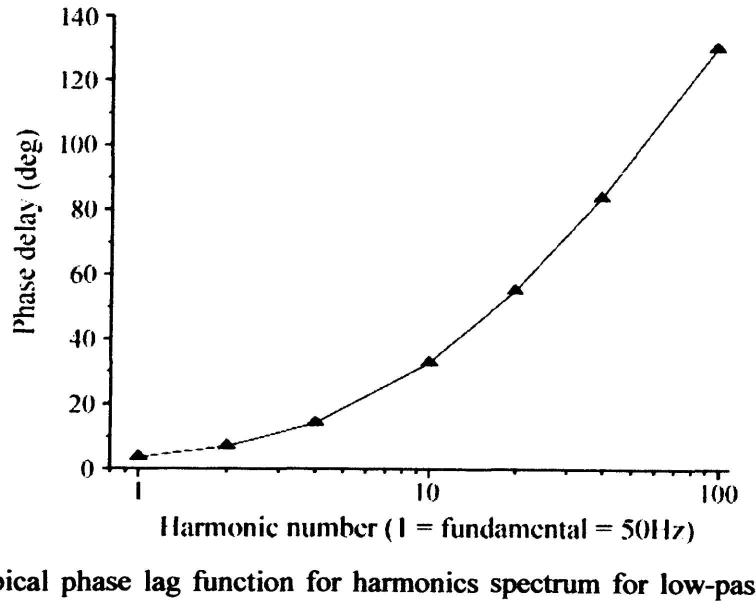

Fig. 4.21. Typical phase lag function for harmonics spectrum for low-pass passive RC filter (R = 2 kΩ, C = 10 nF) and power amplifier MT2400

The array of phase shifts for all harmonics is continuously adapted in every subsequent iteration. Before the data acquisition card generates the output voltage, the waveform computed by the proportional controller (**C** in Fig. 4.20) is fed to the *Correct phase* element (see **D** in Fig. 4.20), which provides a Fourier transform of the waveform, modifies the phase of each harmonic, and then calculates an inverse Fourier transform.

This artificially "distorted" output waveform is then generated by the data acquisition card and "converted" through the non-linear components (low-pass filter, power amplifier, isolation transformer, yoke, and specimen) to the desired shape of the flux density waveform.

As the permeability of the sample under investigation usually changes very rapidly throughout the magnetisation cycle, a greater modification of the controlled signal than predicted by the feedback may occur in the most non-linear regions of the magnetising curve. This would lead to oscillations of the magnitude of the controlled waveform. In practice, feedback gains equal to 0.3 or less successfully prevent this (these are shown as *Gain* and *Angle Gain* icons in **C** and **D** in Fig. 4.20, respectively).

Since in general (taking into consideration the influence of staircase effect [*4.24*]) the data acquisition cards acquires a different number of points per magnetisation cycle than it generates, there is a module responsible for rendering the waveform to another number of points (this is shown as *Change points* icon in Fig. 4.20). A simplified block diagram of the adaptive digital feedback system is presented in Fig. 4.22.

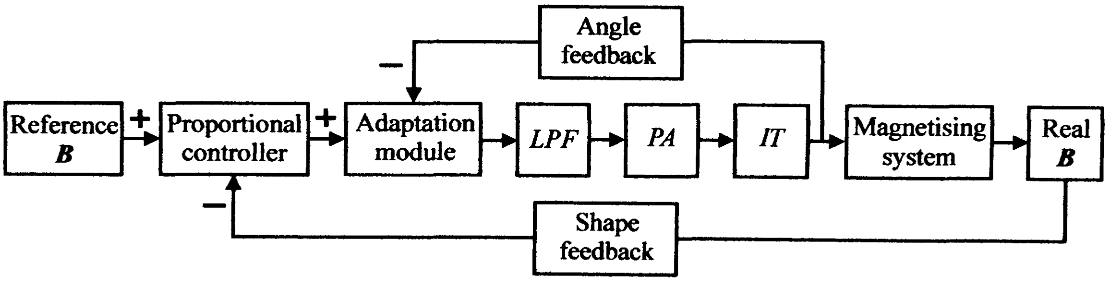

Fig. 4.22. Block diagram of digital adaptive feedback system: *LPF* – low-pass filter, *PA* – power amplifier, *IT* – isolating transformer

The equation for calculating the output voltage waveform in subsequent iterations takes a simple form

$$\boldsymbol{Out}_{(i)} = \boldsymbol{F}_{(i)}\,(\,\boldsymbol{Out'}_{(i)}\,) \tag{4.8}$$

where: i - current iteration, $\boldsymbol{Out}$ - voltage waveform generated by the *DAQ*, $\boldsymbol{Out'}$ is the output waveform calculated for i^{th} iteration by the proportional controller as

$$\boldsymbol{Out'}_{(i)} = \boldsymbol{Out}_{(i\text{-}1)} + \boldsymbol{G} \cdot |\,\boldsymbol{Out}_{(i\text{-}1)}\,| \cdot \boldsymbol{Diff}_{(i)} \tag{4.9}$$

where: $\boldsymbol{G}$ - gain of the proportional controller (shown as *Gain* icon in **C** in Fig. 4.20), $\boldsymbol{Diff}$ - difference waveform calculated from equation (4.7), i-1 - previous iteration.

The waveform $\boldsymbol{Out'}$ from (4.9) is a one period of continuous function and can also be expressed as a finite Fourier series

$$\boldsymbol{Out'}_{(i)} = \sum_{k=1} \left[A_{(k)} \cdot \cos\left(k \cdot 2 \cdot \pi \cdot f \cdot t + \varphi_{(k)} \right) \right]_{(i)} \tag{4.10}$$

where: k - harmonic number, A - magnitude of the k^{th} harmonic, f - magnetising frequency, t - time, φ - phase shift of the k^{th} harmonic.

Symbol $\boldsymbol{F}$ in equation (4.8) denotes a function of phase lead/lag for all harmonics. It is applied by module *Correct phase* in **D** in Fig. 4.20 as

$$\boldsymbol{Out}_{(i)} = \sum_{k=1} \left[A_{(k)} \cdot \cos\left(k \cdot 2 \cdot \pi \cdot f \cdot t + \varphi_{(k)} + \alpha_{(k)} \right) \right]_{(i)} \tag{4.11}$$

where α is the phase lead/lag of the k^{th} harmonic calculated as

$$\alpha_{(k,\,i)} = \alpha_{(k,\,i\text{-}1)} + G_{\alpha} \cdot \left(\alpha_{B\,(k,\,i)} - \alpha_{I\,(k,\,i)} \right) \tag{4.12}$$

where: G_{α} - gain of angle feedback (shown as *Angle Gain* icon in **D** in Fig. 4.20), α_B - phase of the k^{th} harmonic of flux density waveform, α_I - phase of the k^{th} harmonic of magnetising current.

Hence the array of phase shifts for all harmonics which is fed to the module *Correct phase* can be written as

$$\boldsymbol{\alpha} = [\,\alpha_{(1)}\,, \alpha_{(2)}\,, \ldots\,, \alpha_{(n)}\,] \tag{4.13}$$

where: $\boldsymbol{\alpha}$ is an array of phase shifts for all analysed harmonics, α - phase shift for a given harmonic and $\boldsymbol{n}$ - total number of analysed harmonics.

For simplicity, the adaptive digital feedback is described above only for one magnetising channel. The concept remains the same for two-dimensional magnetisation, but there must be as many control threads, as there are magnetising channels - instead of one. In practice this means that the control thread and adaptation module (**B**, **C** and **D** in Fig. 4.20) are simply doubled for all the magnetising channels. Naturally, there is a need for measuring appropriately more signals, in order to have independent information about *B-I* relationship for each magnetising channel.

The algorithm calculates the magnetising channels independently. During the controlling process any mutual dependencies are corrected automatically. This makes the feedback "adaptive", since there is no need for knowing how the magnetising channels interact with each other.

The control is much easier when the magnetising channels have similar magnetic properties; if the magnetising channels differ significantly in their properties, then the controlled arbitrary magnetisation is more difficult. For example, in the case of anisotropic materials the permeability in "easy" and "hard" direction may differ by a few orders of magnitude - in such case the controlling conditions are very difficult to achieve.

Several magnetising systems were used to test the versatility of the control algorithm (Fig. 4.23). These were: toroid, a conventional Epstein frame, a non-standard single strip tester, various *2D* yokes and a three-phase transformer. In all of these cases the adaptive digital feedback proved to be stable.

Data processing can only be carried out once a complete cycle of the magnetising waveform has been acquired. Therefore, the time of each iteration and thus the convergence time depend on the magnetising frequency. As the frequency increases the time of the cycle decreases accordingly, but the number of iterations necessary to achieve a controlled state of magnetisation remains approximately the same (sèe Fig. 4.24). For this reason, a controlled excitation at higher frequencies would take as short as few seconds to approach to required magnetising conditions.

The accuracy of the measurement can be improved by using the averaging of the readings (Fig. 4.24b), but this affects the controlling time. Nevertheless, even as low as 0.5 Hz results have been measured for alternating magnetisation. The highest magnetising frequency at which the samples were tested was 2 kHz and it was limited mainly by the sampling frequency of the data acquisition card, which for PCI-4452 is 200,000 samples per second [*4.25*]. It is assumed that the presented here digital feedback algorithm would work as intended even for higher frequencies.

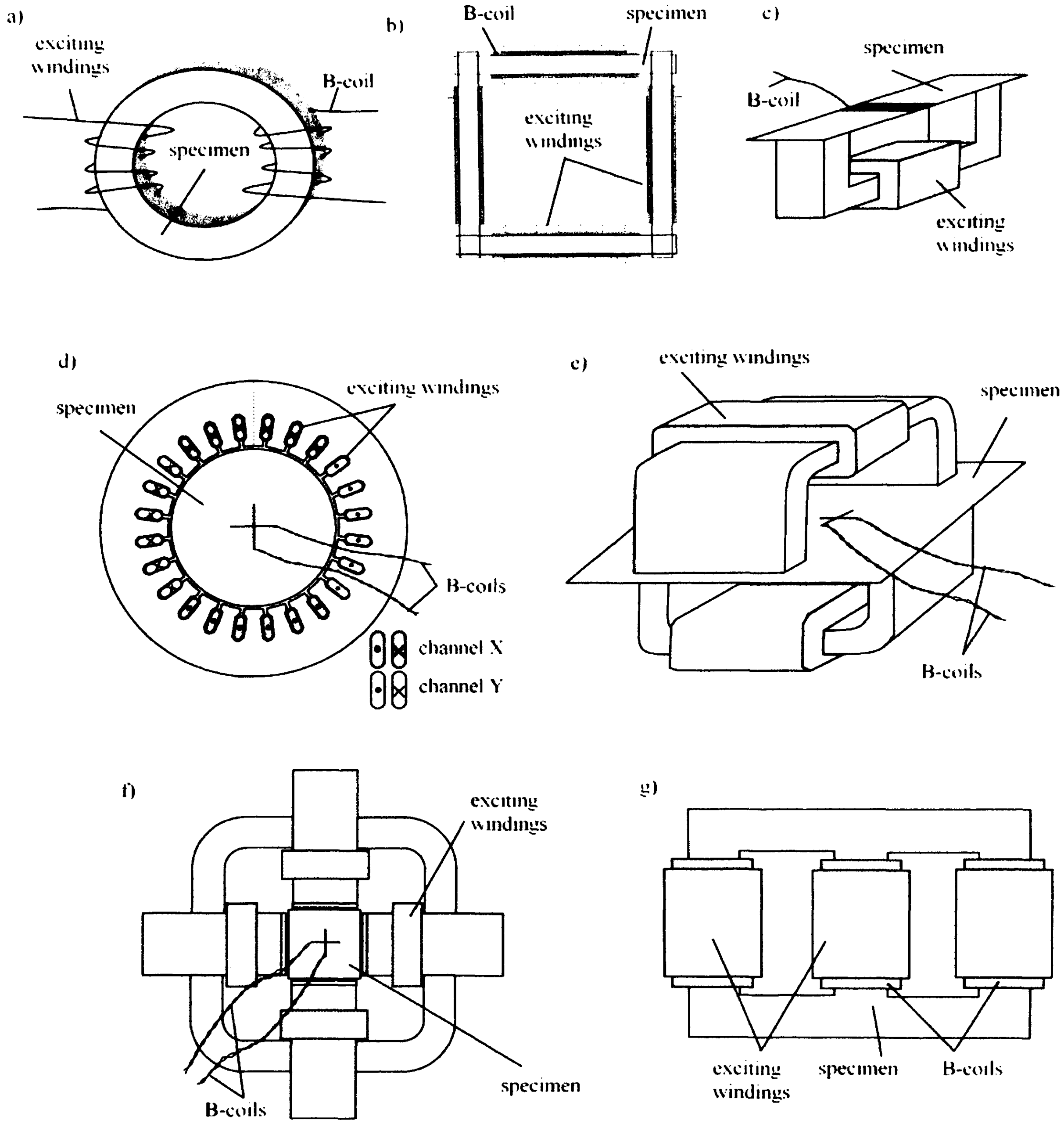

Fig. 4.23. Types of magnetising testers used in investigation: a) toroid, b) Epstein frame, c) single strip tester, d) round *2D* yoke, e) double-sided *2D* yoke, f) planar *2D* yoke, g) small three-phase transformer

Fig. 4.24 presents typical graphs of adaptive digital feedback performance. The feedback starts from zero waveforms, so all the factors have initially 100% error. As the software processes subsequent iterations these factors decrease to zero.

It can be seen from Fig. 4.24 that the percentage error of the form factor, *FF*, of *dB/dt* is well within the limits specified by the international standard for magnetic measurements [*4.26*] and also the percentage error of B_{peak} is within 0.2% of the ideal value.

Typical values of the convergence time for an Epstein frame (Fig. 4.23b) and a 2D yoke (Fig. 4.23f) are presented in Table 4.1. In each case the magnetisation started from zero and was controlled until B_{peak} (in alternating unidirectional magnetisation) or $B_{X\ peak}$ and $B_{Y\ peak}$ (orthogonal B components in rotational magnetisation) reached a satisfactory level of control.

The speed of the controlling algorithm was satisfactory at any magnetising frequency used in this research, which is from 10 Hz to 250Hz.

Table 4.1. Typical values of convergence times for alternating and rotational magnetising conditions

	Conventional grain-oriented electrical steel				Conventional non-oriented electrical steel			
	Epstein frame		*2D* yoke		Epstein frame		*2D* yoke	
Frequency [Hz]	Time [min]	B_{peak} [T]	Time [min]	B_{rot} [T]	Time [min]	B_{peak} [T]	Time [min]	B_{rot} [T]
5	6	1.9	10	1.3	2	1.6	2	1.5
50	1	1.9	1	1.5	1	1.6	1	1.7
1000	1	1.9	0.5	1.0	0.5	1.6	0.5	1.0

The controlling time can be greatly reduced by using pre-recorded controlled measurement. In such case the feedback does not start from a zero level, which allows the convergence time to be reduced down to almost instant control (a few periods of given magnetising frequency). Also, to speed up the control process other techniques may be used, for example those described in [*4.27, 4.28*].

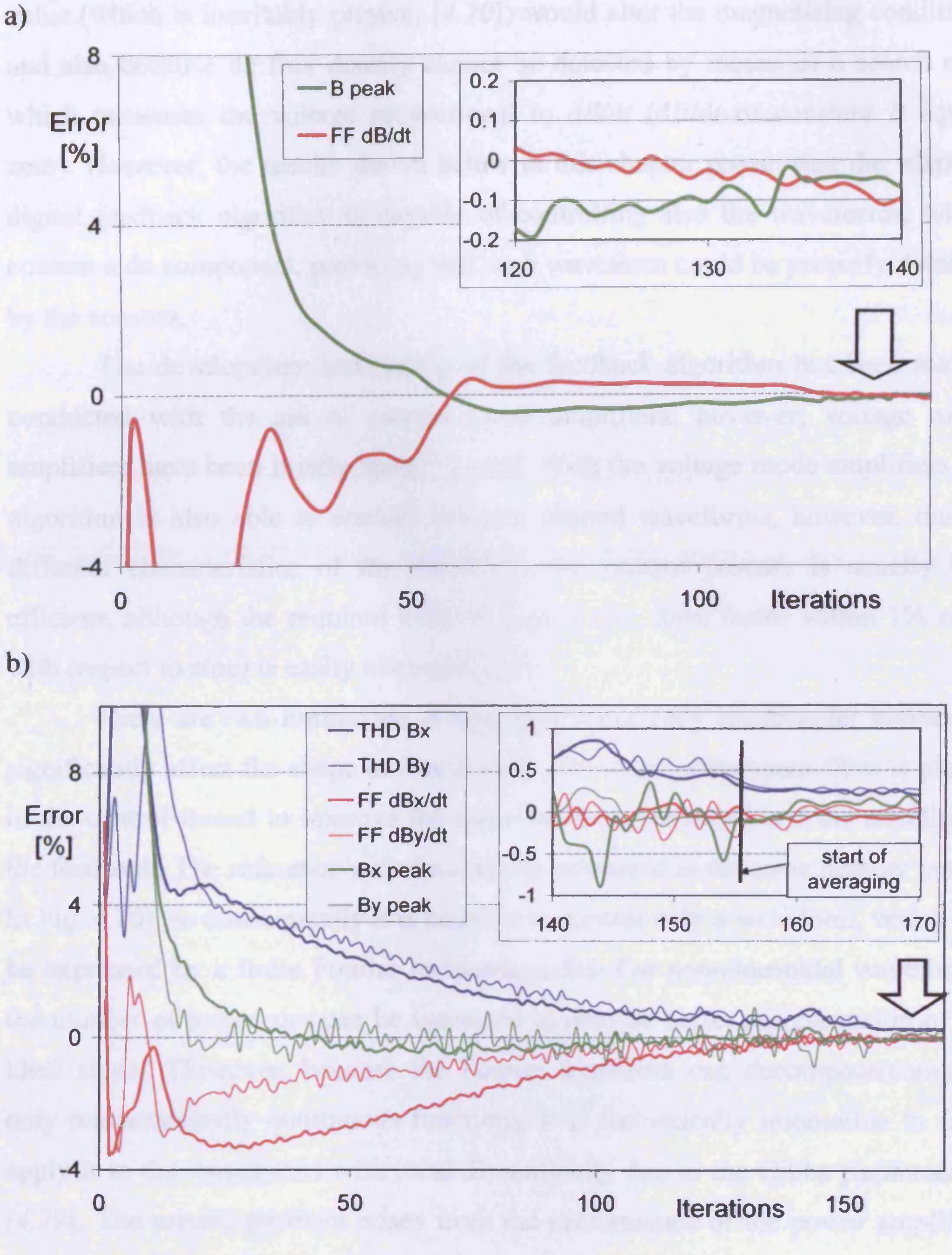

Fig. 4.24. Typical graphs of the performance of the adaptive digital feedback: a) alternating magnetisation at 1 kHz, 1.6 T, non-oriented electrical steel sheet, b) 2D rotational magnetisation at 50 Hz, 1.5 T, conventional grain-oriented electrical steel. (The insets show the magnifications of final the part of controlling process. The inset in Fig. 4.24b also shows the influence of averaging of the readings from 25 periods.)

The described adaptive digital feedback algorithm can be used to provide control for any arbitrary waveform of flux density, such as: sinusoidal, triangular, trapezoidal, PWM, etc., provided they do not contain a dc component. The dc component is prevented by the presence of the *IT*, because its usually unknown value (which is inevitably present, [*4.20*]) would alter the magnetising conditions and also because dc flux density cannot be detected by means of a search coil, which measures the voltage proportional to $\mathrm{d}B/\mathrm{d}t$ ($\mathrm{d}B/\mathrm{d}t$ of constant B equals zero). However, the results shown below in this chapter prove, that the adaptive digital feedback algorithm is capable of controlling also the waveforms, which contain a dc component, providing that such waveform could be properly detected by the sensors.

The development and testing of the feedback algorithm has been mainly conducted with the aid of current mode amplifiers; however, voltage mode amplifiers have been briefly tested as well. With the voltage mode amplifiers the algorithm is also able to control arbitrary shaped waveforms, however, due to different characteristics of the amplifiers the control process is usually less efficient, although the required level of control (i.e. form factor within 1% error with respect to sine) is easily obtainable.

There are two limitations. Since, in practice only lower order harmonics significantly affect the shape of flux density waveform, a low-pass filter is placed in the control thread to improve the speed of data processing and the stability of the feedback. The reference waveform is pre-processed in the same manner (see **C** in Fig. 4.20), so consequently it is possible to control only a waveform, which can be expressed by a finite Fourier harmonic series. For non-sinusoidal waveforms, the number of harmonics can be increased to provide better representation of the ideal signal. However, because the Fourier transform can decompose/compose only mathematically continuous functions, it is theoretically impossible to fully apply it to the waveforms with local discontinuity due to the Gibbs phenomenon [*4.29*]. The second problem arises from the performance of the power amplifier, since it is difficult to drive fast rising current into an inductor. For that reason it is physically impossible to generate a square shaped current waveform even without feedback. Hence the rise time of the output current sets the limits to the shape and frequency of the controlled signal.

In practice, under alternating magnetisation conditions, typically no more than 50 harmonics are sufficient to provide an acceptable level of control for commonly used non-oriented and grain-oriented electrical steel and would be similar to other commercial soft magnetic materials. Under rotational conditions, magnetisation of grain-oriented steel is extremely difficult to control, due to its high anisotropy, and sometimes up to 150 harmonics might be required.

Fig. 4.25 shows the results obtained for testing non-oriented electrical steel in the Epstein frame at 0.5 Hz and 2 kHz. In both cases the shape of flux density waveform has been controlled to be sinusoidal with B_{peak} = 1.46 T. The B waveforms presented Fig. 4.25b are identical, thus only one curve is shown (dashed, black coloured). Obviously the waveforms in Fig. 4.25 b have different times of duration, 2000 ms for 0.5 Hz and 0.5 ms for 2 kHz, therefore they are plotted with respect to the magnetising cycle.

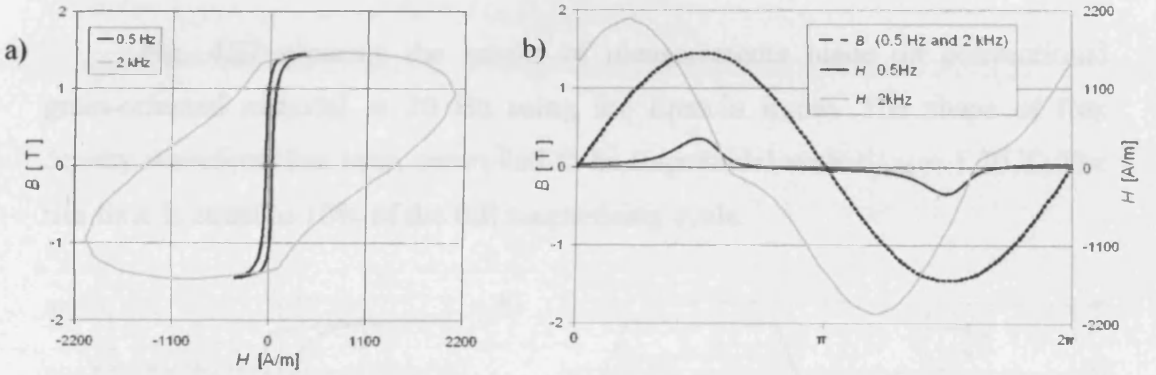

Fig. 4.25. Non-oriented low silicon electrical steel 0.5 mm thick magnetised in an Epstein frame at 0.5 Hz and 2 kHz, 1.46 T: a) *B-H* loops, b) corresponding waveforms of *B* (sinusoidal - controlled) and *H*

Fig. 4.26 presents results of measurement made on conventional grain-oriented material in an Epstein frame at 800 Hz at flux density B_{peak} = 1.95 T. The B waveform is controlled to be sinusoidal.

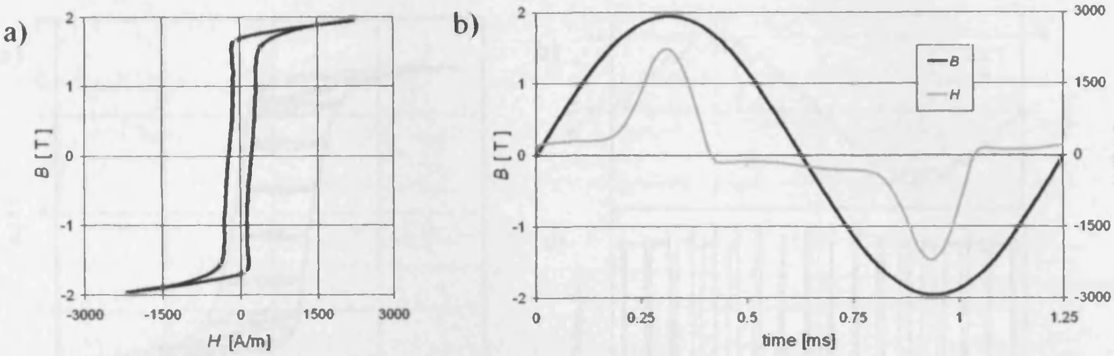

Fig. 4.26. Conventional grain-oriented 3% silicon electrical steel 0.27 mm thick magnetised in an Epstein frame at 800 Hz, 1.95 T: a) *B-H* loop, b) corresponding waveforms of *B* (sinusoidal - controlled) and *H*

Fig. 4.27 presents the results of measurements made on conventional grain-oriented material at 20 Hz using the Epstein frame. The shape of flux density waveform has been controlled to be trapezoidal with B_{peak} = 1.70 T. The rise time is equal to 10% of the full magnetising cycle.

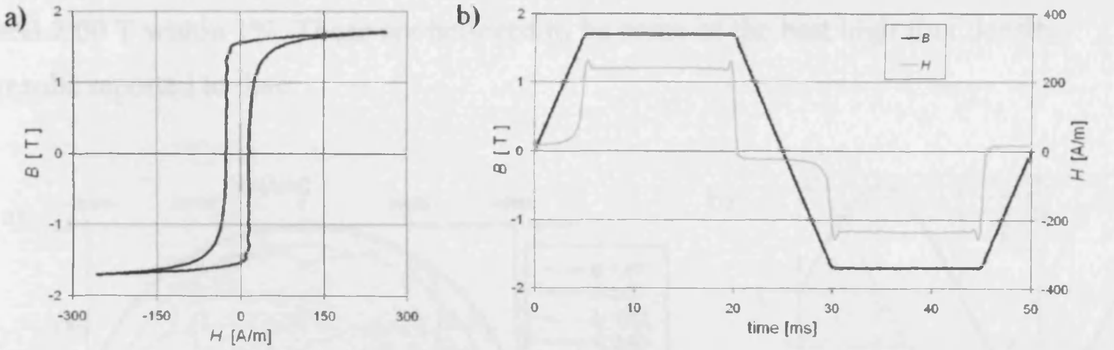

Fig. 4.27. Conventional grain-oriented 3% silicon electrical steel 0.27 mm thick magnetised in Epstein frame at 20 Hz, B_{peak} = 1.70 T: a) *B-H* loop, b) corresponding waveforms of *B* (trapezoidal - controlled) and *H*

An example of a flux density waveform controlled to a typical PWM (pulse width modulated) shape with local minima is shown in Fig. 4.28. The results are acquired for conventional non-oriented electrical steel magnetised in the Epstein frame at a fundamental frequency of 50 Hz with B_{peak} = 1.50 T. The PWM waveform is modulated from a two-level signal with 18 pulses and index modulation[1] $m = 0.8$.

---

[1] Index modulation, *m*, is one of the parameters defining the PWM waveform. It is defined as the ratio of the peak values of modulating (triangle) and modulated (sinusoidal) waveforms. The *m* is usually in a range from 0 to 1.

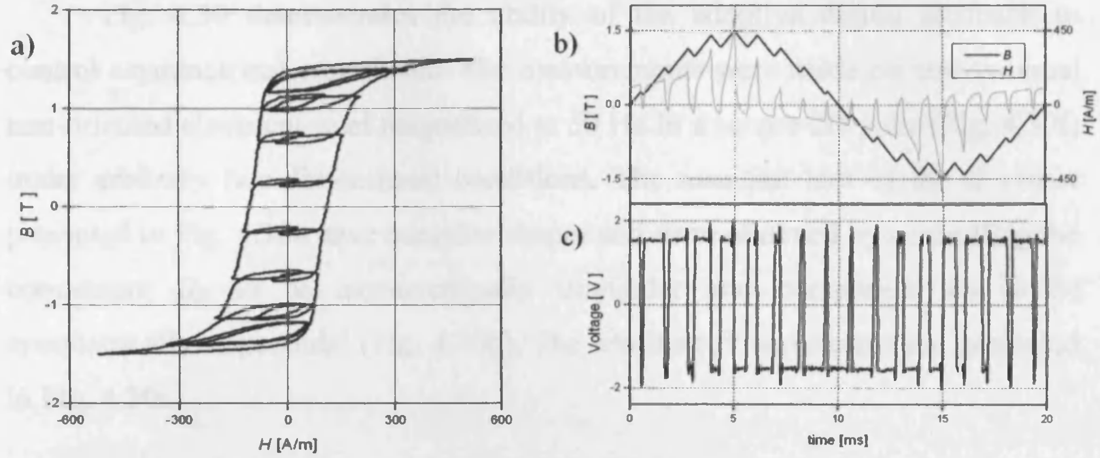

Fig. 4.28. Conventional 0.5 mm thick non-oriented low silicon electrical steel magnetised in Epstein frame at 50 Hz, B_{peak} = 1.50 T: a) *B-H* loop, b) corresponding waveforms of *B* (PWM - controlled) and *H*, c) voltage waveform proportional to *dB/dt*.

The example presented in Fig. 4.29 is obtained using a round 2D yoke (Fig. 4.23d) at 50 Hz for conventional grain-oriented, 3% silicon electrical steel. Rotational magnetisation is controlled to be circular with the radius B_{rot} = 1.80 T and 2.00 T within 1%. Those are believed to be some of the best high flux density results reported to date.

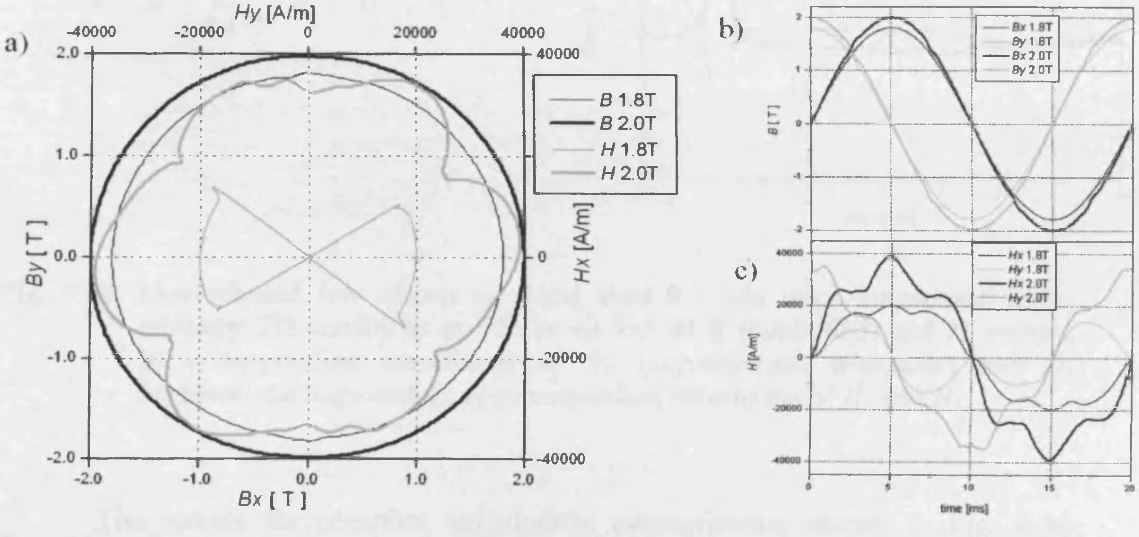

Fig. 4.29. Conventional grain-oriented 3% silicon electrical steel 0.27 mm thick magnetised in *2D* yoke at 50 Hz, 1.80 T and 2.00T: a) loci of *B* (circular - controlled) and *H* vectors, b) corresponding *B* components, c) corresponding *H* components

Fig. 4.30 demonstrates the ability of the adaptive digital feedback to control asymmetrical waveforms. The measurements were made on conventional non-oriented electrical steel magnetised at 50 Hz in a square 2D yoke (Fig. 4.30f) under arbitrary two-dimensional conditions. The resultant loci of the B vector presented in Fig. 4.30a have complex shapes and were obtained by controlling the component B_X to be asymmetrically triangular and component B_Y to be symmetrically trapezoidal (Fig. 4.30b). The resultant H waveforms are presented in Fig. 4.30c.

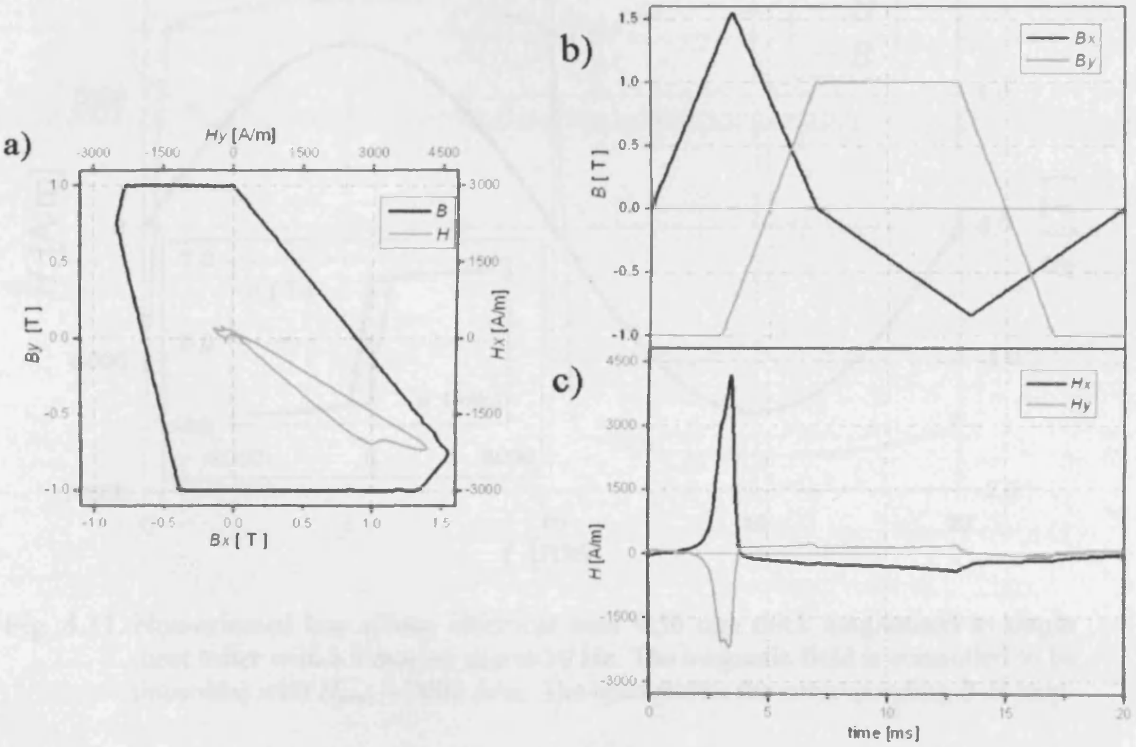

Fig. 4.30. Non-oriented low silicon electrical steel 0.5 mm thick magnetised under arbitrary *2D* conditions at 50 Hz: a) loci of B (controlled) and H vectors, b) corresponding waveforms of B_X (asymmetrical triangular) and B_Y (symmetrical trapezoidal), c) corresponding waveforms of H_X and H_Y

The results for complex asymmetric magnetisation shown in Fig. 4.30 prove that waveforms with a dc component would be controlled – providing that the constant component of the controlled signal is properly detected by an alternative type of sensor (e.g. Hall sensor). However, this has not been tested.

The presented feedback also is capable of controlling arbitrary waveforms of magnetic field strength [*4.30*]. The controlling process is very similar to described above, but the H waveforms are being compared to the reference waveforms. This is achieved by selecting appropriate controlling conditions in thread **B** in Fig. 4.20 (see element *Control B or H*? in Fig. 4.20). The rest of the digital feedback algorithm remains exactly the same as for the B control.

Fig. 4.31 presents the data measured for non-standardised single sheet tester with 2 mm air gap. The material under test is conventional non-oriented, low silicon electrical steel, magnetised at 50 Hz with the $H_{peak} = 7000$ A/m.

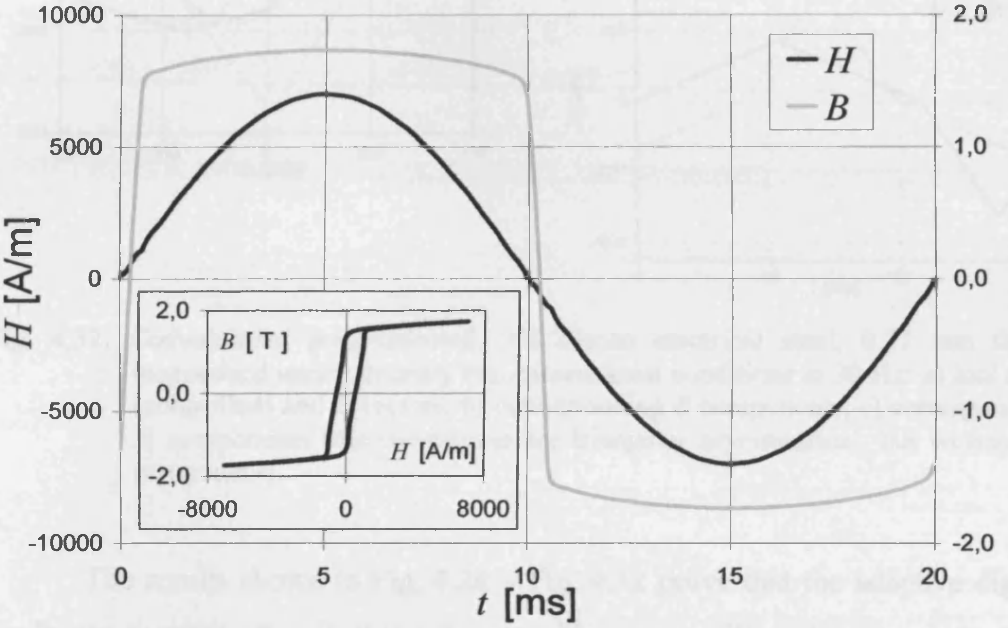

Fig. 4.31. Non-oriented low silicon electrical steel 0.50 mm thick magnetised in single sheet tester with a 2 mm air gap at 50 Hz. The magnetic field is controlled to be sinusoidal with $H_{peak} = 7000$ A/m. The inset shows the corresponding B-H loop

The results shown in Fig. 4.32 are obtained for conventional grain-oriented electrical steel magnetised at 30 Hz under arbitrary two-dimensional conditions with a 2.2 mm air gap. The resultant loci of H vector presented in Fig. 4.32a have rather complex shape and are obtained by controlling the components H_X and H_Y to be asymmetrically triangular (Fig. 4.32c). More results of measurements under controlled magnetic field are presented in **Chapter 5** and in **Appendix A**. The printout of the front panel and the block diagram of the main controlling LabVIEW program are shown in **Appendix B**.

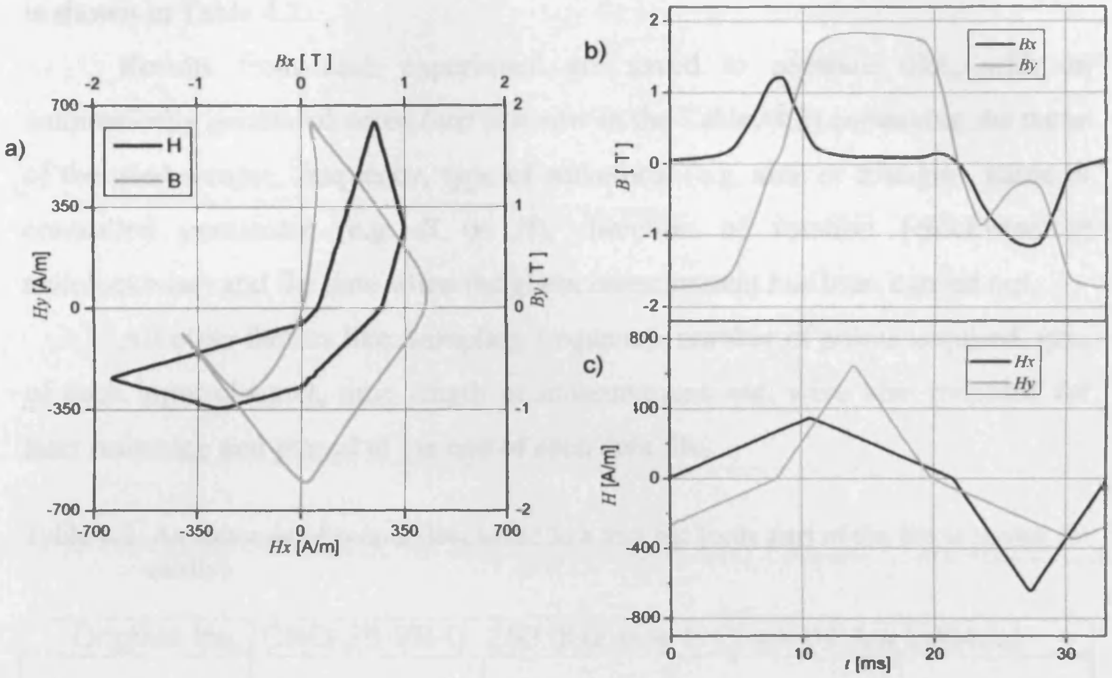

Fig. 4.32. Conventional grain-oriented, 3% silicon electrical steel, 0.27 mm thick, magnetised under arbitrary two-dimensional conditions at 30 Hz: a) loci of H (controlled) and B vectors, b) corresponding B components, c) corresponding H components (the waveforms are triangular asymmetrical, but without dc component)

The results shown in Fig. 4.24 – Fig. 4.32 prove that the adaptive digital feedback algorithm described above is capable of controlling almost any shape of flux density or magnetising field waveform in almost any type of magnetising yoke within a very wide range of frequency and up to saturation magnetisation.

The adaptive digital feedback algorithm presented here is believed to be one of the most versatile and powerful controlling algorithms to date in the field of magnetic measurements.

4.4.2.2. Storing of measured results

The program used for digital feedback and measurements was also equipped with automatic saving of the measured results to the output files. All the results were appropriately formatted and saved together with all other important measuring data to the text files, which could be easily imported to any spreadsheet or other LabVIEW program. An example of the result data saved to the output file is shown in Table 4.2.

Results from each experiment are saved to separate files, with an automatically generated name (see first row in the Table. 4.2) containing the name of the used sample, frequency, type of waveform (e.g. sine or triangle), name of controlled parameter (e.g. *B* or *H*), direction of rotation (clockwise or anticlockwise) and the date when the given measurement has been carried out.

All other factors like: sampling frequency, number of points acquired, gain of each input channel, time length of measurement, etc. were also recorded for later reference and placed at the end of each data file.

Table 4.2. An example of output data saved to a text file (only part of the file is shown for clarity)

Original file:	CNO-25-8R-U 250.0Hz sine B Clock 07 Apr 2004.txt			
Table of power losses and factors				
Bx or Hx [T or A/m]	By or Hy [T or A/m]	Power loss [W/kg]	Peak error X [%]	...
5.00E-01	5.01E-01	9.89E+00	-1.33E-01	...
1.00E+00	1.00E+00	3.38E+01	2.90E-02	...
1.50E+00	1.50E+00	6.94E+01	1.70E-02	...
				...
B and H waveforms:				...
Bx [T]	By [T]	Hx [A/m]	Hy [A/m]	...
9.92E-03	5.00E-01	8.72E+01	6.03E+01	...
2.50E-02	4.99E-01	8.93E+01	5.71E+01	...
3.90E-02	4.98E-01	9.13E+01	5.38E+01	...
9.55E-02	4.90E-01	9.85E+01	4.04E+01	...
...	...	...	...	...

4.4.2.3. Post processing and analysis of the stored data

As can be seen from the Table 4.2, together with the total power loss there are is full information about the waveforms (components) of flux density and magnetic field. This was very useful for thorough analysis of the measurements, and allowed novel conclusions to be derived, which have not published by other researchers so far.

Although the data were in a format, which was very easy to import to any spreadsheet program, most of the analysis of the experimental data have been done through other LabVIEW programs developed only for that purpose by the author of this investigation. The data flow programming implemented in LabVIEW allows manipulating data in any format with great ease – some of the functions used in those programs could not be so easily achieved in spreadsheet based packages. It should be stressed that the analysis performed by the LabVIEW programs written by the author could not be achieved by any commercially available software.

Moreover, the developed LabVIEW programs made possible such sophisticated functions like dynamic manipulations of experimental data (Fig. 4.33) or even animation of vectors of flux density and magnetic field (Fig. 4.34).

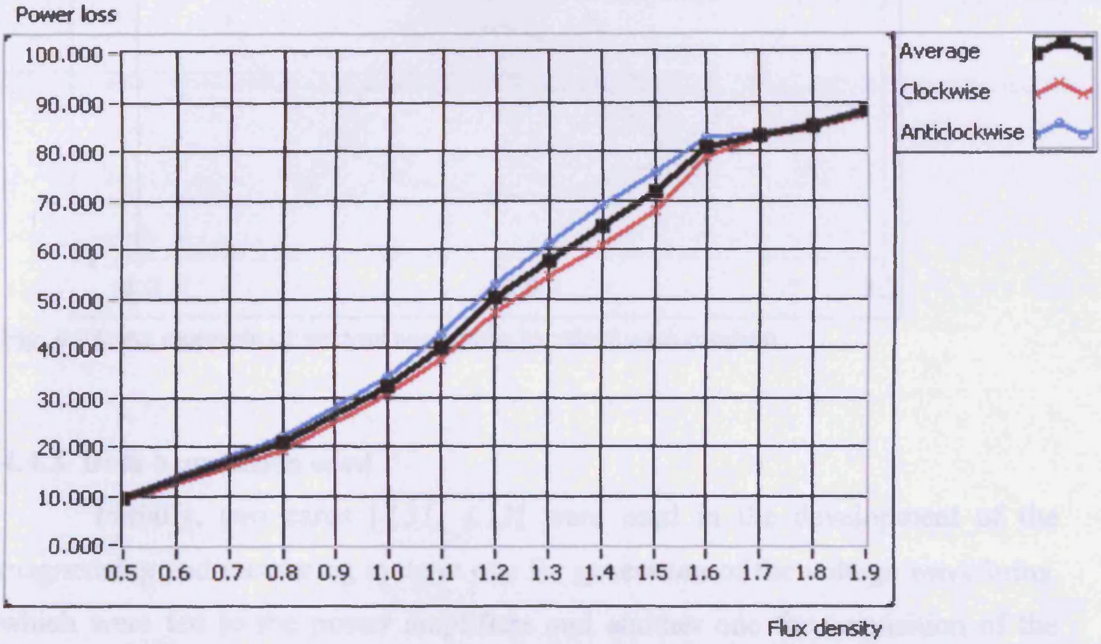

Fig. 4.33. An example of automatic calculation of average power loss from clockwise and anticlockwise measurements (implemented in a post-processing LabVIEW program)

As will be explained later, the positioning of the sensor has a great impact on the results of the calculated power loss. Another program for analysing this influence was developed in LabVIEW. Using information about the waveforms of flux density and magnetic field strength it was possible to analyse the effect of angular sensor displacement on the calculated power loss. The results of such an investigation will be presented in **Chapter 5**.

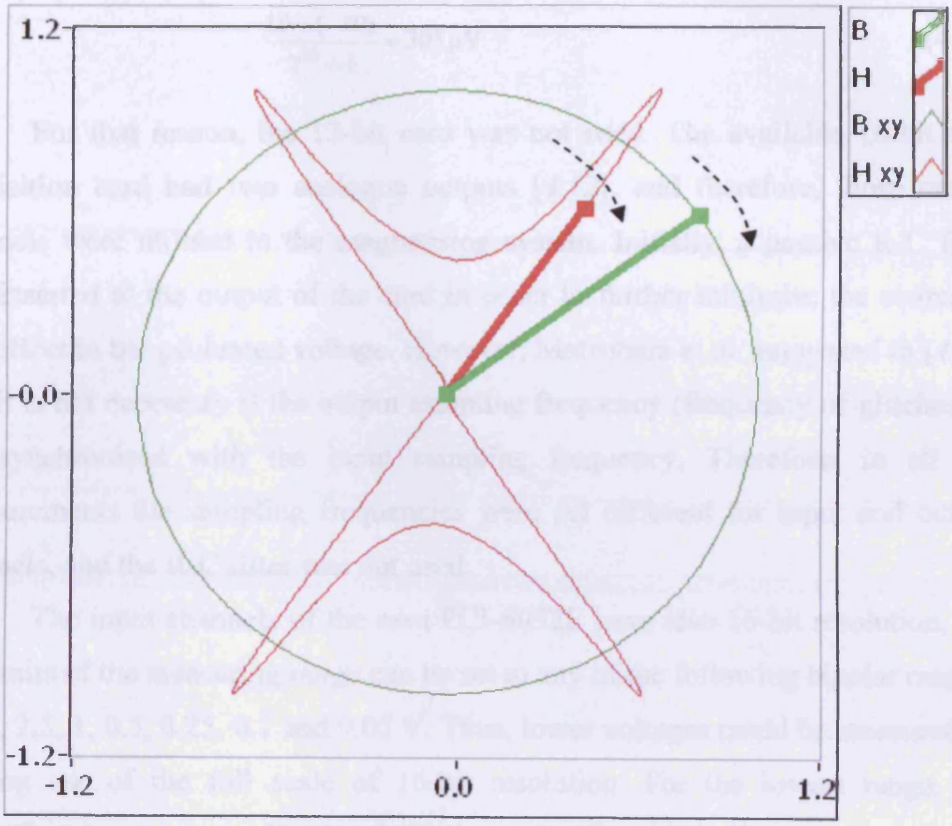

Fig. 4.34. An example of vectors animation for clockwise rotation

4.4.3. Data acquisition card

Initially, two cards [*4.31*, *4.12*] were used in the development of the magnetising and measuring system: one for generation of the voltage waveforms, which were fed to the power amplifiers and another one for acquisition of the sensor signals. The two cards were used in order to position the generation and acquisition connecting wires as far as possible from each other.

However, the digital-to-analogue converters generate staircase-like waveforms [*4.31*], which for the 12-bit resolution card could sometimes produce glitches, which could visibly affect the measured waveforms. The output of such card has one range from –10 to +10 V. Therefore, the smallest change in output voltage is:

$$\frac{10-(-10)}{2^{12}-1}=4.88\,\mathrm{mV} \tag{4.14}$$

In the case of 16-bit cards, the smallest change of output voltage is almost 16 times better:

$$\frac{10-(-10)}{2^{16}-1}=305\,\mu\mathrm{V} \tag{4.15}$$

For that reason, the 12-bit card was not used. The available 16-bit data acquisition card had two analogue outputs [*4.12*], and therefore, those output channels were utilised in the magnetising system. Initially, a passive R-C filter was inserted at the output of the card in order to further minimise the staircase-like effect in the generated voltage. However, Matsubara et al. suggested in [*4.24*] that it is not necessary if the output sampling frequency (frequency of glitches) is not synchronised with the input sampling frequency. Therefore, in all the measurements the sampling frequencies were set different for input and output channels, and the R-C filter was not used.

The input channels of the card PCI-6052E have also 16-bit resolution, but the limits of the measuring range can be set to any of the following bipolar ranges: 10, 5, 2.5, 1, 0.5, 0.25, 0.1 and 0.05 V. Thus, lower voltages could be measured by making use of the full scale of 16-bit resolution. For the lowest range, the resolution was corresponding to a LSB (least significant bit) of:

$$\frac{0.05-(-0.05)}{2^{16}-1}=1.53\,\mu\mathrm{V} \tag{4.16}$$

The resolution can be increased with the aid of dithering and averaging of the measurements from many readings because the input signals contain large amount of noise [*4.32-4.34*]. The noise itself is suppressed by a factor of $\sqrt{n}$, where n is a number of readings used in averaging. (Obviously, the averaging slows down the feedback convergence thus was used only in the final stage, where the measurements were performed after the waveforms were controlled to be within required limits of distortion.)

The concept of increasing of improving the measured signals through dithering and averaging is shown in Fig. 4.35.

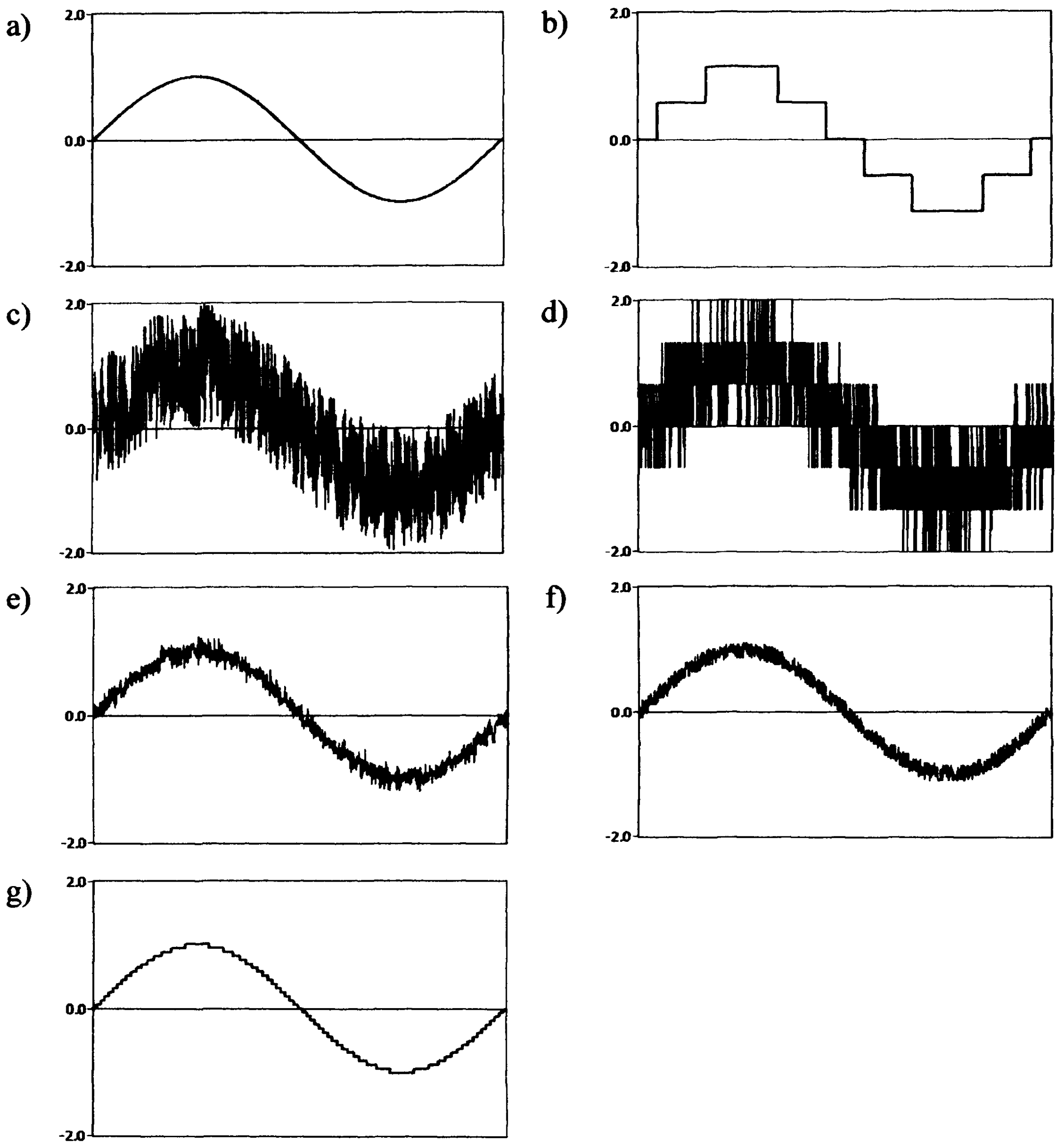

Fig. 4.35. The simulation (performed in LabVIEW program designed by author) of improving of the resolution by means of dithering and averaging: a) ideal signal without noise, b) ideal signal quantised with 3-bit resolution, c) noisy "real" signal, d) noisy signal quantised with 3-bit resolution, e) noisy signal quantised with 3-bit resolution and averaged from 50 random readings, f) noisy signal quantised with 6-bit resolution without averaging and with noise suppressed by a factor of 7, g) ideal input signal quantised with 6-bit resolution

The averaging was implemented in the main LabVIEW program and all the measurements were averaged from 50 readings, which increased the resolution by a factor of 8 (3 bits) and attenuated the noise better than 7 times ($\sqrt{50} = 7.07$). Thus, the final resolution of the measurement was better than 191 nV.

The averaging does not affect the power loss measurements, just the opposite – it increases the accuracy significantly, as described in [*4.35*, *4.36*].

4.5. Rotational single sheet tester

Other researchers have used whole variety of approaches to the magnetising setup; the most important ones are described in detail in **Chapter 3**.

However, none of the magnetising yokes and systems proved to be superior to the others, and there was no clear evidence that one approach led to higher accuracy of the measurement or lower differences in power losses measured in clockwise and anticlockwise direction of rotation.

Taking the above into consideration, the level of obtainable rotational flux density has been taken as a major criterion in the appraisal of the magnetising yoke. It can be seen that that the shape of the sample correlates with the level of flux density achievable for the grain-oriented electrical steel sheet in the following way: cross-shaped sample up to 1.0 T in the area of interest [*4.37*], square sample up to 1.2 T [*4.38*], hexagonal sample up to 1.4 T [*4.39*], round sample up to 2.0 T [*4.40*]. Therefore, the round shape of the sample, or rather compact design of the magnetising yoke allows very high rotational flux density to be achieved. The theoretical prediction that the rotational power loss drops at high flux density was confirmed by means of magnetometer measurement [*4.41*]. However, for many years researchers could not obtain similar results by means of two-phase magnetising systems, mainly due to the problem of not powerful enough power amplifiers or problems with the analogue feedback circuits.

In most of the previous research the best uniformity of the magnetising field is achieved when there was a small air gap between the magnetising yoke and the specimen under test – greater than 0.5 mm. The conditions of the measurements usually require that the sample under test must be made out of a single lamination. Those two reasons also partially dictate the design of the magnetising yoke.

The size of the magnetising yoke has been chosen similar to that described in [*4.40*]. The photograph of the yoke used in this investigation is shown in Fig. 4.36, and simplified views in Fig. 4.37.

Fig. 4.36. The photograph of the round single sheet tester used in the project

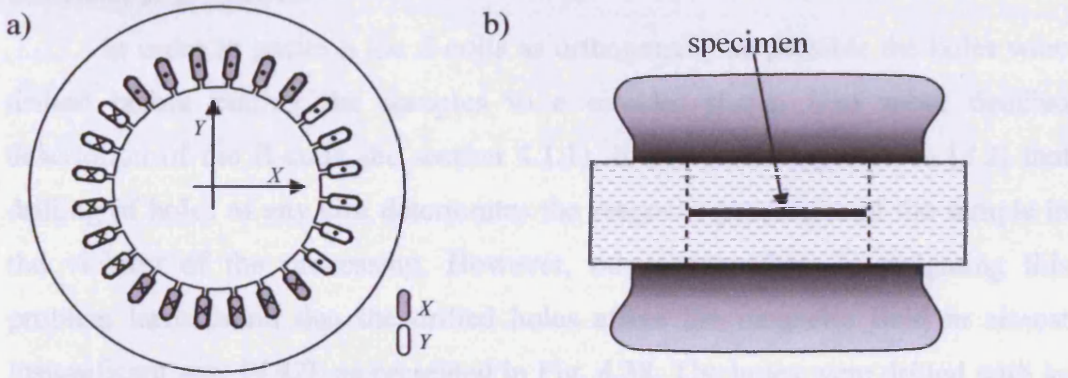

Fig. 4.37. Simplified views of the round magnetising yoke: a) cross-section, b) side view

The magnetic core of the yoke was made from stator of small three-phase electrical motor. The three-phase windings were removed and new two-phase were made from enamelled copper wire 0.55 mm in diameter. Each section of the coil has 30 turns. The external diameter of the yoke is 155 mm and the internal – 84 mm. The "height" of the core was 30 mm. The samples were cut to have 80 mm in diameter (see also section 4.6) as to leave 2 mm of air gap from each side.

The round yoke described in [*4.40*] has winding specially designed to produce close-to-circular magnetic field even without active feedback. This is achieved by varying the number of turns (from 5 to 28) in each part of the exciting coil. Such winding is justified in the electrical machines or for given magnetising conditions, but since the magnetising field inside of the yoke must be distorted anyway in order to produce circular flux density then this requirement is no longer very important. It was tested beforehand that the digital feedback is capable of controlling the shape of the waveforms to arbitrary shape, so it was assumed that it will be able to control the waveforms also in the case of uniform windings. This was tested to prove that the assumption was correct.

The presence of the so-called “teeth” around perimeter of the sample could be a potential problem, since such “teeth” could generate ripples in the strength of rotating magnetising field, but the results presented in [*4.40*] and [*4.15*] show that the uniformity of the field in the centre of the sample is very good.

4.6. Preparation of the samples

The samples were cut as squares 100 x 100 mm in not annealed state. All the samples had to be cut to a circular shape due to the round magnetising yoke described in section 4.5.

In order to position the *B*-coils as orthogonally as possible the holes were drilled before cutting the samples to a circular shape. (For more detailed description of the B-coils see section 4.1.1). It has been suggested in [*4.2*] that drilling of holes of any size deteriorates the magnetic properties of the sample in the vicinity of the processing. However, other researchers investigating this problem have found that the drilled holes affect the magnetic field in almost insignificant way [*4.42*], as presented in Fig. 4.38. The holes were drilled with as small diameter as it was practically convenient, that is 0.30 mm.

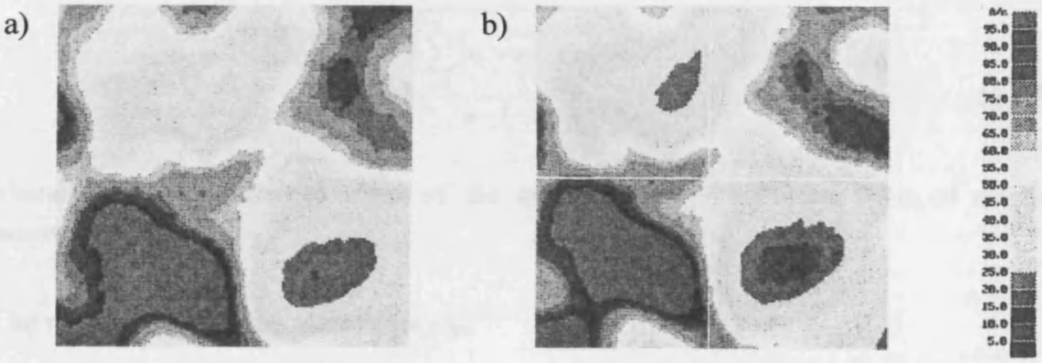

Fig. 4.38. The pattern of magnetic field on the surface of the sample without annealing: a) before drilling, b) after drilling; [*4.42*]

After drilling the holes, all the samples were cut to a circular shape with the aid of lathe. In order not to bend the sheets (the thickness varied from 0.27 to 0.50 mm), all the samples were stacked together between two thick iron plates and then cut as one piece of metal to the desired round shape with the diameter of

80 mm. Obviously, the machining introduced far more stress than the drilling of the holes for the *B*-coils, thus after the machining all the samples were annealed in the hydrogen atmosphere at 800 Celsius degrees for 2 hours.

4.7. Uncertainty of the measurement

The estimation of the uncertainty of any measurement is usually a very complex process. Often, many assumptions have to be made in order to enable to assess the uncertainty at all [*4.43*, *4.44*].

The estimation of the uncertainties of the rotational measuring system presented below has been carried out according to the recommendations given by Sievert et al. in the international Intercomparison [*4.23*].

The uncertainties can be considered separately with regards to their random part and the systematic contribution, but both of them should be combined and treated as if they were equivalent.

4.7.1. Random uncertainties

The random part of uncertainty, characterising the repeatability of the measurement is approximately given by the relative standard deviation, which is calculated using *n* individual measurements, according to:

$$\sigma_r = \frac{1}{x}\sqrt{\frac{\sum_{i=1}^{n}\left(x_i - \bar{x}\right)^2}{n-1}} \qquad (4.17)$$

where: x_i – the measured value of the quantity, $\bar{x}$ – the mean value of all the measurements

The random part of the uncertainty is:

$$u_r = t \cdot k \cdot \sigma_r \cdot \frac{1}{\sqrt{n}} \qquad (4.18)$$

where: t – the T-Student factor, k - the probability factor

For total number of measurements $n = 5$ the T-Student factor is $t = 1.4$, and the probability factor $k = 2$ (for $P = 95\%$) [*4.23*], we obtain:

$$u_r = 1.2522 \cdot \sigma_r \tag{4.19}$$

The measurements were carried out under two different magnetising conditions (i.e. controlled *B* and controlled *H*). Therefore, we can specify two different random uncertainties $u_{r(B)}$ and $u_{r(H)}$ for controlled *B* and *H*, respectively:

$$u_{r(B)} = 1.2522 \cdot \sigma_{r(B)} \tag{4.20a}$$

and

$$u_{r(H)} = 1.2522 \cdot \sigma_{r(H)} \tag{4.20b}$$

4.7.2. Systematic uncertainties

On one hand, a rectangular probability distribution of an individual uncertainty contribution may be an utmost limit to the real distribution, and on the other, the combination of several contributions with rectangular characteristics leads to a Gaussian distribution of the total systematic error, which corresponds to the practical experience [*4.23*].

The measurement of magnetic field strength is achieved by means of two orthogonal sensors. Practically, it can be assumed that both sensors have the same inaccuracy of the measurement. Therefore, we can write that:

$$\varepsilon_H = \varepsilon_{H_X} = \varepsilon_{H_Y} = \sqrt{(W_{H1} \cdot \varepsilon_{H1})^2 + (W_{H2} \cdot \varepsilon_{H2})^2 + (W_{H3} \cdot \varepsilon_{H3})^2 + \ldots} \tag{4.21}$$

where: ε_H , ε_{Hx} , ε_{Hy} – the uncertainty of the sensor, and sensors in direction *X* and *Y*, respectively; $W_{H1,2,3}$ – the corresponding weighting factors; $\varepsilon_{H1,2,3}$ – the estimated maximum errors of the contributing component

Assuming that the inaccuracy of both sensors is practically the same, the uncertainty of magnetic field strength measurement becomes:

$$u_H = \frac{2}{\sqrt{3}} \cdot \sqrt{\varepsilon_{H_X}^2 + \varepsilon_{H_Y}^2} = \frac{2 \cdot \sqrt{2}}{\sqrt{3}} \cdot \varepsilon_H \tag{4.22}$$

where: u_H – total uncertainty of the magnetic field strength measurement; ε_{Hx} , ε_{Hy} – uncertainty of the magnetic field strength measured with sensor in direction *X* and *Y*, respectively

Similarly, for the contribution of flux density errors, we obtain:

$$\varepsilon_B = \varepsilon_{B_X} = \varepsilon_{B_Y} = \sqrt{(W_{B1} \cdot \varepsilon_{B1})^2 + (W_{B2} \cdot \varepsilon_{B2})^2 + (W_{B3} \cdot \varepsilon_{B3})^2 + \ldots} \tag{4.23}$$

where: ε_B , ε_{Bx} , ε_{By} – the uncertainty of the sensor, and sensors in direction X and Y, respectively; $W_{B1,2,3}$ – the corresponding weighting factors; $\varepsilon_{B1,2,3}$ – the estimated maximum errors of the contributing component

and also:

$$u_B = \frac{2}{\sqrt{3}} \cdot \sqrt{\varepsilon_{B_X}^2 + \varepsilon_{B_Y}^2} = \frac{2 \cdot \sqrt{2}}{\sqrt{3}} \cdot \varepsilon_B \tag{4.24}$$

The total systematic uncertainty is then

$$u_s = \sqrt{u_H^2 + u_B^2} \tag{4.25}$$

4.7.3. Total uncertainty

The total uncertainty, u_{tot}, is then calculated by means of the following equation:

$$u_{tot} = \sqrt{u_r^2 + u_s^2} \tag{4.26}$$

The components contributing to the uncertainty of the used *H*-coils and *B*-coils are presented below in the Table 4.3.

For the controlled quantities, the weighting factors in Table 4.3 take value 2, otherwise they are set to 1, as suggested in [*4.23*]. The reason is that any uncertainties of controlled value have much more impact on the measuring conditions than the not controlled quantity, which is simply being measured. Therefore, we can specify two different systematic uncertainty, for controlled *B* it is $u_{s(B)}$, and for controlled *H* it is $u_{s(H)}$.

Substituting the values from the Table 4.3 into equations (4.21)-(4.25), respectively, we obtain: $u_{s(B)} = 6.1\%$, and $u_{s(H)} = 7.2\%$.

Table 4.3. The list of all errors contributing to the systematic uncertainty of the measurement

Origin	Error contribution ε (%)	Weighting factors, W	
		for controlled B	for controlled H
For *H*-coil			
Calibration	0.5	1	2
Voltage measurement	0.01	1	2
Angle between *H*-coils	0.23	1	2
Control of *H*	2.0	0	2
For *B*-coil			
Thickness of the sample	1.0	2	1
Width of the *B*-coils	0.06	2	1
Air flux	1.26	2	1
Voltage measurement	0.01	2	1
Angle between *B*-coils	0.64	2	1
Control of *B*	1.0	2	0

The values in the Table 4.3 have been estimated in the following way:

a) Calibration of the *H*-coils – both *H*-coils have been calibrated as described in section 4.1.3. The maximum error did not exceed 0.5% (for calibration results see **Appendix C**) thus this value was taken for the uncertainty calculations.

b) Voltage measurement – the manufacturer of the data acquisition card guarantees that total error of voltage measurement is below 0.006%; this value was rounded up to 0.01%.

c) Angle between the *H*-coils - the two *H*-coils were positioned at 90 degrees against each other. The misalignment of the coils was below 0.2 degree (see section 4.1.3), thus the percentage error was 0.222% – this number was rounded up to 0.23%.

d) Control of *H* – the form factor of $\mathrm{d}H_X/\mathrm{d}t$ and $\mathrm{d}H_Y/\mathrm{d}t$ components (waveforms) has been controlled to be within ±2%.

e) Thickness of the sample – the thickness has been measured with an aid of electronic micrometer with a precision of 0.0025 mm. The thinnest sample was 0.27 mm thick, which gives an error of measurement 0.926%; this value was rounded up to 1.0%.

f) Width of the B-coils – the distance between the drilled holes was 19.70 mm and the positioning of the holes was better than 0.01 mm. Calculation of the error from these values yields 0.05076%; this was rounded up to 0.06%.

g) Air flux – the maximum strength of measured magnetic field was around 20 kA/m for the flux density not greater than 2.0 T. In a paramagnetic material magnetic field of 20 kA/m corresponds to 25.13 mT, thus the error caused by the air flux would be not greater than 1.26 %.

h) Angle between B-coils – the two B-coils were positioned at 90 degrees against each other (see section 4.1.1). The angular misalignment will be discussed in details in section 5.2, and for one coil it can reach up to 0.573 degree; thus the percentage error for 90 degrees would be 0.64%.

i) Control of B – the form factor of $\mathrm{d}B_X/\mathrm{d}t$ and $\mathrm{d}B_Y/\mathrm{d}t$ components (waveforms) has been controlled to be within ±1%.

It has been suggested in [*4.23*] that the random uncertainty should be assessed for each measurement point (i.e. each level of measured flux density). Therefore, a similar approach has been taken; also for controlled H. (All results with the error bars are shown in **Appendix D**.)

Four types of samples were measured: non-oriented, conventional grain-oriented, double grain-oriented and high permeability grain-oriented electrical steel sheet. It can be seen from Table 4.4 that the repeatability of the measurement varies according to the type of sample. Clearly, the uncertainty is linked with the anisotropy of the material under test – more anisotropic materials exhibit greater scattering of the data.

It has been suggested in [*4.23*] that the final random uncertainty should be averaged over all measurements and all samples on the condition that random uncertainties should follow a normal distribution. Therefore the random uncertainties averaged over all frequencies and all samples are $u_{r\,(B)} = 4.7\%$ and $u_{r\,(H)} = 5.6\%$ for controlled B and H, respectively.

Table 4.4. Random percentage uncertainties for all samples and frequencies

	Random uncertainties [%]							
	non-oriented		conventional grain-oriented		double grain-oriented		high permeability grain-oriented	
	for controlled		for controlled		for controlled		for controlled	
frequency	*B*	*H*	*B*	*H*	*B*	*H*	*B*	*H*
10 Hz	1.4	11.8	5.3	8.5	7.2	10.5	9.5	5.0
50 Hz	1.5	3.0	5.3	4.4	3.3	4.7	9.8	5.4
250 Hz	1.0	3.0	3.6	3.7	3.4	4.0	5.0	2.7
average	**1.3**	**5.9**	**4.8**	**5.5**	**4.6**	**6.4**	**8.1**	**4.4**

	controlled *B*	**controlled *H***
averaged over all samples and frequencies	**4.7**	**5.6**

Having the systematic and random components of the uncertainty it is possible now to calculate total uncertainty of the measuring system. If all four materials are included, the total uncertainties are for controlled *B* and *H*, respectively: $u_{tot\,(B)} = 7.0\%$ and $u_{tot\,(H)} = 9.1\%$.

The total uncertainties for various measuring systems given in [*4.23*] are within a range from 3.6% to 11.1%, however the value 3.6% is known to be under estimated [*4.23*], so the more realistic range is from 7.8% to 11.1%. Thus value 7.0% is better that the best uncertainty given in [*4.23*]. The value 9.1% is calculated for controlled *H* conditions, so it should not be directly compared with the uncertainties assessed under controlled *B* conditions. Nevertheless, it is still within the limits given in [*4.23*], although the control of *H* under lower fields is far more difficult to achieve than the control of *B*.

It should be stressed that some of the values in [*4.23*] for systematic uncertainties were estimated for much lower flux density and magnetic fields (e.g. air flux). Therefore, the measuring system described above is even more accurate for the measurements at lower controlled flux density or magnetic field. However, the total accuracy estimated for the measuring system described above is valid at any level of magnetisation used in this investigation.

4.8. References to Chapter 4

[*4.1*] Loisos G., Moses A.J., Critical evaluation and limitations of localised flux density measurements in electrical steels, IEEE Transactions on Magnetics, Vol. 37, No 4, 2001, pp. 2755-2757

[*4.2*] Loisos G., Novel flux density measurement methods cof examining the influence of cutting on magnetic properties of electrical steels, PhD thesis, Cardiff Univesity, United Kingdom, 2002

[*4.3*] **Zurek S.**, Meydan T., A novel capacitive flux density sensor, Proceedings of 5th Conference on European Magnetic Sensors and Actuators (EMSA), 4-7 July 2004, Cardiff, United Kingdom

[*4.4*] Vorrichtung zum Messen des Wechselinduktionsflusses oder der Flussanderung in ferromagnetischen Materialien aus der Induktionsspannung, (*Apparatus for the measurement of the rate of change of magnetic induction or flux density in ferromagnetic materials from induced voltage*, in German), Austrian Patent Nr 180990

[*4.5*] Jones M.H., A practical introduction to electronic circuits, Second edition, Cambridge University Press, 1992

[*4.6*] Fluke 187/189 True-rms Digital multimeters, Extended specifications, Fluke Corporation, 2000, Internet: www.fluke.com, (November 2004)

[*4.7*] Agilent 54600-Series Oscilloscopes, Data Sheet, Agilent Technologies, 2000, Internet: www.agilent.com, (November 2004)

[*4.8*] Model 2001, Multimeter, Operator's Manual, Keithley, 1992, Internet: www.keithley.com, (November 2004)

[*4.9*] Johnk C.T.A., Engineering electromagnetic fields & waves, Willey International Edition, New York, USA, 1975

[*4.10*] **Zurek S.**, Meydan T., Digital feedback controlled RSST system, Proceedings of 16th Soft Magnetic Materials Conference (SMM), Dusseldorf, Germany, 2003

[*4.11*] Sievert J., Studies on the measurement of two-dimensional magnetic phenomena in electrical sheet steel at PTB, Proceedings of 1st international workshop on magnetic properties of electrical sheet steel under two-dimensional excitation, Braunschweig, 1992

[*4.12*] DAQ PCI-6052E/6053E User Manual, National Instruments, Multifunction I/O Board for PCI/PXI/1394 Bus Computers, 1999

[*4.13*] Radley S.G., Moses A.J., Apparatus for experimental simulation of magnetic flux and power loss distribution in a turbogenerator stator core, IEEE Transactions on Magnetics, Vol. Mag-17, No. 3, 1981, pp. 1311-1316

[*4.14*] Bajorek R., Bajorek J., Rygal R., **Zurek S.**, Soinski M., A compact SST for investigation of both alternating and rotational magnetisation, Proceedings of 6th international workshop on 1&2-dimensional magnetic measurement and testing, Bad Gastein, Austria, September 2001

[*4.15*] Gorican V., Jesenik M., Hamler A., Stumberger B., Trlep M., Performance of RRSST at higher flux densities in the case of GO materials, Proceedings of 7th international workshop on 1&2 dimensional magnetic measurement and testing, Ludenscheid, Germany, September 2002

[*4.16*] Bajorek R., Bajorek J., System MAG-TD200 do pomiaru dynamicznych wlasciwosci magnetycznych ferromagnetykow miekkich w polach przemiennych i wirujacych, (*System MAG-TD200 for the measurements of dynamic properties of soft magnetic materials in alternating and rotational fields*, in Polish), Przeglad Elektrotechniczny, R. 80, Nr 2/2004, Poland, 2004, pp. 107-110

[*4.17*] PGA204/205, Programmable gain instrumentation amplifier, Burr-Brown Corporation, Texas Instruments Inc., 1991

[*4.18*] Wan Mahadi W.N.L., Design and development of a novel two-dimensional magnetic measurement system for electrical steels, PhD thesis, Wolfson Centre for Magnetics Technology, School of Engineering, Cardiff University, United Kingdom, 1996

[*4.19*] Kasin S., Is your data inaccurate because of instrumentation amplifier settling time?, Application Note 045, National Instruments, Internet: www.ni.com, (November 2004)

[*4.20*] Micro-Tech®, Analogue/Crown MT600, MT1200, MT2400 Power Amplifiers, Reference Manual, Analogue Associates Ltd., 2001

[*4.21*] **Zurek S.**, Two-dimensional magnetisation system, Operation manual, Wolfson Centre for Magnetics Technology, School of Engineering, Cardiff University, United Kingdom, September 2003 (*internal documentation*)

[*4.22*] BridgeVIEW™ and LabVIEW™ G Programming Reference Manual, National Instruments, 1998

[*4.23*] Sievert J., Ahlers H., Birkfeld M., Conmut B., Fiorillo F., Hempel K.A., Kochmann T., Lebouc A., Meydan T., Moses A.J., Rietto A.M., Intercomparison of measurements of magnetic losses in electrical sheet steel under rotation flux conditions, Commission of the European Communities, Report EUR 16255 EN, EC Brussels, Luxembourg, 1995

[*4.24*] Matsubara K., Nakata T., Takahashi N., Fujiwara K., Nakano M., Zhu H.L., Aoki H., Effect of staircase output voltage waveform of a D/A converter on iron losses measured using an H coil, Journal of Magnetism and Magnetic Materials, vol. 160, 1996, pp. 185-186

[*4.25*] DAQ PCI-4451/4452 User Manual, Dynamic Signal Acquisition Device for PCI, National Instruments, 1998

[*4.26*] International Electrotechnical Commission IEC 60404-2 (1996-03), Magnetic materials - Part 2: Methods of measurement of the magnetic properties of electrical steel sheet and strip by means of an Epstein frame

[*4.27*] Spornic S.A, Kedous-Lebouc A., Cornut B., Numerical waveform control for rotational single sheet testers, Journal de Physique. IV, Vol. 8(2), 1998, pp. 741-744

[*4.28*] Makaveev D., Maes J., Melkebeek J., Controlled circular magnetization of electrical steel in rotational single sheet testers, IEEE Transactions on Magnetics, Vol. 37, No. 4, 2001, pp. 2740-2742

[*4.29*] Cunningham E.P., Digital filtering: An introduction, Houghton Mifflin Company, Boston, Toronto, 1992, pp. 273-276

[*4.30*] **Zurek S.**, Marketos P., Meydan T., Control of arbitrary waveforms by means of adaptive digital feedback algorithm, Przeglad Elektrotechniczny (*Electrotechnical Review*), R. 80, Nr 2/2004, Poland, 2004, pp. 122-125

[*4.31*] DAQ PCI/PXI-6711/6713 User Manual, National Instruments, Analog Voltage Output Device for PCI/PXI/CompactPCI, 1998

[*4.32*] Hanks J., Five critical accuracy technologies for data acquisition, National Instruments, Internet: www.ni.com/accuracy, (June 2004)

[*4.33*] Ando B., Graziani S., Adding noise to improve measurement, IEEE Instrumentation & Measurement Magazine, Vol. 56, 2001, pp. 24-31

[*4.34*] Aumala O., Fundamentals and trends of digital measurement, Measurement, Vol. 26, 1999, pp. 45-54

[*4.35*] Gorican V., Hribernik B., Hamler A., Nakata T., The measurement of power losses at high magnetic field densities or at small cross-section of test specimen using the averaging, Journal of Magnetism and Magnetic Materials, Vol. 215-216, 2000, pp. 693-695

[*4.36*] Ishihara Y., Isozumi A., Todaka T., Nakata T., Comparison of two averaging methods for improving the measurement accuracy of power loss, Journal of Magnetism and Magnetic Materials, Vol. 215-216, 2000, pp. 696-699

[*4.37*] Moses A.J., Thomas B., Measurement of rotating flux in silicon iron laminations, IEEE Transactions on Magnetics, Vol. Mag-9, No. 4, 1973, pp. 651-654

[*4.38*] Sievert J., Ahlers H., Birkfeld M., Cornut B., Fiorillo F., Hempel K.A., Kochmann T., Kedous-Lebouc A., Meydan T., Moses A.J., Rietto A.M., European intercomparison of measurements of rotational power loss in electrical sheet steel, Journal of Magnetism and Magnetic Materials, 160 (1996), pp. 115-118

[*4.39*] Krismanic G., Kitz E., Mehnen L., Leiss E., Krell C., Pfützner H., A computerized design for exact control of two dimensional induction patterns, Proceedings of 7th international workshop on 1&2 dimensional magnetic measurement and testing, Ludenscheid, Germany, September 2002

[*4.40*] Gorican V., Hamler A., Hribernik B., Jesenik M., Trlep M., 2-D measurements of magnetic properties using a round RSST, Proceedings of 6th international workshop on 1&2-dimensional magnetic measurement and testing, Bad Gastein, Austria, September 2000

[*4.41*] Brailsford F., Rotational hysteresis loss in electrical sheet steels, Journal of the Institution of Electrical Engineers, Vol. 83, 566-575, 1938

[*4.42*] Tumanski S., Investigations of 2D parameters of electrical steels, Proceedings of 6th international workshop on 1&2-dimensional magnetic measurement and testing, Bad Gastein, Austria, September 2000

[*4.43*] Hayward A.T.J., Repeatability and accuracy, Mechanical Engineering Publications Ltd., London, 1977

[*4.44*] Professional Group S4 (Fundamental aspects of measurement), Half-day Colloquium on *Uncertainties made easy*, Savoy Place, London, October 1996

Chapter Five
Discussion and analysis of experimental results

5.1. The difference between clockwise and anticlockwise power losses due to angular misalignment of the sensors

It is well known that the power losses differ when measured in clockwise (*CW*) and anticlockwise (*ACW*) direction of rotation. This causes divergence in measured results, despite greatest care taken in order to minimise the errors [*5.1*]. In most cases the power loss is calculated by means of equation (2.8).

It was suggested that this difference might be attributed to genuine magnetic phenomena [*5.2-5.5*]. However, it has also been pointed out that the difference between *CW* and *ACW* measurements is greatly influenced by the non-orthogonal *H*-sensors [*5.6, 5.7*] (see Fig. 5.1).

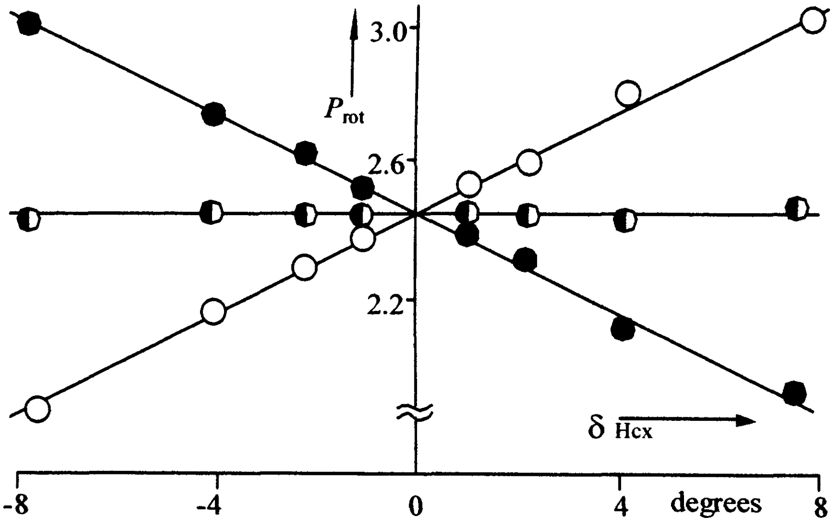

Fig. 5.1. Angular misalignment of *H* sensors as a factor influencing power loss measurement; white circles - clockwise rotation, black circles - anticlockwise rotation, black-and-white circles - averaged power loss; [*5.6*]

It was proposed that in such case the correct value of total rotational power loss could by obtained by averaging the CW and ACW power loss:

$$P_{av} = \frac{P_{CW} + P_{ACW}}{2} \tag{5.1}$$

where: P_{av} - averaged power loss, [W/kg]; P_{CW}, P_{ACW} - total power loss obtained for *CW* and *ACW* direction of rotation, respectively [W/kg].

This approach was widely accepted ever since and was also used in an European project on intercomparison of measurements of magnetic losses in electrical sheet steel under rotating flux conditions [*5.1*].

In the case of purely circular flux density the orthogonal components B_X and B_Y are sinusoidal. The orthogonal components of magnetic field, H_X and H_Y, are in general non-sinusoidal, but only their fundamental (i.e. sinusoidal) components give contribution to the power loss and the higher harmonics can be neglected [*5.8*]. Thus, assuming that H leads B, we can write; for CW rotation:

$$B_X(t)_{CW} = B_X \cdot \sin(\omega \cdot t) \tag{5.2a}$$

$$B_Y(t)_{CW} = B_Y \cdot \cos(\omega \cdot t) \tag{5.2b}$$

$$H_X(t)_{CW} = H_X \cdot \sin(\omega \cdot t + \phi) \tag{5.2c}$$

$$H_Y(t)_{CW} = H_Y \cdot \cos(\omega \cdot t + \phi) \tag{5.2d}$$

and for ACW rotation

$$B_X(t)_{ACW} = B_X \cdot \sin(\omega \cdot t) \tag{5.3a}$$

$$B_Y(t)_{ACW} = -B_Y \cdot \cos(\omega \cdot t) \tag{5.3b}$$

$$H_X(t)_{ACW} = H_X \cdot \sin(\omega \cdot t + \phi) \tag{5.3c}$$

$$H_Y(t)_{ACW} = -H_Y \cdot \cos(\omega \cdot t + \phi) \tag{5.3d}$$

where: $B_X(t)$, $B_Y(t)$, $H_X(t)$, $H_Y(t)$ - orthogonal components of B or H, respectively; B_X, B_Y, H_X, H_Y - peak value of B or H orthogonal components, respectively, [T] or [A/m]; $\omega = 2 \cdot \pi \cdot f$ - angular frequency, [rad/s]; t - time, [s]; ϕ - angle of phase shift between B and H vector, [rad].

Therefore, substituting equations (5.3) into (2.8) we can write for CW rotation:

$$P_{CW} = \frac{f}{D} \cdot \int_0^T \left[H_X(t)_{CW} \cdot \frac{d\left(B_X(t)_{CW}\right)}{dt} + H_Y(t)_{CW} \cdot \frac{d\left(B_Y(t)_{CW}\right)}{dt} \right] dt \tag{5.4}$$

Similarly for the ACW rotation the equation (2.8) takes a form

$$P_{ACW} = \frac{f}{D} \cdot \int_0^T \left[H_X(t)_{ACW} \cdot \frac{d\left(B_X(t)_{ACW}\right)}{dt} + H_Y(t)_{ACW} \cdot \frac{d\left(B_Y(t)_{ACW}\right)}{dt} \right] dt \tag{5.5}$$

Absolute values of components B_Y and H_Y in equations (5.3b) and (5.3d) for *ACW* rotation are equal to those for *CW* rotation in equations (5.2b) and (5.2d). The minus signs cancel; therefore equation (5.5) becomes identical to (5.4) and gives exactly the same number. By definition, in this case equation (5.1) provides the correct value of the total power loss in circular magnetisation

$$P_{CW} = P_{ACW} = P_{av} = \frac{P_{CW} + P_{ACW}}{2} \tag{5.6}$$

Nevertheless, the above is only true if there is no angular misalignment between *B* and *H* sensors. Positioning of the sensors is prone to some inaccuracy, and any angular misalignment leads to additive errors in the results obtained from equation (5.1).

For the sake of simplicity, let us consider that the *B* sensors are orthogonal and positioned as desired. H_X and H_Y sensors are not orthogonal and placed at arbitrary angles α and β, respectively. For that reason the *H* sensors will detect signals different from expected, as presented in Fig. 5.2.

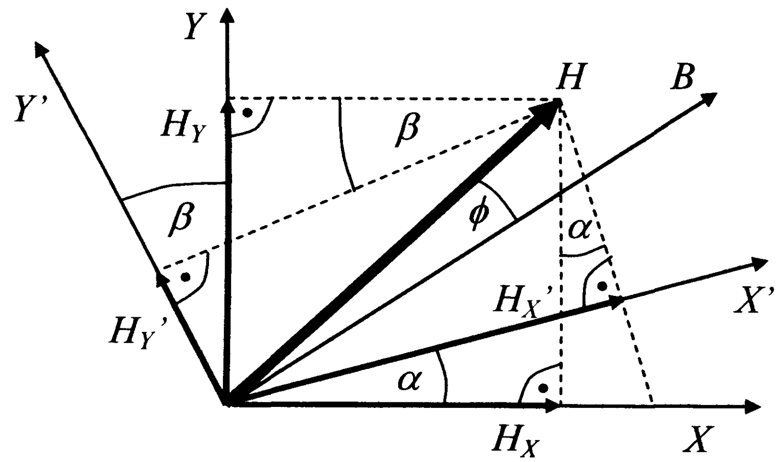

Fig. 5.2. Vector diagram for positioning of *H* sensors

It can be seen from Fig. 5.2 that

$$H_X = \frac{H_X'}{\cos(\alpha)} - H_Y \cdot \tan(\alpha) \tag{5.7a}$$

$$H_Y = \frac{H_Y'}{\cos(\beta)} + H_X \cdot \tan(\beta) \tag{5.7b}$$

By solving the system of equations (5.7) we can calculate the real components H_X and H_Y from the measured H_X' and H_Y' and known angles α and β

$$H_X = \frac{H_X' \cdot \cos(\beta) - H_Y' \cdot \sin(\alpha)}{\cos(\alpha)\cdot\cos(\beta) + \sin(\alpha)\cdot\sin(\beta)} \tag{5.8a}$$

$$H_Y = \frac{H_Y' \cdot \cos(\alpha) + H_X' \cdot \sin(\beta)}{\cos(\alpha)\cdot\cos(\beta) + \sin(\alpha)\cdot\sin(\beta)} \tag{5.8b}$$

Solving for H_X' and H_Y' from equations (5.7):

$$H_X' = H_X \cdot \cos(\alpha) + H_Y \cdot \sin(\alpha) \tag{5.9a}$$

$$H_Y' = H_Y \cdot \cos(\beta) - H_X \cdot \sin(\beta) \tag{5.9b}$$

If the misalignment of the H sensors is neglected, the measured components H_X' and H_Y' are assumed to be the components H_X and H_Y. Hence, substituting equations (5.9) into equations (5.2) and (5.3) we obtain; for *CW* rotation:

$$B_X''(t)_{CW} = B_X \cdot \sin(\omega \cdot t) \tag{5.10a}$$

$$B_Y''(t)_{CW} = B_Y \cdot \cos(\omega \cdot t) \tag{5.10b}$$

$$H_X''(t)_{CW} = H_X \cdot \sin(\omega \cdot t + \phi)\cdot\cos(\alpha) + H_Y \cdot \cos(\omega \cdot t + \phi)\cdot\sin(\alpha) \tag{5.10c}$$

$$H_Y''(t)_{CW} = H_Y \cdot \cos(\omega \cdot t + \phi)\cdot\cos(\beta) - H_X \cdot \sin(\omega \cdot t + \phi)\cdot\sin(\beta) \tag{5.10d}$$

and for *ACW* rotation

$$B_X''(t)_{ACW} = B_X \cdot \sin(\omega \cdot t) \tag{5.11a}$$

$$B_Y''(t)_{ACW} = -B_Y \cdot \cos(\omega \cdot t) \tag{5.11b}$$

$$H_X''(t)_{ACW} = H_X \cdot \sin(\omega \cdot t + \phi)\cdot\cos(\alpha) - H_Y \cdot \cos(\omega \cdot t + \phi)\cdot\sin(\alpha) \tag{5.11c}$$

$$H_Y''(t)_{ACW} = -H_Y \cdot \cos(\omega \cdot t + \phi)\cdot\cos(\beta) + H_X \cdot \sin(\omega \cdot t + \phi)\cdot\sin(\beta) \tag{5.11d}$$

where: α, β - angular misalignment of H_X and H_Y sensors, respectively, [rad].

If the equations (5.10) and (5.11) are substituted into equation (2.8) they will not yield identical results. Since the functions $B(t)$ and $H(t)$ are not linear, the averaging from P_{CW} and P_{ACW} will not give the true value of power loss (Fig. 5.3). The percentage error between true and averaged value can be calculated as:

$$Error = \frac{P_{true} - P_{av}}{P_{true}} \cdot 100\% \qquad (5.12)$$

where: P_{true} - true value of power loss, [W/kg].

The true power loss depends on the values of B, H and ϕ. However, the calculated power loss depends also on angles α and β. If $\alpha = \beta = 0$ then the true and calculated values are equal. In any other case the averaged value of power loss is always lower than the true value (Fig. 5.3).

The equations (5.9) were introduced by Salz and Hempel in [5.9] in a slightly different way. The authors concluded that the difference in *CW* and *ACW* losses could be overcome by averaging, but the H loci and the angle between B and H vectors would remain erroneous even after averaging.

The rotational measurements of power loss are commonly made under controlled conditions. Therefore, for sake of simplicity let us take the positions of B sensors as a reference.

In a general case, taking into account the factors described above, the angles α and β cannot be avoided and they are always present to a greater or a lesser extent. Moreover, only the inaccuracy can be estimated, whilst the angles α and β will remain unknown.

However, the task can be reversed. The equations (5.8) allows obtaining the "real" H components, depending on the values of α and β. If these angles are guaranteed to be smaller than 7.5 degrees, the power loss averaged from *CW* and *ACW* measurement can be treated as a very close approximation of the true value (error below 1% - see Fig. 5.3). In such case, manipulation of the angles α and β can be used as a method of bringing the *CW* and *ACW* power loss as close as possible to the averaged value. If in this process the angles α and β are minimised, then also the averaged power loss gets closer to the true value. If the averaged power loss is calculated at the same time, then the repetition of that process will result in finding the global optimal values for α and β, at which the *CW* and *ACW* losses are closest to the average value, and therefore the average is closest to the true value. The components H_X and H_Y used in all equations have to be recalculated for every point in the measured H waveforms. For instance, the data acquisition card used in this investigation allowed acquiring 1024 points per period of waveform at 50 Hz of magnetising frequency. Therefore, all 1024 points have to be "corrected" as to minimise the *CW-ACW* power loss differences. The tests show that the resolution of such method is at the level of single minutes that is less than 0.02 degrees.

As an example let us consider the following measured data. The sample under test is non-oriented electrical steel, 0.5 mm thick, magnetised at 50 Hz under circular flux density of 1.0 T. The measured peak values are: $B_X = B_Y = 1.0$ T, $H_X = 112$ A/m and $H_Y = 133$ A/m. The positioning of the *B* and *H* sensors is assumed to be ideal. The angle between fundamental components of *B* and *H* (compare Fig. 5.2) is found to be $\phi = 43.1$ deg. Substituting these values into equations (5.2) and (5.3) and then into (5.5) and (5.5) yield with calculated $P_{CW} = P_{ACW} = P_{AV} = 3.371$ W/kg, while the power loss averaged from *CW* and *ACW* measurements is $P_{AV} = 3.376$ W/kg.

If these values are used in equations (5.10) and (5.11), and the angles α and β are varied independently - by using equations (2.8), (5.1) and (5.12) we can calculate the function of percentage error for the whole ranges of α and β. Fig. 5.3 depicts the surface graphs for $-10 \text{ deg} \leq \alpha \leq 10 \text{ deg}$ and $-10 \text{ deg} \leq \beta \leq 10 \text{ deg}$.

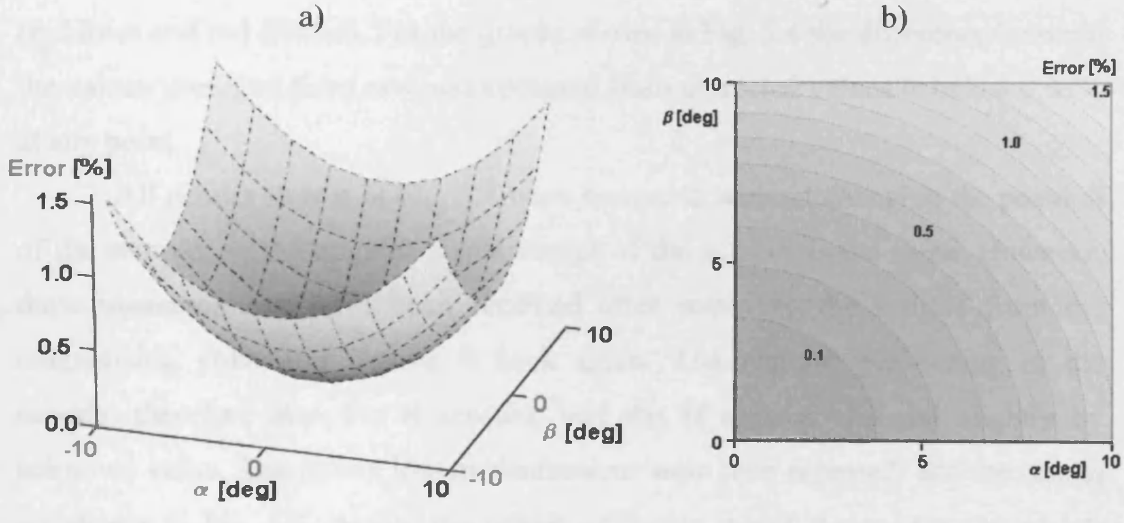

Fig. 5.3. The influence of angular misalignment of the sensors H_X (angle α) and H_Y (angle β) on the value of averaged power loss: a) three-dimensional surface graph; b) top view (only first quadrant is shown for clarity)

Despite, that for α and β lower than 5 deg, the error is small (less than 0.4%), its additive character prevents from eliminating it by averaging the reading from many measurements (see also section 4.4.3). The overall accuracy of the rotational measurement system is usually not better than 7% [*5.1*], so error of this level cannot be detected directly from the measurements. Nevertheless, the inaccuracy might be as big as several percents for greater angular misalignment, e.g. for $\alpha = \beta = 10$ deg (see Fig. 5.3).

The positions of the holes in the sample (thus the B sensors) are assumed to be ideal as they were made with an aid of precision machining and additionally measured by means of travelling microscope with the accuracy better than 0.01 mm. The H coils (H sensors) were manufactured as described in section 4.1.3.

Fig. 5.4. presents results measured for non-oriented electrical steel. It can be seen that for higher flux density the difference between *CW* and *ACW* power loss slightly increases (especially in Fig. 5.4c and Fig. 5.4d). It has been assumed that the H coils are perfectly orthogonal (i.e. $\alpha = \beta$) and only their misalignment with respect to the B coils affected the power loss measurement. The real position of the H coils was not known, therefore values α and β in equations (5.8) were modified by trial-and-error method in order to minimise the difference between *CW* and *ACW*. For the measurement presented in Fig. 5.4 it was found that the optimal value $\alpha = \beta = +0.06$ deg. It is worth noting that the loss averaged from corrected values is almost identical to the loss averaged from raw measurements (red lines and red circles). For the graphs shown in Fig. 5.4 the difference between the values averaged from raw and averaged from corrected values is below 0.07% at any point.

All results shown in Fig. 5.4 were measured without changing the position of the sample, so the angular displacement of the sensors is the same. However, these measurements have been repeated after removing the sample from the magnetising yoke and putting it back again. The angular positioning of the sample, therefore also the B sensors, and the H sensors changed slightly by unknown value. The power loss measurements were then repeated, and the results are shown in Fig. 5.5. Again, the values of angles α and β were found by trial-and-error method. As it can be seen from Fig. 5.5 this time the value of relative angular displacement of the H sensors with respect to B sensors changed to $\alpha = \beta = +0.40$ deg.

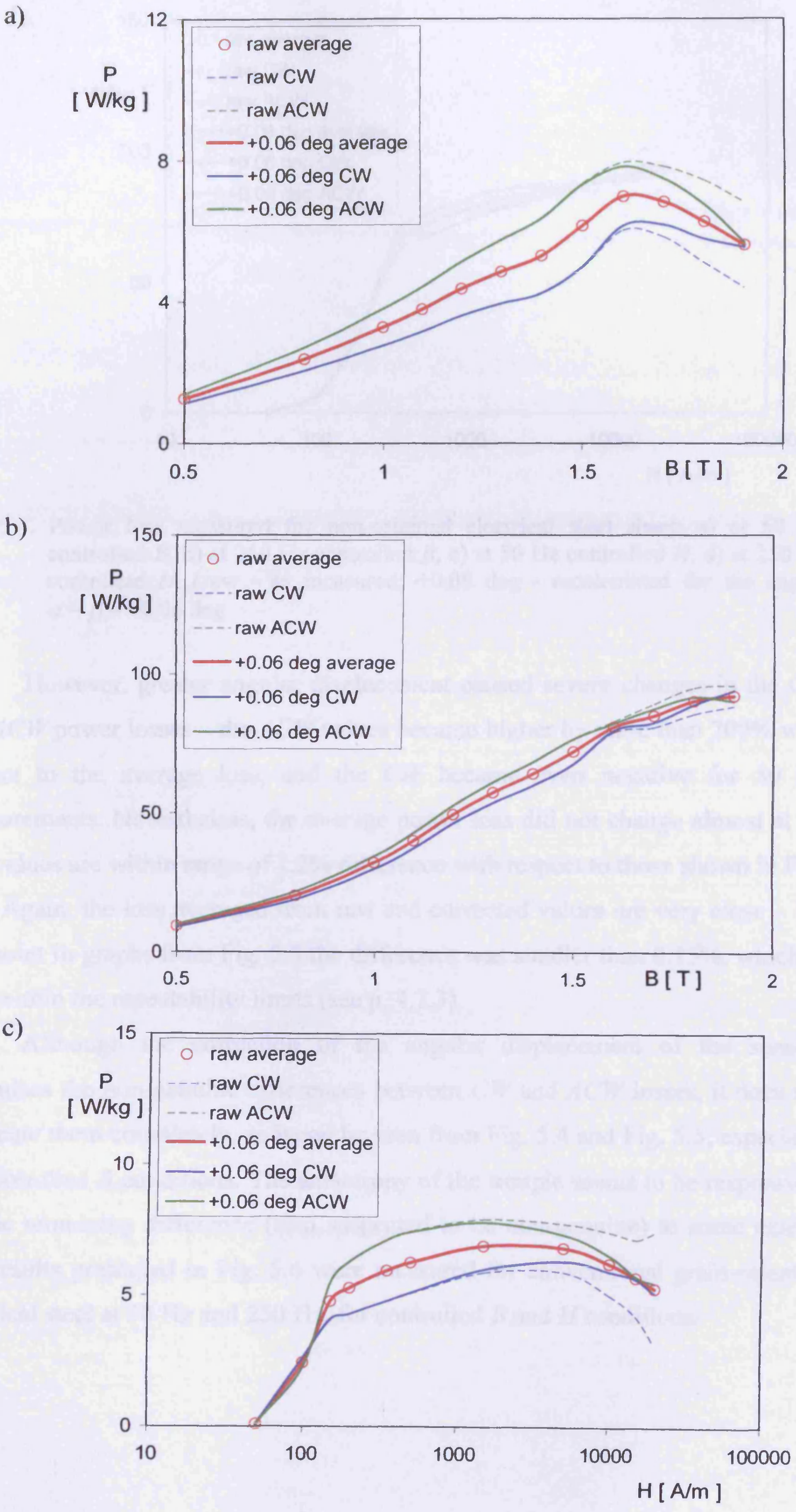
a)
P
[W/kg]
12
8
4
0
0.5
1
1.5
B [T]
2
raw average
raw CW
raw ACW
+0.06 deg average
+0.06 deg CW
+0.06 deg ACW
b)
P
[W/kg]
150
100
50
0
0.5
1
1.5
B [T]
2
raw average
raw CW
raw ACW
+0.06 deg average
+0.06 deg CW
+0.06 deg ACW
c)
P
[W/kg]
15
10
5
0
10
100
1000
10000
100000
H [A/m]
raw average
raw CW
raw ACW
+0.06 deg average
+0.06 deg CW
+0.06 deg ACW

d)

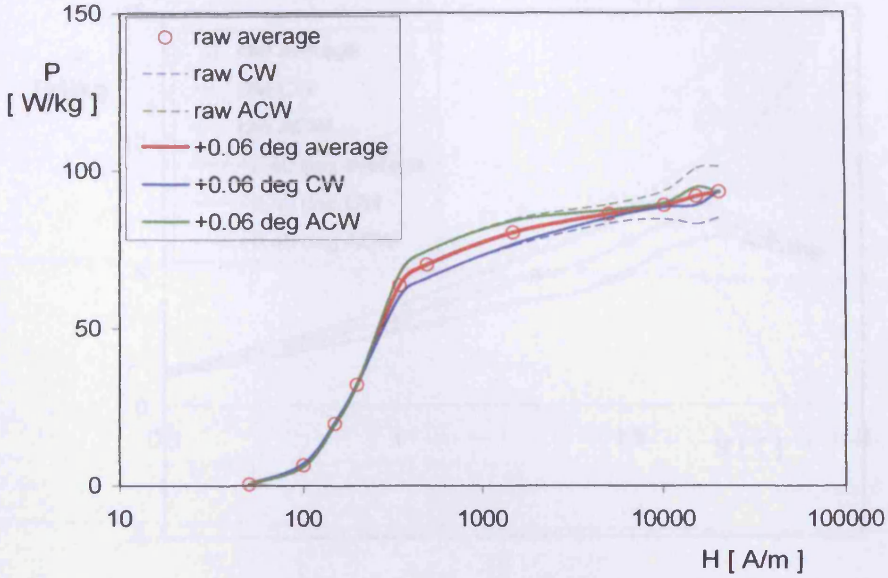

Fig. 5.4. Power loss measured for non-oriented electrical steel sheet: a) at 50 Hz controlled *B*, b) at 250 Hz controlled *B*, c) at 50 Hz controlled *H*, d) at 250 Hz controlled *H*, (raw - as measured; +0.06 deg - recalculated for the angles $\alpha = \beta = +0.06$ deg

However, greater angular displacement caused severe changes in the *CW* and *ACW* power losses – the *ACW* values became higher by more than 200% with respect to the average loss, and the *CW* became even negative for 50 Hz measurements. Nevertheless, the average power loss did not change almost at all (the values are within range of 1.2% difference with respect to those shown in Fig. 5.4). Again, the loss averaged from raw and corrected values are very close – for any point in graphs from Fig. 5.5 the difference was smaller than 0.15%, which is well within the repeatability limits (see p. 4.7.3).

Although the correction of the angular displacement of the sensors minimises the non-genuine differences between *CW* and *ACW* losses, it does not eliminate them completely, as it can be seen from Fig. 5.4 and Fig. 5.5; especially for controlled *B* conditions. The anisotropy of the sample seems to be responsible for the remaining difference (also suspected to be non-genuine) to some extent. The results presented in Fig. 5.6 were measured for conventional grain-oriented electrical steel at 50 Hz and 250 Hz, for controlled *B* and *H* conditions.

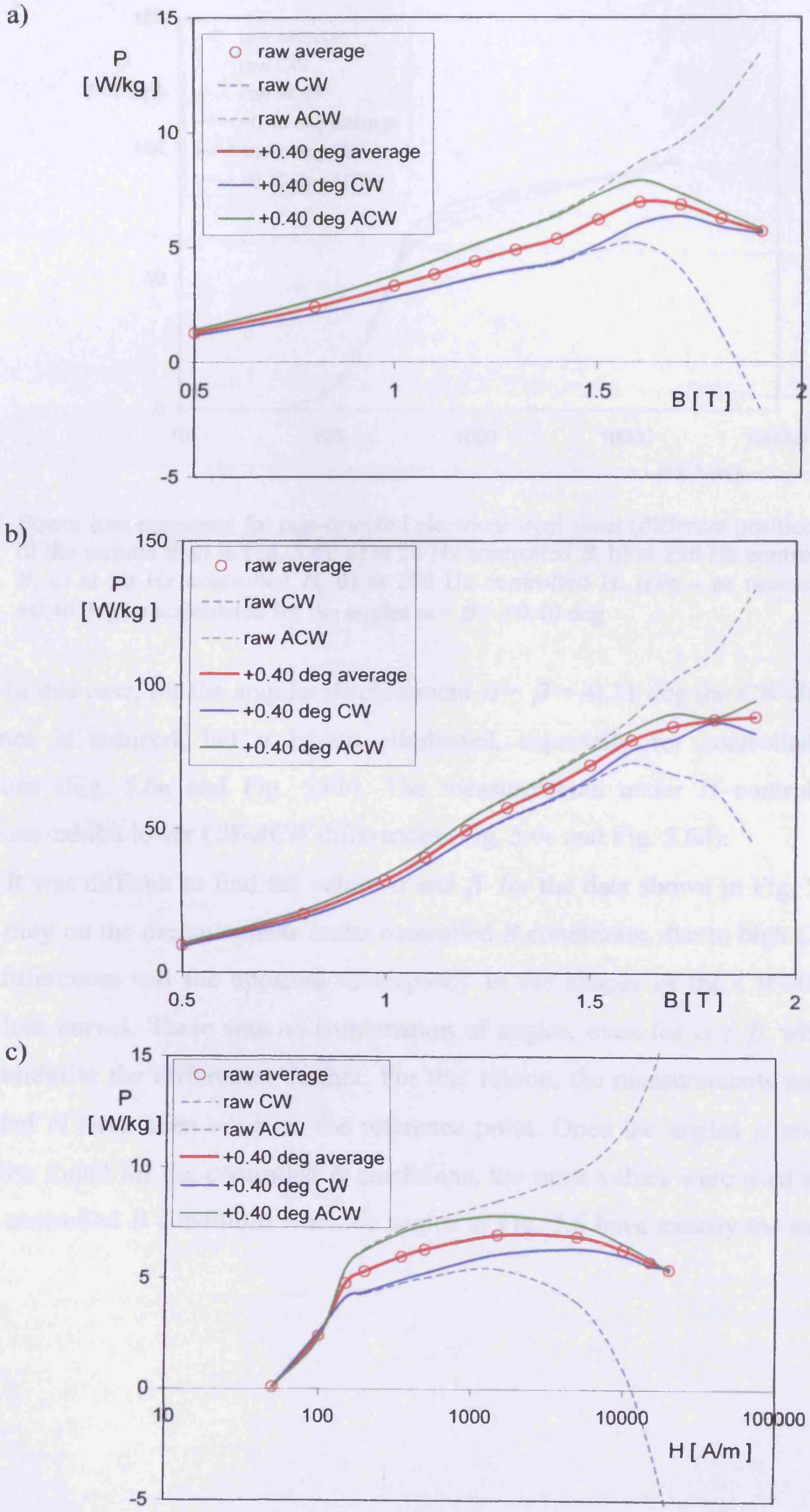
a)
P
[W/kg]
15
10
5
0
-5
0.5
1
1.5
B [T]
2
raw average
raw CW
raw ACW
+0.40 deg average
+0.40 deg CW
+0.40 deg ACW
b)
P
[W/kg]
150
100
50
0
0.5
1
1.5
B [T]
2
raw average
raw CW
raw ACW
+0.40 deg average
+0.40 deg CW
+0.40 deg ACW
c)
P
[W/kg]
15
10
5
0
-5
10
100
1000
10000
100000
H [A/m]
raw average
raw CW
raw ACW
+0.40 deg average
+0.40 deg CW
+0.40 deg ACW

d)

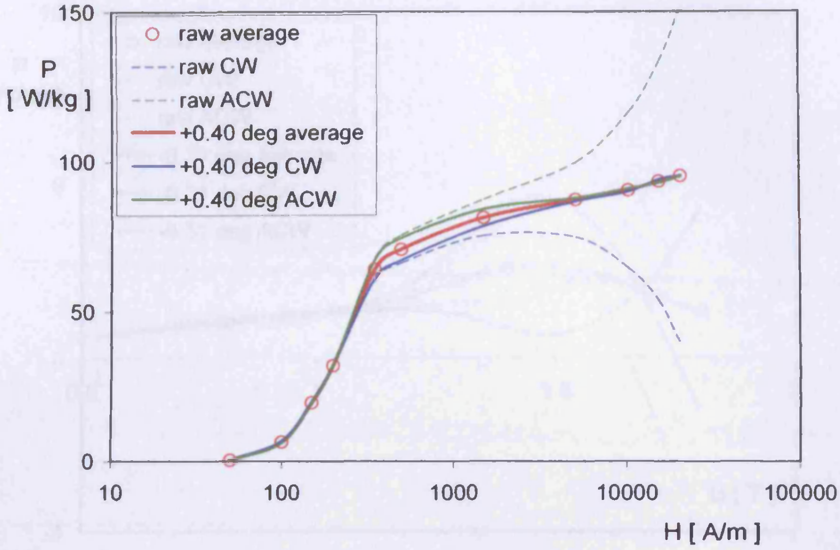

Fig. 5.5. Power loss measured for non-oriented electrical steel sheet (different positioning of the sample than in Fig. 5.4): a) at 50 Hz controlled *B*, b) at 250 Hz controlled *B*, c) at 50 Hz controlled *H*, d) at 250 Hz controlled H, (raw - as measured; +0.40 deg - recalculated for the angles $\alpha = \beta = +0.40$ deg

In this case, for the angular displacement $\alpha = \beta = -0.31$ deg the *CW-ACW* difference is reduced, but it is not eliminated, especially for controlled *B* conditions (Fig. 5.6a and Fig. 5.6b). The measurements under *H* controlled conditions exhibit lower *CW-ACW* differences (Fig. 5.6c and Fig. 5.6d).

It was difficult to find the values α and β for the data shown in Fig. 5.6, basing only on the measurements under controlled *B* conditions, due to high *CW-ACW* differences and the apparent discrepancy in the shapes of the *CW-ACW* power loss curves. There was no combination of angles, even for $\alpha \neq \beta$, which could minimise the differences further. For that reason, the measurements under controlled *H* have been taken as the reference point. Once the angles α and β have been found for the controlled *H* conditions, the same values were used also for the controlled *B* conditions – all the angles in Fig. 5.6 have exactly the same value.

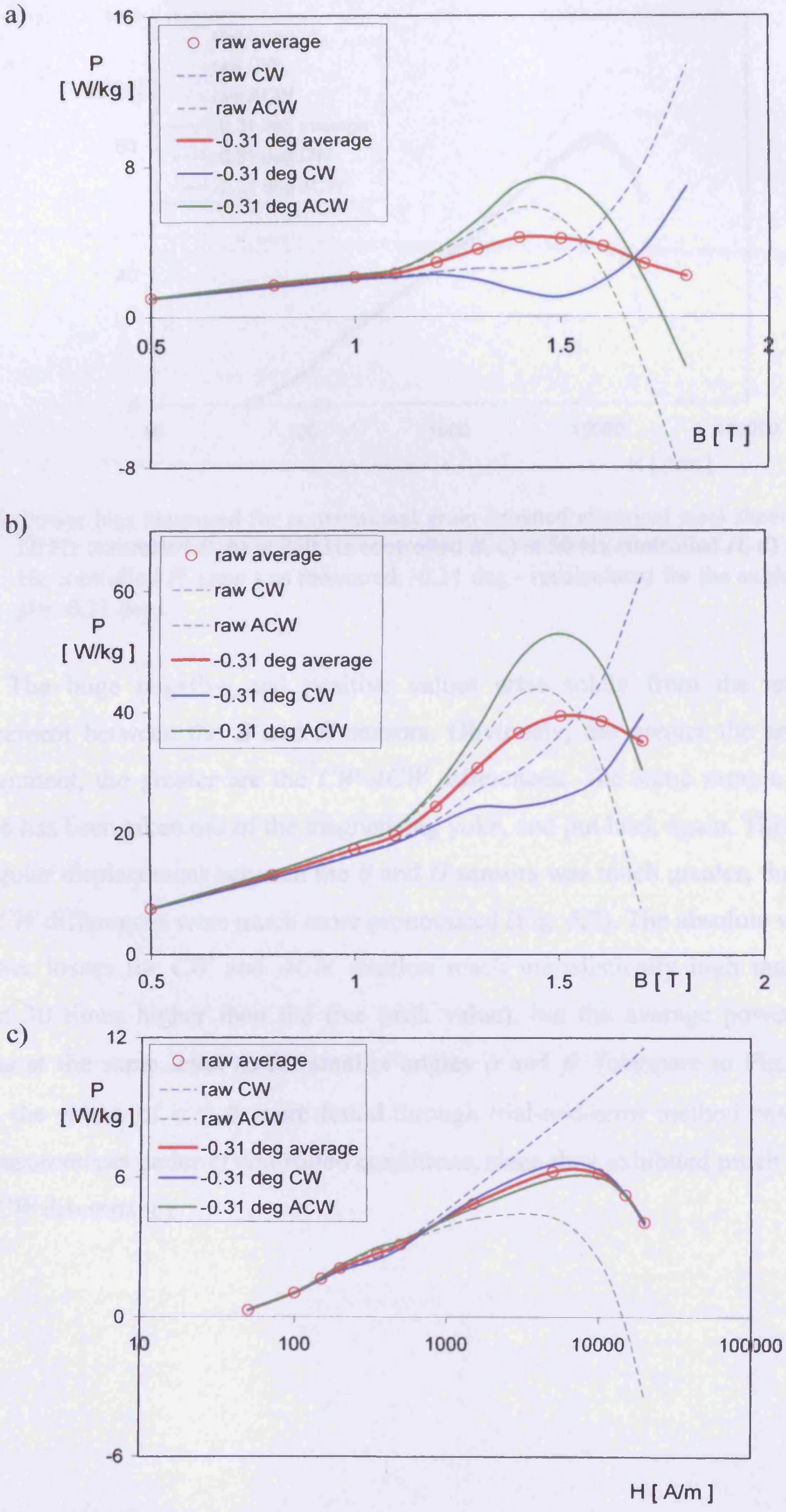
a)
16
P
[W/kg]
8
0
-8
0.5
1
1.5
2
B [T]
raw average
raw CW
raw ACW
-0.31 deg average
-0.31 deg CW
-0.31 deg ACW
b)
60
40
20
0
P
[W/kg]
0.5
1
1.5
B [T]
2
raw average
raw CW
raw ACW
-0.31 deg average
-0.31 deg CW
-0.31 deg ACW
c)
12
6
0
-6
P
[W/kg]
10
100
1000
10000
100000
H [A/m]
raw average
raw CW
raw ACW
-0.31 deg average
-0.31 deg CW
-0.31 deg ACW

d)

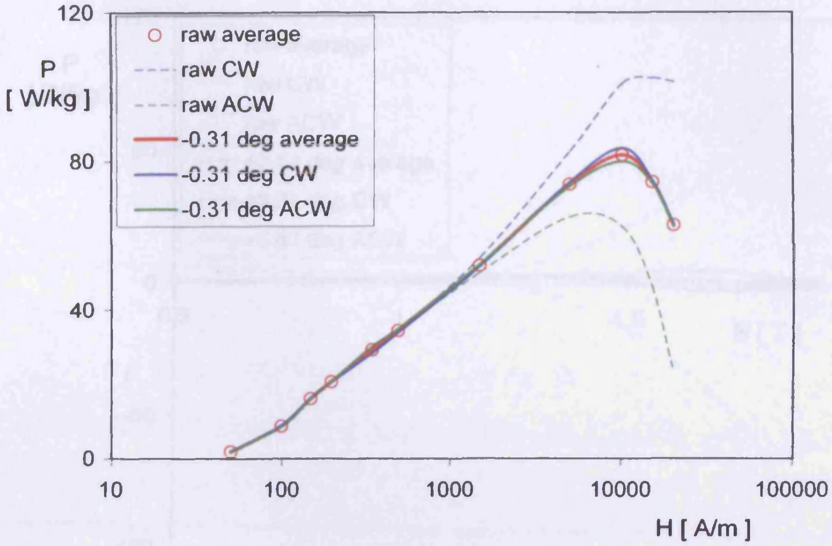

Fig. 5.6. Power loss measured for conventional grain-oriented electrical steel sheet: a) at 50 Hz controlled *B*, b) at 250 Hz controlled *B*, c) at 50 Hz controlled *H*, d) at 250 Hz controlled *H*, (raw - as measured; -0.31 deg - recalculated for the angles $\alpha = \beta = -0.31$ deg)

The huge negative and positive values arise solely from the angular displacement between the *B* and *H* sensors. Obviously, the greater the angular misalignment, the greater are the *CW-ACW* differences. The same sample as in Fig. 5.6 has been taken out of the magnetising yoke, and put back again. This time the angular displacement between the *B* and *H* sensors was much greater, thus the *CW-ACW* differences were much more pronounced (Fig. 5.7). The absolute values of power losses for *CW* and *ACW* rotation reach unrealistically high numbers (almost 30 times higher than the true peak value), but the average power loss remains at the same level as for smaller angles α and β (compare to Fig. 5.3). Again, the values of $\alpha = \beta$ were found through trial-and-error method based on the measurements under *H* controlled conditions, since they exhibited much lower *CW-ACW* discrepancy.

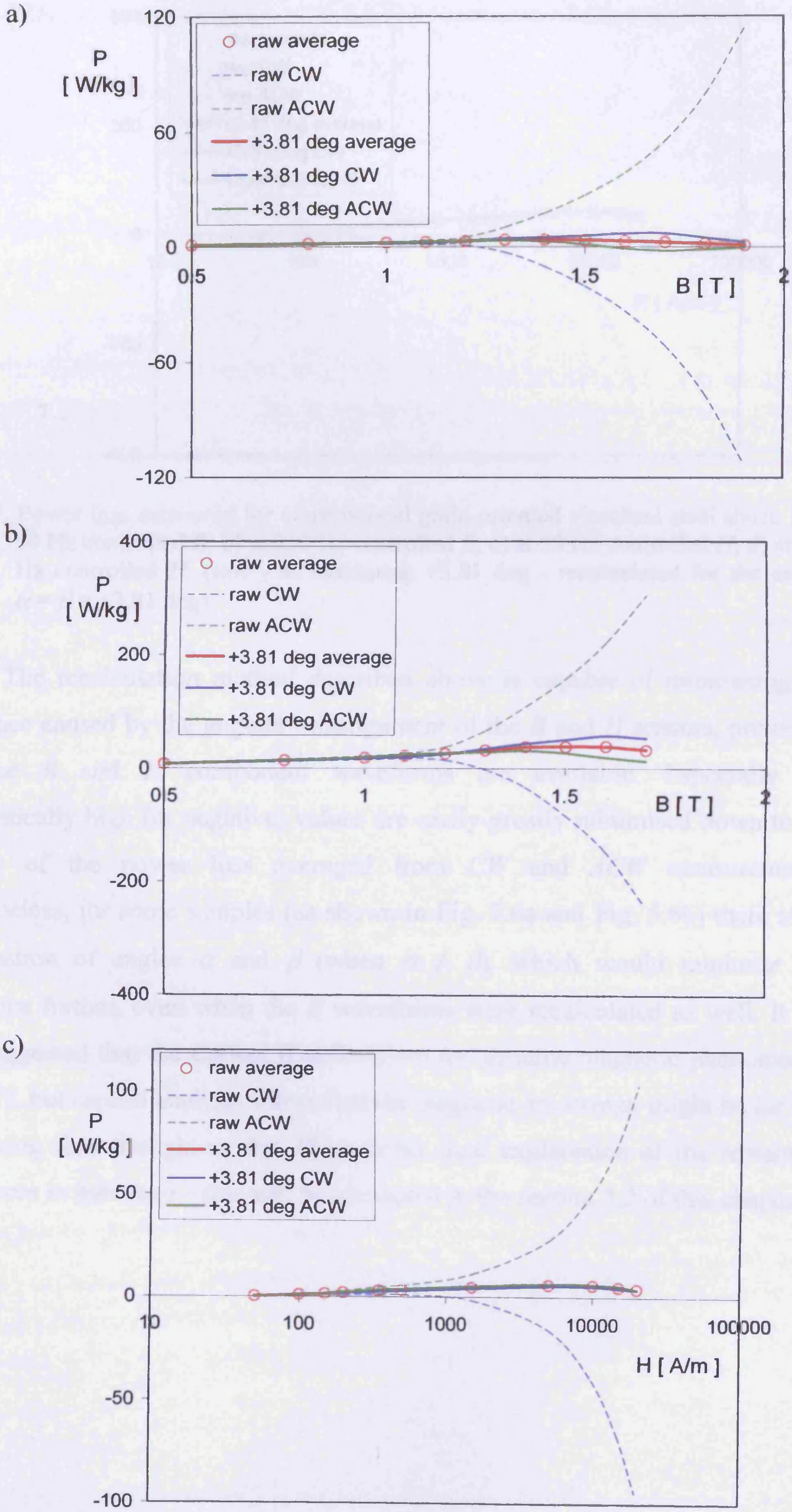
a)
P
[W/kg]
120
60
0
-60
-120
0.5
1
1.5
2
B [T]
raw average
raw CW
raw ACW
+3.81 deg average
+3.81 deg CW
+3.81 deg ACW
b)
P
[W/kg]
400
200
0
-200
-400
0.5
1
1.5
2
B [T]
raw average
raw CW
raw ACW
+3.81 deg average
+3.81 deg CW
+3.81 deg ACW
c)
P
[W/kg]
100
50
0
-50
-100
10
100
1000
10000
100000
H [A/m]
raw average
raw CW
raw ACW
+3.81 deg average
+3.81 deg CW
+3.81 deg ACW

d)

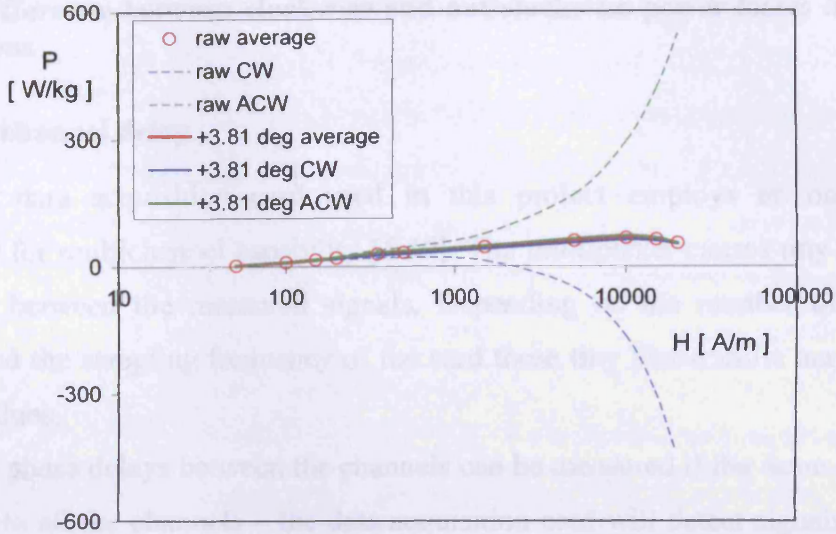

Fig. 5.7. Power loss measured for conventional grain-oriented electrical steel sheet: a) at 50 Hz controlled *B*, b) at 250 Hz controlled *B*, c) at 50 Hz controlled *H*, d) at 250 Hz controlled *H*, (raw - as measured; +3.81 deg - recalculated for the angles $\alpha = \beta = +3.81$ deg)

The recalculation method described above is capable of minimising the difference caused by the angular misalignment of the *B* and *H* sensors, providing that the *B* and *H* component waveforms are available. Especially the unrealistically high (or negative) values are easily greatly minimised down to the vicinity of the power loss averaged from *CW* and *ACW* measurements. Nevertheless, for some samples (as shown in Fig. 5.6a and Fig. 5.6b) there is no combination of angles α and β (when $\alpha \neq \beta$), which would minimise the difference further, even when the *B* waveforms were recalculated as well. It has been suggested that the *CW-ACW* differences are genuine magnetic phenomenon [*5.2-5.5*], but careful analysis shows that the magnetic anisotropy might be far less influencing than thought so far. There is no clear explanation of the remaining differences in literature – this will be attempted in the section 5.2 of this chapter.

5.2. The difference between clockwise and anticlockwise power losses due to other reasons

5.2.1. Interchannel delay

The data acquisition card used in this project employs an onboard multiplexer for multichannel capability [*5.10*]. The multiplexer causes tiny phase differences between the measured signals. Depending on the number of used channels and the sampling frequency of the card these tiny phase shifts may take different values.

The phase delays between the channels can be measured if the same signal is supplied to all the channels – the data acquisition card will detect signals with different phases, which could be easily detected by the numerical calculations. The concept of this method is shown in Fig. 5.8.

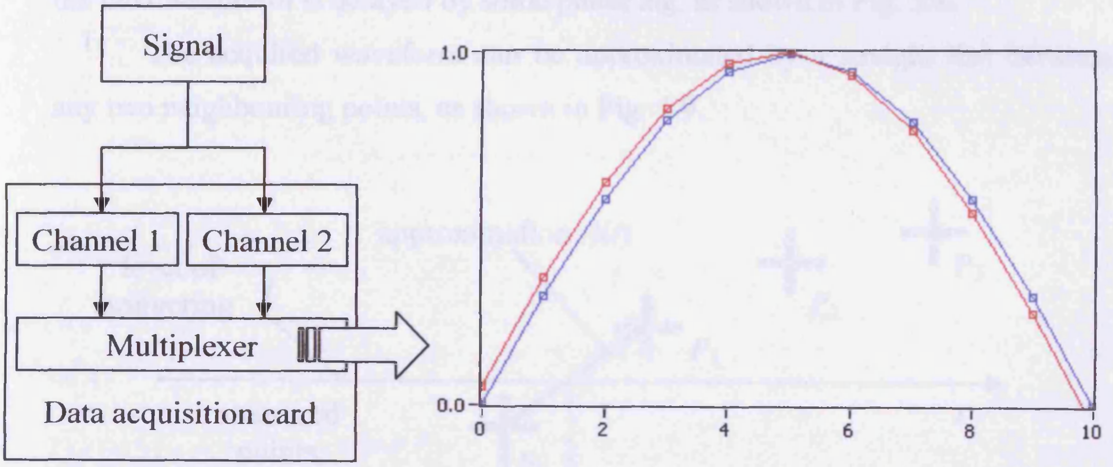

Fig. 5.8. The concept of detection of the phase delays between subsequent channels of the data acquisition card; blue line represents the signal from Channel 1 (phase is equal to zero), red line represents the signal from Channel 2 (with the phase shift)

The delay times of the multiplexer were measured over wide range of frequencies. It has been found (see **Appendix E**) that the delay, γ, obeys the following equation [*5.11*]:

$$\gamma = \frac{360\,\text{deg}}{\text{points}\cdot\text{channels}} \qquad (5.13)$$

where: points – number of points per one period of acquired waveform, channels – number of channels used by multiplexer

The typical parameters for a measurement at 50 Hz are 1024 points and 7 channels (see section 4.2); which yields around 0.05 deg of phase shift between the two neighbouring input channels, but as much as 0.3 deg between the first and last channels. The value may not seem to be significant, but if not taken into account it will cause major errors in the calculation of the total power loss. For example, it has been shown in Fig. 5.4 that the phase shift between the sensors signals due to angular misalignment at the level of 0.06 deg influences the *CW* and *ACW* losses in significant way. The value of 0.3 deg can easily lead to negative power losses, as presented in Fig. 5.5. A simple mathematical method can be utilised in order to minimise the interchannel delay by a great factor.

The real analogue signal is acquired by the card as a one dimensional array of numbers, which correspond to the values equally distributed in the times space. For sake of simplicity, let us assume that the ideal waveform starts from zero, and the next waveform is delayed by some phase lag, as shown in Fig. 5.8.

The acquired waveform can be approximated by a straight line between any two neighbouring points, as shown in Fig. 5.9.

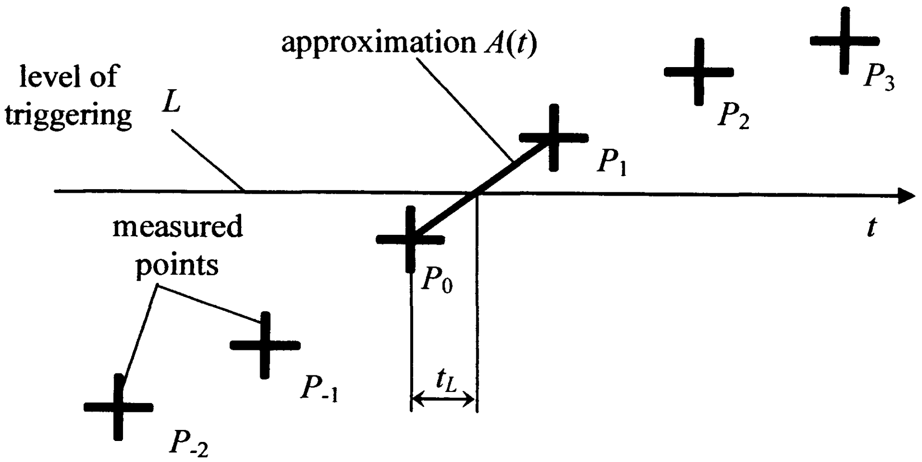

Fig. 5.9. The approximation of the waveform by a straight line between two neighbouring points

Knowing the values of P_1 and P_0 (the data acquisition card gives direct numbers also for so-called "pre-triggered" points [*5.10*, *5.12*]), as well as the time between two neighbouring points (defined by the sampling frequency of the card), the equation of the approximation $A(t)$ can be determined (assuming time of P_0 as zero) as follows:

$$A(t) = (P_1 - P_0) \cdot t + P_0 \tag{5.14}$$

Taking the values from Fig. 5.9 we can write that:

$$L = (P_1 - P_0) \cdot t_L + P_0 \tag{5.15}$$

which allows calculating the time t_L, which is the time from the point P_0 to the zero point, at which the value should be acquired:

$$t_L = (L - P_0) / (P_1 - P_0) \tag{5.16}$$

The time between any pair of neighbouring points is constant, thus the time t_L can be used for calculating the expected time between each measured point and the value of this point.

For the pair of points P_0 and P_1 from Fig. 5.9 we can calculate the value of expected point at the time t_L

$$A(t_L) = (P_1 - P_0) \cdot t_L + P_0 \tag{5.17}$$

Substituting equation (5.16) into (5.17) by definition we obtain L

$$A(t_L) = (P_1 - P_0) \cdot (L - P_0) / (P_1 - P_0) + P_0 = L = P'_1 \tag{5.18}$$

where: P'_1 - corrected value of P_1.

Equation (5.17) may be used subsequently for any pair of neighbouring points. Generally we can write that:

$$A(t_{i-1} + t_L) = (P_i - P_{i-1}) \cdot t_L + P_{i-1} = (P_i - P_{i-1}) \cdot (L - P_0) / (P_1 - P_0) + P_{i-1} = P'_i \tag{5.19}$$

where: i - number of subsequent point, P' - the value of corrected point.

If the equation (5.19) is used for all pairs of neighbouring points in the acquired waveform it results with significant reduction of the delay time t_D (Fig. 5.10).

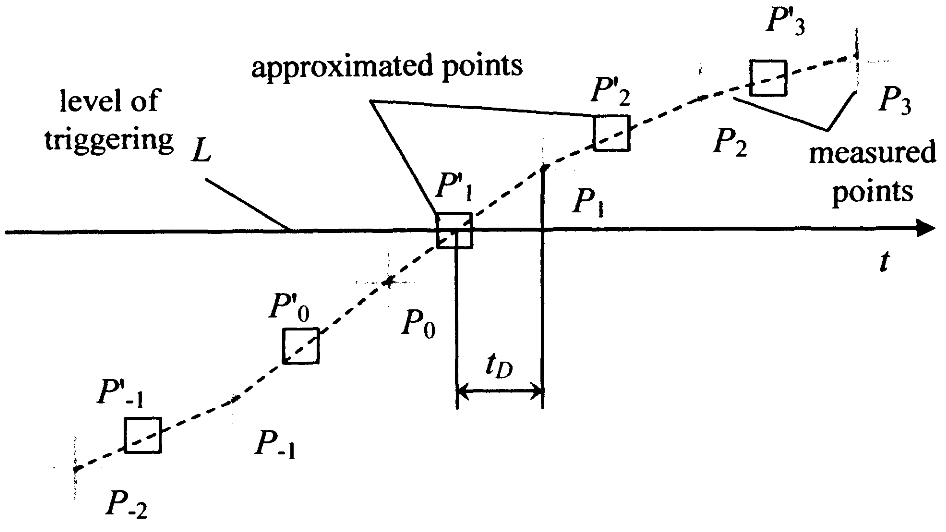

Fig. 5.10. The technique of reduction of the time delay t_D. Crosses denote the acquired points, squares denote the points corrected by means of equation (5.19).

Of course, the technique above is described only for one channel. However, all measured waveforms have to be recalculated by means of equation (5.19), but taking into account the fact the delay grows for each subsequent channel. Thus, the final equation to be used is:

$$A(t_{i-1} + t_{d(k)}) = (P_i - P_{i-1}) \cdot t_{d(k)} + P_{i-1} = P'_i \qquad (5.20)$$

The influence of the interchannel delay would be present also in the alternating measurements, since there would be a phase difference between the measured B and H. It has been verified that for higher flux density the angle between the B and H decreases, thus any constant phase shift between the measured signals would contribute more and more at higher flux. By analysing the data measured in the Epstein frame it was possible to measure the phase shift between the B and H waveforms. The measurements have been carried out with the simultaneous sampling card (i.e. no multiplexer) *[5.12]*. If the magnitudes of the B and H waveforms and the phase shift between them are taken into account, then the theoretical contribution of the phase lag between B and H signal can be plotted as in Fig. 5.11.

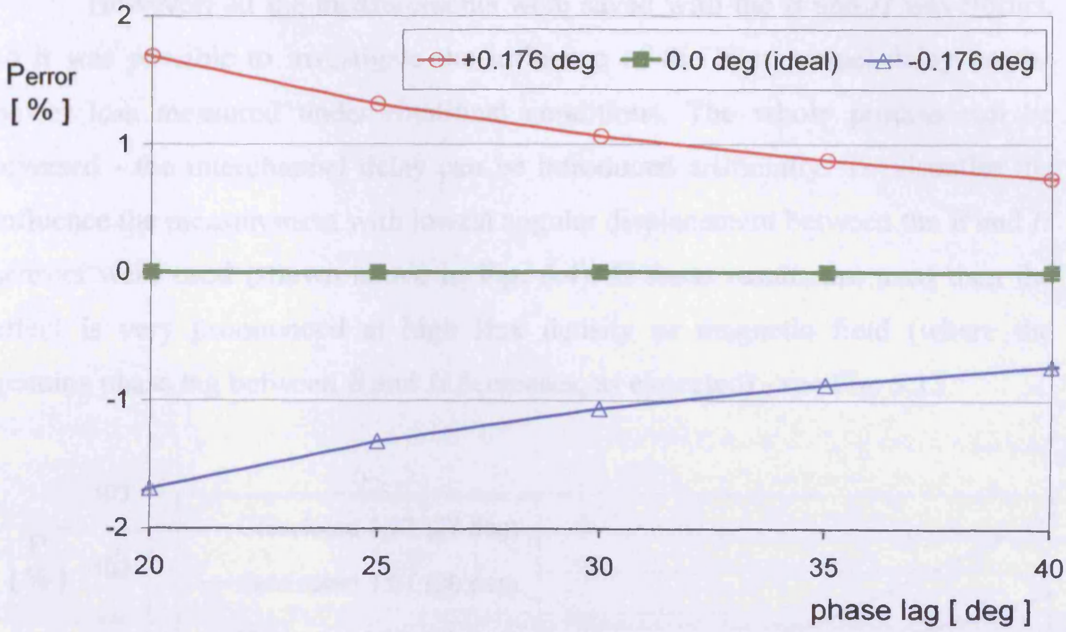

Fig. 5.11. Theoretical influence of interchannel delay on the power loss measurement. *Y* axis represents relative change in power loss per cent. Green line at zero is equivalent to ideal measurement (i.e. no interchannel delay). Upper red curve represents the case when signal *H* is read before *B*; for lower blue curve signal *B* is read before *H*. Typical interchannel delay for card PCI-6052E is used; 0.176 deg = 360 degrees / (1024 points · 2 channels)

Using the theoretical results presented in Fig. 5.11 it became possible to compare the real measured results with the prediction. This time, the card with the multiplexer has been used in the measurements of power loss by means of an Epstein frame. The number of points has been varied so as to achieve various interchannel delays according to equation (5.13). The negative values were achieved by changing the order of connection of the signals to the card. The comparison between the theoretically calculated values and the data measured by the data acquisition card with the multiplexer is shown in Fig. 5.12.

All the points but one in each line in Fig. 5.12 are measured without the interchannel delay correction. The point where the correction is used is identical to the theoretical value predicted. This measurement has been repeated several times in order to exclude coincidental results. The difference between the measured and theoretical values was so small that potential remaining influence stayed below the level of detection. Comparing the results obtained by cards without and with the multiplexer allowed "calibration" of the latter one in terms of reducing the interchannel delay to an undetectable level. Thus, all the results were measured with the automatic correction of the interchannel delay.

However, all the measurements were saved with the *B* and *H* waveforms, so it was possible to investigate the influence of the interchannel delay on the power loss measured under rotational conditions. The whole process can be reversed - the interchannel delay can be introduced artificially. To visualise the influence the measurement with lowest angular displacement between the *B* and *H* sensors were used (shown above in Fig. 5.4). If those results are used then the effect is very pronounced at high flux density or magnetic field (where the genuine phase lag between *B* and *H* decreases, as expected) - see Fig. 5.13.

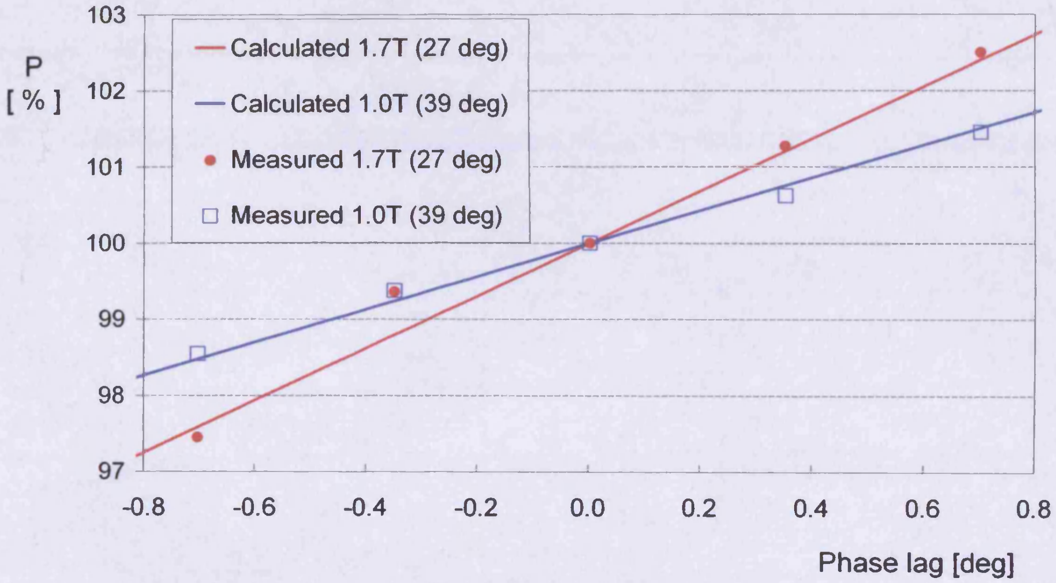

Fig. 5.12. The influence of interchannel delay on power loss measurement. The data was obtained for conventional grain-oriented material magnetised at 50Hz in Epstein frame. The flux density was controlled to be sinusoidal with the peak value 1.0 T and 1.7 T, respectively. The phase difference between fundamental components of H and B waveforms is 39 deg for 1.0 T and 27 deg for 1.7 T

It is worth noting that the character of this error is additive – the averaging from *CW* and *ACW* measurements does not "cancel" this effect, since the delay has always the same sign and always introduces either only positive, or only negative error, which sign depends only on the order of multiplexing in the data acquisition card – as shown in Fig. 5.13.

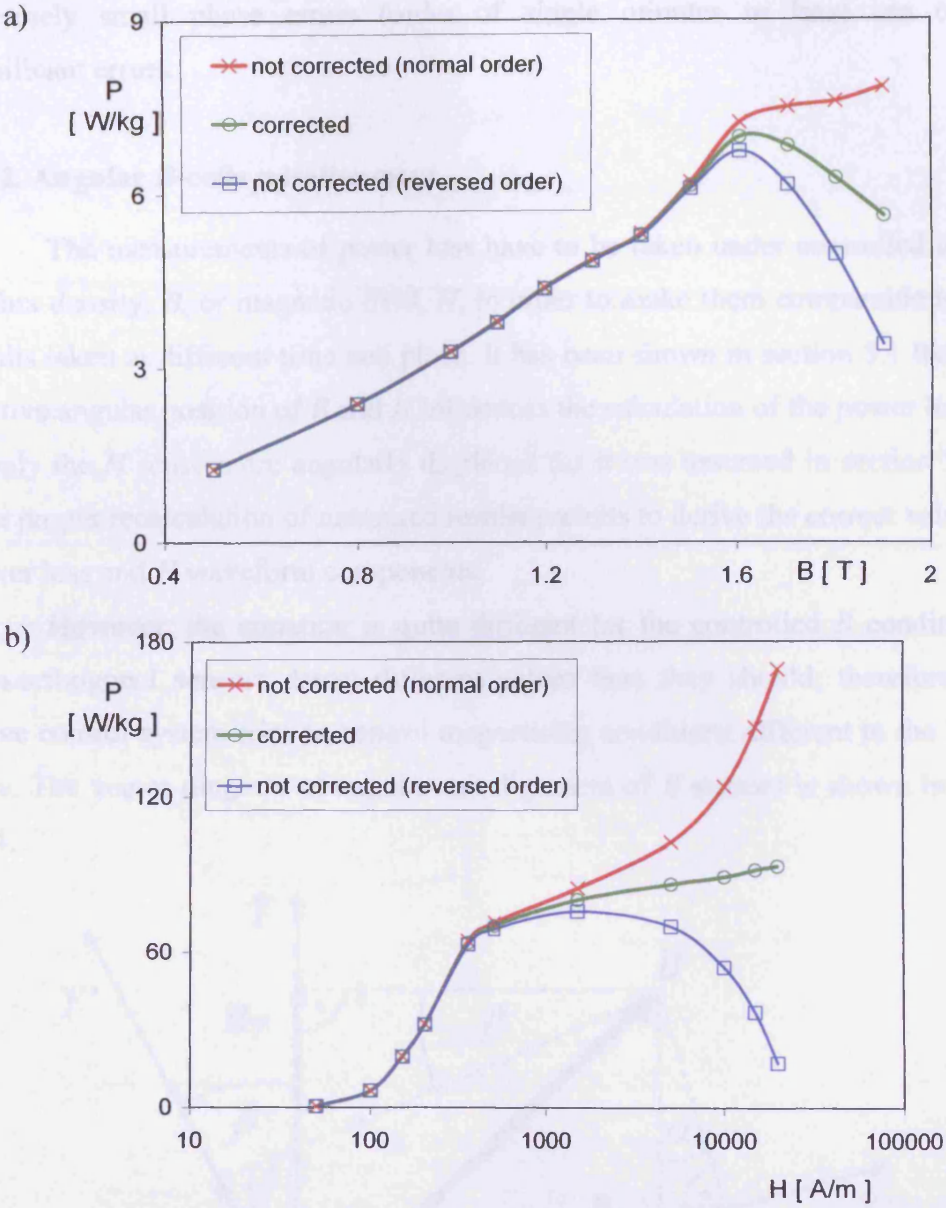

Fig. 5.13. The influence of the interchannel delay on the power loss from Fig. 5.4: a) at 50 Hz, controlled *B*; b) at 250 Hz, controlled *H*; (only averaged values are shown, normal order – the order of signal connections is normal, reversed order – the order of signals is reversed)

The method of reducing of the interchannel delay is not perfect, since it approximates the acquired waveform with short straight lines. Thus, there might be a remaining component of the tiny phase shift between the measured signals, which will keep influencing the final value of the power loss. Obviously, this problem should not appear when the data acquisition cards without the multiplexer are used. However, this example is given here to highlight that even extremely small phase errors (order of single minutes or less) can cause significant errors.

5.2.2. Angular B-coils misalignment

The measurements of power loss have to be taken under controlled shape of flux density, B, or magnetic field, H, in order to make them comparable to the results taken at different time and place. It has been shown in section 5.1 that the relative angular position of B and H influences the calculation of the power losses. If only the H sensors are angularly displaced (as it was assumed in section 5.1.), then proper recalculation of measured results permits to derive the correct value of power loss and H waveform components.

However, the situation is quite different for the controlled B conditions. Non-orthogonal sensors detect different values than they should; therefore the active control system tries to control magnetising conditions different to the ideal ones. The vector diagram of angular misalignment of B sensors is shown in Fig. 5.14.

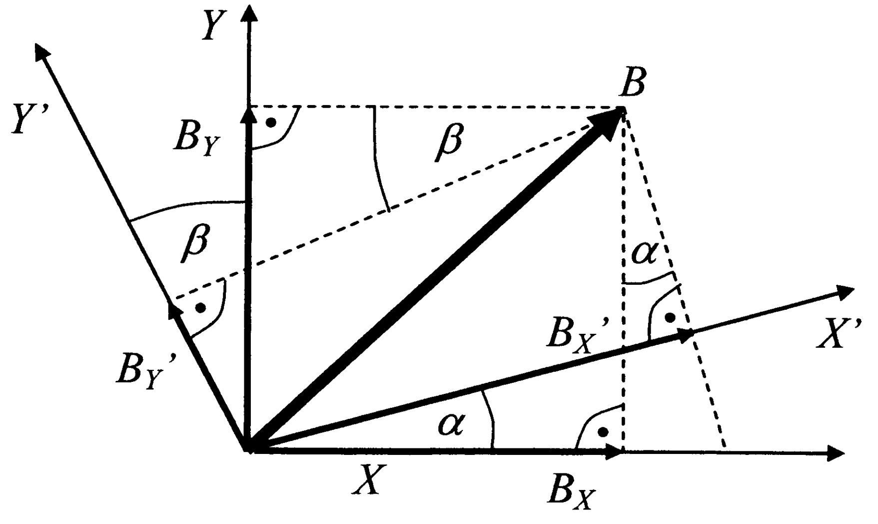

Fig. 5.14. Vector diagram of misalignment of the B sensors

In the case of magnetisation under circular flux density, the components are of sinusoidal shape and the sensors produce signals as follows, for CW rotation:

$$B_X''(t)_{CW} = B_X \cdot \sin(\omega \cdot t) \cdot \cos(\alpha) + B_Y \cdot \cos(\omega \cdot t) \cdot \sin(\alpha) \tag{5.21a}$$

$$B_Y''(t)_{CW} = B_Y \cdot \cos(\omega \cdot t) \cdot \cos(\beta) - B_X \cdot \sin(\omega \cdot t) \cdot \sin(\beta) \tag{5.21b}$$

and for *ACW* rotation:

$$B_X''(t)_{ACW} = B_X \cdot \sin(\omega \cdot t) \cdot \cos(\alpha) - B_Y \cdot \cos(\omega \cdot t) \cdot \sin(\alpha) \tag{5.22a}$$

$$B_Y''(t)_{ACW} = -B_Y \cdot \cos(\omega \cdot t) \cdot \cos(\beta) + B_X \cdot \sin(\omega \cdot t) \cdot \sin(\beta) \tag{5.22b}$$

Consequently, the active feedback algorithm or electronic circuit used in the magnetising setup will endeavour to control the components to different magnitudes and phases than it should. The resultant loci of B vector will not be elliptical, which will inevitably have an impact on the power loss measured, as it can be seen from Fig. 5.15.

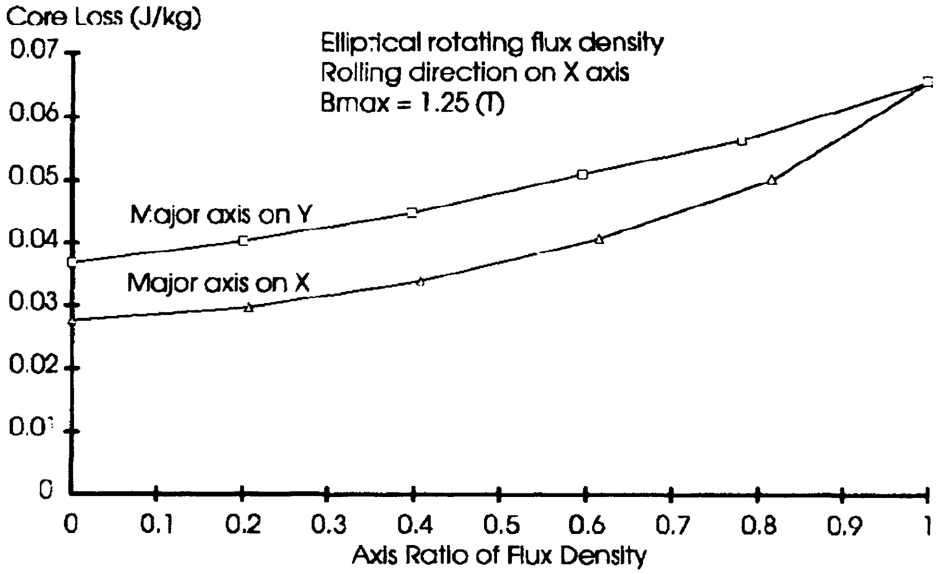

Fig. 5.15. The ellipticity of the magnetisation as a factor influencing the power loss [*5.13*]

In most previous rotational investigations [*5.1*] the B coils are used as the sensors of flux density. The typical width of the B coil is around 20 mm. Depending on the diameter of the drilled holes and the wire, there might be an angular displacement of the sensor as depicted in Fig. 5.16.

The holes could be treated as positioned ideally (to some extent), since they can be drilled with the use of very precise machines, typically with an accuracy better than 0.01 mm.

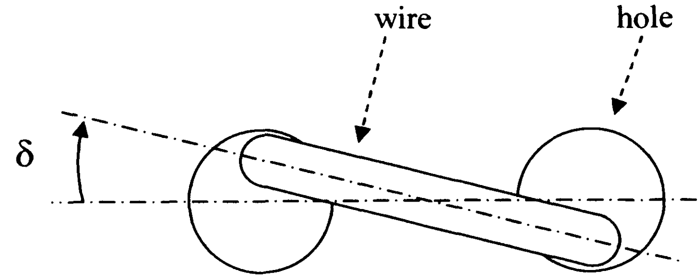

Fig. 5.16. Possible angular displacement, δ, of a single-turn search coil (not in scale)

The holes need to be as small as possible, but the diameters below 0.3 mm are practically difficult to drill. If the wire has 0.1 mm in diameter then theoretically the angular misalignment for one coil could be as high as 0.573 deg, thus the maximum relative angular displacement between coils for X and Y direction could reach 1.16 deg. When one of the components of flux density is delayed by such phase (corresponding to such angular misalignment) then it is clearly visible than the resulting figure is not a circle but an ellipse, which is not symmetrical about any of the axes, as it is shown in Fig. 5.17.

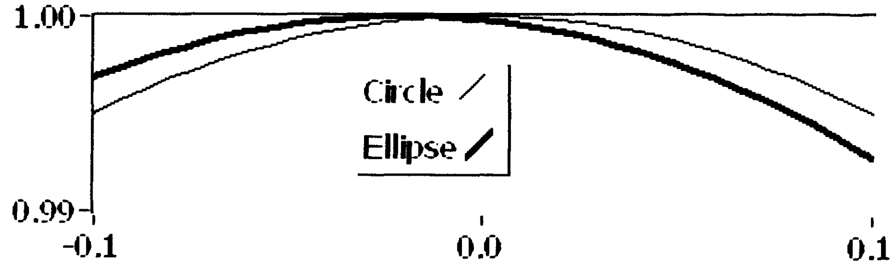

Fig. 5.17. Change from circle to ellipse due to phase delay between components (magnification of a part of the circle)

Therefore, the resultant loci of H vector are also asymmetrical and the asymmetry is greater for greater angular displacement of the B sensors, due to the greater "miscontrol" (that is non-ideal control due to incorrect shapes or phase shifts between the controlled waveform) of the ideal circular flux. Some examples for different positions of the B sensors are shown in Fig. 5.18. The misalignment of the B sensor as small as 1 degree corresponds to the asymmetry of H loci even up to several hundreds of A/m, as highlighted in Fig. 5.18a.

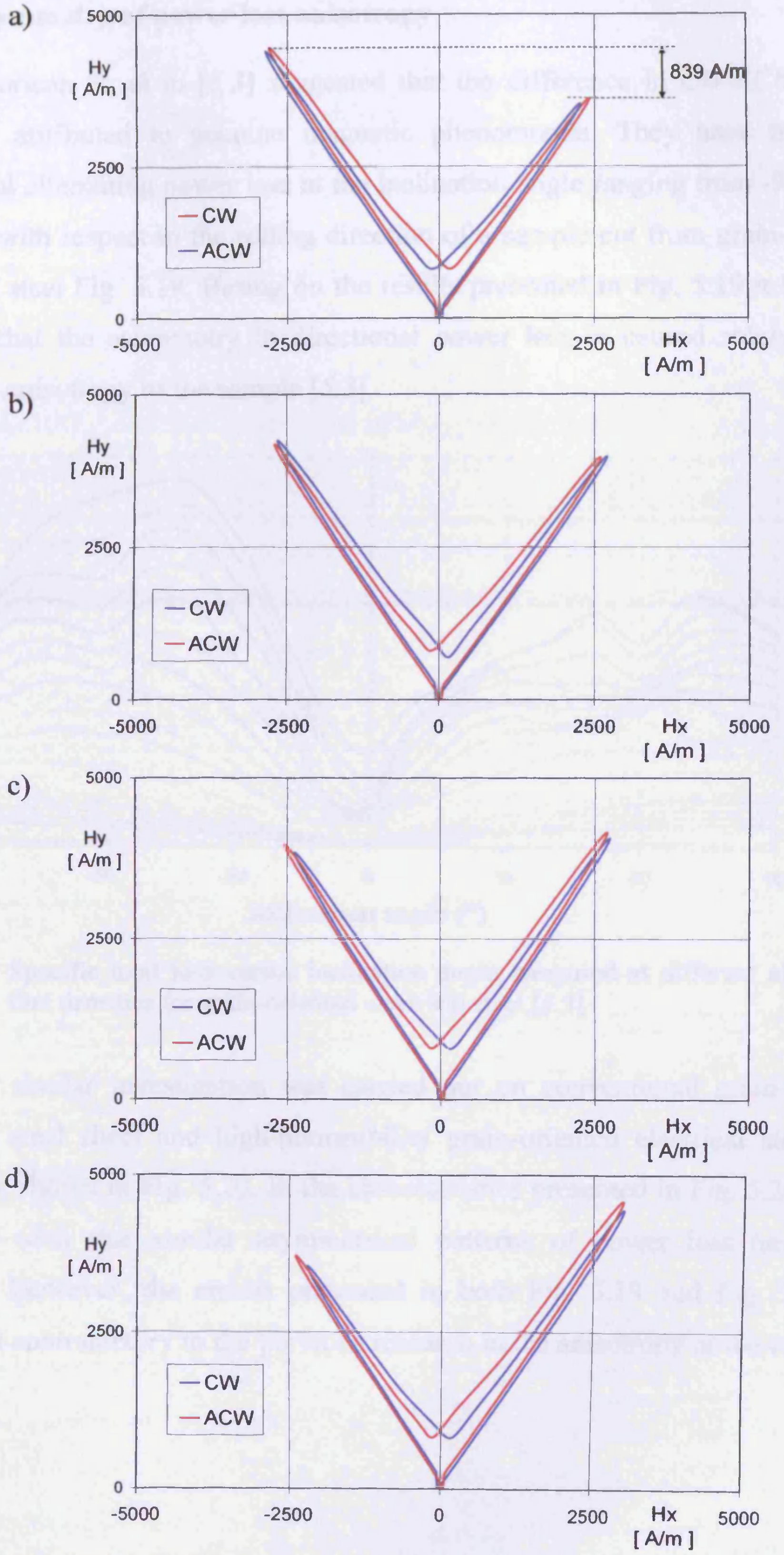

Fig. 5.18. Asymmetry in *H* loci due to misalignments of the *B* sensors measured for conventional grain-oriented electrical steel (only top half of the graphs are shown for clarity), positions of the sensors are $B_X = 0.0$ deg: a) $B_Y = 91.0$ deg, b) $B_Y = 90.0$ deg, c) $B_Y = 89.0$ deg, d) $B_Y = 88.0$ deg; thick line – *CW* rotation, thin line – *ACW* rotation

5.2.3. Asymmetry of power loss anisotropy

Gorican et. al in [*5.3*] suggested that the difference in *CW-ACW* power losses is attributed to genuine magnetic phenomenon. They have measured directional alternating power loss at the inclination angle ranging from -90 deg to +90 deg with respect to the rolling direction of a sample cut from grain-oriented electrical steel Fig. 5.19. Basing on the results presented in Fig. 5.19 it has been claimed that the asymmetry in directional power loss is caused solely by the magnetic anisotropy of the sample [*5.3*].

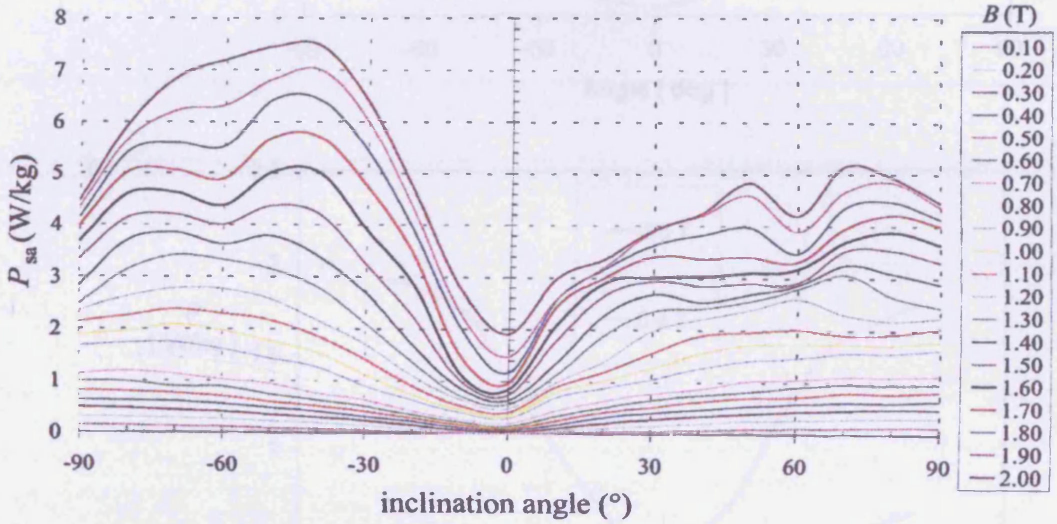

Fig. 5.19. Specific total loss versus inclination angle measured at different alternating flux densities for grain-oriented electrical steel [*5.3*]

A similar investigation was carried out on conventional grain-oriented electrical steel sheet and high-permeability grain-oriented electrical steel. The results are shown in Fig. 5.20. In the characteristics presented in Fig. 5.20, it can be easily seen that similar asymmetrical patterns of power loss have been obtained. However, the results presented in both Fig. 5.19 and Fig. 5.20 are somewhat contradictory to the previous research in the anisotropy of the electrical steels.

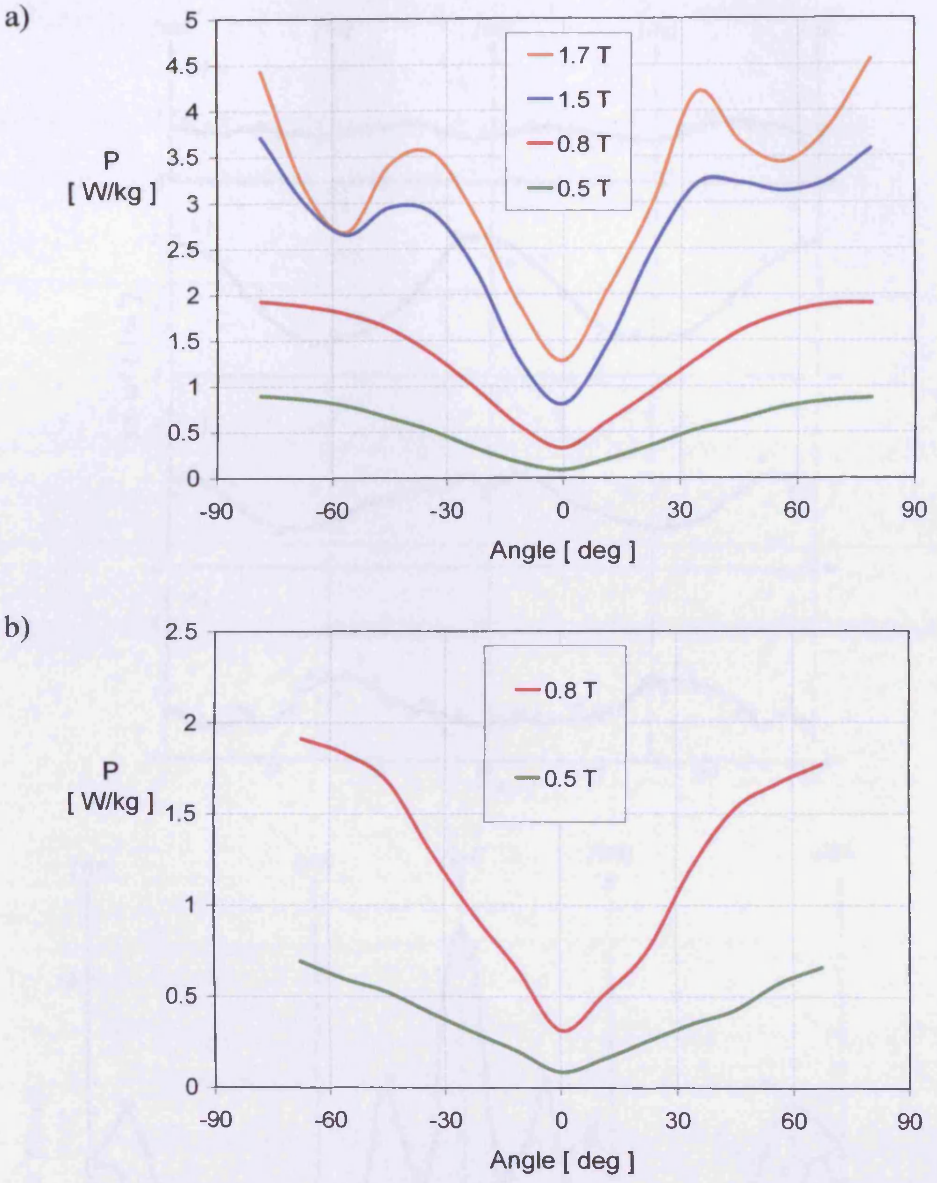

Fig. 5.20. Specific total loss versus inclination angle measured at 50 Hz and different alternating flux densities for: a) conventional grain-oriented electrical steel, b) high-permeability grain-oriented electrical steel

Zbroszczyk et al. in [*5.14*] presented results measured for single crystal Fe-3.25%Si, as shown in Fig. 5.21. There is some scattering of the measured points, but clearly the angular characteristics are quite symmetrical about the *Y* axis, which is not the case for the results shown in Fig. 5.19 and Fig. 5.20. The samples under test used in [*5.14*] was a single crystal, therefore all the graphs by definition should be symmetrical.

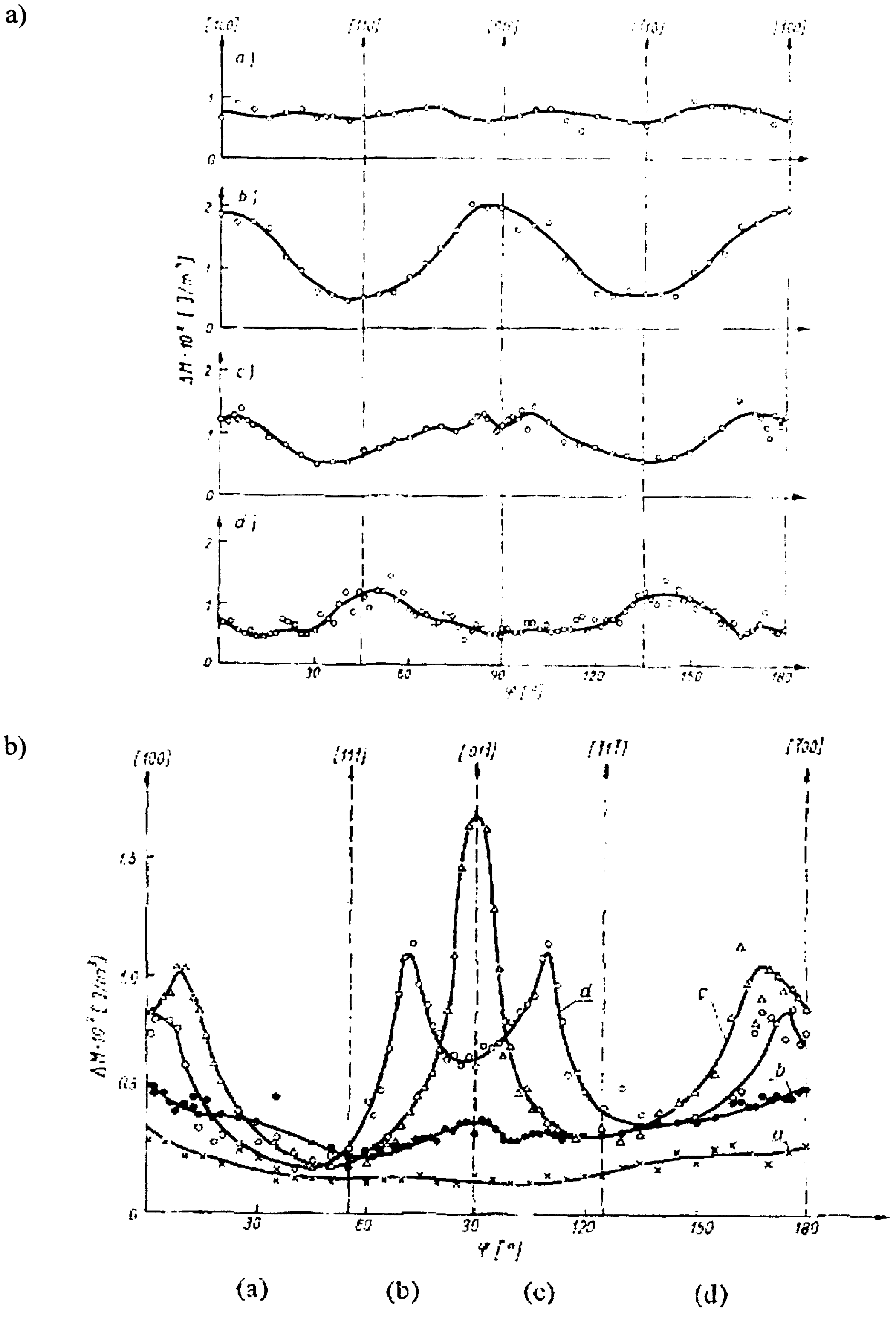

Fig. 5.21. Angular distribution of losses in Fe-3.25%Si single crystal of plane orientation: a) (001), b) (011) [*5.14*]

Soinski in [*5.15*] presented results measured for commercially available grain-oriented electrical steel (grade M4) – see Fig. 5.22. In this case, the scattering of the measured points for power losses has not been shown, and all the curves are almost ideally symmetrical about the *Y* axis.

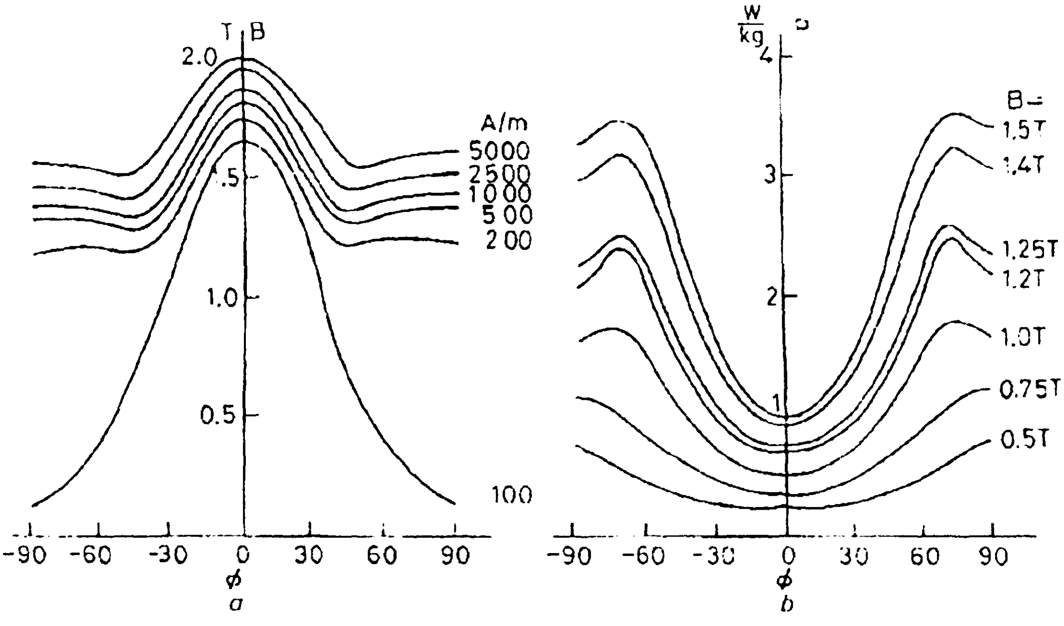

Fig. 5.22. Angular distribution of losses in commercial grain-oriented electrical steel (grade M4) versus the inclination angle of the magnetisation [*5.15*]

Therefore, is should be concluded that the asymmetry of the power loss curves shown in Fig. 5.19 and Fig. 5.20 is not attributed to the genuine magnetic phenomenon, at least not all of the asymmetry. Let us compare the curves for 1.0 T from Fig. 5.19 and Fig. 5.20a. It can be seen the curve in Fig. 5.19 (yellow line) is asymmetric – the left part is above 2 W/kg, whilst the right part is visibly below 2 W/kg. The curve in Fig. 5.20a for 1.0 T (red line) is almost perfectly symmetrical about the *Y* axis – with very similar values of power loss (just below 2 W/kg). Similar applies to the curves measured at 0.5 T, but this is visible only after magnification of the Fig. 5.19.

The experimental results show that the *CW-ACW* difference is higher for the samples with greater anisotropy (compare Fig. 5.5 and Fig. 5.6). However, it is also shown, that even very small angular displacement of the *B* sensors can cause significant differences in the controlled magnetising conditions (as demonstrated in Fig. 5.18). The effect is more pronounced for the sample with greater anisotropy, because smaller changes in the level of controlled *B* will be responsible for large changes in magnetic field, thus the power loss. It can be seen in Fig. 5.20b that both curves (i.e. for 0.5 T and 1.0 T) are somewhat asymmetrical about the Y axis. It is suspected, that small angular misalignment of the B sensors is responsible for the most of the asymmetry presented in Fig. 5.19 and Fig. 5.20. The results presented in Fig. 5.18a are measured under the condition, where the B_X coil was assumed to be positioned ideally, and the B_Y coil was artificially rotated by means of equations (5.8) by the angle -1.0 deg. When both the coils B_X and B_Y where assumed to be positioned ideally (i.e. no software correction by means of equations (5.8)), then it is also clear that they were not exactly at the positions of 0.0 deg and 90.0 deg. This can be clearly seen from Fig. 5.18b, where still the left "arm" of the graph has higher maximum than the right one. Fig. 5.18c shows that the correction of the position of the B_Y coil by +1.0 deg reverse the situation (i.e. the right maximum is higher), but the difference between the left and right maxima is approximately the same as in Fig. 5.18b. Therefore, the true position of the B_Y coil is probably somewhere around 0.5 deg, which is in the range of error resulting from the diameter of drilled holes and the thickness of the used wire (compare Fig. 5.16).

On the other hand, the results shown in Fig. 5.21 and Fig. 5.22 are not perfectly symmetrical about the Y axis. The asymmetry is present also for the single crystal of Fe-Si, so it could be suspected that either the crystal was not ideal or the measurement method was less accurate than it was claimed, that is better than 0.1% [*5.14*]. Even if the magnetic asymmetry exists it cannot be responsible for such great asymmetry in power loss characteristics as presented in Fig. 5.19 and Fig. 5.20.

As it can be seen from Fig. 5.18, the loci of H vector have almost equal peaks of magnetic field strength for *CW* and *ACW* direction of rotation. However, the shapes are slightly different, especially in the vicinity of the Y axis (Fig. 5.23).

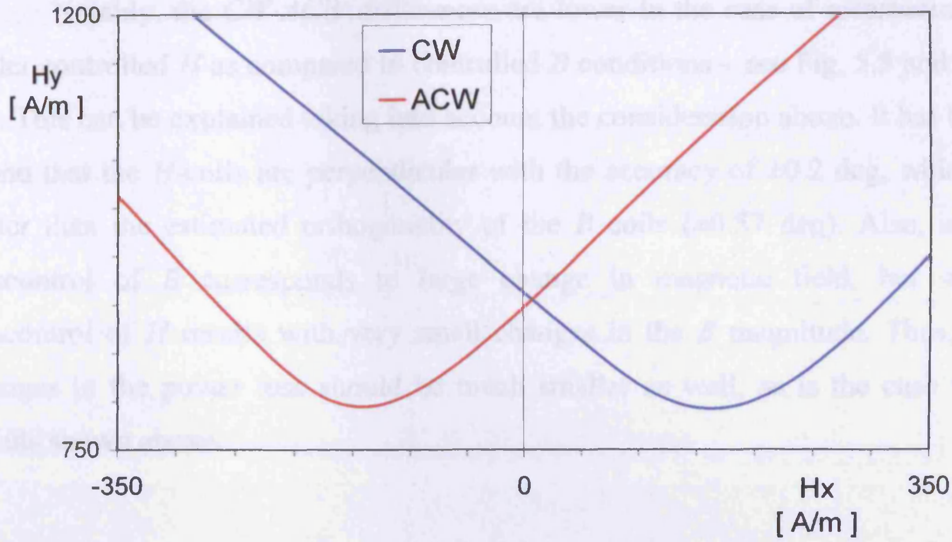

Fig. 5.23. The magnification of the vicinity of the *Y* axis from Fig. 5.18c

A closer look at the *H* loci shown in Fig. 5.18 allows the deduction that the magnetising conditions in the *CW* and *ACW* direction are not exactly the same if there is angular misalignment in the *B* coils. However, the influence on the calculated power loss resulting from the *B* coil misalignment could not be investigated using the measured results, since the changes were smaller than the repeatability of the measuring system Fig. 5.24 (see also section 4.7.3 and **Appendix D**).

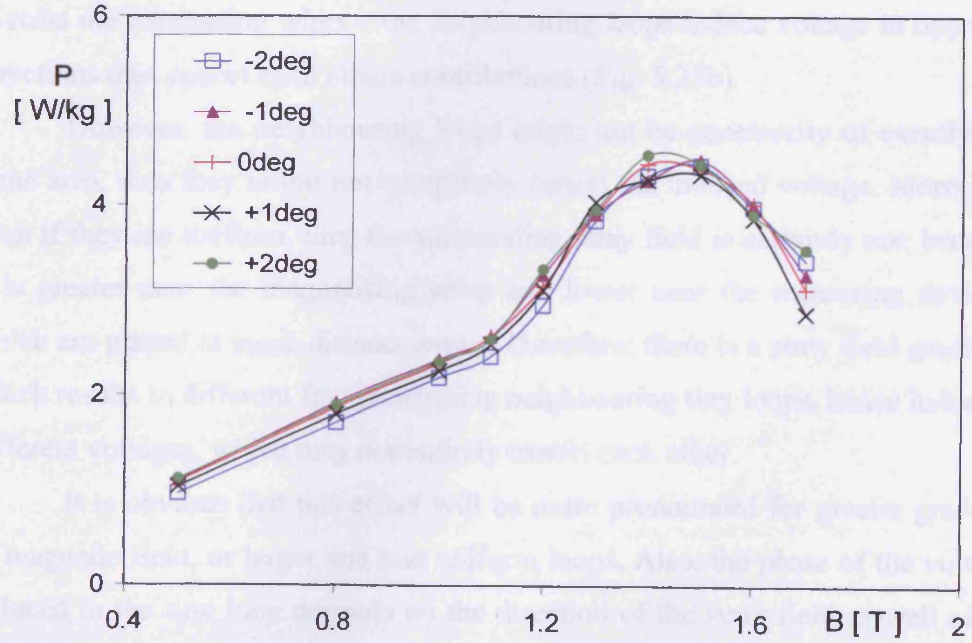

Fig. 5.24. The average power loss for different misalignments of B_Y sensor, for the data from Fig. 5.18

Notably, the *CW-ACW* differences are lower in the case of measurements under controlled *H* as compared to controlled *B* conditions – see Fig. 5.5 and Fig. 5.6. This can be explained taking into account the consideration above. It has been found that the *H*-coils are perpendicular with the accuracy of ±0.2 deg, which is better than the estimated orthogonality of the *B* coils (±0.57 deg). Also, small miscontrol of *B* corresponds to large change in magnetic field, but small miscontrol of *H* results with very small changes in the *B* magnitude. Thus, the changes in the power loss should be much smaller as well, as is the case with results shown above.

5.2.4. Twisting of the connecting wires

A time-varying flux induces a voltage in any coil or loop enwrapping that flux. The value of that voltage is directly proportional to the change of flux and to the area enclosed by the coil (e.g. sensor), according to equation (4.1).

However, the voltage induced in the sensor must be conveyed to a meter or other measuring devices. Most commonly the sensor is simply connected by means of conducting wires. If the connection is made as is shown in Fig. 5.25a, then the unintentional loop will "pick up" some stray magnetic field inevitably affecting the voltage measured by the meter. The simplest method to avoid this is to twist the connecting wires – the neighbouring loops induce voltage in opposite directions thus cancel each others contributions (Fig. 5.25b).

However, the neighbouring loops might not be necessarily of exactly the same area, thus they might not completely cancel the induced voltage. Moreover, even if they are uniform, then the surrounding stray field is certainly not, because it is greater near the magnetising setup and lower near the measuring devices, which are placed at some distance away. Therefore, there is a stray field gradient, which results in different flux penetrating neighbouring tiny loops, hence inducing different voltages, which may not entirely cancel each other.

It is obvious that this effect will be more pronounced for greater gradient of magnetic field, or larger and less uniform loops. Also, the phase of the voltage induced in the tiny loop depends on the direction of the stray field as well as on the location of the twisted wires. Thus it is very difficult to investigate this phenomenon and to draw some clear conclusions. Nevertheless some attempts have been made and the measured results are shown below.

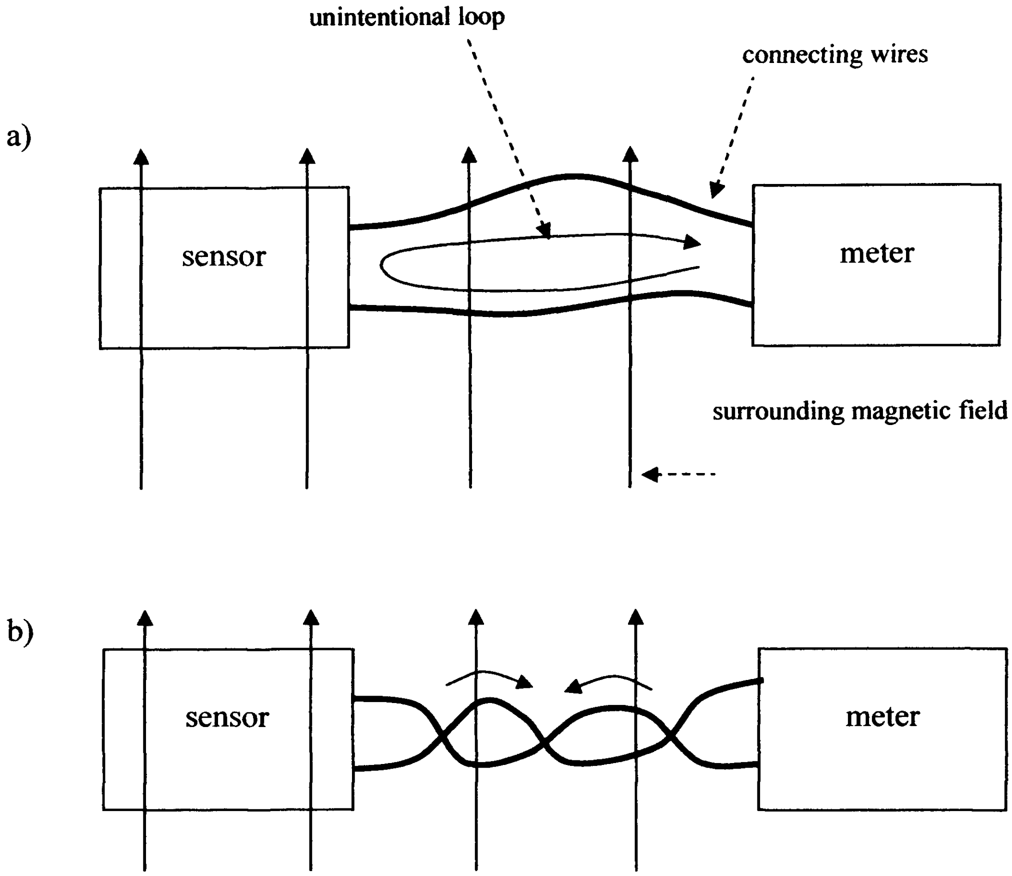

Fig. 5.25. A sensor connected to a meter: a) connecting wires are not twisted and create unintentional loop, b) connecting wires are twisted in order to minimise the influence of the stray magnetic field (the small neighbouring loops cancel each other)

The *B* coils described in **Chapter 4** have been replaced with twisted and short-circuited wires (Fig. 5.26).

Fig. 5.26. Twisted and short-circuited connecting wires (not in scale)

Then, these short-circuited wires were located away from the magnetising setup to ensure that the stray magnetic field penetrating the twisted wires is of negligible magnitude. The *H* coils were placed as usual inside of the magnetising yoke. A controlled magnetising field was generated inside of the yoke

(Fig. 5.27a). The parameters of a B coil (cross-sectional area, thickness of the sample) were set as if there would be an ordinary B coil. Obviously, there should be no voltage detected by the short-circuited wires, and the measured power loss should be equal zero at any magnetic field.

The power loss calculation was attempted from the configuration shown in Fig. 5.27, and the results are presented in Fig. 5.28a. It can be seen that the power loss calculated from the acquired signal is not zero as expected, but it is small value. The *CW* and *ACW* components have similar characteristics. The so-called calculated "power loss" value should be attributed to the ambient noise and interference emanated from the magnetising yoke.

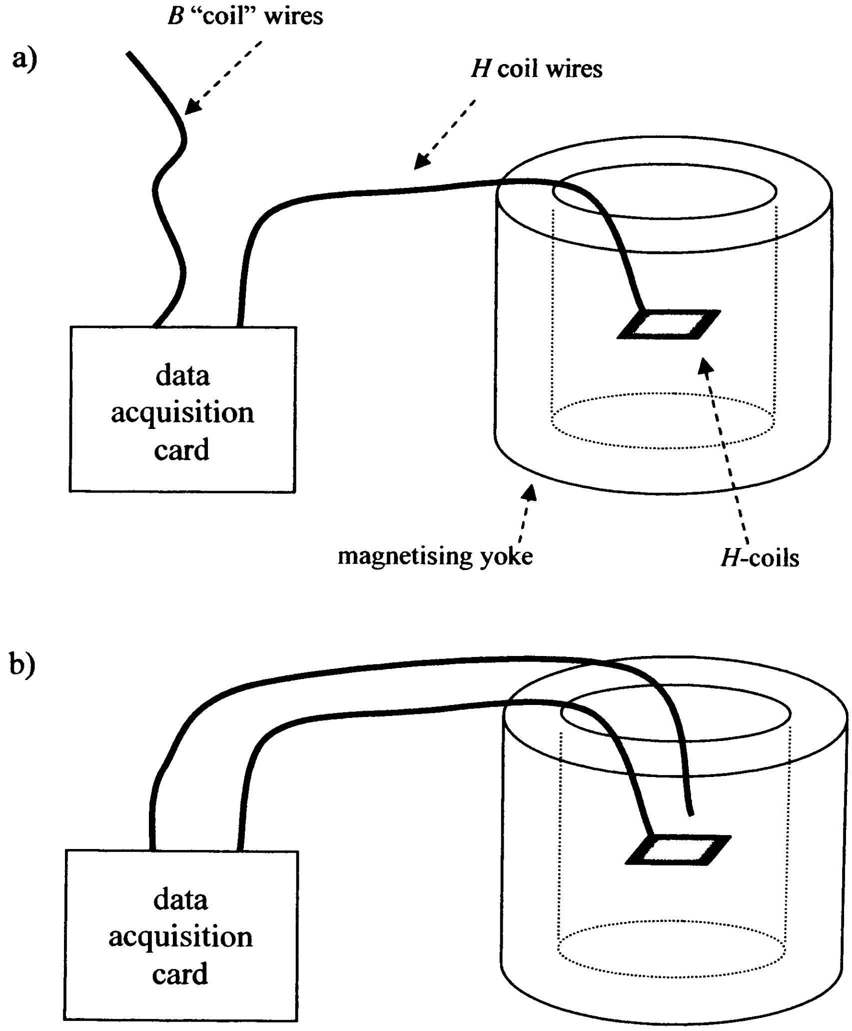

Fig. 5.27. Testing of the twisting of the connecting wires, with: a) wires outside of the magnetising yoke, b) wires inside of the magnetising yoke; (sample not shown for clarity, compare to Fig. 4.36 and 4.37 in section 4.5)

When the twisted and short-circuited wires were inserted into the magnetising yoke (Fig. 5.27b), the calculated "power loss" exhibited completely different behaviour, as it is shown in Fig. 5.28b. The average power loss is still at very low level indicating that the averaging eliminates the difference between *CW* and *ACW* values. The "power losses" calculated for *CW* and *ACW* direction of rotation read high values. However, it has been shown above that the very high or low values of calculated power loss should be attributed only to the angular misalignment of the sensors (Fig. 5.7). In the case of short-circuited wires the angular position could be much larger than a few degrees, thus the calculated values of "power loss" could reach much higher values.

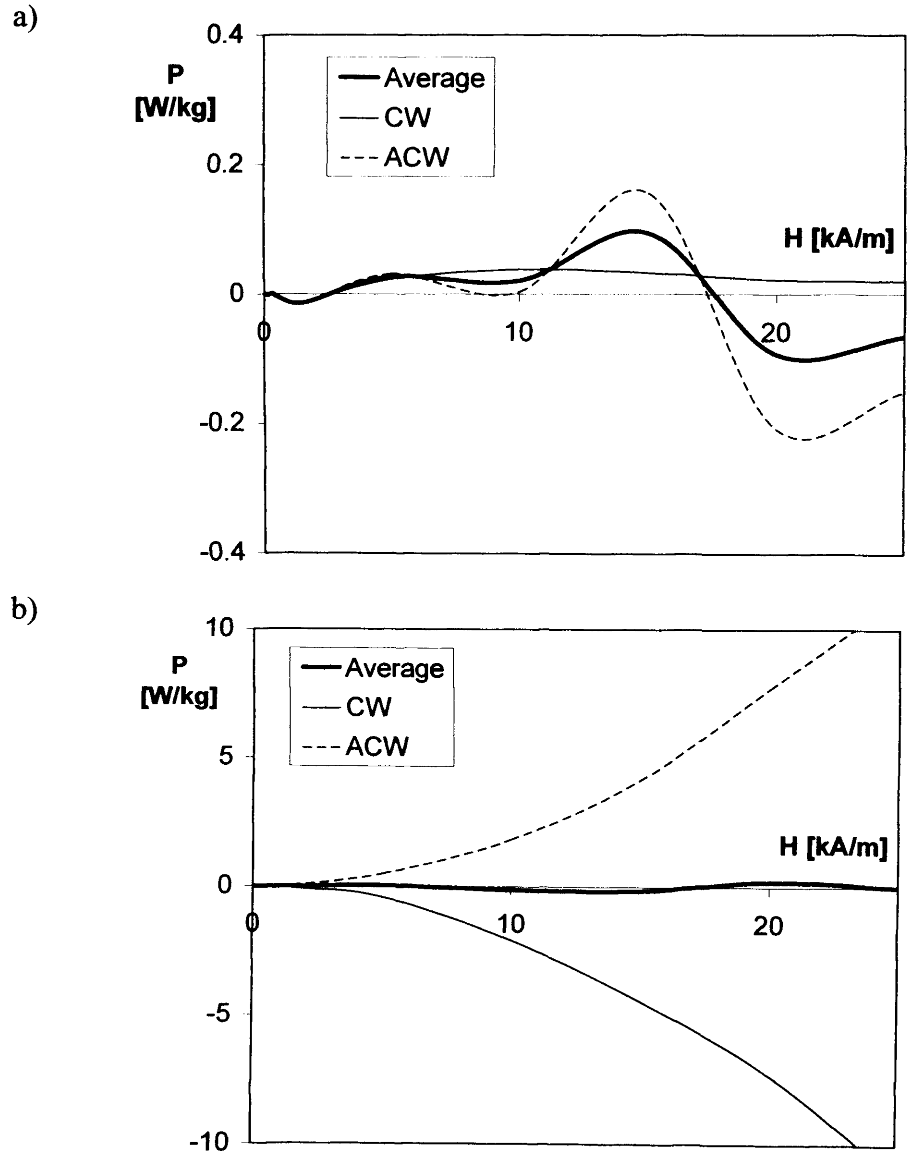

Fig. 5.28. Typical examples of the "power loss" calculated at 50 Hz, for configuration from: a) Fig. 5.27a; b) Fig. 5.27b

The experimentation indicated the values of "power loss" calculated for wires depend very strongly on the positioning of the connecting wires, and also on gradient of the stray field. If the short-circuited wires were physically relocated then the calculated "losses" changed, as expected.

The connecting wires used in this investigation (for the short-circuited wires and for all the samples under test) were 0.1 mm in diameter and were carefully twisted with the aid of small electric motor, ensuring very tight (i.e. small loops) and uniform twisting, which could not be achieved by manual winding.

The experiment was repeated by short-circuited "*B* coils" made from copper wire 0.05 mm in diameter, under previous experimental conditions. The results are shown in Fig. 5.29.

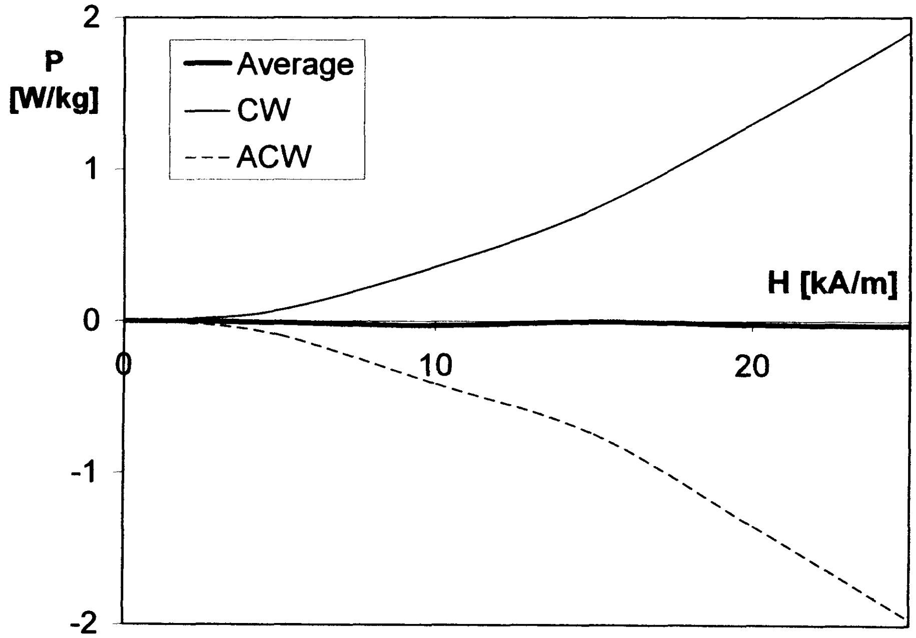

Fig. 5.29. The "power loss" calculated in the configuration from Fig. 5.27 for the 0.05 mm wires

It is clear from the comparison of the results from Fig. 5.28b and Fig. 5.29 that using thinner wires, hence reducing of the areas of the small loops, the unwanted influence of the stray field decreased as expected, but on the other hand, it did not eliminate it completely.

In any of the cases presented in Fig. 5.28b and Fig. 5.29 the averaging from *CW* and *ACW* eliminates the potential influence of the picking up of the stray field. Thus the average power loss measured should not be influenced. However, the *CW* and *ACW* losses might be affected.

The measurement of power loss could not be repeated with the *B* coils made from thinner wire, since the insulation of the wire was damaged very easily by the sharp edges of the samples. The influence of the twisting of the wires should be more carefully studied in future, as it would affect the measurements under alternating magnetising conditions. It is surprising that this effect is not widely described in the literature.

5.3. The difference between power losses measured under controlled *B* and controlled *H* conditions

It has been previously suggested that the measurements of rotational power loss should be made not only under controlled *B*, but also under controlled *H* conditions [*5.5*, *5.16*, *5.17*]. There are many publications showing the results measured under controlled *B*, but very few for the controlled *H*. This might be attributed to the fact that the control of *H* is more difficult to achieve than the control of *B*. The analogue electronic feedback circuits could not ensure proper control at higher level of magnetisation. For that reason the European Intercomparison [*5.18*] has been carried out only up to 1.2 T for grain-oriented electrical steel.

Direct comparison of power loss characteristics for controlled *B* and controlled *H* is impossible, due to the non-linear magnetic properties of the soft magnetic materials. If linear *H* scale is plotted then the graph is not very clear and difficult to interpret (see Fig. 5.30). However, if the *H* scale is logarithmic then the shape of the power loss characteristic somehow resembles the power loss under the controlled *B*, as will be shown below.

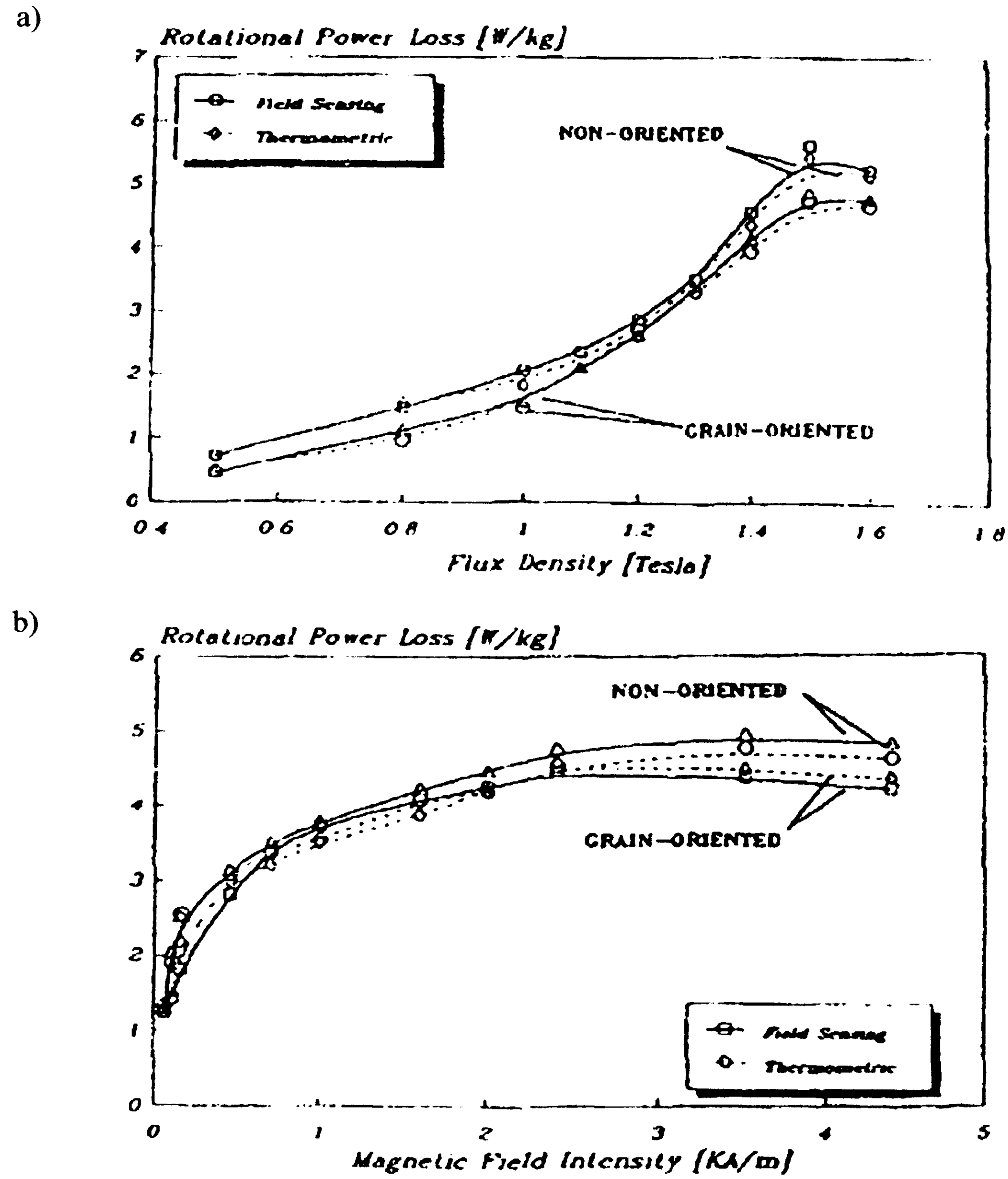

Fig. 5.30. The power loss characteristics under controlled: a) flux density, b) magnetic field [*5.5*]

The comparison of power losses measured under controlled *B* and controlled *H* conditions for non-oriented electrical steel is presented in Fig. 5.31. Let us define the ratio of peak power losses, R_P, as follows (see Fig. 5.31b):

$$R_P = P_{peak\,(H)} \,/\, P_{peak\,(B)} \tag{5.23}$$

where: $P_{peak\,(H)}$ – peak value of power loss under controlled *H*; $P_{peak\,(B)}$ - peak value of power loss under controlled *B*

For the results shown in Fig. 5.31 the R_P is 1.05 and 0.99, for 10 Hz and 50 Hz, respectively. (For 250 Hz the power loss does not exhibit the peak so R_P could not be calculated. The lack of peak is caused by very high eddy current losses, due to the thickness of the sample. This effect will be discussed in detail later.) Therefore, the R_P remains similar for different magnetising frequency, due to the low anisotropy of the sample, as expected. For fully isotropic materials, the R_P should equal unity at any frequency, because the controlled B conditions would be synonymous to controlled H conditions. However, if the material under test is anisotropic, then the R_P might vary with frequency.

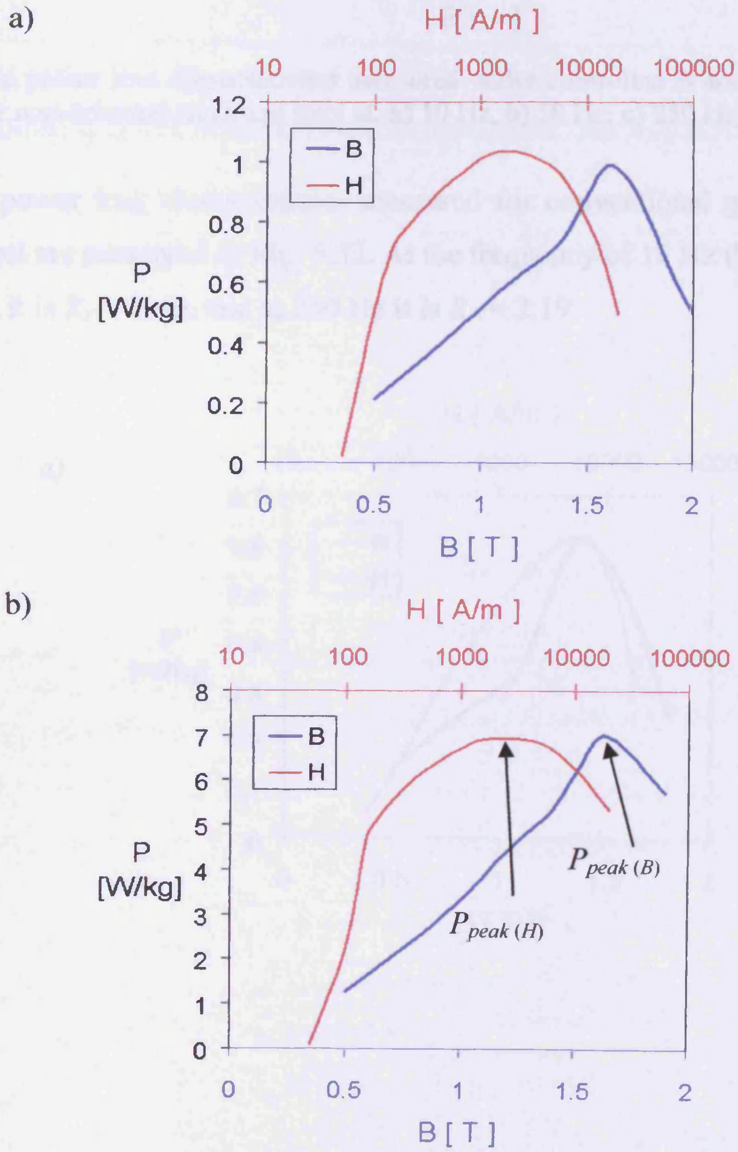

c)

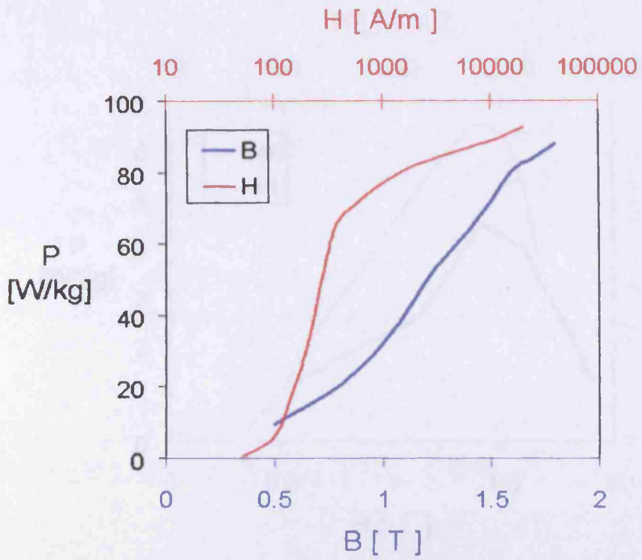

Fig. 5.31. The power loss characteristics measured under controlled *B* and controlled *H* for non-oriented electrical steel at: a) 10 Hz, b) 50 Hz, c) 250 Hz

The power loss characteristics measured for conventional grain-oriented electrical steel are presented in Fig. 5.32. At the frequency of 10 Hz the R_P is 1.00, but at 50 Hz it is $R_P = 1.46$, and at 250 Hz it is $R_P = 2.19$.

a)

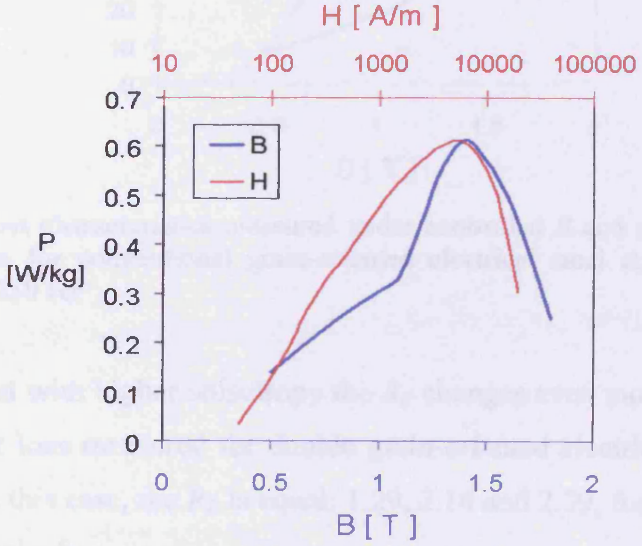

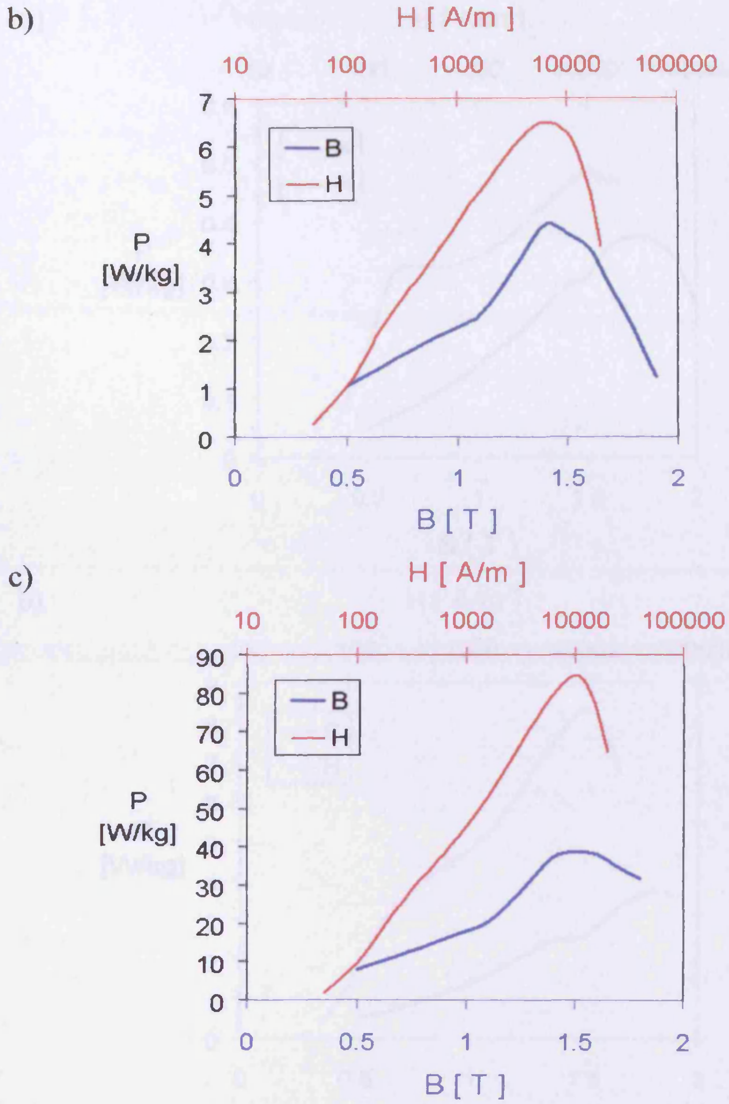

Fig. 5.32. The power loss characteristics measured under controlled *B* and controlled *H* magnetisation for conventional grain-oriented electrical steel at: a) 10 Hz, b) 50 Hz, c) 250 Hz

For the material with higher anisotropy the R_P changes even more with the frequency. The power loss measured for double grain-oriented electrical steel is shown in Fig. 5.33. In this case, the R_P is equal: 1.29, 2.14 and 2.39, for 10 Hz, 50 Hz and 250 Hz, respectively.

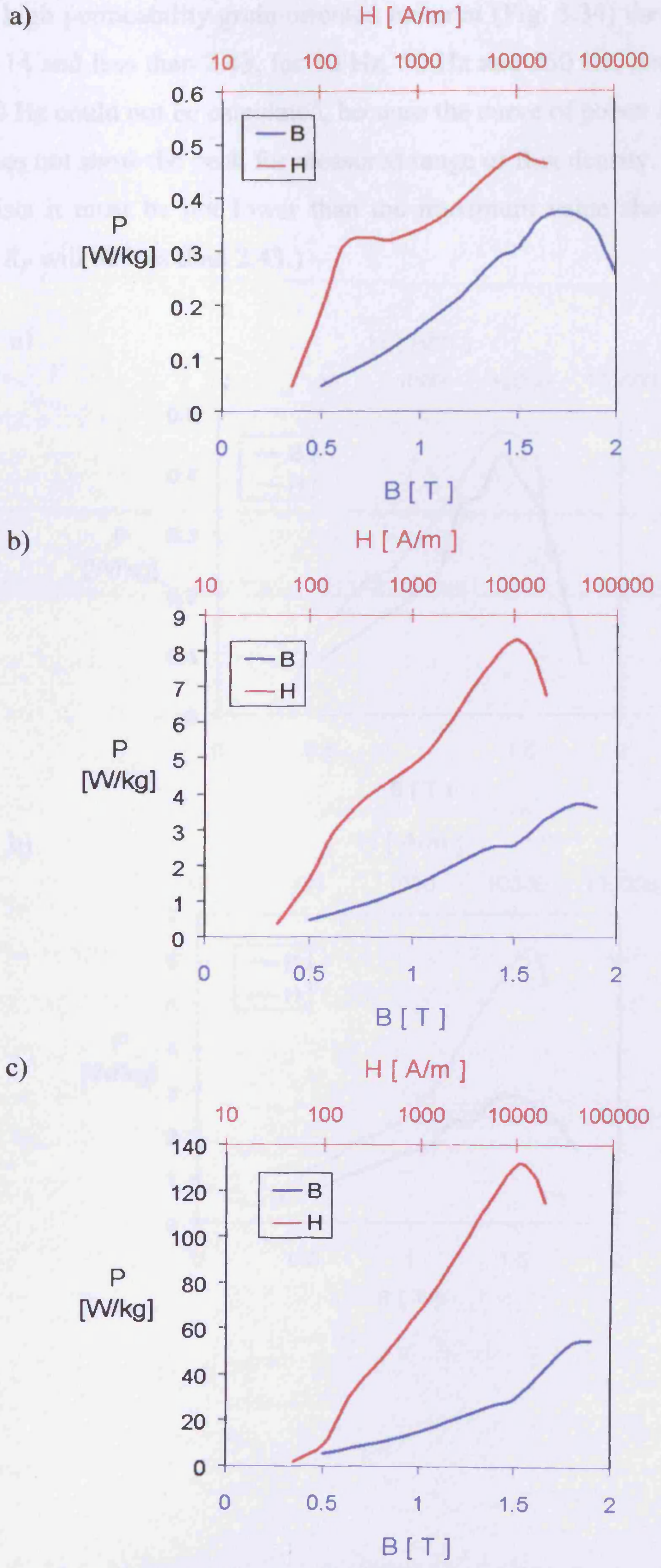

Fig. 5.33. The power loss characteristics measured under controlled *B* and controlled *H* for double grain-oriented electrical steel at: a) 10 Hz, b) 50 Hz, c) 250 Hz

For the high permeability grain oriented material (Fig. 5.34) the values of R_P are: 1.07, 2.14 and less than 2.43, for 10 Hz, 50 Hz and 250 Hz, respectively. (The R_P for 250 Hz could not be calculated, because the curve of power loss under controlled B does not show the peak for measured range of flux density. However, if the peak exists it must be not lower than the maximum value shown in the graph, thus the R_P will be less than 2.43.)

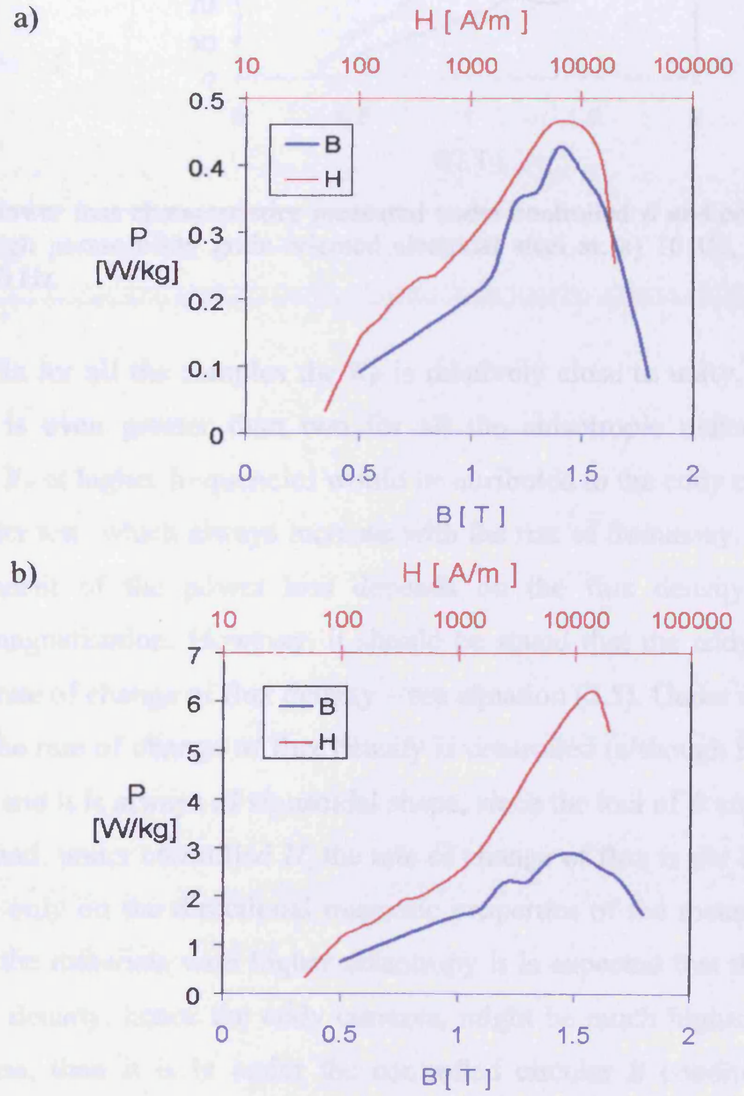

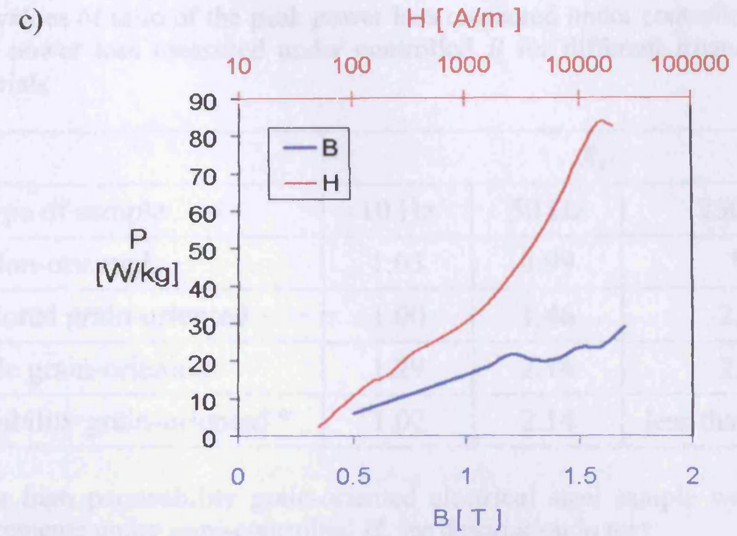

Fig. 5.34. The power loss characteristics measured under controlled B and controlled H for high permeability grain-oriented electrical steel at: a) 10 Hz, b) 50 Hz, c) 250 Hz

At 10 Hz for all the samples the R_P is relatively close to unity, at higher frequencies it is even greater than two for all the anisotropic materials. The increase of the R_P at higher frequencies would be attributed to the eddy currents in the sample under test, which always increase with the rise of frequency. The eddy current component of the power loss depends on the flux density and the frequency of magnetisation. However, it should be stated that the eddy currents depend on the rate of change of flux density – see equation (2.5). Under controlled B conditions, the rate of change of flux density is controlled (although it depends on frequency), and it is always of sinusoidal shape, since the loci of B are circular. On the other hand, under controlled H, the rate of change of flux is not controlled and it depends only on the directional magnetic properties of the material under test. Thus, for the materials with higher anisotropy it is expected that the rate of change of flux density, hence the eddy currents, might be much higher in some intervals of time, than it is in under the controlled circular B conditions. The comparison of the R_P values for all the samples and frequencies is shown in Table 5.1.

Table 5.1. The values of ratio of the peak power loss measured under controlled *H* to the peak power loss measured under controlled *B* for different frequencies and materials

	R_P		
Type of sample	10 Hz	50 Hz	250 Hz
Non-oriented	1.05	0.99	**
Conventional grain-oriented	1.00	1.46	2.19
Double grain-oriented	1.29	2.14	2.39
High-permeability grain-oriented *	1.07	2.14	less than 2.43**

* the values for high permeability grain-oriented electrical steel sample were derived from the measurements under semi-controlled *H*, see description in text
** see description in the text

The comparison of the rate of change of flux, d*B*/d*t*, at 50 Hz and for all the materials is shown in Fig. 5.35. All the curves shown are plotted for the peak of the power loss in the Fig. 5.31-5.36. The d*B*/d*t* for the controlled *B* conditions would be very similar for all the materials, since the peaks of power loss are in the range of 1.4–1.8 T. The shape of all such curves is by definition sinusoidal, thus only one blue line for non-oriented electrical steel is shown for clarity. The peak of d*B*/d*t* reaches a value $0.52 \cdot 10^{-3}$ T/s.

However, the d*B*/d*t* for the controlled *H* conditions differ and they are plotted for each type of sample in Fig. 5.35. The peak values of power loss in Fig. 5.31-Fig. 5.34 fall in a range from 1.5-15 kA/m. The red curve represents the d*B*/d*t* for non-oriented electrical steel. As can be seen from Fig. 5.35 it is quite close to the sinusoidal blue line representing the d*B*/d*t* for controlled *B* conditions, as expected, since the material has low anisotropy. The peak value of d*B*/d*t* is $0.66 \cdot 10^{-3}$ T/s.

The black line represents the d*B*/d*t* for the conventional grain-oriented electrical steel. For this material the d*B*/d*t* has completely different shape and its peak is $3.19 \cdot 10^{-3}$ T/s. The green line for double grain-oriented electrical steel has the maximum of $3.56 \cdot 10^{-3}$ T/s, and the orange curve for high-permeability grain-oriented steel reaches a peak equal to $3.47 \cdot 10^{-3}$ T/s.

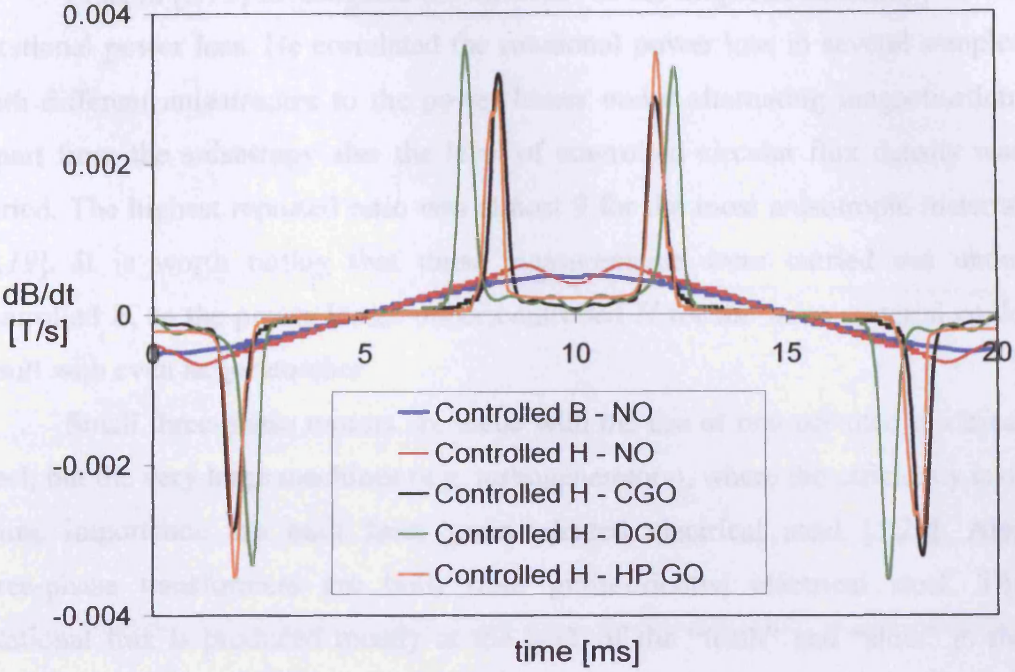

Fig. 5.35. Comparison of rate of change of flux density for different samples at 50 Hz; see detailed description in the text

Although, the peak of d*B*/d*t* under controlled *H* is several times higher than the peak of d*B*/d*t* under controlled *B*, not only the peak value is important, but also the overall shape, which is integrated during the power loss calculation (see equation (2.8)). As it can be seen from Fig. 5.35 the peaks of d*B*/d*t* are at different positions with respect to time, their magnitudes are different, and also their shapes are not the same. All these factors contribute during the power loss and are causing higher power loss as compared to the controlled *B* conditions.

The power loss under circular *B* (controlled) could be as high as 2.5 times of the power losses under standardised alternating magnetising conditions (see Fig. 5.15). The power loss under controlled *H* conditions might reach 2.5 times of the power loss under controlled *B* conditions (see R_P values in Table 5.1). Therefore, the power loss under controlled rotational *H* conditions could be more than six times of the power loss under standardised alternating magnetising conditions widely used in the industry. The measurement under controlled *H* conditions for high permeability grain-oriented electrical steel could not be performed, but it is estimated that the values of R_P given in Table 5.1 could be even higher.

Pluta in [*5.19*] investigated the influence of the magnetic anisotropy on the rotational power loss. He correlated the rotational power loss in several samples with different anisotropies to the power losses under alternating magnetisation. Apart from the anisotropy also the level of controlled circular flux density was varied. The highest reported ratio was almost 9 for the most anisotropic material [*5.19*]. It is worth noting that those measurements were carried out under controlled B, so the power losses under controlled H for the same material could result with even larger number.

Small three-phase motors are made with the use of non-oriented electrical steel, but the very large machines (e.g. turbogenerators), where the efficiency is of prime importance are built from grain-oriented electrical steel [*5.20*]. Also three-phase transformers are built from grain-oriented electrical steel. The rotational flux is produced mostly at the back of the "teeth" and "slots" in the magnetic cores of rotating machines (see Fig. 2.7). In the three-phase rotating machines the magnetic field produces elliptical and circular rotation of the flux density vector, therefore the magnetising conditions are closer to the controlled B conditions. However, in the T-joins of the transformers the B loci resemble the lozenge shape (Fig. 2.7), which is similar to those produced under H controlled conditions, as shown in Fig. 5.36. In electrical machines most of the rotational magnetisation has elliptical shape, but in the regions were the magnetisation is circular the power losses generated in the T-joins of the three-phase transformers may reach very high local power losses, as discussed above.

Underestimation of such high increase in local power loss, e.g. in the T-joints of three-phase transformers, may lead to overheating of the magnetic material, deterioration of its properties, and in consequence even to the destruction of the whole device.

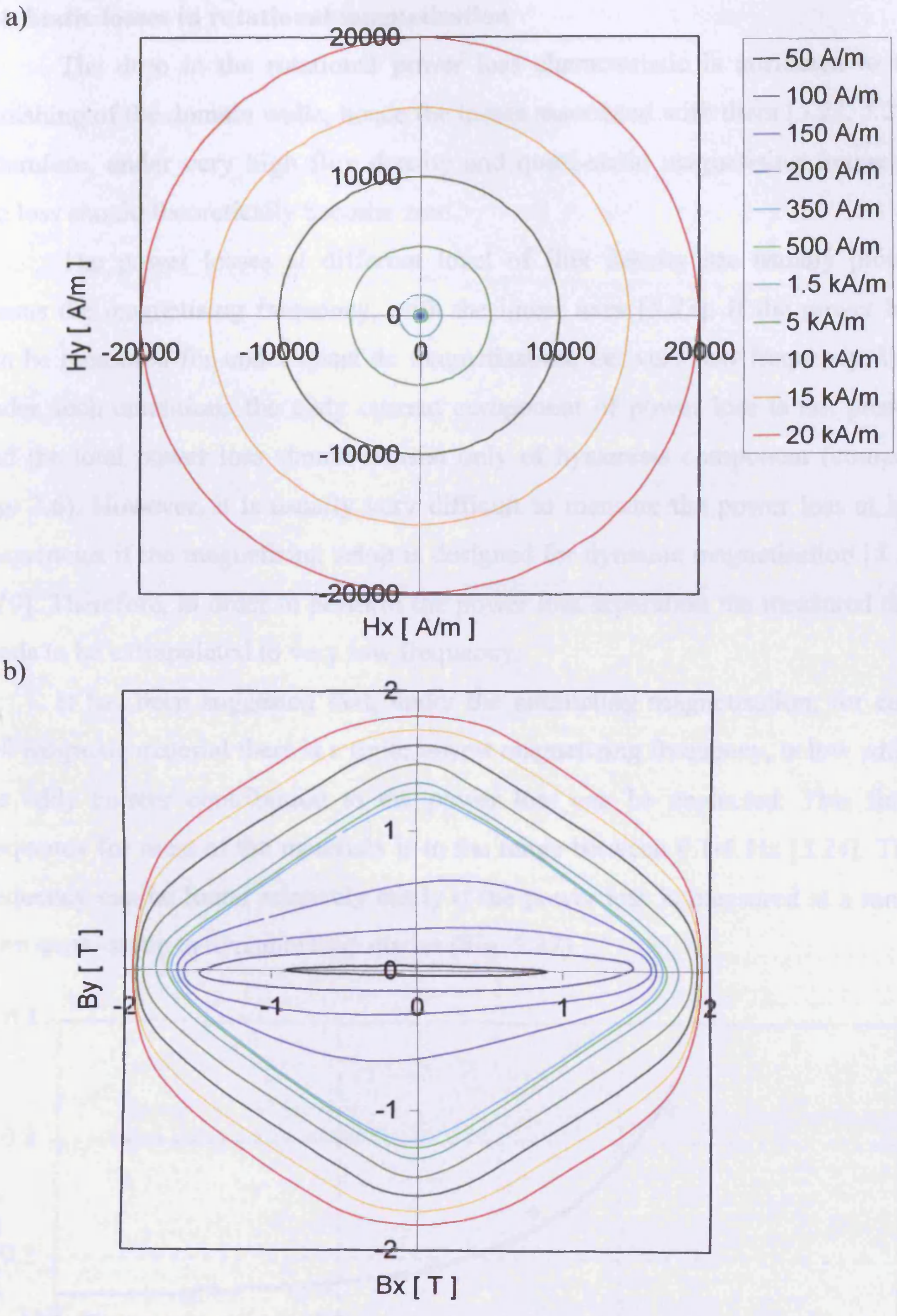

Fig. 5.36. The patterns measured for conventional grain-oriented electrical steel at 50 Hz under controlled *H* conditions: a) *H* loci, b) *B* loci

5.4. Static losses in rotational magnetisation

The drop in the rotational power loss characteristic is attributed to the vanishing of the domain walls, hence the losses associated with them [*5.21*, *5.22*]. Therefore, under very high flux density and quasi-static magnetising frequency the loss should theoretically become zero.

The power losses at different level of flux density are usually plotted versus the magnetising frequency, with the linear axes [*5.23*]. If the power loss can be measured for under quasi dc magnetisation, i.e. very low frequency, then under such conditions the eddy current component of power loss is not present and the total power loss should consist only of hysteresis component (compare Fig. 2.6). However, it is usually very difficult to measure the power loss at low frequencies if the magnetising setup is designed for dynamic magnetisation [*5.18*, *5.19*]. Therefore, in order to perform the power loss separation the measured data needs to be extrapolated to very low frequency.

It has been suggested that, under the alternating magnetisation, for each soft magnetic material there is a finite lowest magnetising frequency, below which the eddy current contribution to the power loss can be neglected. This finite frequency for most of the materials is in the range between 0.1-5 Hz [*5.24*]. This frequency can be found relatively easily if the power loss is measured at a range from quasi-static to dynamic frequencies (Fig. 5.37).

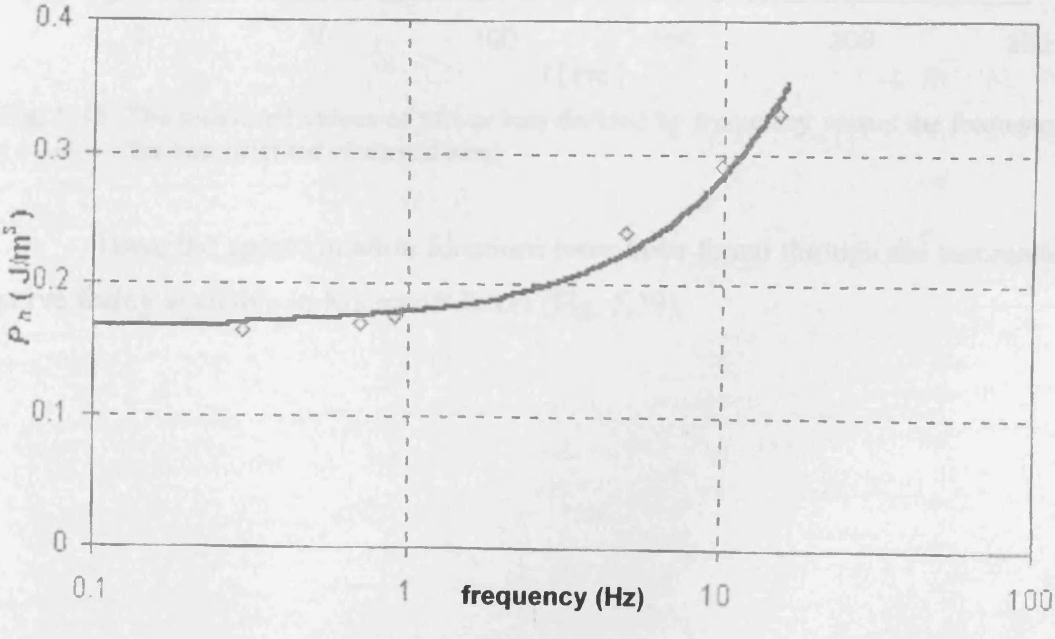

Fig. 5.37. Power loss measured for different magnetising frequencies and the approximating function [*5.24*]

The power loss separation method based on the principle described above has been used frequently in the past and up to date [*5.23*], although it still to be confirmed whether this method gives meaningful results. There are not many examples of power loss separation for the rotational magnetisation in the literature. However, if the method is to be used then the concept should be the same as for the alternating losses.

The sample cut from non-oriented electrical steel has been measured in the frequency range from 2 Hz to 250 Hz. The measured power losses have been divided by the frequency and plotted versus the frequency, as shown in Fig. 5.38.

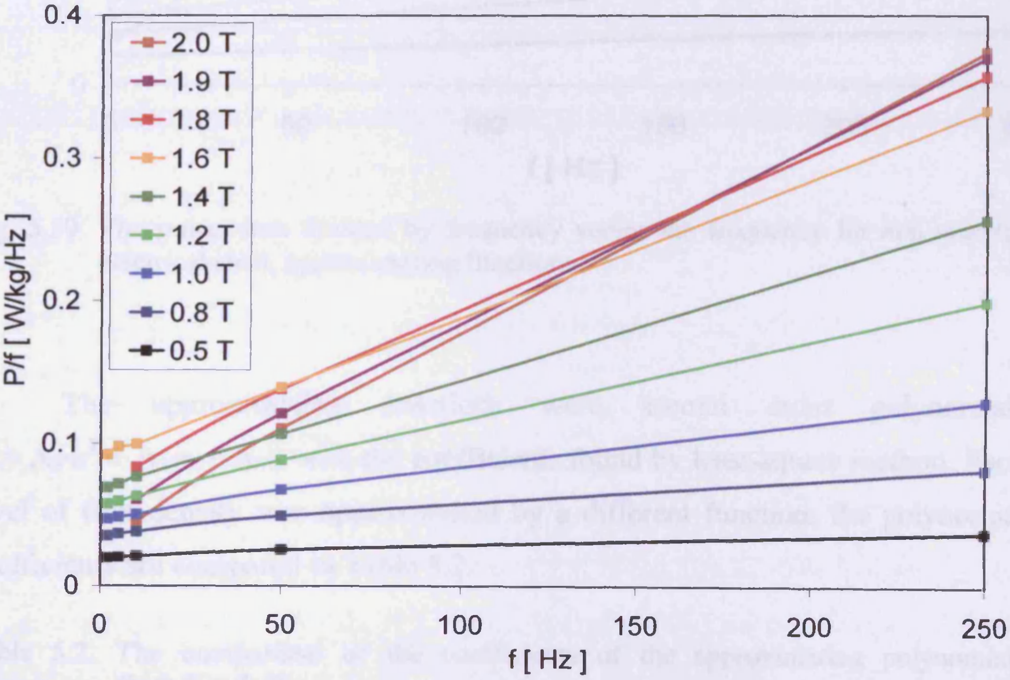

Fig. 5.38. The measured values of power loss divided by frequency versus the frequency for non-oriented electrical steel

Then, the approximation functions have been found through the automatic curve fitting available in Microsoft Excel (Fig. 5.39).

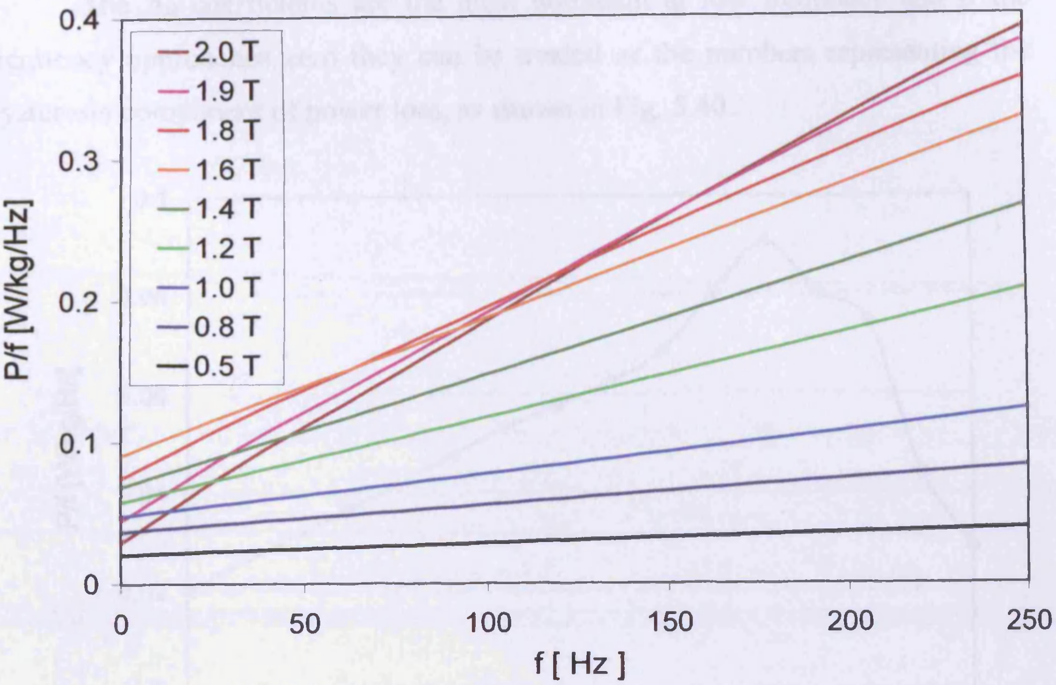

Fig. 5.39. The power loss divided by frequency versus the frequency for non-oriented electrical steel, approximating functions

The approximating functions were second order polynomials ($y = A_2 \cdot x^2 + A_1 \cdot x + A_0$), with the coefficients found by least-square method. Each level of flux density was approximated by a different function; the polynomial coefficients are compared in Table 5.2.

Table 5.2. The comparison of the coefficients of the approximating polynomials from Fig. 5.39

B [T]	A_2	A_1	A_0
0.5	-0.00000006	0.00009	0.0203
0.8	-0.00000006	0.0002	0.0365
1.0	0.000000005	0.0003	0.0477
1.1	0.00000002	0.0004	0.0532
1.2	0.000000001	0.0006	0.0576
1.3	-0.00000004	0.0007	0.0623
1.4	-0.00000004	0.0008	0.0683
1.5	-0.0000001	0.0009	0.0804
1.6	-0.0000002	0.001	0.0904
1.7	-0.0000004	0.0012	0.0805
1.8	-0.0000007	0.0013	0.0743
1.9	-0.000001	0.0016	0.0442
2.0	-0.000001	0.0017	0.0288

The A_0 coefficients are the most dominant at low frequency and if the frequency approaches zero they can be treated as the numbers representing the hysteresis component of power loss, as shown in Fig. 5.40.

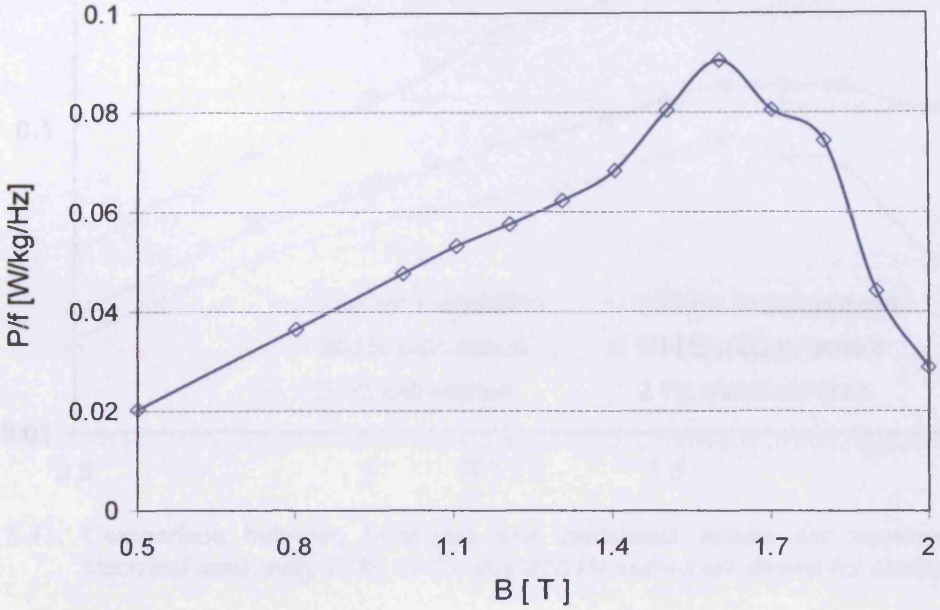

Fig. 5.40. The static hysteresis losses for non-oriented electrical steel

As it can be seen from Fig. 5.40 the hysteresis power loss component decreases after reaching a peak at 1.6 T. Although the sample was magnetised to $B = 2.0$ T, the power loss did not decrease to zero, or even to the vicinity of zero – in fact it is still higher than the losses for 0.5 T. It is assumed that the sample was not saturated, since the air flux was not compensated, and for the magnetic field of 20 kA/m would contribute around 25 mT to the flux detected by the *B* coils. It can be seen from Fig. 5.40 that around 2.0 T the power loss drops very quickly, therefore even small change in flux density would cause large change in the value of power loss. On the other hand, the rate of change of power loss also decreases – therefore it is difficult to predict if the value would reach zero, as was suggested in the Ewing theory [*5.22*].

The agreement between the measured data and the approximation described above is quite good, with the maximum error being below 7.6% at any measured point, but for most of the points being within ±5%. The comparison of the measured and calculated results is shown in Fig. 5.41.

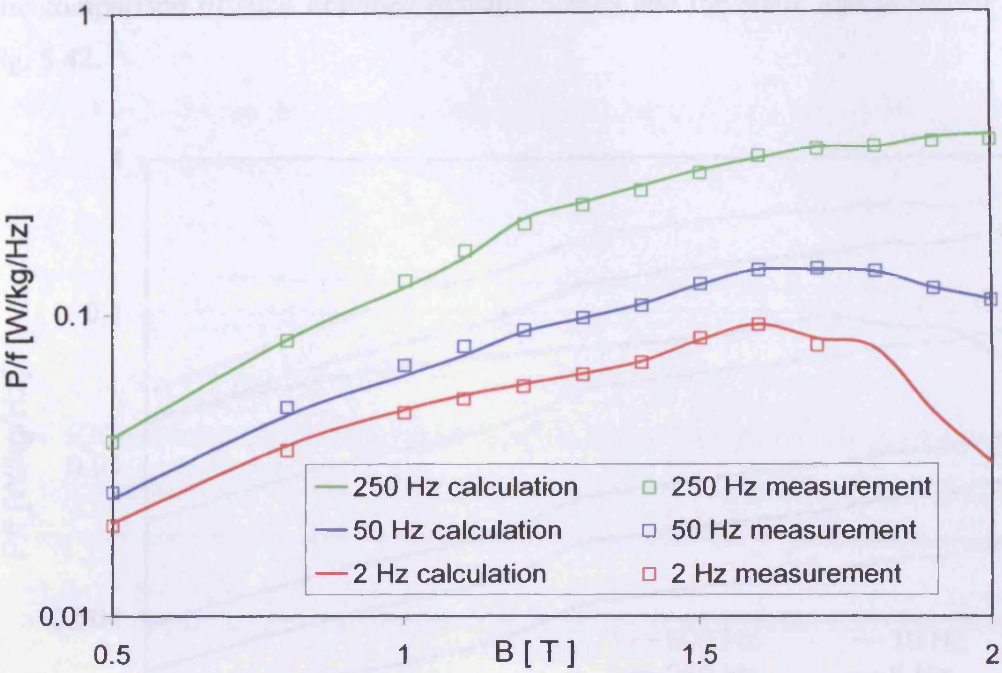

Fig. 5.41. Comparison between measured and calculated results for non-oriented electrical steel; only 2 Hz, 50 Hz and 250 Hz curves are shown for clarity

However, at low frequencies (below 10 Hz) the data was measured only up to 1.7 T, due to limitations of the magnetising system. Thus, the extrapolation functions might be less accurately approximated and the accuracy of the extrapolation could be influenced.

5.5. Dynamic losses in rotational magnetisation

The results shown in Fig. 5.31-5.34 indicate the influence of the frequency on the total power loss. For all the presented measurements the total power loss raised with frequency, as expected. All the results measured at 10 Hz exhibit clear peak in total power loss plotted versus controlled *B* or *H*. However, at 50 Hz the peaks are somewhat less visible, and at 250 Hz they vanish for certain types of electrical steels. This behaviour could be explained on the ground of dynamic power losses generated in the sample, mainly due to the eddy currents.

In order to investigate the increase in the dynamic power loss with the frequency let us subtract the calculated static power loss presented in Fig. 5.40 (the non-oriented electrical steel) from the measured values for all frequencies.

The comparison of such obtained dynamic losses and the static loss is shown in Fig. 5.42.

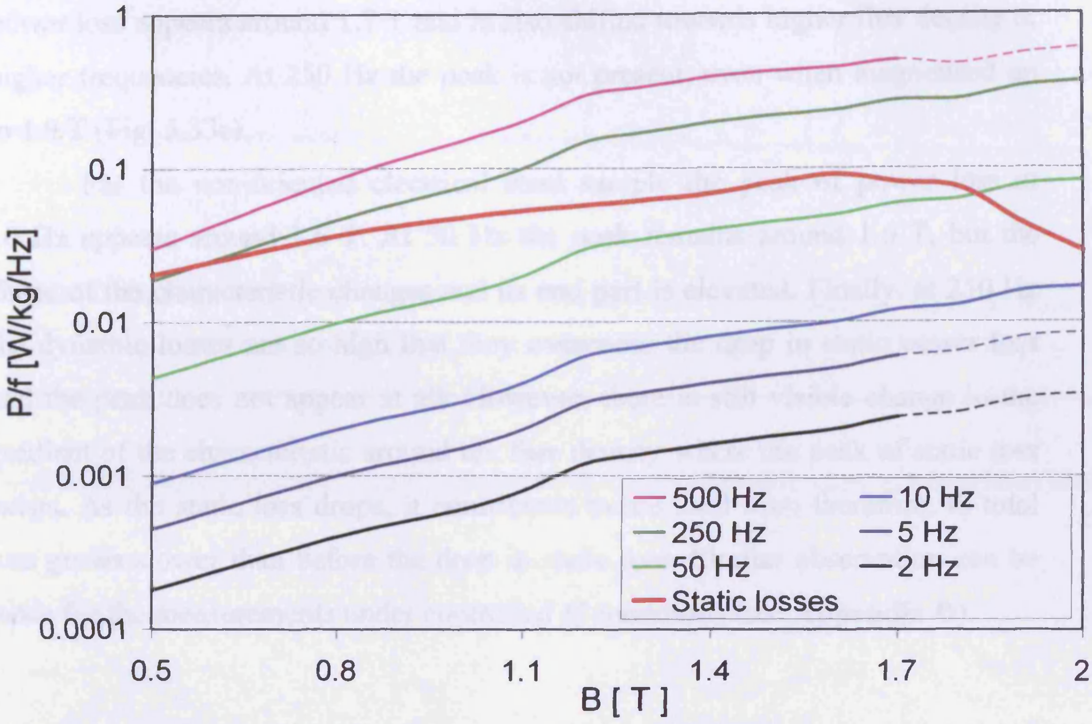

Fig. 5.42. The comparison of static and dynamic power losses for non-oriented electrical steel, the dashed parts of curves correspond to extrapolated values

For the frequencies below 50 Hz the peak value of static loss is higher than the dynamic losses, which grow with the increase of *B*. However, for 250 Hz and 500 Hz the dynamic losses are much greater (note the logarithmic scale on *Y* axis). Therefore, the data in Fig. 5.42 indicate that the power loss should not exhibit a peak. This can also be verified from data obtained on a different sample cut from the same grade of non-oriented electrical steel, since the peak in power loss characteristic does not exist – see Fig. 5.31c.

The non-oriented electrical steel sample had the thickness of 0.50 mm; therefore, the eddy current component was much greater than in other, thinner samples tested in this investigation. The conventional grain-oriented and high permeability grain-oriented electrical steel samples had the thickness of 0.27 mm. The peak value of power loss in both of these materials for the frequency 10 Hz falls around 1.4 T. As the frequency increases, the peak shifts towards 1.5 T and beyond, due to growing contribution of the eddy currents (see Fig. 5.32 and Fig. 5.34). The peak in power loss for the high permeability grain-oriented steel at

250 Hz is not obtained probably due to not sufficient magnetisation of the sample (only 1.7 T).

The double grain-oriented electrical steel is 0.35 mm thick. The peak of power loss appears around 1.7 T and is also shifted towards higher flux density at higher frequencies. At 250 Hz the peak is not present, even when magnetised up to 1.9 T (Fig. 5.33c).

For the non-oriented electrical steel sample the peak of power loss at 10 Hz appears around 1.6 T. At 50 Hz the peak remains around 1.6 T, but the shape of the characteristic changes and its end part is elevated. Finally, at 250 Hz the dynamic losses are so high that they overcome the drop in static power loss and the peak does not appear at all. However, there is still visible change in the gradient of the characteristic around the flux density where the peak of static loss exists. As the static loss drops, it contributes to the total loss; therefore, to total loss grows slower than before the drop in static loss. Similar observation can be made for the measurements under controlled *H* conditions (see **Appendix D**).

5.6. Summary

Power loss measurements in soft magnetic materials under alternating magnetisation are internationally standardised [*5.25-5.27*]. However, even between the standardised methods the discrepancy could be as high as a few percent. Nevertheless, these methods of measurements are widely used in science and industry, because they are by far the most reliable.

The power loss measurements under two-dimensional and rotational excitation are not standardised. One of the problems to be overcome is the design of the magnetising yoke – none of the systems presented in **Chapter 3** has been proved to be superior to the others. Another problem is posed by the method of power loss measurements. The most widely used is the fieldmetric technique, although the thermal method is also employed. The latter one in theory should measure the physical power losses occurring in the material under test since any loss dissipated in the sample would cause the rise of its temperature. However, in case of controlled magnetising conditions the flux density and magnetic field sensors have to be used anyway, thus the magnetising set-up becomes very complex and difficult to use.

The fieldmetric technique its most widely used due to its practicality of use. However, in the simplest case at least four sensors have to be used: two for flux density and two for magnetic field. The accuracy of these sensors directly affects the power loss measurements thus great care should be taken during the production/manufacturing of these sensors. Nevertheless, as it has been proved above, not only the accuracy of the sensors affects the accuracy of the power loss measurement, but also their angular positioning. As it can be seen from the sections above even the sensors made with precise machining may still severely influence the power loss measurements.

It has also been proved that the signal conditioning in the measurement of rotational power loss is very important – much more than in alternating measurements. It has been found that even very small phase shifts (of the order of single minutes) between the measured signals could greatly influence the calculated power loss. If possible a simultaneous-sampling data acquisition card should be used, if not – the interchannel delay should be taken into account and mathematically corrected. Also, use of any electronic circuit (e.g. signal amplifiers) between the sensors and the data acquisition card could influence the power loss measurement, since such electronics could introduce some phase delay in the processed signals.

It has been proved in this investigation that the twisting of the connecting wires is very important and it can be a potential source of problems in power loss measurements. The connecting wires, especially those connecting the sensors, should be always twisted as tightly as possible. It has been found that thinner wires could be twisted more tightly, thus the stray field component could be minimised. However, the twisting is not widely reported in the literature. The full effect of twisting of sensor wires could not be investigated because it was beyond the aims of this investigation.

All these factors combined together make precise measurements of power losses under rotational magnetisation difficult. However, most of the errors can be minimised if the appropriate steps as defined in this investigation are taken into account.

5.6. References to Chapter 5

[*5.1*] Sievert J., Ahlers H., Birkfeld M., Cornut B., Fiorillo F., Hempel K.A., Kochmann T., Kedous-Lebouc A., Meydan T., Moses A.J., Rietto A.M., Intercomparison of measurements of magnetic losses in electrical sheet steel under rotating flux conditions, Report EUR 16225 EN, Commission of the European Communities, Brussels, Luxembourg, 1995

[*5.2*] Alinejad-Beromi Y., Moses A.J., Meydan T., New aspects of rotational field and flux measurement in electrical steel, Journal of Magnetism and Magnetic Materials, Vol 112 (1992), pp. 135-138

[*5.3*] Gorican V., Jesenik M., Hamler A,. Stumberger B., Trlep M., Performance of round rotational single sheet tester (RRSST) at higher flux densities in the case of GO materials, Proceedings of 7th international workshop on 1&2 dimensional magnetic measurement and testing, Ludenscheid, Germany, September 2002

[*5.4*] Salz W., A two-dimensional measuring equipment for electrical steel, IEEE Transactions on Magnetics, Vol. 30, No 3, 1994, pp. 1253-1257

[*5.5*] Gumaidh A.M., Meydan T., Moses A.J., Characterisation of magnetic materials under two-dimensional excitation, Proceedings of IEEE Intermag Conference Digests, Stockholm, Sweden, 1993

[*5.6*] Sievert J., Recent advances in the one- and two-dimensional magnetic measurements technique for electrical sheet steel, IEEE Transactions on Magnetics, Vol. 26, No 5, 1990, pp. 2553-2558

[*5.7*] Sievert J., Studies on the measurement of two-dimensional magnetic phenomena in electrical sheet steel at PTB, Proceedings of 1st international workshop on magnetic properties of electrical sheet steel under two-dimensional excitation, Braunschweig, Germany, April 1992

[*5.8*] Atallah K., Howe D., Calculation of the rotational power loss in electrical steel laminations from measured H and B, IEEE Transaction on Magnetics, Vol. 29, No 6, 1993, pp. 3547-3549

[*5.9*] Salz W., Hempel K.A., Which field sensors are suitable for a rotating flux apparatus?, Proceedings of 1st international workshop on magnetic properties of electrical sheet steel under two-dimensional excitation, Braunschweig, Germany, April 1992

[*5.10*] DAQ PCI-6052E/6053E User Manual, National Instruments, Multifunction I/O Board for PCI/PXI/1394 Bus Computers, 1999

[*5.11*] **Zurek S.**, Meydan T., Precise post-triggering and correction of interchannel delay for alternating and two-dimensional measurements of magnetic properties, Proceedings of 8th international workshop on 1&2-dimensional magnetic measurement and testing, Ghent, Belgium, September, 2004

[*5.12*] DAQ PCI-4451/4452 User Manual, Dynamic Signal Acquisition Device for PCI, National Instruments, 1998

[*5.13*] Zhu J.G., Ramsden V.S., Improved formulations for rotational core losses in rotating electrical machines, IEEE Transactions on Magnetics, Vol. 34, No. 4, 1998, pp. 2234-2242

[*5.14*] Zbroszczyk J., Drabecki J., Wyslocki B., Angular distribution of rotational hysteresis losses in Fe-3.25%Si single crystals with orientations (001) and (011), IEEE Transactions on Magnetics, Vol. Mag-17, No. 3, 1981, pp. 1975-1282

[*5.15*] Soinski M., Angular dependencies in Fe-based commercial soft magnetic materials, IEE Proceedings-A, Vol. 139, No. 6, 1992, pp. 273-278

[*5.16*] Hasenzagl A., Weiser B., Pfutzner H., Novel 3-phase excited single sheet tester for rotational magnetization, Journal of Magnetism and Magnetic Materials, 160 (1996), pp. 180-182

[*5.17*] Moses A.J., Meydan T., **Zurek S.**, Potential problems in interpretation of angular variation of B and *H* in electrical steel under rotational magnetisation conditions, Proceedings of 11th International Symposium on Applied Electromagnetics & Mechanics (ISEM), Versailles, France, May 2003

[*5.18*] Sievert J., Ahlers H., Birkfeld M., Cornut B., Fiorillo F., Hempel K.A., Kochmann T., Kedous-Lebouc A., Meydan T., Moses A.J., Rietto A.M., European intercomparison of measurements of rotational power loss in electrical sheet steel, Journal of Magnetism and Magnetic Materials, Vol. 160, 1996, pp. 115-118

[*5.19*] Pluta W., Wplyw anizotropii magnetycznej blach elektrotechnicznych na straty mocy przy przemagnesowaniu obrotowym, (*The influence of magnetic anisotropy of electrical steel sheets on the power loss under rotational magnetisation*, in Polish), PhD thesis, Technical University of Lodz, Poland, 2001

[*5.20*] Beckley P., Electrical Steels, European Electrical Steels, Newport, South Wales, UK, 2000

[*5.21*] Spooner T., Properties and testing of magnetic materials, McGraw-Hill Book Company Inc., London, UK, 1927

[*5.22*] Bozorth R.M., Ferromagnetism, D. Van Nostrand Company, Inc., Princeton, New Jersey, USA, 1951

[*5.23*] Bertotti G., General properties of power losses in soft ferromagnetic materials, IEEE Transactions on Magnetics, Vol. 24, No 1, 1988, pp. 621-630

[*5.24*] Gozdur R., Wyznaczanie quasi-statycznej petli histerezy blach elektrotechnicznych, (*Determining quasi-static hysteresis loop of electrical steel*, in Polish), Przeglad Elektrotechniczny (*Electrotechnical Review*), R. 80, Nr 2/2004, Poland, February, 2004, pp. 147-149

[*5.25*] International Electrotechnical Commission IEC 60404-2 (1996-03), Magnetic materials - Part 2: Methods of measurement of the magnetic properties of electrical steel sheet and strip by means of an Epstein frame

[*5.26*] International Electrotechnical Commission IEC 60404-11 (1999-01), Magnetic materials - Part 11: Method of test for the determination of surface insulation resistance of magnetic sheet and strip

[*5.27*] International Electrotechnical Commission IEC 60404-6 (2003-06), Magnetic materials - Part 6: Methods of measurement of the magnetic properties of magnetically soft metallic and powder materials at frequencies in the range 20 Hz to 200 kHz by the use of ring specimens

Chapter six

Conclusions

1. The theoretical calculations show that if the electrical contacts in the needle probe technique are replaced by capacitive coupling, then it should be possible to measure the localised flux density in a truly non-destructive way. However, this has not been confirmed by the experimentation, as the very high output impedance of the sensor influences the measurement carried out by commonly available oscilloscopes or voltmeters. Further investigation is required if the capacitive method is to be used in the measurements of localised flux density.

2. The novel adaptive iterative feedback algorithm, which has been designed and developed in this investigation, is capable of controlling arbitrary shape of flux density or magnetic field waveforms without any knowledge about the magnetic properties of sample under test or the magnetising setup. The feedback algorithm has been successfully tested in the following magnetising systems: one-phase (single sheet testers, Epstein frame, toroid), two-phase (rotational single sheet testers), three-phase (transformer). The tested range of flux density (depending on the material under test) was up to 95% of saturation and the magnetic field up to 30 kA/m. The frequency varied in the range from 0.5 Hz to 2 kHz.

3. The most important factor affecting the difference between the rotational power losses measured in clockwise and anticlockwise direction of rotation is the angular misalignment of the sensors of flux density and magnetic field.

4. A method for minimising the difference between the rotational power losses measured in clockwise and anticlockwise direction of rotation has been developed, mathematically described and implemented in the software of the measuring system. This method allows finding the unknown angular positioning of the sensors with the accuracy of single minutes (0.02 degrees). The difference can be greatly minimised, but cannot be completely eliminated by means of this method. The remaining

difference is caused by other factors and it is greater for the measurements under controlled *B* conditions and smaller for controlled *H* conditions.

5. If the flux density and magnetic field sensors are angularly displaced, then the averaging from clockwise and anticlockwise rotational power losses causes an additive error in the average power loss. For the angular misalignment of the sensors smaller than ±10 degrees the value of the error does not exceed 1.6%, thus it is much smaller than the overall accuracy of the measuring system. For the angular displacement smaller than ±5 degrees the error is below 0.4% and practically can be neglected, as it is around 20 times smaller than the total inaccuracy of the measuring system.

6. Tight twisting of the connecting wires is important and the experiments show that it may influence the calculated power losses. The averaging from clockwise and anticlockwise rotational power loss greatly minimises this influence yielding the correct value of the total power loss. Thinner twisted connecting wires pick up lower stray field due to smaller loops, thus making the measurement more accurate, as expected.

7. The non-orthogonal sensors may cause different rotational magnetising conditions for clockwise and anticlockwise direction of rotation. The loci of the magnetic field for controlled circular flux density changes up to several hundreds amperes per metre for the non-orthogonality as little as ±1 degrees. However, for such small angular misalignment of the flux density sensors the rotational power loss measured in clockwise and anticlockwise direction of rotation does not differ significantly – this influence could not be quantified because it was lower than the repeatability of the measuring system.

8. The asymmetry in power loss anisotropy measured by means of two-dimensional (alternating) excitation is probably not a genuine magnetic phenomenon, because the measurements carried out by means of magnetometer and the Epstein frame show otherwise. Most likely, the asymmetry in power loss anisotropy is caused by small angular misalignment of the flux density sensors.

9. A method for reducing of the interchannel delay in multichannel data acquisition card equipped with a multiplexer has been developed and implemented. The interchannel delay was a possible source of error in the measurements of rotational power loss. After the correction the interchannel delay was minimised to an undetectable level, thus the accuracy of power loss measurement has been improved.

10. The peak in the characteristics of rotational power loss measured for electrical steels under controlled flux density and controlled magnetic field conditions depends on the anisotropy of the sample: for isotropic materials the peaks are equal, for anisotropic materials the peak losses measured under controlled rotational magnetic field are much higher than the peak losses measured under controlled rotational flux density. The ratio is up to 2.4, which makes the power loss under controlled rotational magnetic field more than six times of those measured under alternating magnetisation under controlled sinusoidal flux density for highly anisotropic materials.

11. The differences in rotational power losses measured in clockwise and anticlockwise direction of rotation are smaller for controlled magnetic field than for controlled flux density conditions. It is suspected that this could be caused by better orthogonality of the magnetic field sensors. However, it should be noted that the controlled rotational magnetising field conditions are closer to those existing in some parts of magnetic cores of real electrical machines. Therefore, more attention should be brought to the measurements under controlled rotational magnetic field as opposed to controlled rotational flux density conditions.

12. The quasi-static rotational power loss does not approach zero even for as high flux density as 2.0 T for non-oriented electrical steel sheet 0.5 mm thick.

13. The dynamic rotational power losses due to eddy currents play an increasing role at higher frequencies causing the vanishing of the peak in the total rotational power loss at the frequency above 50 Hz for non-oriented electrical steel sheet 0.5 mm thick.

Appendix A

Loci of flux density and magnetic field

Four types of electrical steels have been measured under controlled rotational flux density or controlled rotational magnetic field conditions at 10 Hz, 50 Hz and 250 Hz in clockwise and anticlockwise direction of rotation.

The results for non-oriented electrical sheet steel under circular flux density are shown in Figures A-1 to A-3, and under circular magnetic field in Figures A-4 to A-6.

The results for conventional grain-oriented electrical sheet steel under circular flux density are shown in Figures A-7 to A-10, and under circular magnetic field in Figures A-11 to A-12.

The results for double-oriented electrical sheet steel under circular flux density are shown in Figures A-13 to A-15, and under circular magnetic field in Figures A-16 to A-18.

The results for high-permeability grain-oriented electrical sheet steel under circular flux density are shown in Figures A-19 to A-21, and under semi-controlled circular magnetic field in Figures A-22 to A-24.

The control of rotational magnetic field in the magnetising yoke with an air gap is much more difficult than control of flux density. In the case of high-permeability grain-oriented electrical sheet steel it was impossible to apply the control at some levels of magnetic field. Thus, it has been decided to control just the peak values of the magnetic field, whilst the shapes of magnetising currents were set to be sinusoidal.

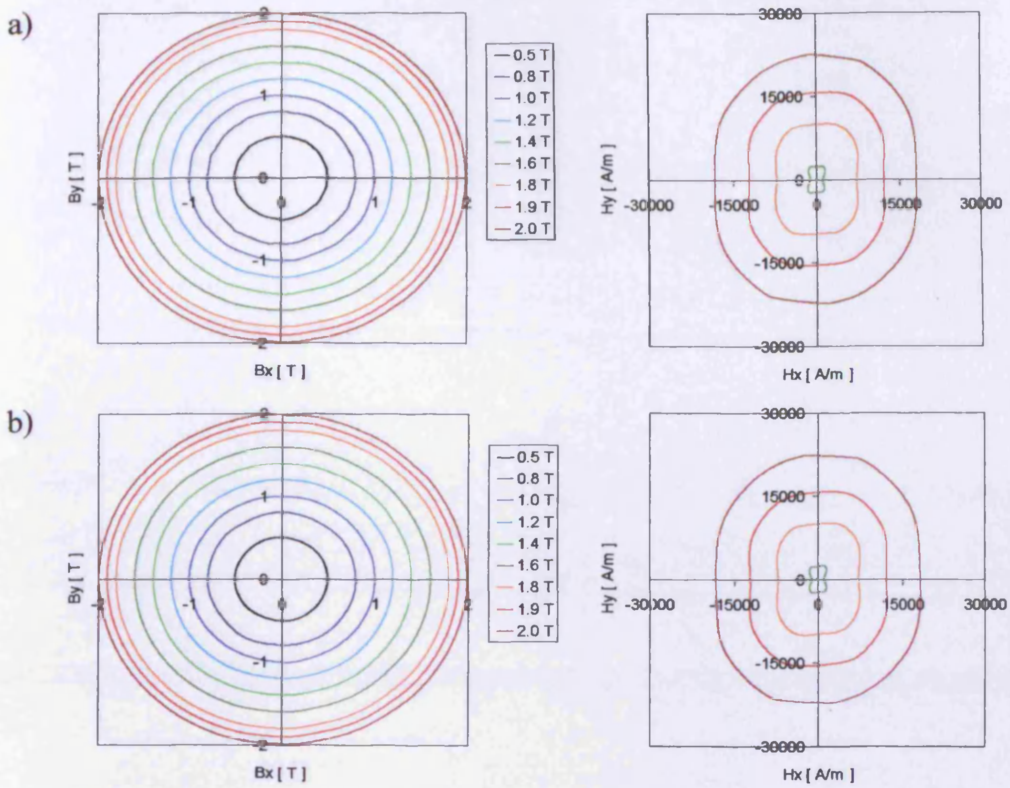

Fig. A-1. The results for non-oriented electrical steel sheet measured under circular flux density at 10 Hz: a) clockwise, b) anticlockwise

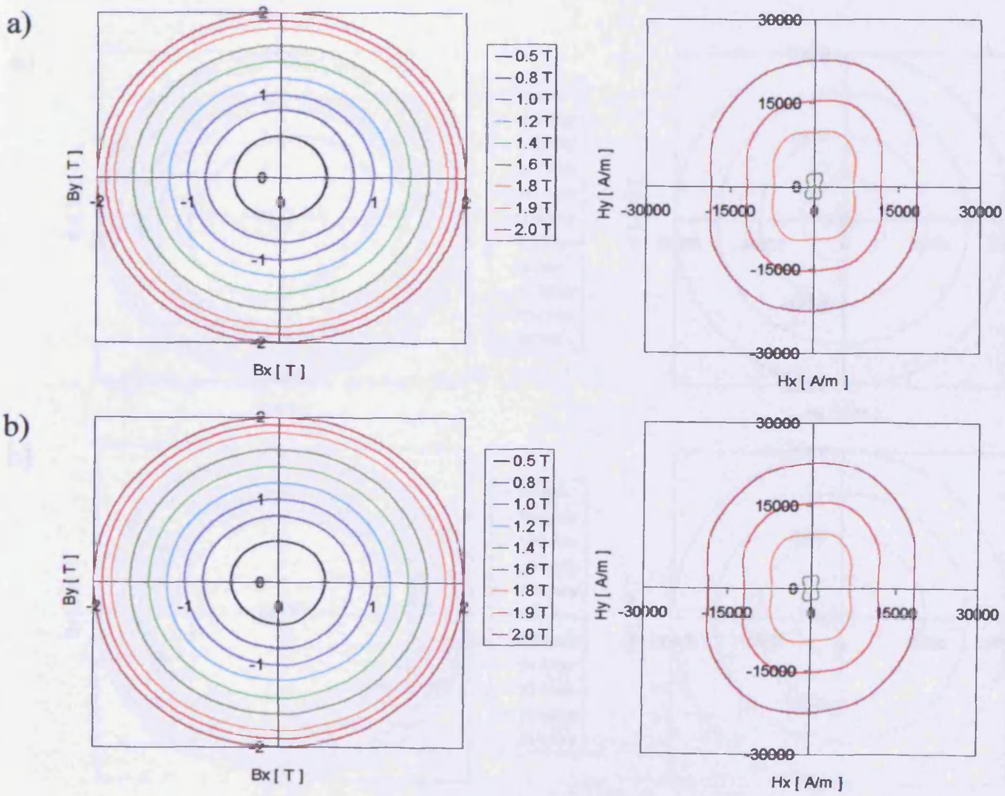

Fig. A-2. The results for non-oriented electrical steel sheet measured under circular flux density at 50 Hz: a) clockwise, b) anticlockwise

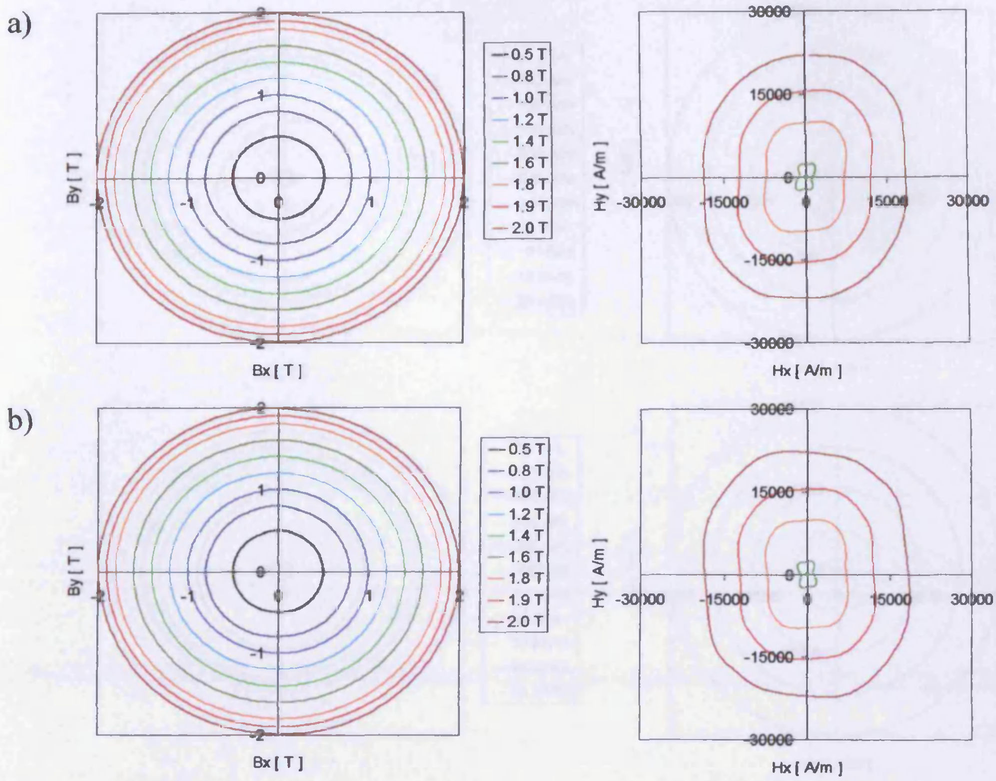

Fig. A-3. The results for non-oriented electrical steel sheet measured under circular flux density at 250 Hz: a) clockwise, b) anticlockwise

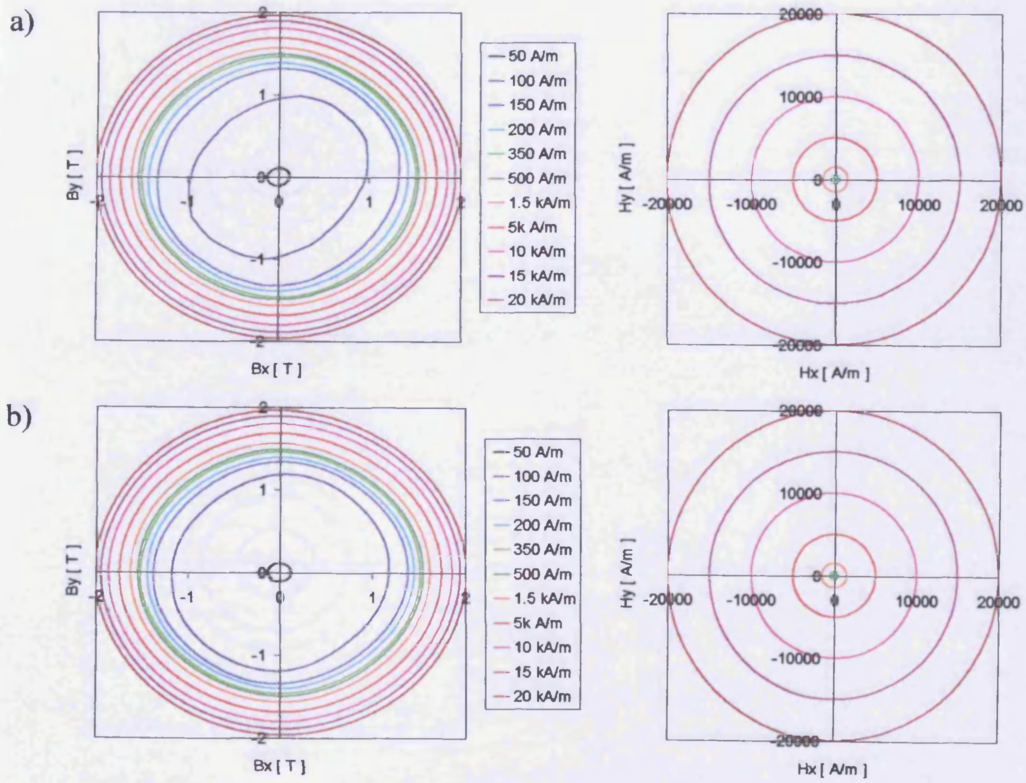

Fig. A-4. The results for non-oriented electrical steel sheet measured under circular magnetic field at 10 Hz: a) clockwise, b) anticlockwise

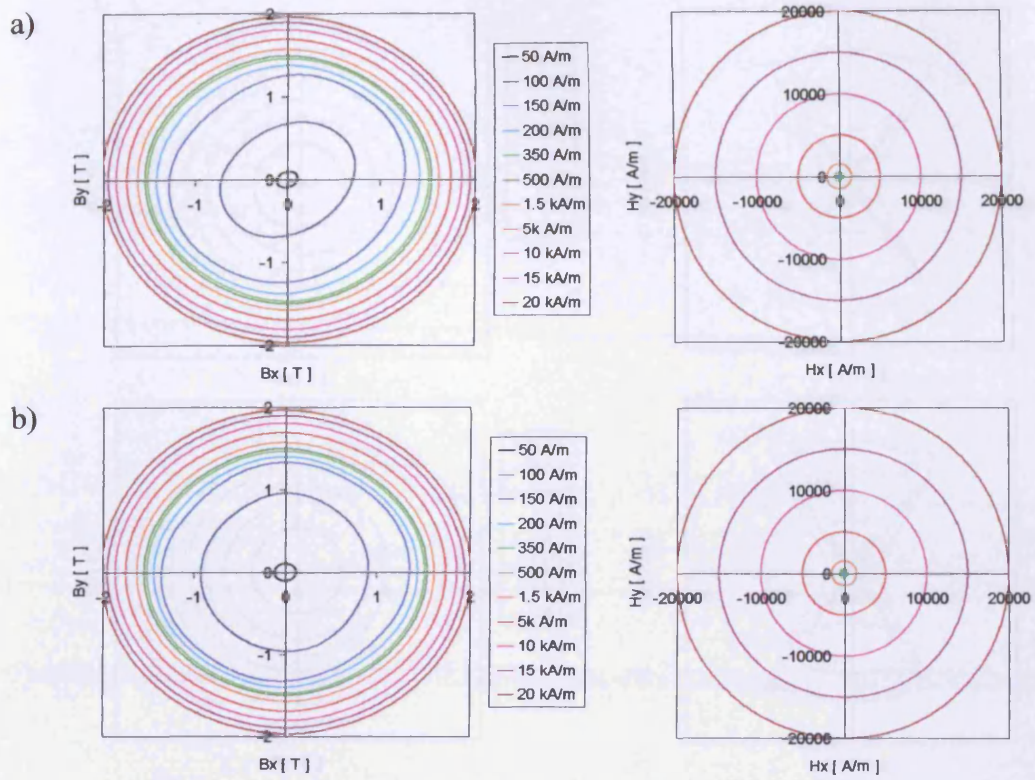

Fig. A-5. The results for non-oriented electrical steel sheet measured under circular magnetic field at 50 Hz: a) clockwise, b) anticlockwise

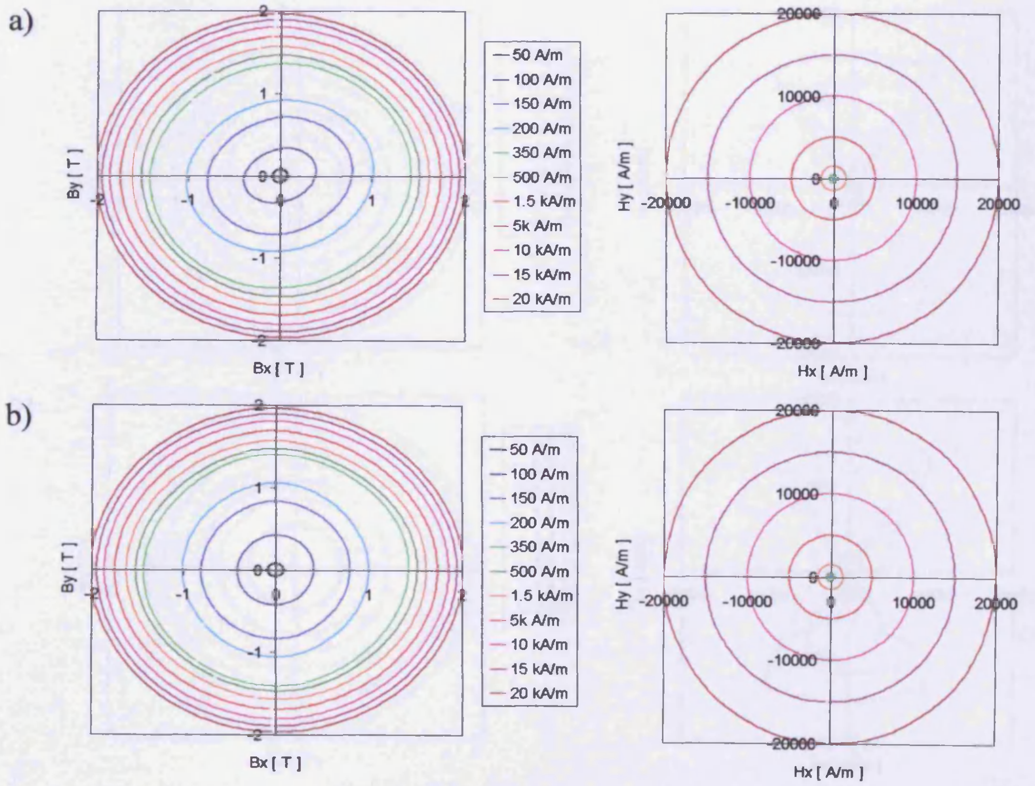

Fig. A-6. The results for non-oriented electrical steel sheet measured under circular magnetic field at 250 Hz: a) clockwise, b) anticlockwise

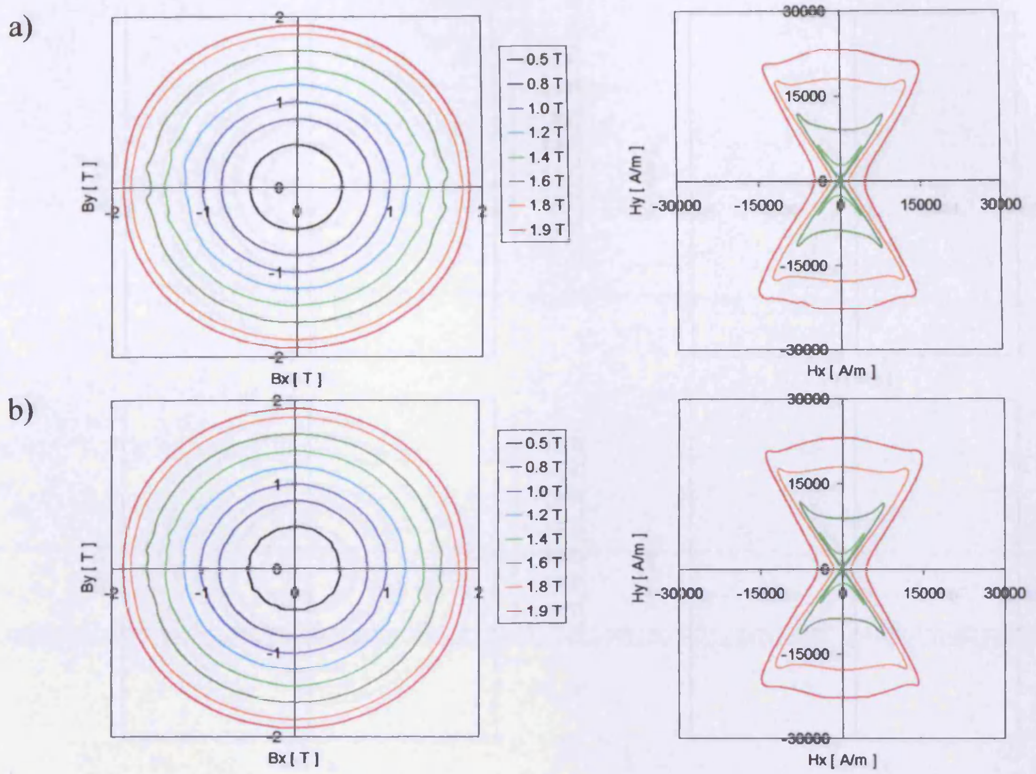

Fig. A-7. The results for conventional grain-oriented electrical steel sheet measured under circular flux density at 10 Hz: a) clockwise, b) anticlockwise

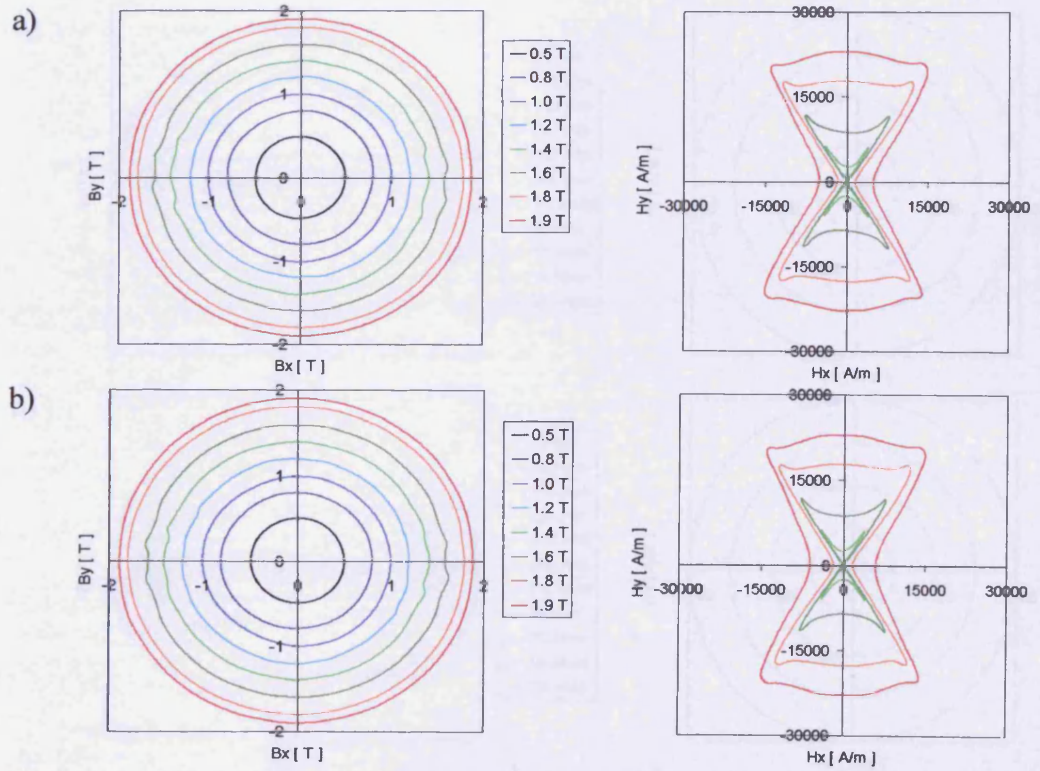

Fig. A-8. The results for conventional grain-oriented electrical steel sheet measured under circular flux density at 50 Hz: a) clockwise, b) anticlockwise

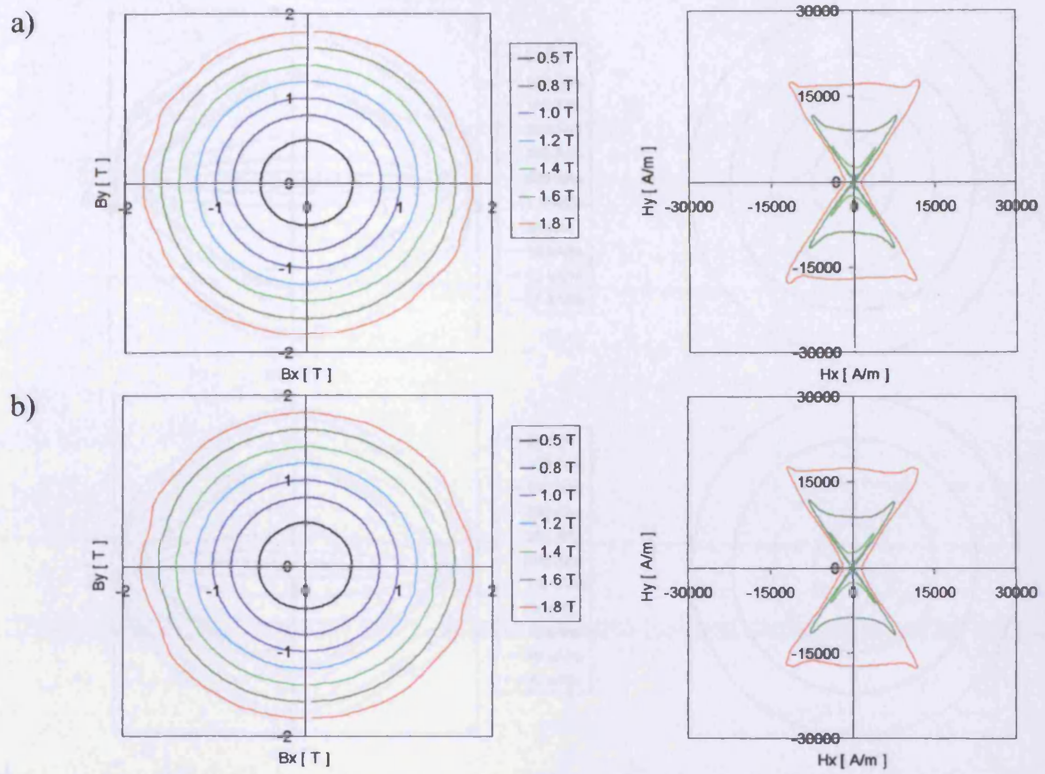

Fig. A-9. The results for conventional grain-oriented electrical steel sheet measured under circular flux density at 250 Hz: a) clockwise, b) anticlockwise

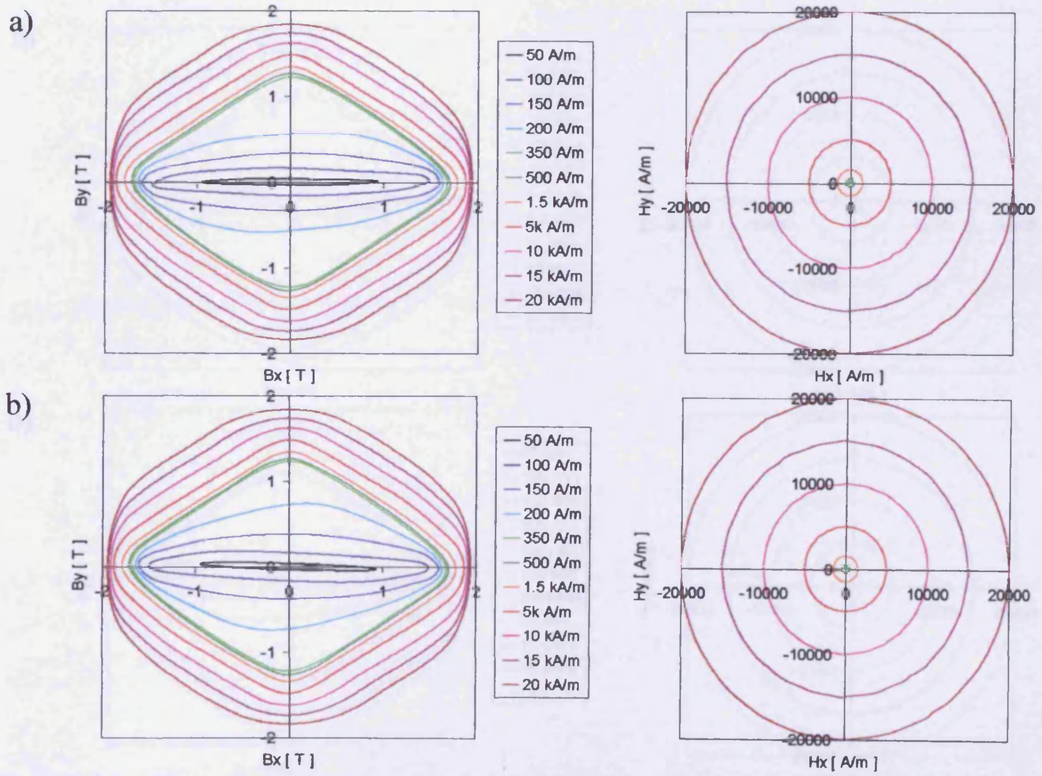

Fig. A-10. The results for conventional grain-oriented electrical steel sheet measured under circular magnetic field at 10 Hz: a) clockwise, b) anticlockwise

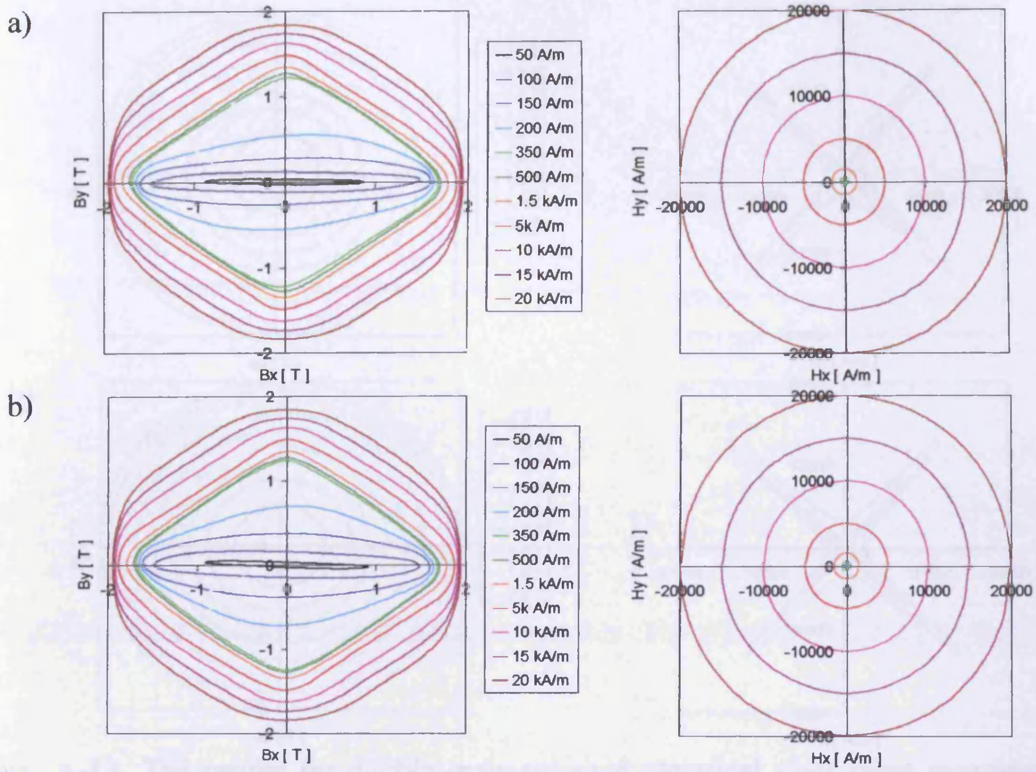

Fig. A-11. The results for conventional grain-oriented electrical steel sheet measured under circular magnetic field at 50 Hz: a) clockwise, b) anticlockwise

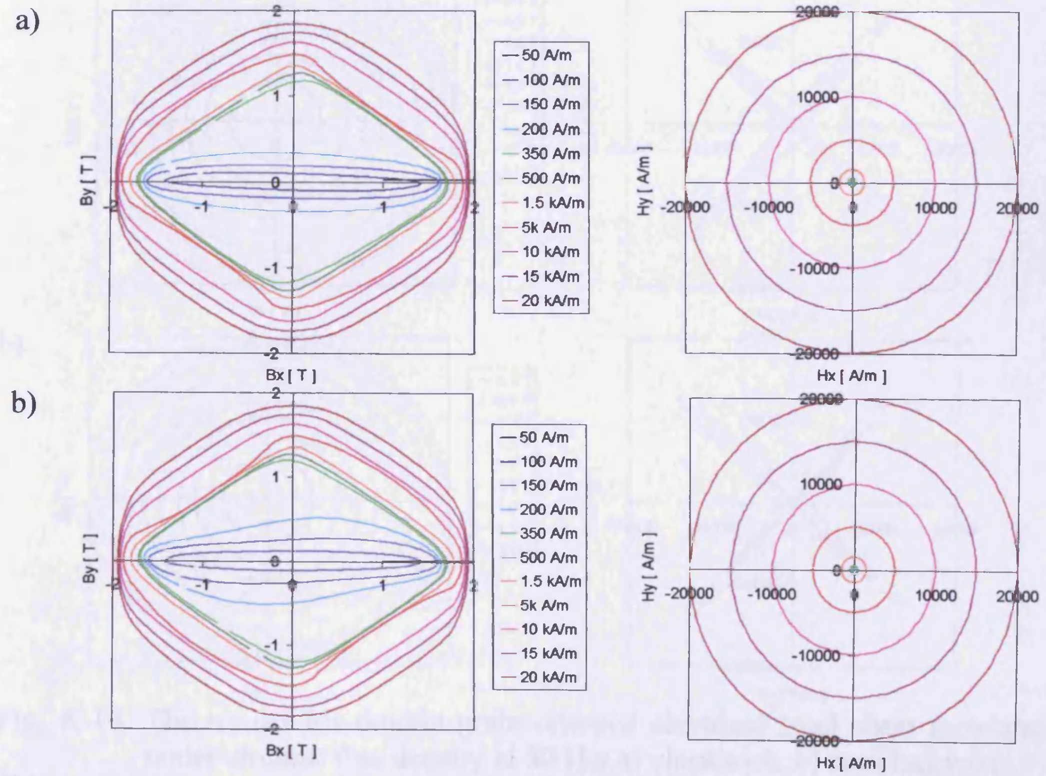

Fig. A-12. The results for conventional grain-oriented electrical steel sheet measured under circular magnetic field at 250 Hz: a) clockwise, b) anticlockwise

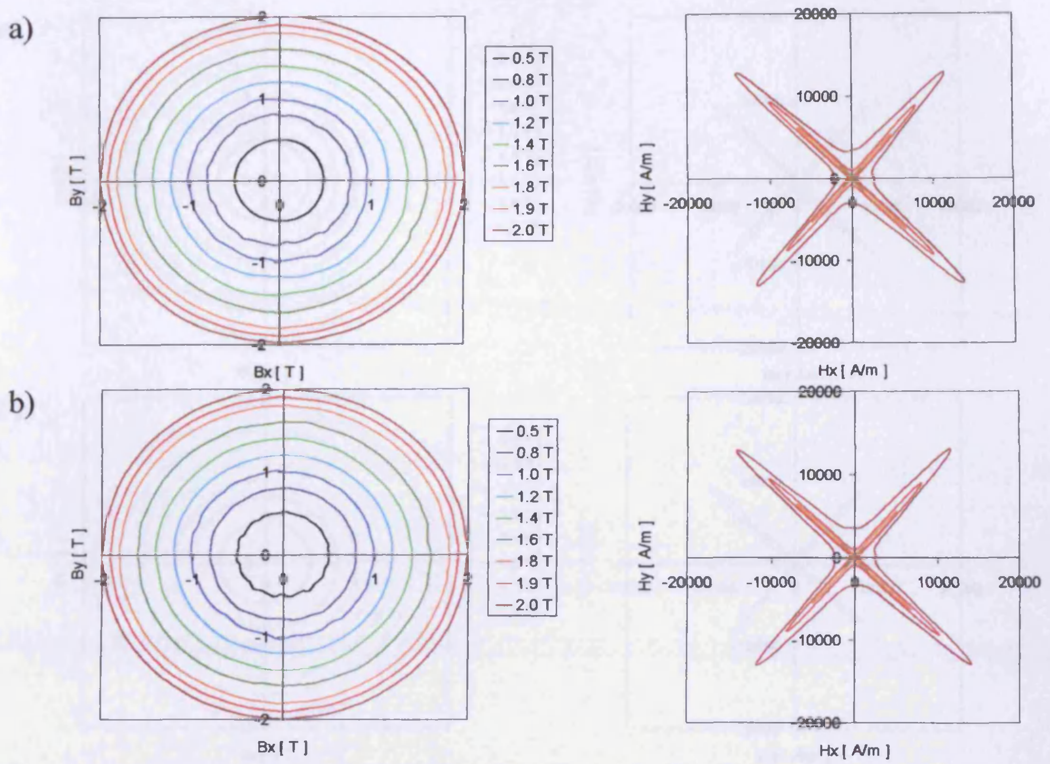

Fig. A-13. The results for double grain-oriented electrical steel sheet measured under circular flux density at 10 Hz: a) clockwise, b) anticlockwise

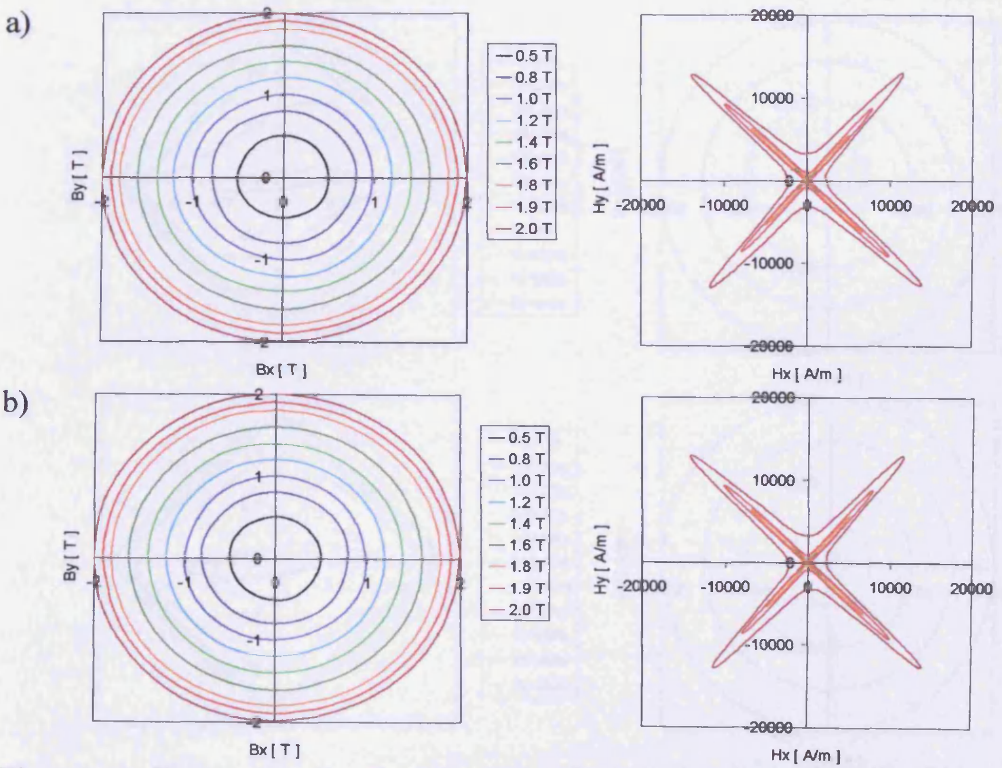

Fig. A-14. The results for double grain-oriented electrical steel sheet measured under circular flux density at 50 Hz: a) clockwise, b) anticlockwise

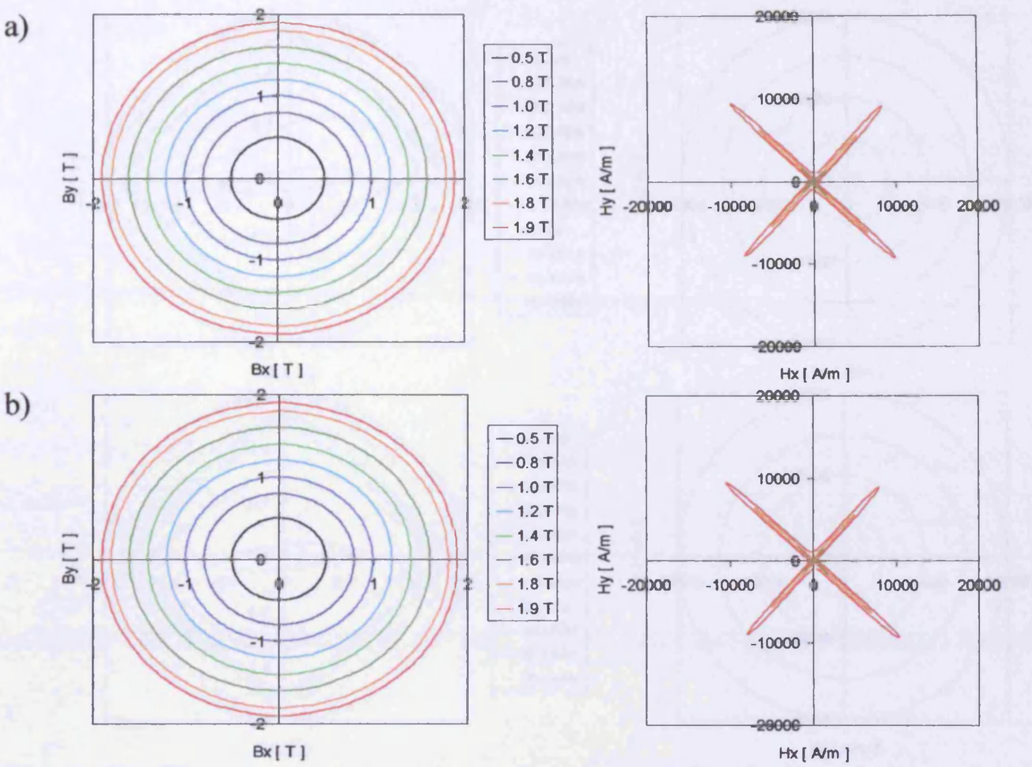

Fig. A-15. The results for double grain-oriented electrical steel sheet measured under circular flux density at 250 Hz: a) clockwise, b) anticlockwise

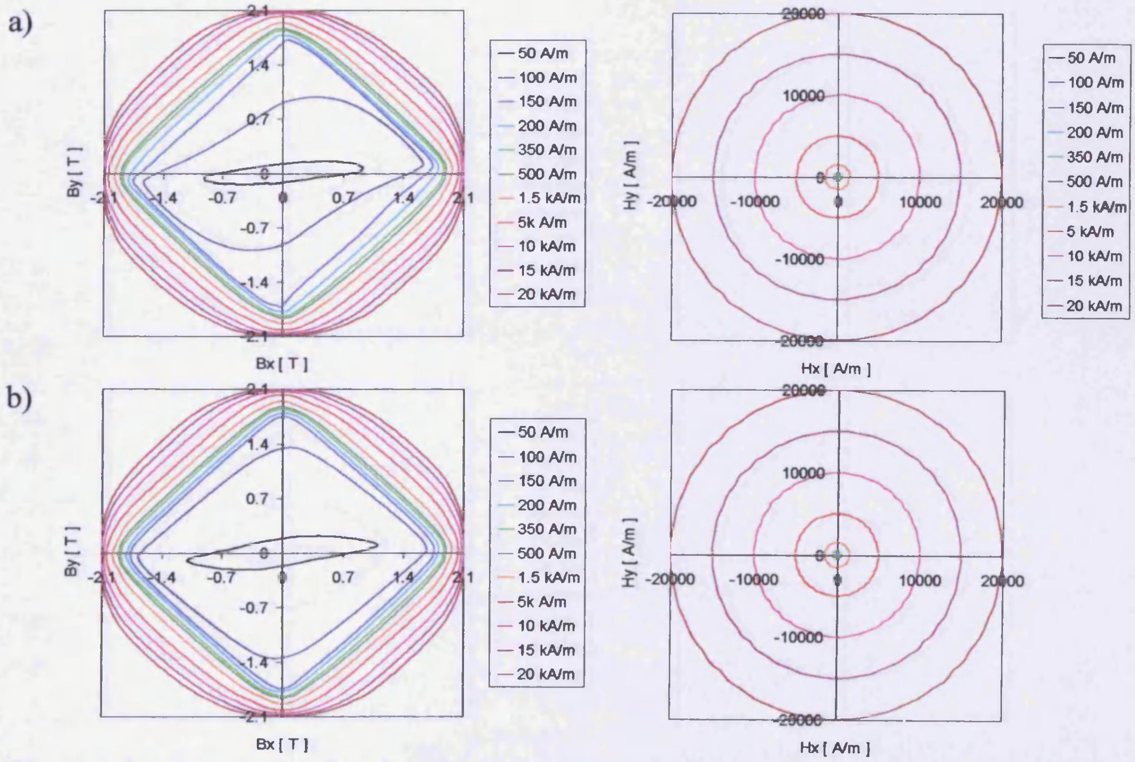

Fig. A-16. The results for double grain-oriented electrical steel sheet measured under circular magnetic field at 10 Hz: a) clockwise, b) anticlockwise

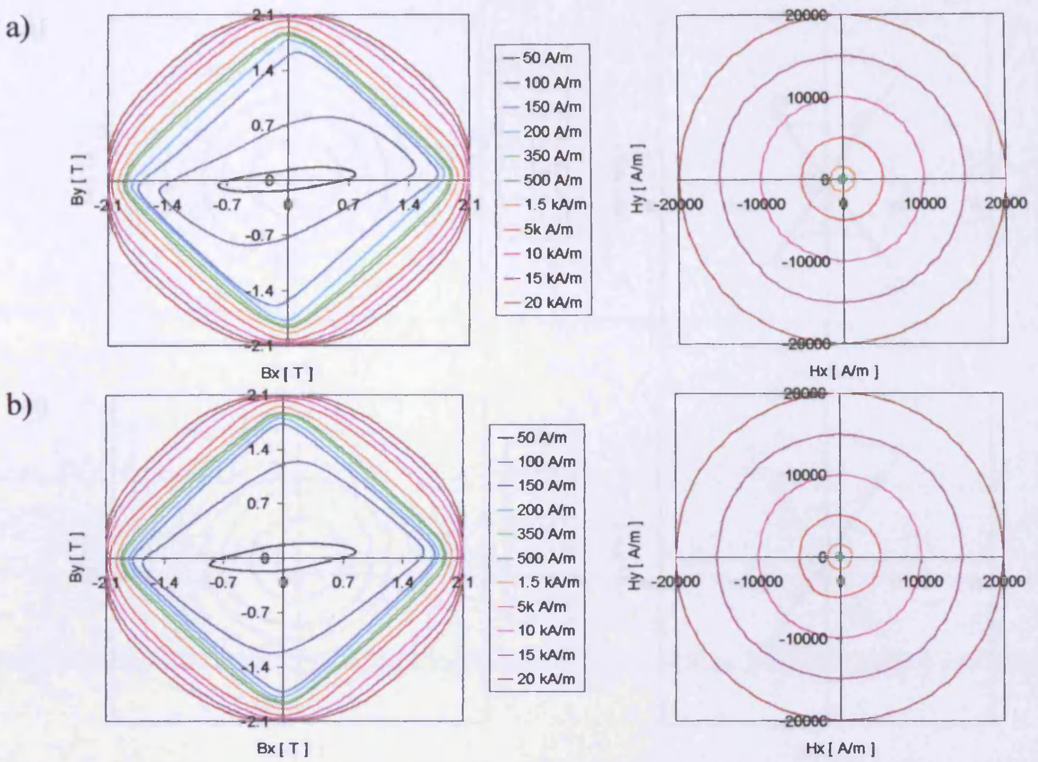

Fig. A-17. The results for double grain-oriented electrical steel sheet measured under circular magnetic field at 50 Hz: a) clockwise, b) anticlockwise

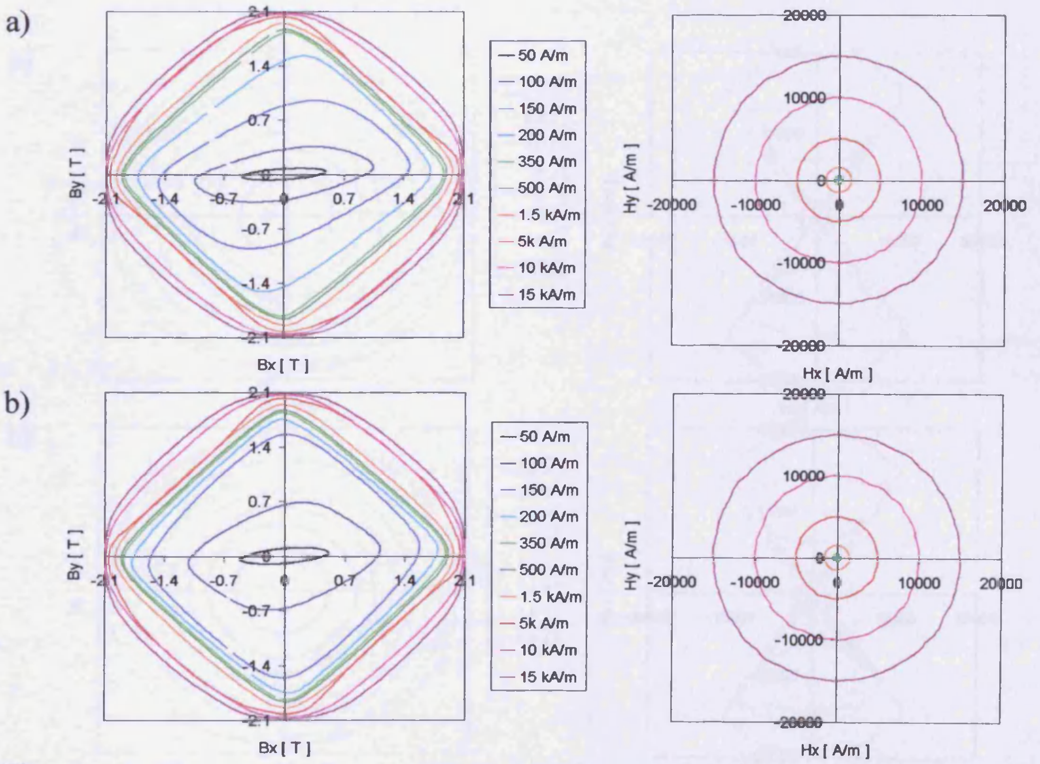

Fig. A-18. The results for double grain-oriented electrical steel sheet measured under circular magnetic field at 250 Hz: a) clockwise, b) anticlockwise

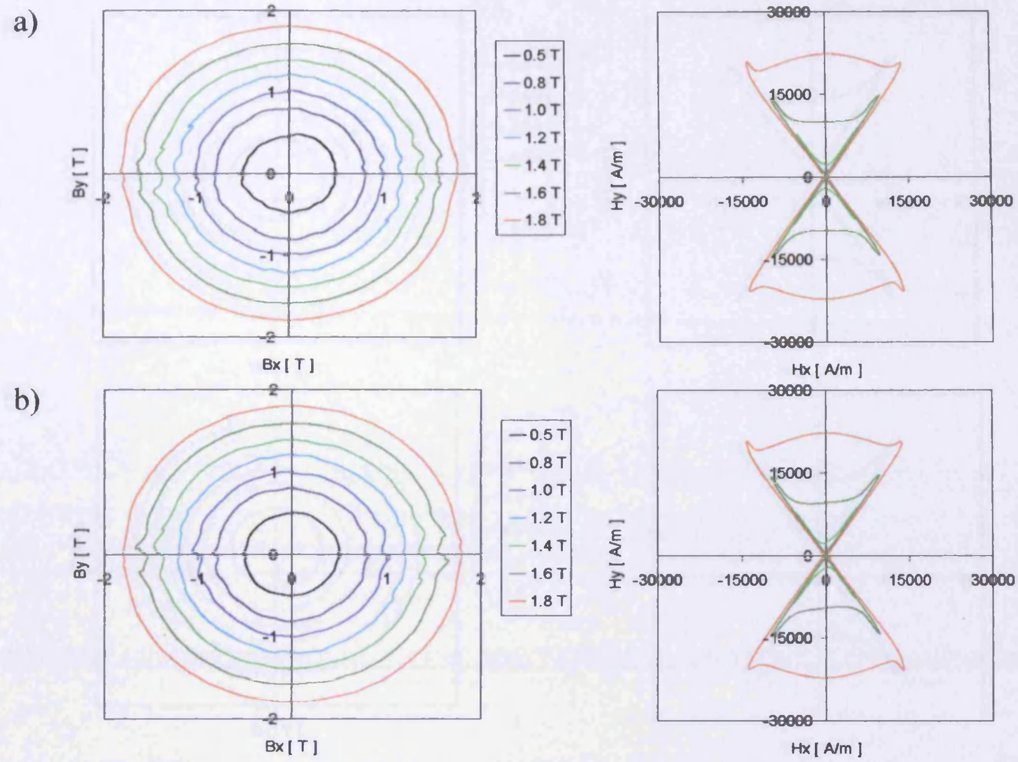

Fig. A-19. The results for high permeability grain-oriented electrical steel sheet measured under circular flux density at 10 Hz: a) clockwise, b) anticlockwise

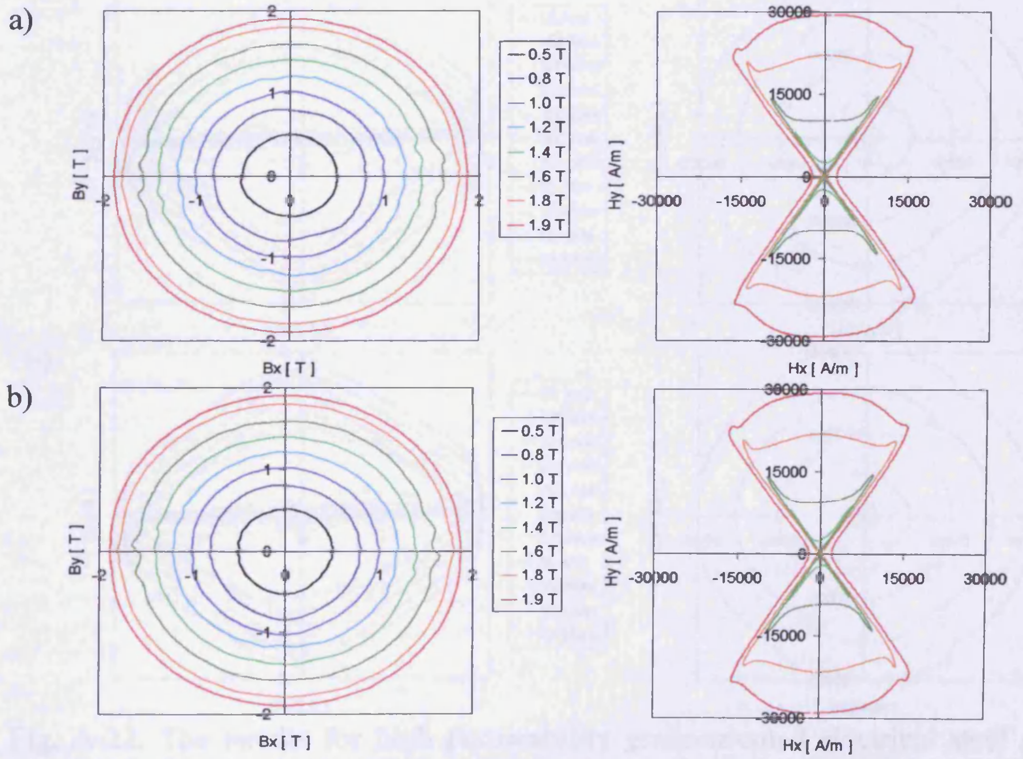

Fig. A-20. The results for high permeability grain-oriented electrical steel sheet measured under circular flux density at 50 Hz: a) clockwise, b) anticlockwise

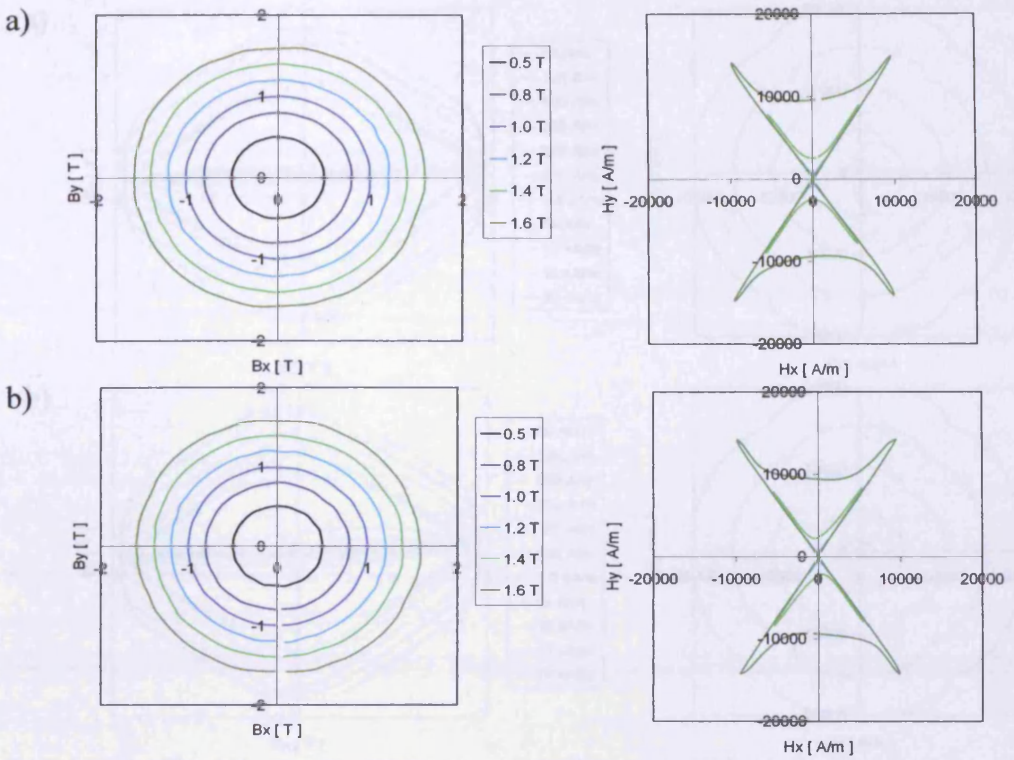

Fig. A-21. The results for high permeability grain-oriented electrical steel sheet measured under circular flux density at 250 Hz: a) clockwise, b) anticlockwise

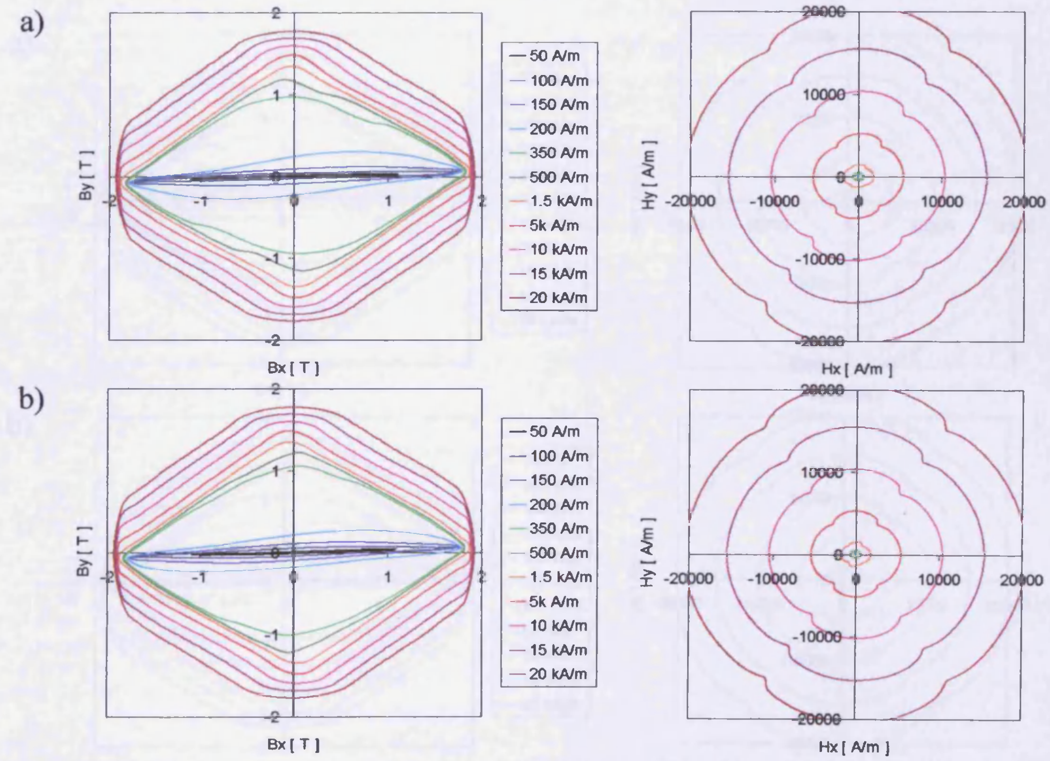

Fig. A-22. The results for high permeability grain-oriented electrical steel sheet measured under pseudo-controlled magnetic field (only the magnetising currents were set to sinusoidal shapes) at 10 Hz: a) clockwise, b) anticlockwise

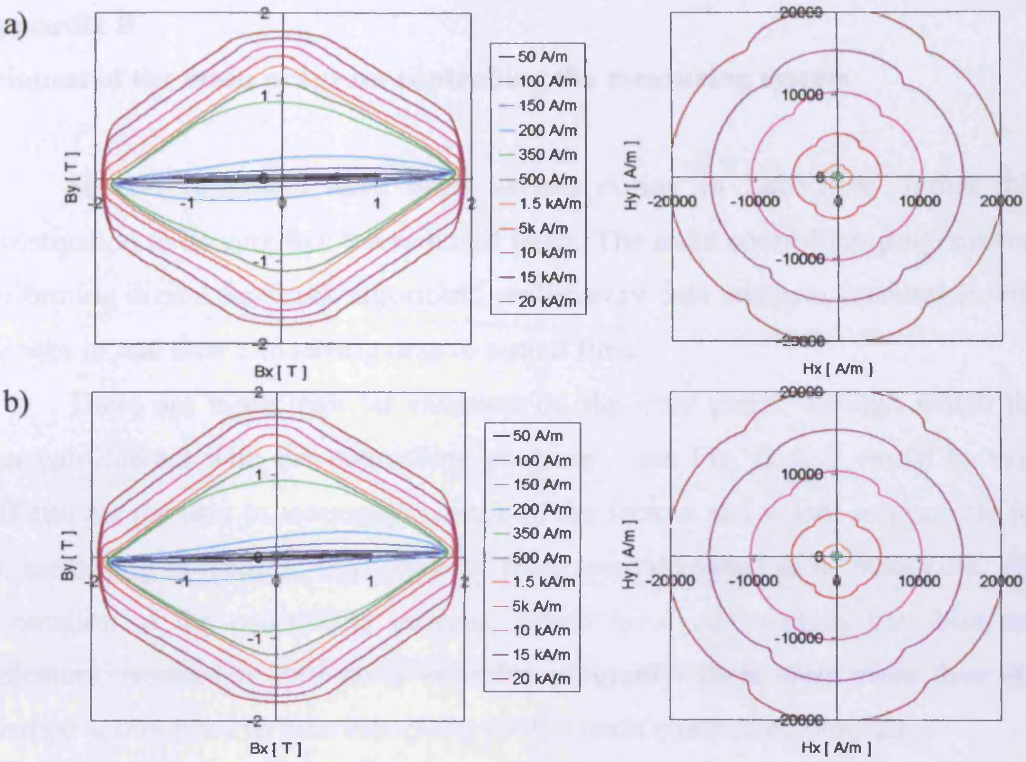

Fig. A-23. The results for high permeability grain-oriented electrical steel sheet measured under pseudo-controlled magnetic field (only the magnetising currents were set to sinusoidal shapes) at 50 Hz: a) clockwise, b) anticlockwise

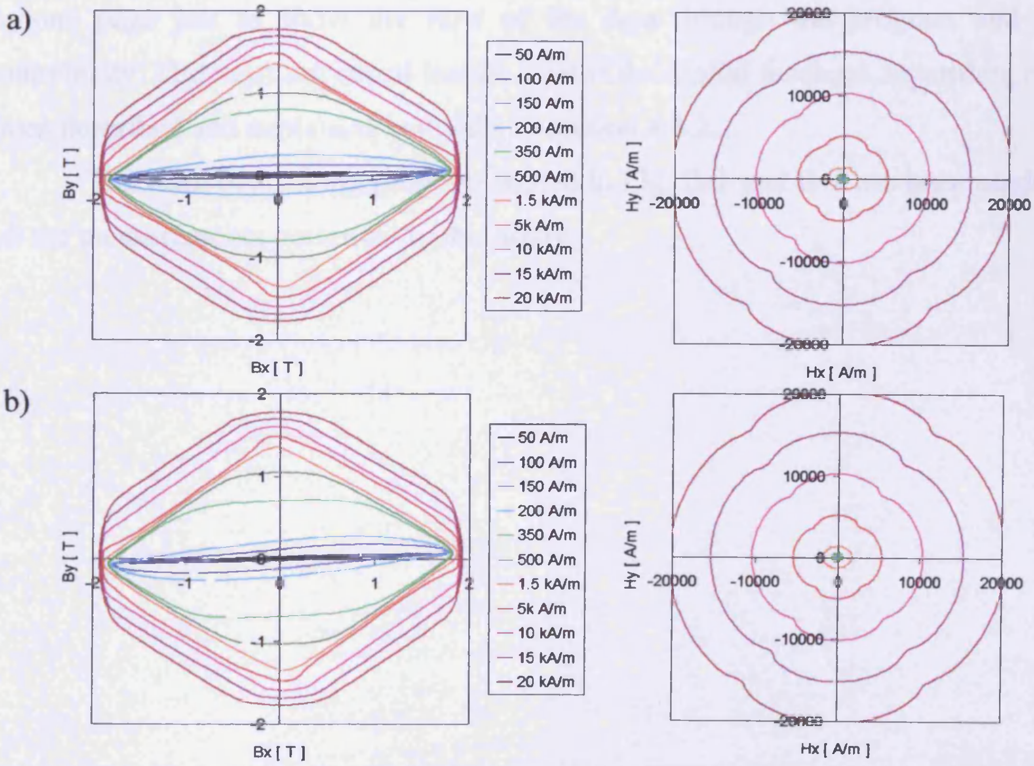

Fig. A-24. The results for high permeability grain-oriented electrical steel sheet measured under pseudo-controlled magnetic field (only the magnetising currents were set to sinusoidal shapes) at 250 Hz: a) clockwise, b) anticlockwise

Appendix B
Printout of the main program controlling the measuring system

Several programs have been written during in LabVIEW during this investigation to accomplish the required tasks. The main controlling program was performing digital feedback algorithm, preliminary data analysis, interaction with the user in real time and saving data to output files.

There are more than 60 elements on the front panel, through which the user can interact with the controlling program – see Fig. B-1. It would be very difficult for the user to manually control all the factors and values responsible for the measuring procedure, thus some of them were designed to be automatic. The automation of the controlling process, which involved so many variables and indicators, resulted in extremely complex program - there were more than one hundred subroutines written especially for the main controlling program.

The printout of the block diagram of the main controlling program is shown in Fig. B-2. The actual block diagram was occupying several computer screens and would be difficult to follow if normally printed. It has been minimised to one page just to show the flow of the data through the program and its complexity. The most important feature, that is the digital feedback algorithm, has been described and explained in details in section 4.4.2.1.

The main controlling program shown in Fig. B-1 and B-2 has been used in all the measurements presented in this study.

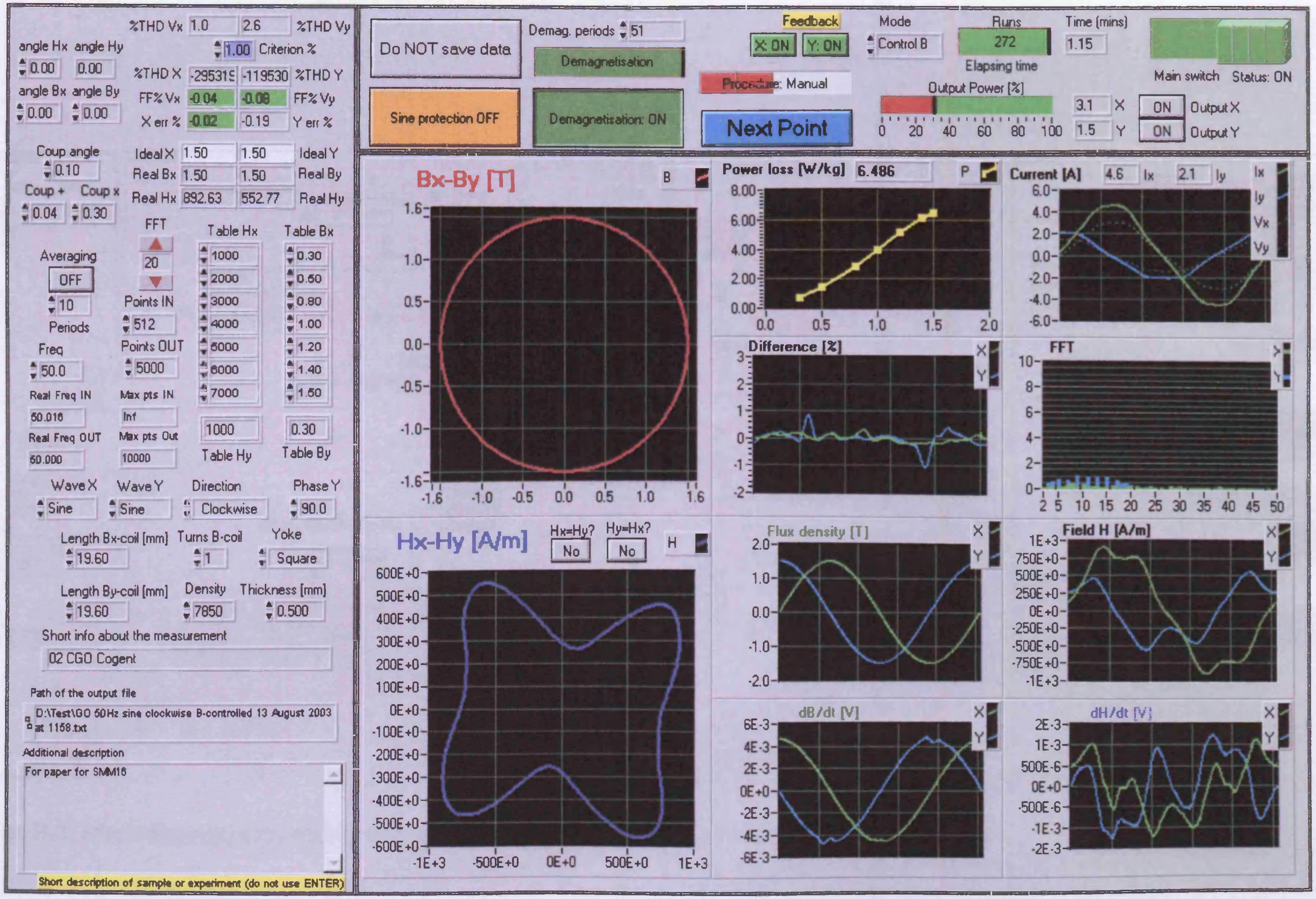

%THD Vx 1.0 2.6 %THD Vy
1.00 Criterion %
angle Hx 0.00 angle Hy 0.00
%THD X -295319 -119530 %THD Y
angle Bx 0.00 angle By 0.00
FF% Vx -0.04 -0.08 FF% Vy
X err % -0.02 -0.19 Y err %
Coup angle 0.10
Ideal X 1.50 1.50 Ideal Y
Real Bx 1.50 1.50 Real By
Coup + 0.04 Coup x 0.30
Real Hx 892.63 552.77 Real Hy
FFT 20
Averaging OFF
Periods 10
Points IN 512
Freq 50.0
Points OUT 5000
Real Freq IN 50.016
Max pts IN Inf
Real Freq OUT 50.000
Max pts Out 10000

Table Hx	Table Bx
1000	0.30
2000	0.50
3000	0.80
4000	1.00
5000	1.20
6000	1.40
7000	1.50

Table Hy 1000
Table By 0.30
Wave X Sine
Wave Y Sine
Direction Clockwise
Phase Y 90.0
Length Bx-coil [mm] 19.60
Turns B-coil 1
Yoke Square
Length By-coil [mm] 19.60
Density 7850
Thickness [mm] 0.500
Short info about the measurement: 02 CGO Cogent
Path of the output file: D:\Test\GO 50Hz sine clockwise B-controlled 13 August 2003 at 1158.txt
Additional description: For paper for SMM16

Demag. periods 51
Procedure: Manual
Mode Control B
Runs 272
Time (mins) 1.15
Status: ON
Output Power [%] 0 20 40 60 80 100
3.1 X
1.5 Y
ON Output X
ON Output Y
Power loss [W/kg] 6.486
Current [A] 4.6 Ix 2.1 Iy
Hx=Hy? No
Hy=Hx? No

Fig. B-1. Front panel of the main program (written in LabVIEW®) controlling the measuring system.

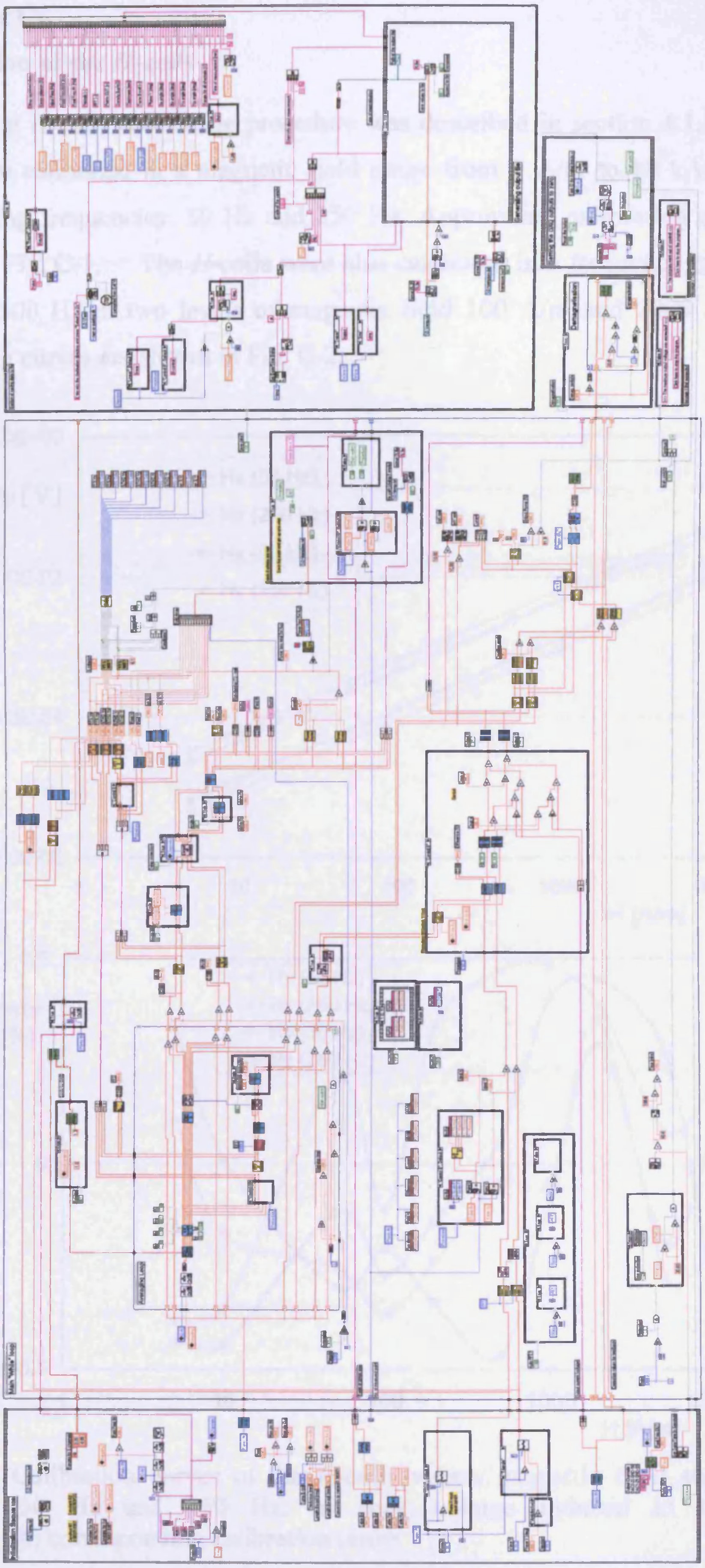

Fig. B-2. Block diagram of the main program (written in LabVIEW®) controlling the measuring system.

Appendix C

Calibration of the *H*-coils

The *H*-coils calibrating procedure was described in section 4.1.3. The *H*-coils were calibrated in a magnetic field range from 5 A/m to 10 kA/m at two magnetising frequencies: 50 Hz and 250 Hz. Appropriate calibrating curves are shown in Fig. C-1. The *H*-coils were also calibrated in a frequency range from 5 Hz to 500 Hz at two levels of magnetic field 100 A/m and 2000 A/m. The calibrating curves are shown in Fig. C-2.

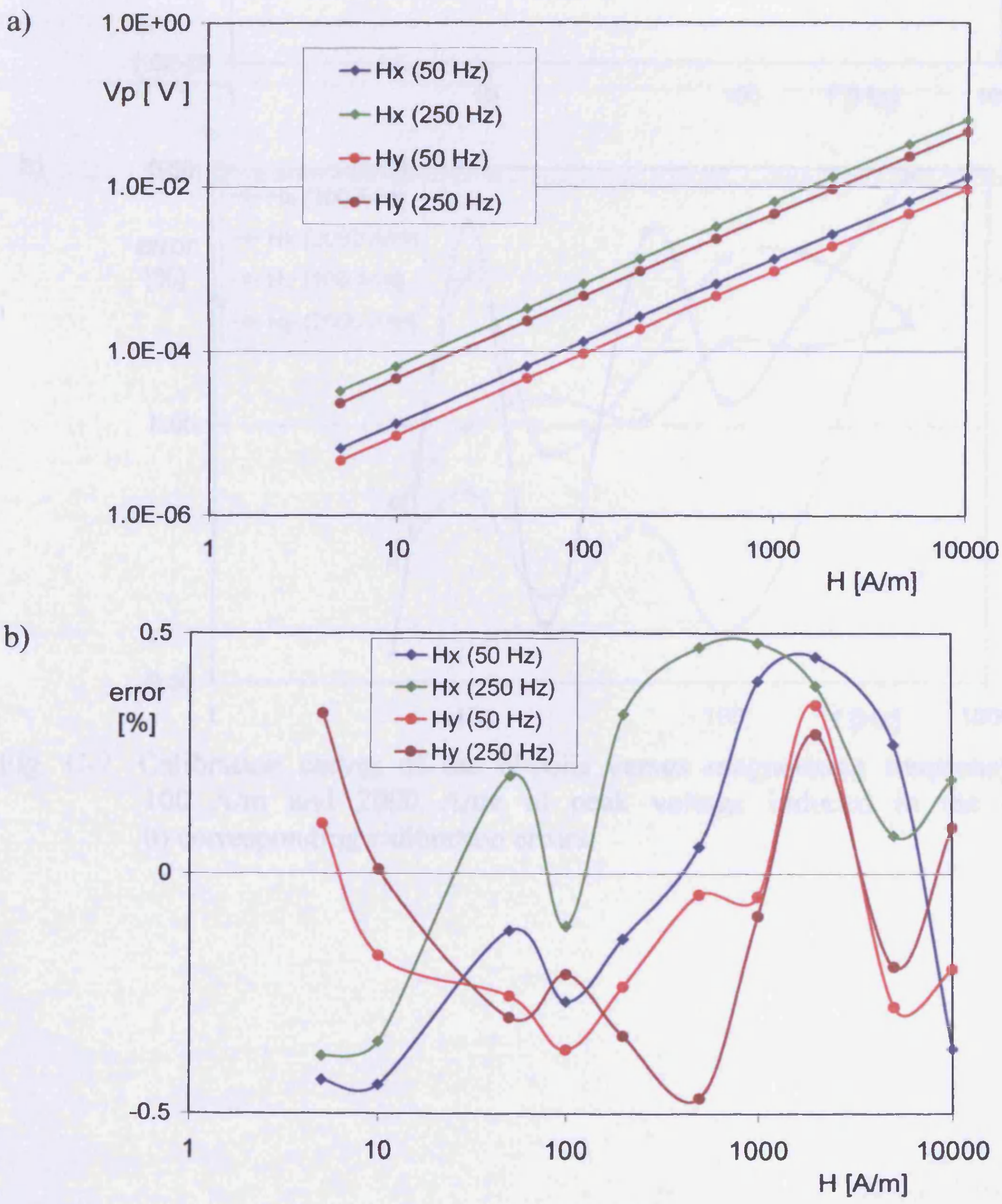

Fig. C-1. Calibration curves of the *H*-coils versus magnetic field strength for 50 Hz and 250 Hz: a) peak voltage induced in the coils, b) corresponding calibration errors

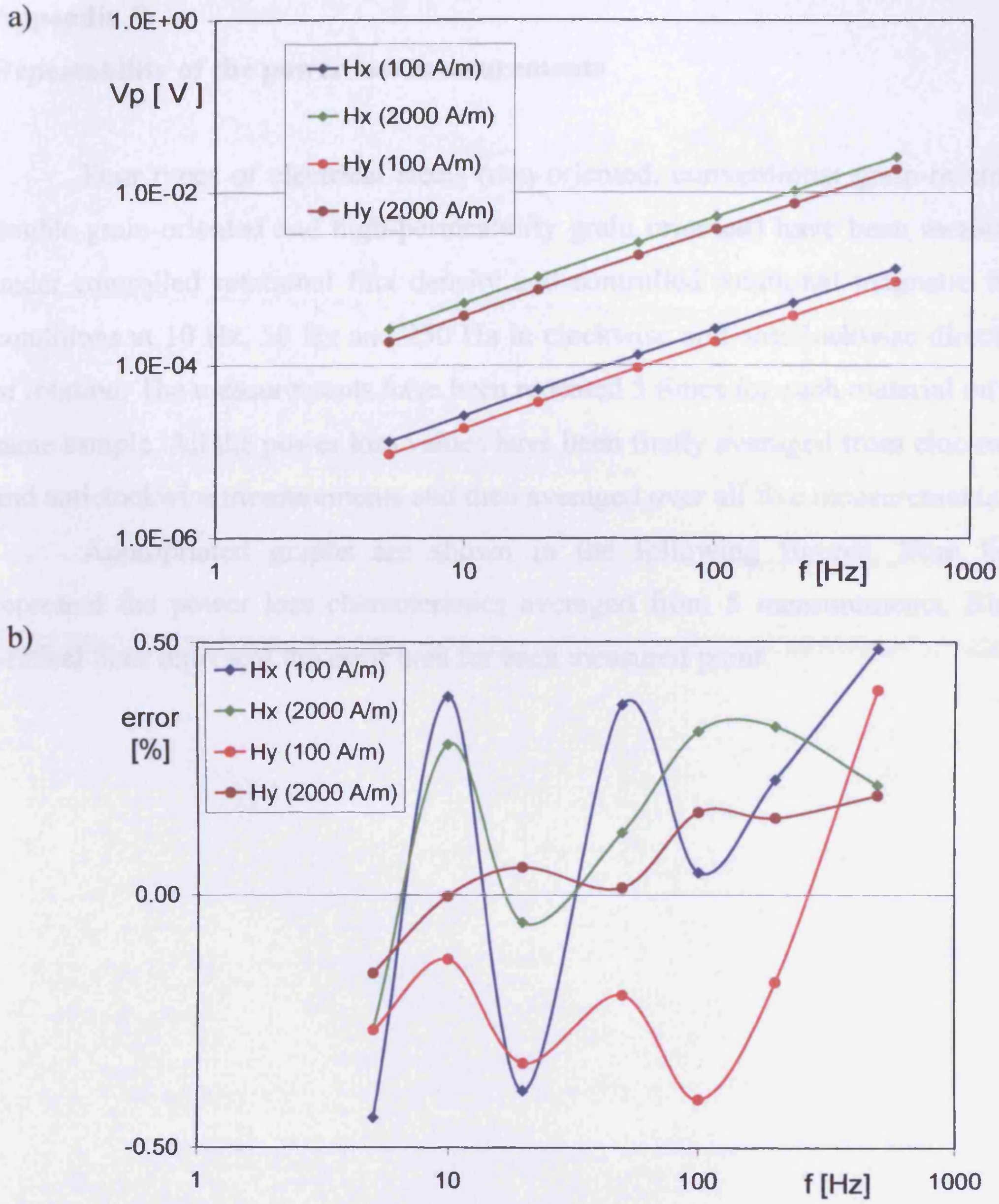

Fig. C-2. Calibration curves of the *H*-coils versus magnetising frequency for 100 A/m and 2000 A/m: a) peak voltage induced in the coils, b) corresponding calibration errors

Appendix D
Repeatability of the power loss measurements

Four types of electrical steels (non-oriented, conventional grain-oriented, double grain-oriented and high-permeability grain oriented) have been measured under controlled rotational flux density and controlled rotational magnetic field conditions at 10 Hz, 50 Hz and 250 Hz in clockwise and anticlockwise direction of rotation. The measurements have been repeated 5 times for each material on the same sample. All the power loss values have been firstly averaged from clockwise and anticlockwise measurements and then averaged over all five measurements.

Appropriated graphs are shown in the following figures. Blue lines represent the power loss characteristics averaged from 5 measurements. Black vertical lines represent the error bars for each measured point.

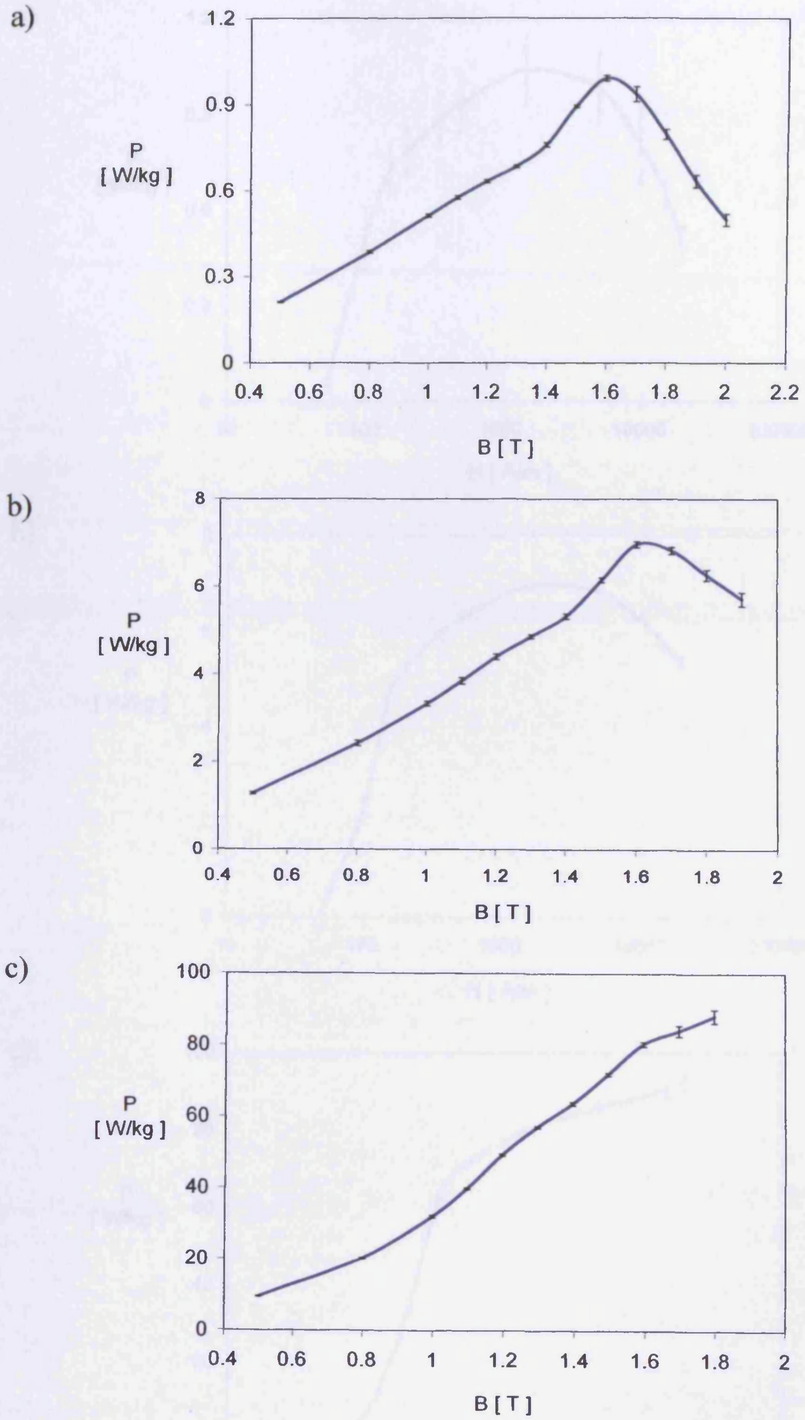

Fig. D-1. Power loss versus radius of controlled circular flux density for non-oriented electrical steel sheet measured at: a) 10 Hz, b) 50 Hz, c) 250 Hz

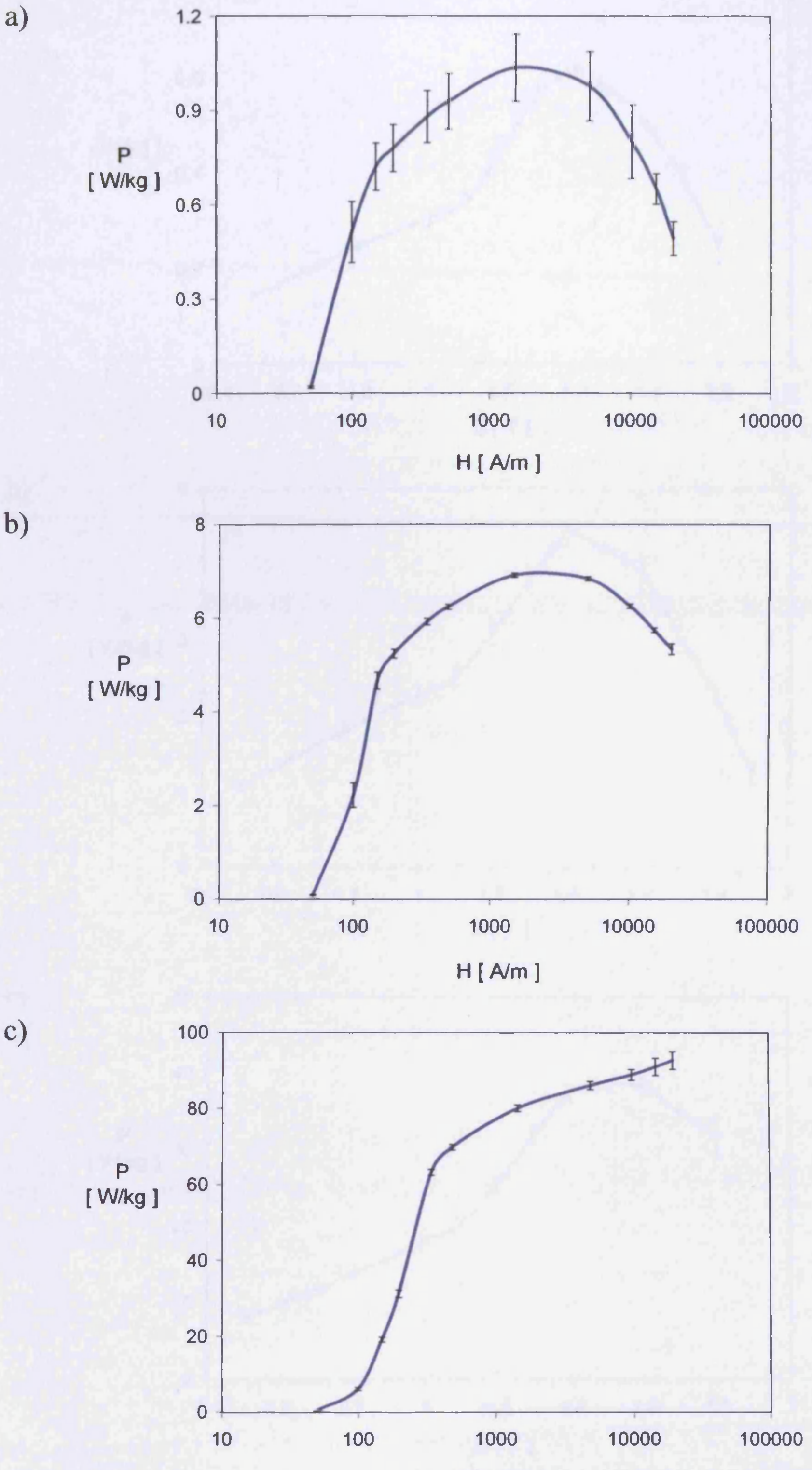

Fig. D-2. Power loss versus radius of controlled circular magnetic field for non-oriented electrical steel sheet measured at: a) 10 Hz, b) 50 Hz, c) 250 Hz

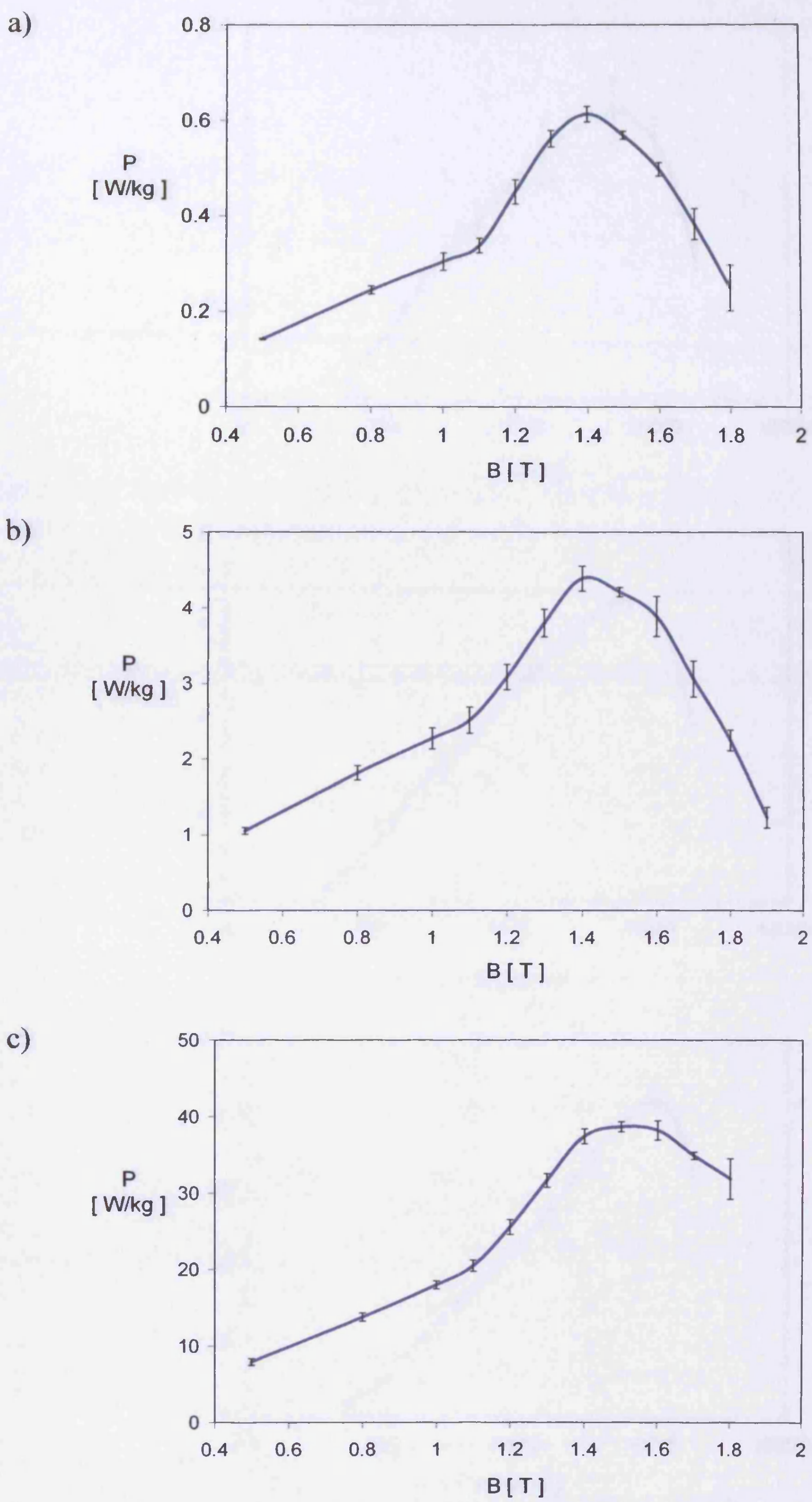

Fig. D-3. Power loss versus radius of controlled circular flux density for conventional grain-oriented electrical steel sheet measured at: a) 10 Hz, b) 50 Hz, c) 250 Hz

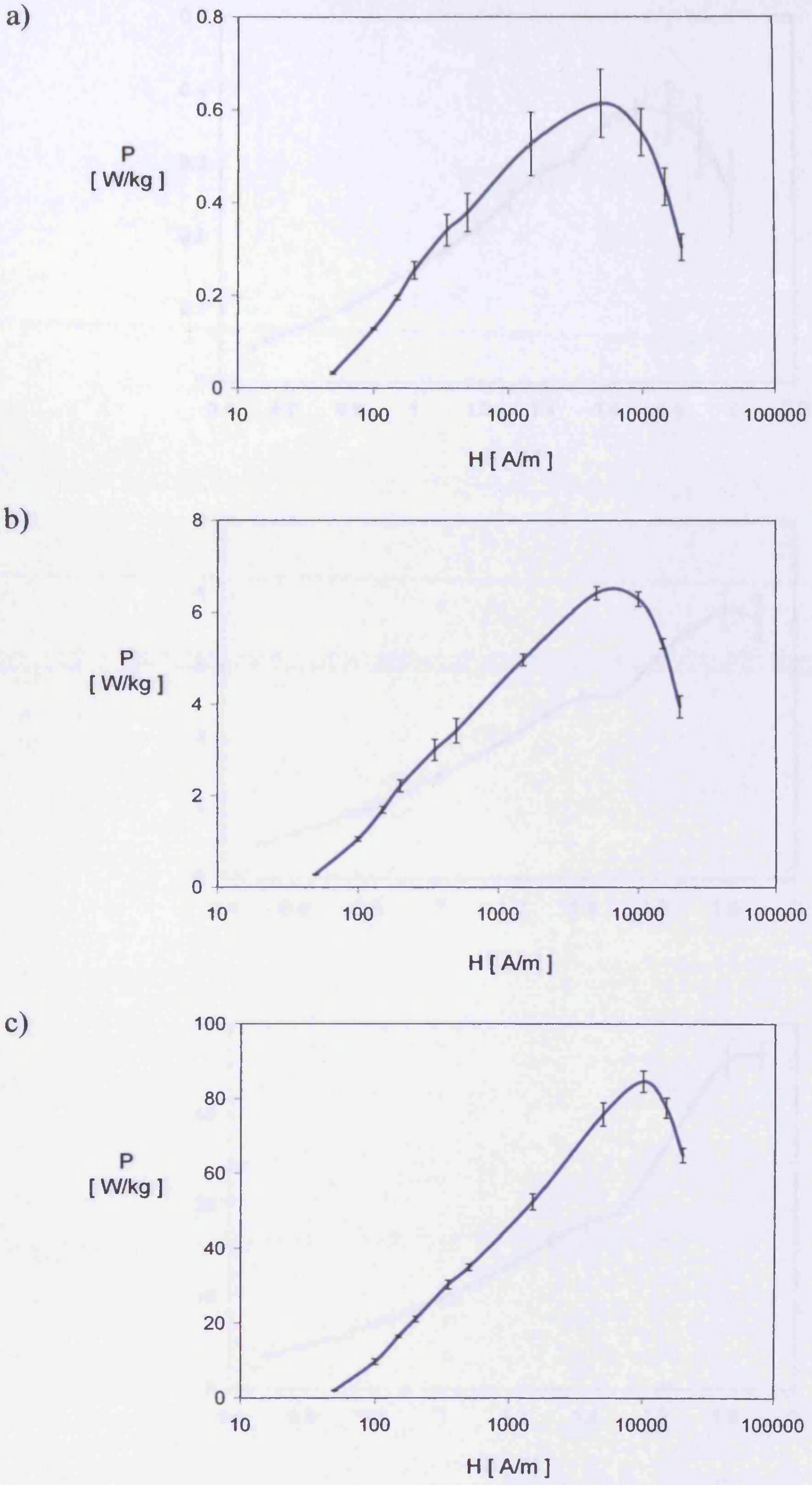

Fig. D-4. Power loss versus radius of controlled circular magnetic field for conventional grain-oriented electrical steel sheet measured at: a) 10 Hz, b) 50 Hz, c) 250 Hz

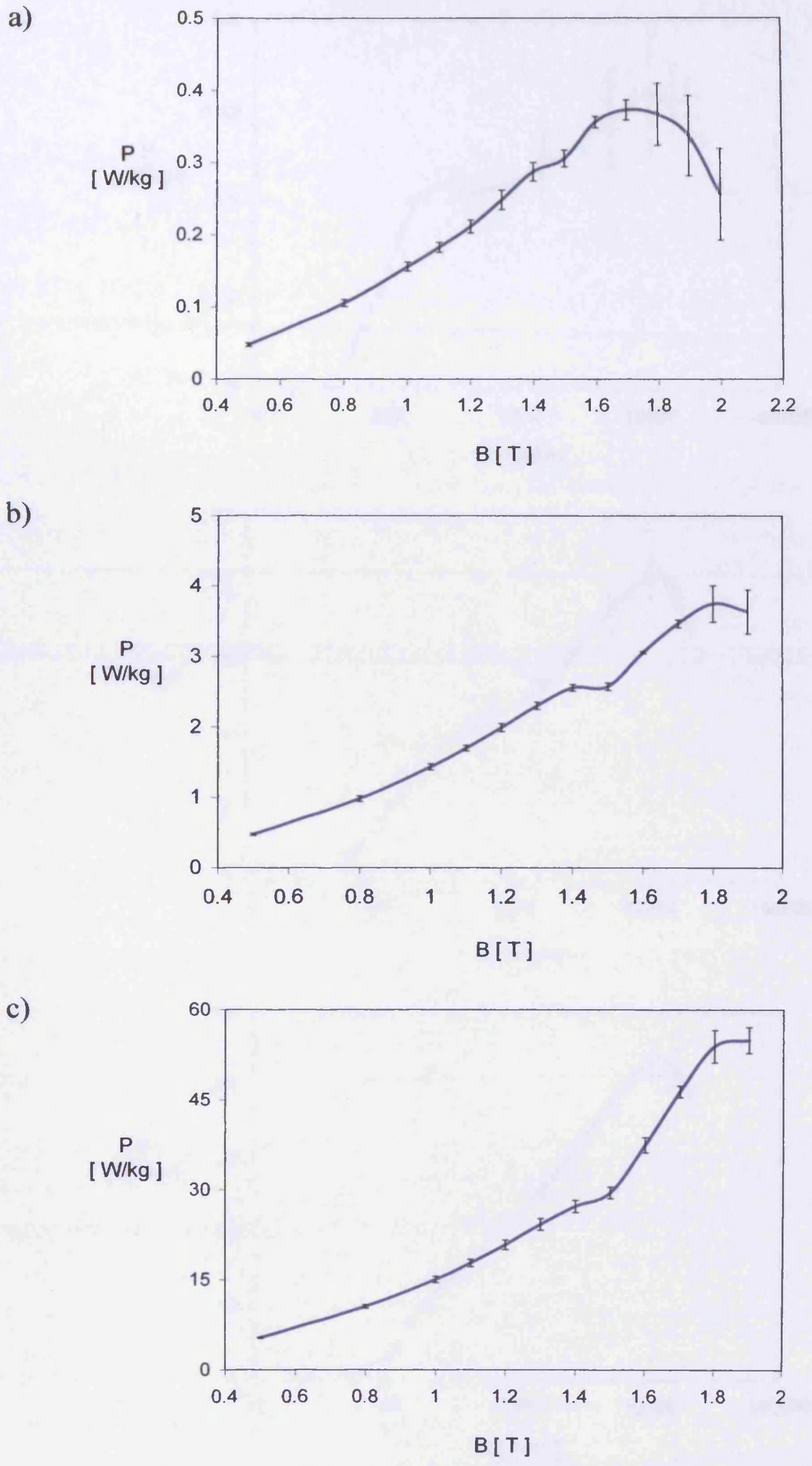

Fig. D-5. Power loss versus radius of controlled circular flux density for double grain-oriented electrical steel sheet measured at: a) 10 Hz, b) 50 Hz, c) 250 Hz

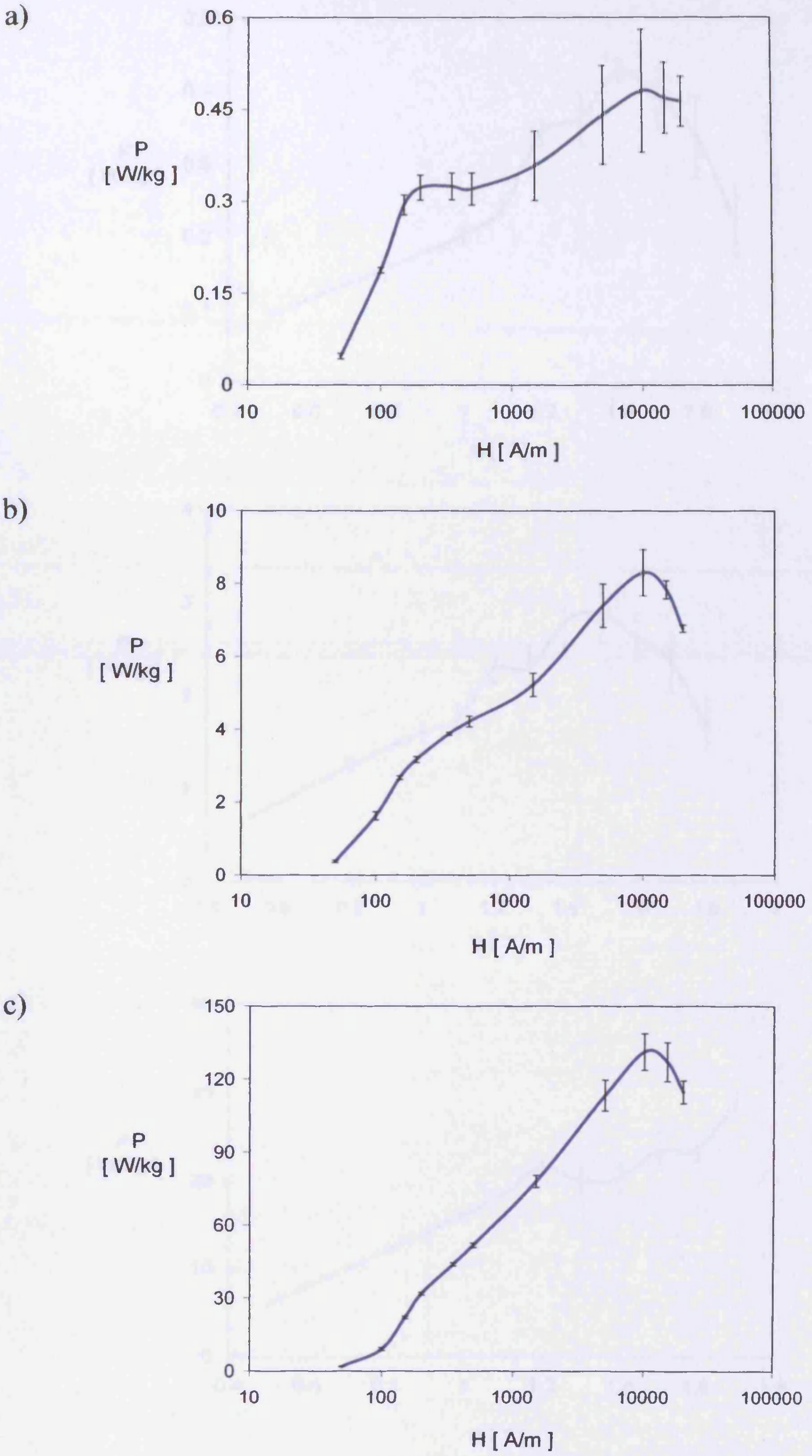

Fig. D-6. Power loss versus radius of controlled circular magnetic field for double grain-oriented electrical steel sheet measured at: a) 10 Hz, b) 50 Hz, c) 250 Hz

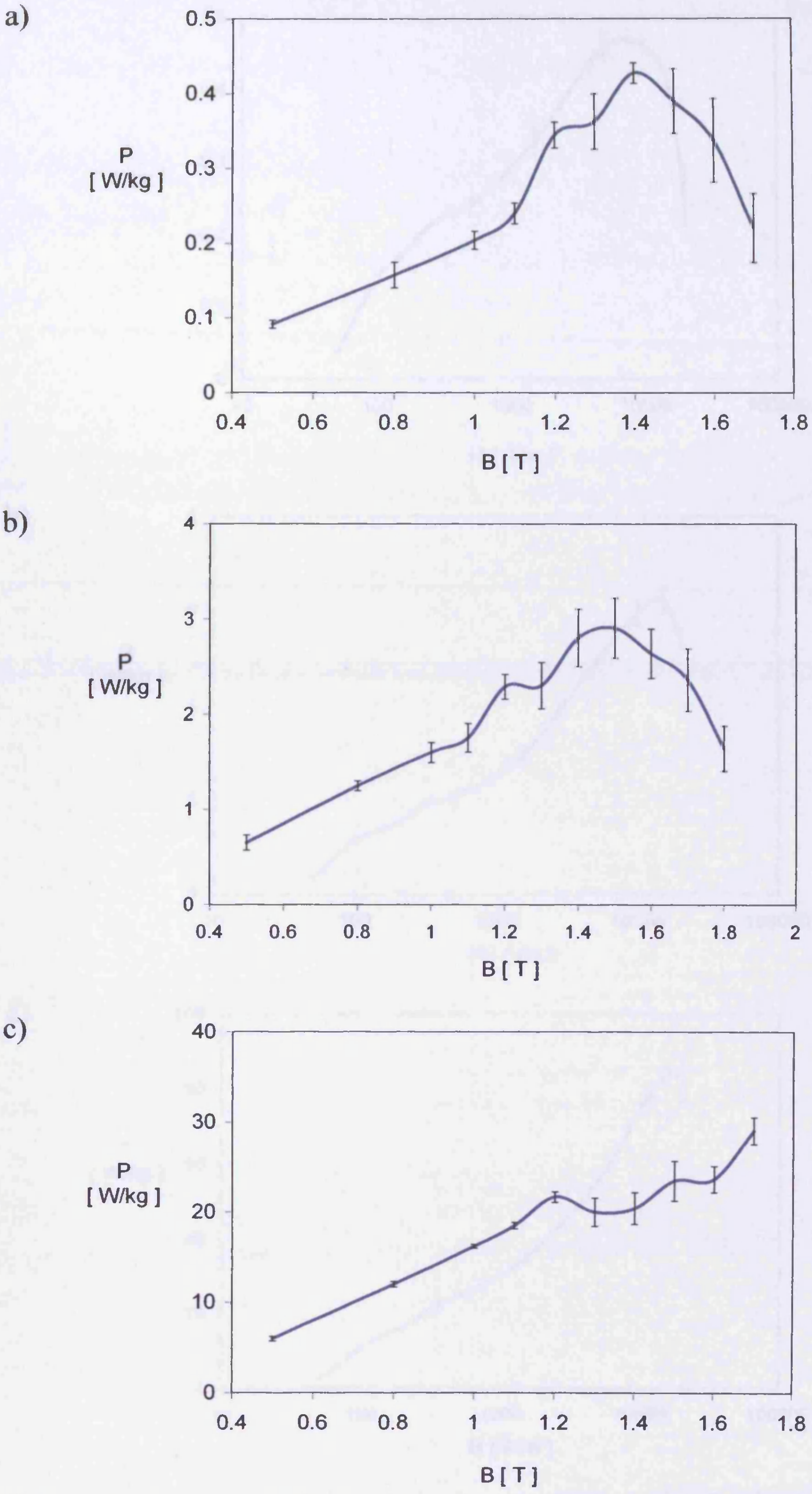

Fig. D-7. Power loss versus radius of controlled circular flux density for high-permeability grain-oriented electrical steel sheet measured at: a) 10 Hz, b) 50 Hz, c) 250 Hz

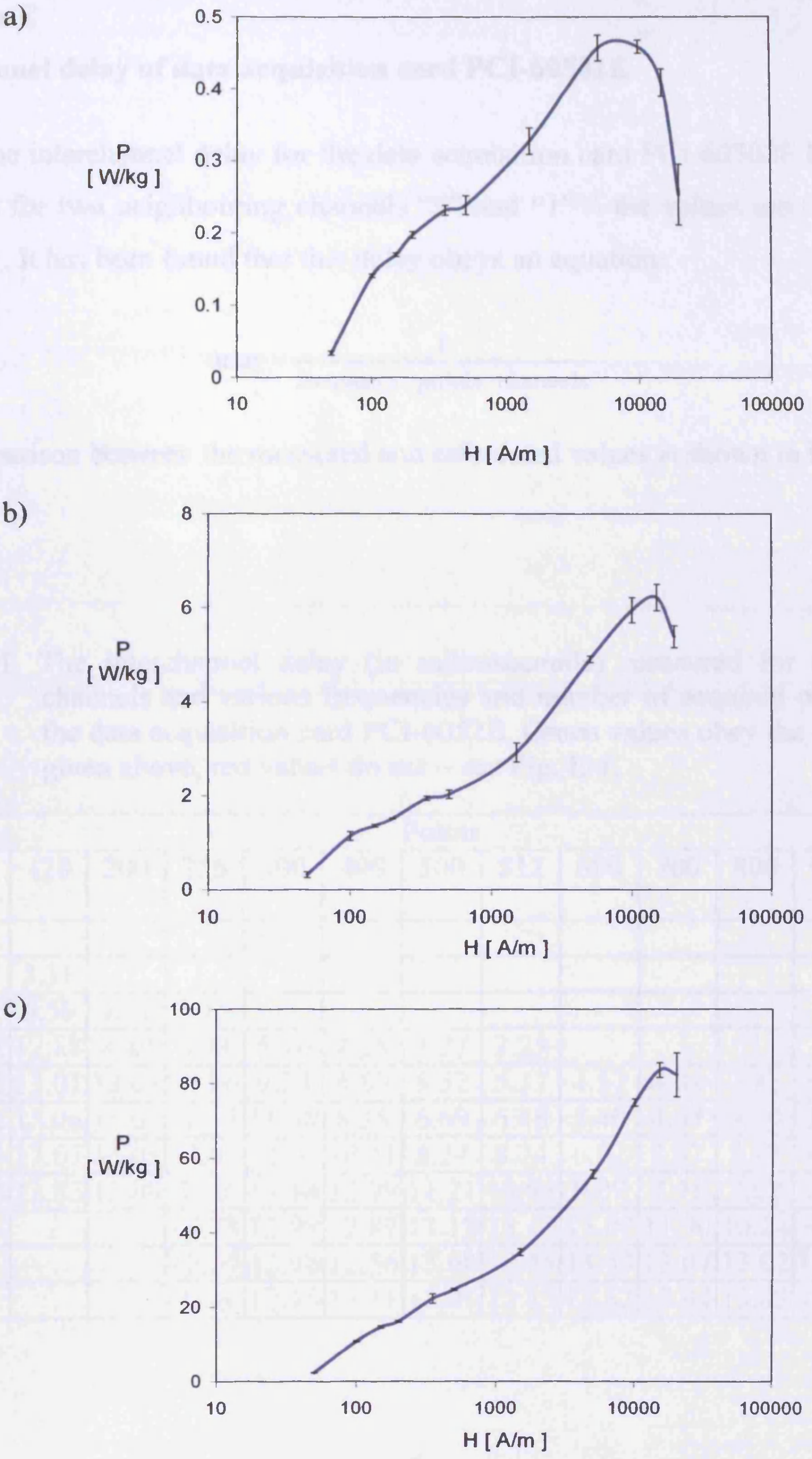

Fig. D-8. Power loss versus radius of semi-controlled magnetic field (see the magnetic field loci in Fig. A-22, A-23 and A-24 in **Appendix A**) for high-permeability grain-oriented electrical steel sheet measured at: a) 10 Hz, b) 50 Hz, c) 250 Hz

Appendix E

Interchannel delay of data acquisition card PCI-60502E

The interchannel delay for the data acquisition card PCI-60502E has been measured for two neighbouring channels "0" and "1" – the values are given in Table E-1. It has been found that this delay obeys an equation:

$$\text{delay} = \frac{1}{\text{frequency} \cdot \text{points} \cdot \text{channels}}$$

The comparison between the measured and calculated values is shown in Fig. E-1.

Table E-1. The interchannel delay (in microseconds) measured for 6 active channels and various frequencies and number of acquired points for the data acquisition card PCI-6052E. Green values obey the equation given above, red values do not – see Fig. E-1.

	Points												
Freq. [Hz]	100	128	200	256	300	400	500	512	600	700	800	900	1000
500	3.33												
400	4.17	3.31											
200	8.30	6.56	4.11	3.15									
100	12.71	12.88	8.40	6.38	5.40	4.28	3.27	3.25					
60	13.05	13.01	13.05	10.86	9.24	6.89	5.52	5.37	4.57	4.04	3.42	3.07	
50	13.04	13.06	13.07	12.93	11.08	8.35	6.69	6.48	5.40	4.67	4.10	3.65	3.33
40	12.93	13.07	13.05	13.02	12.94	10.41	8.24	8.24	6.92	5.97	5.13	4.71	4.17
30	12.88	12.85	13.09	13.2	13.14	12.99	11.21	10.93	9.09	7.91	7.02	5.99	5.63
20				13.23	12.98	12.87	13.18	13.15	13.07	11.90	10.24	9.32	8.30
10				12.59	12.96	12.56	13.08	13.45	13.43	13.07	13.02	13.08	12.92
5				12.6	12.75	13.11	13.05	12.89	13.62	13.94	13.03	12.88	13.72

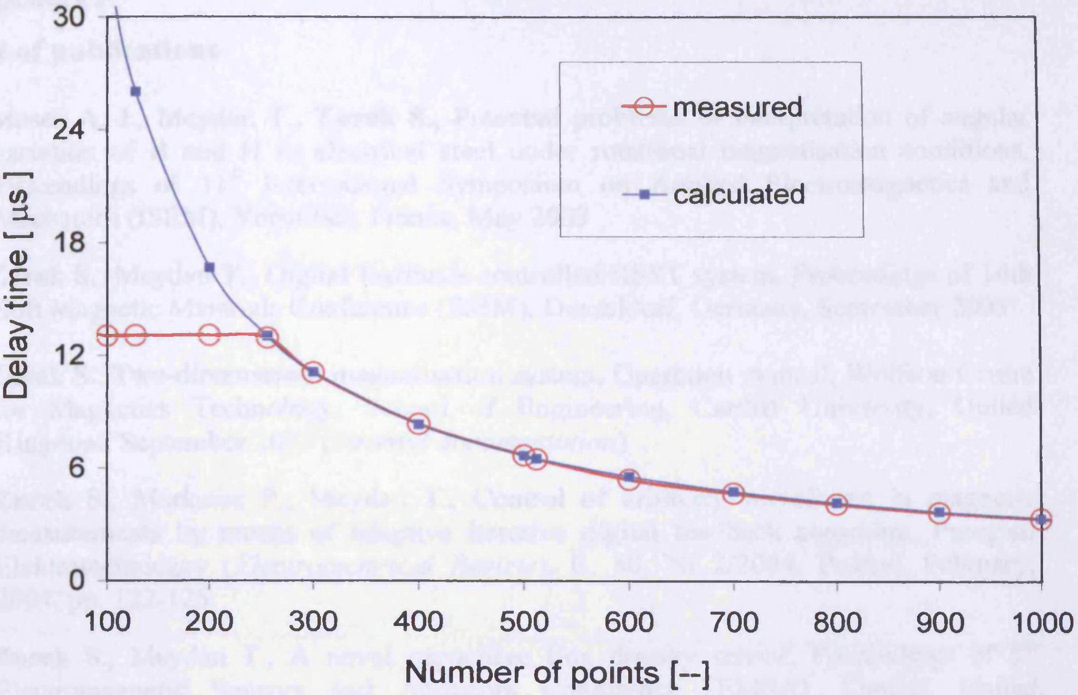

Fig. E-1. The comparison between measured and calculated interchannel delay (in microseconds) for the data acquisition card PCI-6052E for 6 active channels. In the interval of interest the calculated delay obeys the proposed equation.

Appendix F

List of publications

1. Moses A. J., Meydan T., **Zurek S.**, Potential problems in interpretation of angular variation of B and H in electrical steel under rotational magnetisation conditions, Proceedings of 11th International Symposium on Applied Electromagnetics and Mechanics (ISEM), Versailles, France, May 2003
2. **Zurek S.**, Meydan T., Digital feedback controlled RSST system, Proceedings of 16th Soft Magnetic Materials Conference (SMM), Dusseldorf, Germany, September 2003
3. **Zurek S.**, Two-dimensional magnetisation system, Operation manual, Wolfson Centre for Magnetics Technology, School of Engineering, Cardiff University, United Kingdom, September 2003 (*internal documentation*)
4. **Zurek S.**, Marketos P., Meydan T., Control of arbitrary waveforms in magnetic measurements by means of adaptive iterative digital feedback algorithm, Przeglad Elektrotechniczny (*Electrotechnical Review*), R. 80, Nr 2/2004, Poland, February, 2004, pp. 122-125
5. **Zurek S.**, Meydan T., A novel capacitive flux density sensor, Proceedings of 5th Electromagnetic Sensors and Actuators Conference (EMSA), Cardiff, United Kingdom, July 2004
6. Thant P.P.P., **Zurek S.**, Meydan T., Walmsley D., Control of tip oscillation in magnetostrictive dental scalers, Proceedings of 5th Electromagnetic Sensors and Actuators Conference (EMSA), Cardiff, United Kingdom, July 2004
7. Patel H.V., **Zurek S.**, Meydan T., Jiles D.C., A new adaptive automated feedback system for Barkhausen signal measurement, Proceedings of 5th Electromagnetic Sensors and Actuators Conference (EMSA), Cardiff, United Kingdom, July 2004
8. **Zurek S.**, Marketos P., Meydan T., Moses A. J., Use of novel adaptive digital feedback for magnetic measurements under controlled magnetizing conditions, IEEE Transactions on Magnetics, (in press, accepted for publication in September 2004)
9. **Zurek S.**, Meydan T., Precise post-triggering and correction of interchannel delay for alternating and two-dimensional measurements of magnetic properties, Proceedings of 8th International workshop on 1&2D magnetic measurement and testing (2DM), Ghent, Belgium, September 2004
10. **Zurek S.**, Meydan T., Quasi-static and dynamic rotational losses in non-oriented electrical steel sheet, (to be published in 17th Soft Magnetic Materials Conference SMM in Bratislava, Slovakia, September 2005)